Università degli Studi di Palermo

AREA QUALITÀ, PROGRAMMAZIONE E SUPPORTO STRATEGICO
SETTORE STRATEGIA PER LA RICERCA
U. O. DOTTORATI

Dottorato in Scienze Molecolari e Biomolecolari

Dipartimento di Scienze e Tecnologie Biologiche Chimiche e Farmaceutiche

Settore Scientifico Disciplinare CHIM/09

MULTIFUNCTIONAL POLYSACCHARIDES-DERIVED HYDROGELS WITH ANTIMICROBIAL PROPERTIES FOR INFECTED SKIN WOUND HEALING

IL DOTTORE

GIUSEPPINA BISCARI

IL COORDINATORE

Chi.mo Prof. GIOVANNA PITARRESI

IL TUTOR

Chi.mo Prof. GIOVANNA PITARRESI

IL CO-TUTOR

Chi.mo Prof. CALOGERO FIORICA

CICLO XXXVI

ANNO CONSEGUIMENTO TITOLO 2023

1. Introduction

1.1 The skin tissue - anatomy and pathophysiology of wound healing

The skin is the largest organ of the body and is the main defense barrier against harmful external physical, chemical, and biological agents.[1] It consists of three layers: the epidermis, the dermis, and the subcutaneous layer.[2] The epidermis is the superficial layer that forms the interface with the external environment and acts as a true physical barrier, preventing the entry of pathogenic microorganisms and other external harmful agents. The epidermis is basically made up of five layers. Starting from the deepest layer and moving towards the surface, the layers of the epidermis are: basal, spinous, granular, clear, and horny.[3] Each layer of the epidermis serves a specific purpose in protecting and renewing the skin, contributing to its overall functionality. They have various cell types including melanocytes, Merkel cells, Langerhans cells, $CD8^+$ T lymphocytes, corneocytes, and stem cells;[4,5] in the basal layer of the epidermis (innermost layer) the most representative population of cells present are the keratinocytes, which have the ability to pass to the upper layers, up to the stratum corneum (outermost layer), following a differentiation process.[6] The dermis is the middle layer, a tissue that acts as a mechanical support; it consists mainly of collagen, blood and lymph vessels, sweat glands, nerve cells, and mesenchymal stem cells (MSC);[7] the latter can differentiate into chondrocytes, osteocytes, adipocytes, smooth muscle cells, hematopoietic cells, neurons and glia cells.[8] Mesenchymal stem cells in the skin play a key role in the regeneration of skin tissues, producing growth factors and cytokines that support healing and offering therapeutic potential for skin conditions. Cells, mainly fibroblasts, are immersed in an extracellular matrix (ECM) consisting of proteins (mainly collagen), glycoproteins, proteoglycans, ions, and water.[9,10] The subcutaneous layer is a support and reserve tissue for the epidermis and dermis and consists of adipocytes, macrophages, fibroblasts, blood vessels

and nerves.[11] Following an injury, the skin loses its main protective barrier function. An ~~extremely~~ complex pathophysiological healing process is triggered, characterized by a cascade of events that are regulated step-by-step by various biological molecules and cell types.[12] In order to study the right therapy for treating skin wounds, it is essential to know the events that lead to the healing and regeneration process.[13] The pathophysiological healing process can be described by distinguishing four phases: hemostasis, inflammation, proliferation, and remodeling (**Figure 1**).[14]

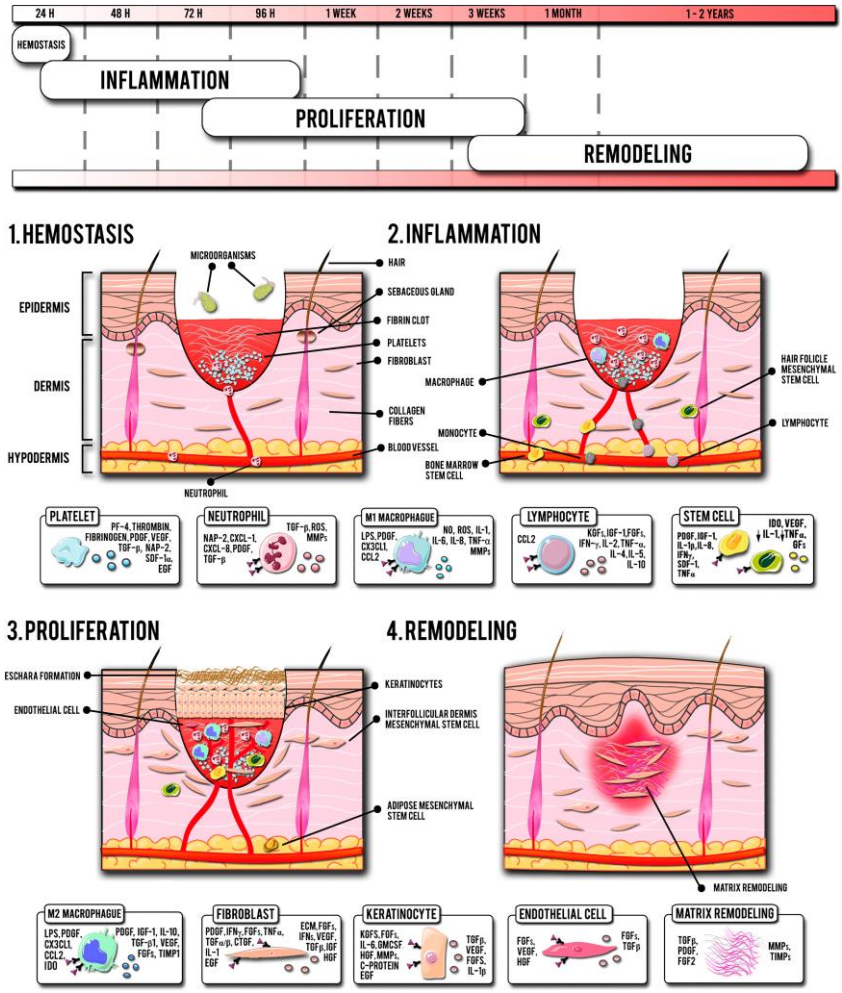

Figure 1. The normal wound healing process in 4 phases: haemostasis, inflammation, proliferation and remodeling.[13]

The hemostasis phase begins immediately after the injury, aims to limit bleeding, and forms a fibrin clot that acts as an anchoring structure for the cells involved in the subsequent steps.[15] In this phase, platelets release a number of growth factors (PF-4, VEGF, EGF, PDGF, TGF-β), chemokines, and cytokines (NAP-2, SDF-1α), which induce the migration of neutrophils, monocytes and macrophages into the wound bed.[16–19] With the advent of these cell types comes the inflammatory phase, during which macrophages cleanse the wound of bacteria, foreign bodies, cell debris, damaged extracellular matrix proteins, and neutrophils, secreting matrix metalloproteases (MMPs), antimicrobial peptides (AP) and reactive oxygen species (ROS), act on the bacterial walls of pathogens, preventing or extinguishing infection.[20] At the same time, monocytes differentiate into type 1 macrophages (pro-inflammatory) and amplify the inflammatory process mediated by nitric oxide (NO), ROS, interleukins (IL-1, IL-6, IL-8), tumor necrosis factor α (TNF-α) and metalloproteases (MMP).[21] During this phase, T-lymphocytes are called up, which stimulates the release of insulin growth factor 1 (IGF-1), fibroblast growth factor (FGF), and keratinocyte growth factor (KGF).[16,22,23] Phenotypic differentiation of M1 macrophages into M2 macrophages (from pro-inflammatory to anti-inflammatory) occurs, which induces the release of growth factors (VEGF, PDGF, IGF-1, FGF) and the tissue inhibitor of metalloproteases 1 (TIMP1), which inhibits further degradation of the extracellular matrix (ECM).[24] The large number of growth and chemotactic factors released at the level of the wound bed leads to the proliferation phase, in which indoleamine 2,3-deoxygenase (IDO) is released, which reduces the amount of ROS present and causes an increase in oxygen, which is crucial for the mesenchymal stem cells (MSCs), which begin to infiltrate, to differentiate into fibroblasts (oxygen-dependent cells).[25,26] Thus, there is simultaneous under-regulation of the inflammatory response, over-regulation of the anti-inflammatory response, and deposition of extracellular matrix by fibroblasts with the formation of granulation tissue, a provisional, richly vascularised tissue

that will serve as the basis for subsequent remodeling.[27] There is also a gradual differentiation and proliferation of keratinocytes, which induce re-epithelisation, forming cell layers that form the barrier in the stratum corneum.[28,29] Finally, the fibroblasts differentiate into myofibroblasts, containing actomyosin, which by contracting promotes wound closure.[14] During the final remodeling phase, fibroblasts promote the replacement of type III collagen, whose degradation is mediated by metalloproteases, with type I collagen. Consequently, in this phase, there is a reduction in cell migration, and vascularisation, then a decrease in granulation tissue, and finally the formation of scar tissue.[30,31] Dysregulation of the expression of proteins or cells involved in the wound-healing process can lead to the formation of a chronic wound, so it is crucial to encourage the correct skin regeneration process.[13] Certain pathologies, such as arterial and venous insufficiency, hypertension, diabetes, obesity, cardiovascular and autoimmune diseases can lead to a failure of the normal wound healing process by inducing the formation of venous lesions of the lower limbs, arterial ulcers, diabetic foot ulcers.[22,32] A wound is considered chronic when the healing process has not taken place within three months of the injury event.[33] In chronic wounds, the up-regulation of pro-inflammatory mediators and metalloproteases occurs simultaneously with the down-regulation of anti-inflammatory mediators and tissue inhibitors of metalloproteases.[34] There is also altered cellular expression, with neutrophils showing morphological abnormalities and tending to remain in the wound for a long time, leading to an imbalance in ROS production; M1 macrophages do not differentiate into M2 macrophages; fibroblasts have a reduced proliferative capacity as there is not enough oxygen; and keratinocytes are unable to differentiate or are hyperproliferative.[35–38] All of this results in a persistent inflammatory environment, amplified by colonization by pathogens, thus susceptible to infections that are difficult to eradicate, and also in the insufficient formation of functional ECM and the failure to produce granulation tissue, thus

the inability to proceed to the proliferative phase.[13] Neutrophils play a key role in mediating the response against pathogens; in fact, following damage they intervene through the production of ROS, which is the main weapon of defense against microorganisms. Therefore, the migration of neutrophils must be finely regulated, because a deficiency of neutrophils can lead to the onset of serious infections due to uncontrolled microbial proliferation; but an excess of neutrophils can also amplify the inflammatory process, leading to the excessive production of ROS, which can slow down or even block the healing process due to the high oxidative stress.[39] Thus, in chronically damaged tissue, a hypoxic condition occurs, due to the destruction of blood vessels and increased oxygen consumption by cells in the wound bed, which slows down the tissue repair process, blocking fibroblast proliferation and angiogenesis, inhibiting collagen synthesis and increasing the risk of infection.[40]

In this context, the main obstacle in the process of tissue repair is the onset of infection; the injured skin loses its barrier function, as a result, microorganisms penetrate into the deeper layers and find a favorable environment in which to proliferate, impeding the regeneration process.[41] The pathogens most frequently isolated from skin wounds, chronic or otherwise, are Gram-negative, such as *P. aeruginosa* and *E. coli*, and Gram-positive, such as *S. aureus* and *S. pyogenes*.[42] These micro-organisms can produce a biofilm on acute wounds inducing chronic wound formation. A biofilm consists of an aggregate of sessile bacterial cells, belonging to various species, immersed in a polymer matrix produced by them, resistant to penetration by antimicrobials and immune system cells. The presence of bacteria, both in free form and incorporated into biofilms, is particularly detrimental to the wound-healing process, especially when bacteria reach a critical colonization level. Microbial colonization delays the healing process and increases inflammation by producing excessive granulation tissue, which often develops into extensive and disfiguring scars. The presence of diverse

microbial flora in wounds makes treating patients more difficult, especially when the biofilms of chronic wounds are mostly composed of a large number of resistant microorganisms. Clearly, in order to stimulate the healing process, treatment with antibiotics is essential. Over the years, inappropriate use and misuse of antimicrobial drugs have led to the emergence of multidrug-resistant (MDR) microbes, which pose a serious threat to public health, particularly in hospital-acquired infections, due to biofilm formation, horizontal gene transfer and microbial mutations.[43] In the past, antibiotics were administered systemically to treat severe skin wounds or chronic wounds, such as diabetic foot. However, this method has significant drawbacks as it requires large doses of drug to ensure effective concentrations at the affected site. These high doses increase the risk of side effects as the drug spreads to other parts of the body. In addition, in chronic wounds with poor vascularity, the amount of drug reaching the wound through the bloodstream is often insufficient to inhibit bacterial growth.[44] Applying broad-spectrum antibiotics directly to the wound using medicated gauze or dressings has been the preferred method. However, this approach has limitations. For example, topical antibiotics such as neomycin or gentamicin can cause local irritation and contact dermatitis.[45] Even concentrating the drug directly on the wound cannot overcome the problem of antibiotic resistance, as multi-resistant strains of bacteria remain insensitive to even high doses of common antibiotics.[46–48] According to the WHO report on antimicrobial resistance, antimicrobials used to treat common infections are showing high rates of resistance. An estimated 700,000 people worldwide die each year because of antimicrobial resistance. This number could reach 10 million by 2050 if no action is taken to reduce this phenomenon or develop new antibiotics.[46–48] Antibiotic resistance is a serious problem in the treatment of chronic wounds, which has led to the need to find alternative therapeutic strategies to the commonly used treatments. There is therefore an urgent need to

develop new antimicrobial agents that can be applied topically to wounds to overcome the limitations of traditional treatments described above.

1.2 Therapeutic strategies for the treatment of skin wounds

1.2.1 Limitations of traditional wound healing approaches

In recent decades, research into new therapeutic strategies for the treatment of chronic skin wounds has gained considerable importance both in terms of improving quality of life and life expectancy and for economic reasons.[13] Indeed, around 40 million patients worldwide suffer from chronic skin wounds, a number that has reached epidemic proportions and is comparable to that of carcinoma patients.[49,50] The production of therapeutic systems that can be used to treat this type of wound could have a major economic and social impact.[13] Since ancient times, attempts have been made to remedy these problems, for example in a stone tablet dating back to 2200 B.C., the so-called "*three healing gestures"* were found engraved, i.e. the three gestures to be made after a wound: wash it, dress it and finally cover it. The Chinese, Sumerians and Egyptians, on the other hand, envisaged the use of beer, vinegar, wine, milk, animal fat, leaves, tree resin, and honey in the treatment of wounds.[21,51] Wound dressing techniques (bandages, gauze, etc.) do not allow adequate tissue rehydration, cause pain upon removal, and do not adhere tightly to the wound site, reducing applicability. Gauzes or bandages may be displaced by body movements, especially when the wound is located in places subject to greater stress such as the knee, ankle, or wrist, reducing patient compliance.[52]

1.2.2 Novel wound healing approaches

The research for the most appropriate therapeutic solution is still ongoing that can be simultaneously smart, multifunctional and also improve patient compliance. An ideal system for this type of application should have specific requirements, such as biocompatibility, biodegradability, favouring the hydration of damaged tissue and eliminating exudate, allowing gas exchange with the outside, adapting to the wound bed and resisting mechanical deformations induced by movement (self-healing ability), being able to remain attached to the often irregular perimeter of the wound without being washed away by biological fluids (adhesiveness) and inhibiting microbial growth (**Figure 2**).[42] Only in recent years have innovative therapeutic strategies appeared, thanks to the discovery of new biomaterials applicable in tissue engineering and knowledge of the pathways and molecules involved in the wound regeneration process.[53] Several smart stimulus-responsive therapeutic systems capable of inducing on-demand drug release have been developed, including semi-permeable films, 3D scaffolds, microparticles, nanoparticles or nanofibres that can be activated by an exogenous (electromagnetic radiation, ultrasound) or endogenous (pH, enzymes) stimulus.[1]

1.2.2.1 Hydrogels

Figure 2. Properties of an ideal wound care system compared to the properties of hydrogels.[42]

As **Figure 2** shows, there are numerous requirements that an ideal wound treatment system should possess. Hydrogels are systems with comparable characteristics to those mentioned in the figure.[41] In fact, from a technological point of view, hydrogels are semi-solid preparations in which the colloid-sized dispersed phase forms a three-dimensional network that retains the liquid dispersant phase. Most hydrogels used in the pharmaceutical field consist of water-like macromolecular colloids that are solvated and induce gel formation through the formation of intra- and intermolecular bonds of various kinds (both covalent and non-covalent). From a technological point of view, considering its composition, even native ECM can be considered a hydrogel. In fact, the ECM is a complex three-dimensional network of extracellular macromolecules found in all tissues and organs in the body. The

native ECM is an intricate and diverse structure, consisting of not only polymers but also a combination of proteins, glycosaminoglycans, collagen, and other biomolecules. It provides structural and mechanical support to cells, biochemical signaling, and a framework for cells to adhere, migrate, and function properly. This is also the reason why hydrogels are the pharmaceutical systems of choice in the regenerative treatment of skin wounds.[54–56] The ability to incorporate a high water content allows excess exudate in the wound bed to be absorbed while maintaining a hydrated environment. This process is critical to avoid tissue maceration and to eliminate nutrients used by microorganisms for their proliferation.[57,58] The porous structure of the hydrogel promotes the passage of gases, in particular oxygen, which is essential in the process of tissue repair so that cells can proliferate and form granulation tissue.[59] Many of the medical devices currently used in the clinic for the treatment of skin wounds are xerogels obtained by freeze-drying hydrogels. These systems are actual sponges that are applied to the wound bed and form the hydrogel following the absorption of physiological fluids. While the application of a preformed system can be advantageous in terms of ease of application, it has major limitations related to its poor ability to optimally adapt to the wound bed from a morphological and mechanical perspective. This issue leads to imperfect covering resulting in a reduced stay of the hydrogel on the wound bed, consequently leading to infection and inducing an inflammatory response.[12] Injectable hydrogels overcome these problems, as they can perfectly cover the wound bed, following the irregular wound margins and reaching the deepest tissues. Typically, these systems are applied through the aid of a syringe in the form of a fluid pre-gel (sol), which at the site of administration undergoes a sol-gel transition taking the shape of the locus in which it is applied (in situ forming).[52,60] In-situ gelling can be induced by pH variation, temperature and ionic strength.[61–64] Cross-linking processes play a crucial role in determining the internal structure of hydrogels. Consequently, the intrinsic properties of hydrogels are closely linked

to the cross-linking processes that characterize them.[65] As a result, the enrichment of the functional capabilities of hydrogels is closely linked to the innovation of manufacturing strategies. Chemical methods focus on producing stable hydrogels with adequate mechanical properties, while physical approaches take advantage of biocompatibility, avoiding the use of chemical agents for cross-linking. A synergistic approach combining physical and chemical methods would be beneficial to achieve an optimal balance of hydrogel properties. Indeed, several studies have demonstrated the effectiveness of hybrid crosslinking strategies in obtaining hydrogels capable of self-healing and even suitable for injection.[66] For example, a double cross-linked hydrogel has been developed by combining physical cross-linking based on hydrogen bonds and chemical cross-linking through imine bonds.[67] This type of hydrogel has shown exceptional self-healing capabilities. In addition, physical crosslinking can serve as a second crosslinking layer to increase the mechanical strength of the hydrogel. Consequently, a comprehensive approach to cross-linking in the hydrogel formation process opens up new perspectives for the production of smart, self-healing hydrogels.[68,69] In this context, the concept of cross-linking based on dynamic covalent chemistry (DCC) has found applications in various fields, including the development of combinatorial molecular libraries, thermosensitive shape-shifting polymers, bioconjugation strategies, injectable and self-healing, controlled drug release and pH-responsive hydrogels, as well as in three-dimensional culture for tissue engineering, fits well.[68–75] Among the dynamic covalent chemistry reactions, there are some that are part of the so-called "click-chemistry".[76] Utilization of “click chemistry” for design and fabrication of functional hydrogels grown rapidly since 2001.[77] Chemical reactions that are termed click reactions possess advantages such as high yields under mild conditions, fewer by-products, high specificity and selectivity. A wide variety of functional groups can act as attractive candidates for the fabrication of complex polymeric materials.[78] (**Figure 3**).

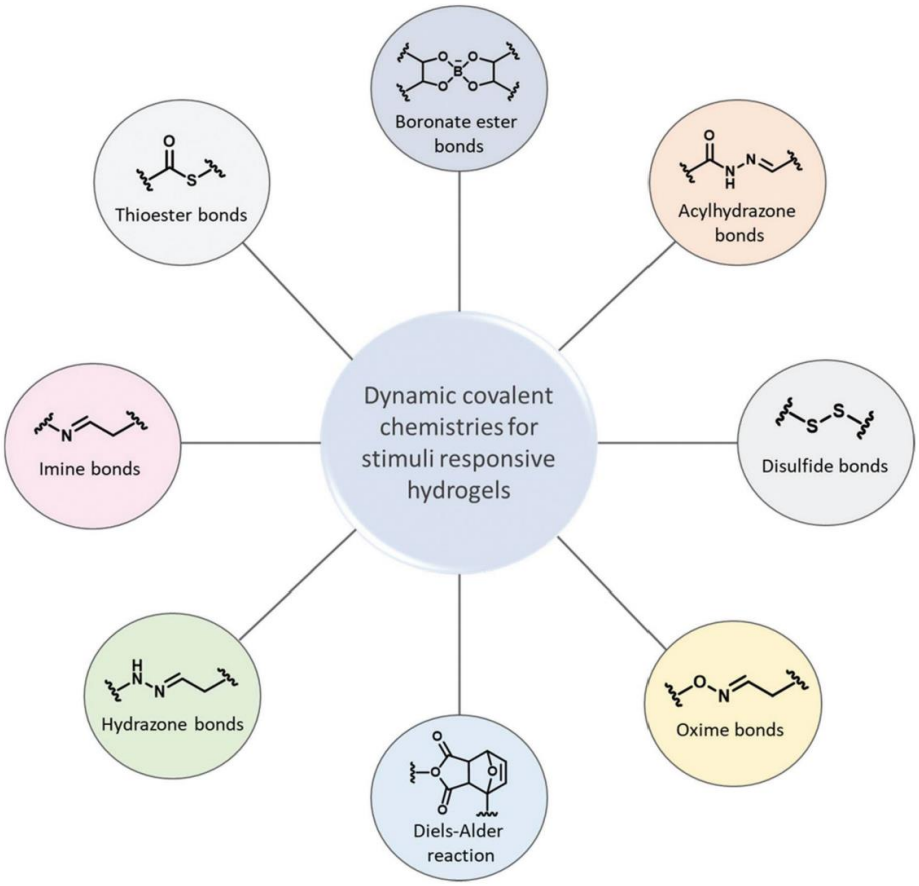

Figure 3. Dynamic covalent bonds are used for the preparation of hydrogels.[79]

Among these, an interesting reaction is the one that leads to the formation of the imine bond, which occurs between amino and aldehyde groups to generate an imine bond in physiological conditions. This process can be readily employed in the creation of injectable hydrogels.[80] Schiff base takes advantage of the dynamic equilibrium between the imine bonds and the aldehyde and amine reagents; such bonds can be considered pseudo-covalent bonds. The breaking and forming of imine bonds occurs within the hydrogel networks,

giving the latter the ability to self-repair.[81] For example, a self-healing polymer hydrogel can be fabricated through self-crosslinking between the amino group from acrylamide-modified chitin (AMC) and the dialdehyde group (ADA) from oxidized alginate. The ability to self-heal also depends on the molar ratio of AMC to ADA, as well as the surrounding pH (**Figure 4**).[82]

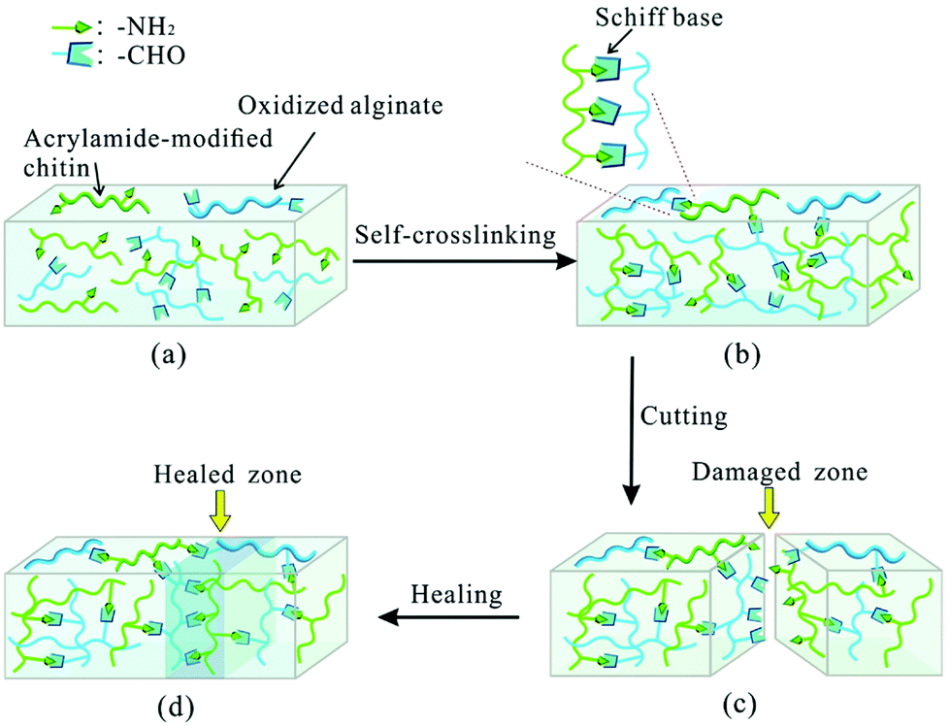

Figure 4. Schematic illustration of imine bond formation and self-healing process, *via* Schiff Base linkage between the amino group of acrylamide-modified chitin (AMC) and the dialdehyde group (ADA) of oxidized alginate.[82]

One of the inherent drawbacks of injectable hydrogels is their insufficient adhesion to the wound bed, making them prone to being swiftly displaced and eliminated from the application site upon contact with biological fluids. For this reason, various research groups have made numerous efforts in recent years to produce hydrogels with tissue-adhesive capabilities that can bind tightly to native

tissues even under conditions of high hydration and isolate the wound site from possible colonization by surrounding microorganisms.[83–86] One approach employed for this objective involves modifying the initial biomaterial with catechol structures, developing biomaterials mussels-inspired.[41] They are responsible for the characteristic adhesion of mussels to reefs and are able to promote the adhesion of biomaterial to biological tissues by establishing both physical and covalent bonds with ECM proteins. In fact, the mussel adhesion is remarkably strong and long-lasting, with rapid fixation that remains stable over a wide temperature range, from – 40 °C to + 40 °C, as well as changes in humidity and salinity.[87] This extraordinary tenacity is attributed to marine mussel adhesive proteins (MAPs), which contain L-3,4-dihydroxyphenylalanine (DOPA) in their composition, achieved via post-translational modifications of tyrosine (**Figure 5**).[88–91]

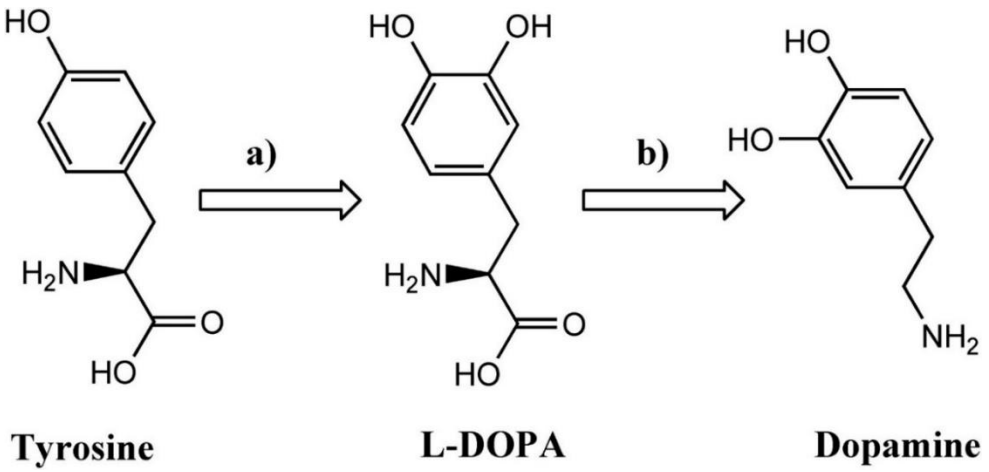

Figure 5. Dopamine biosynthesis: the enzyme tyrosine hydroxylase with tetrahydrobiopterin cofactor converts Tyrosine to L-DOPA (**a**); the enzyme aromatic L-amino acid decarboxylase with vitamin B6 cofactor converts L-DOPA into dopamine (**b**). [92]

This adhesive property is particularly due to the reactivity of the catechol groups present in dopamine, arousing considerable interest. Furthermore, dopamine can undergo easy oxidation and polymerization, generating polydopamine (pDA) (**Figure 13**), which has also been considered to improve the adhesion of materials.[93,94] DOPA, a substance found in mussels, exists in two different forms: non-oxidized and oxidized. The non-oxidized form

playing an essential role in adhesion to inorganic substrates, as depicted in **Figure 6a**.[95,96] The non-oxidized form is important for mussels to stick to surfaces like rocks or other inorganic materials. This adhesion is achieved through a binding between the metal ions present in the mussel glues (such as zinc, copper, and iron) and the catechol groups in the non-oxidized DOPA. This creates a bond that helps mussels stick to these surfaces.[97] On the other hand, the oxidized form of DOPA is essential for mussels to stick to organic surfaces. (**Figure 6g**), In this form, the substance helps mussels resist moisture in wet environments. This is because the oxidized DOPA can create strong bonds by linking with other molecules present in organic surfaces, like proteins containing amine or thiol groups. This process involves reactions that form a tough and resistant compound, helping mussels stick to organic surfaces.[98] Indeed, oxidative species can interact with each other via aryl-aryl bonds (**Figure 6d**), perform Michael-type additions or develop Schiff base reactions with with proteins containing amino (or thiol) groups (**Figure 6e-f**) to form a strong cohesive matrix.[99–101] In summary, looking at the most relevant reactions of catechol groups and quinones depicted in **Figure 6**, catechols demonstrate a greater ability to form noncovalent bonds through reversible adhesion to inorganic materials, hydrogen bonds between catechols and quinones, and reversible complexation with metal ions.[102] In summary, the non-oxidized form of DOPA (catechols) primarily creates reversible bonds with inorganic surfaces through coordination with metal ions. Meanwhile, the oxidized form of DOPA (quinones) tends to form stronger, irreversible bonds with organic surfaces by linking with proteins and other molecules containing specific functional groups. The exceptional adhesion strength of mussels therefore derives from the coexistence of oxidized and non-oxidized forms of catechol groups and their possible cross-linking through oxidation, metallic bonding with redox reactions or the action of enzymes.[102–104] According to the study conducted by Yu and collaborators, catechol groups are mainly responsible for adhesive bonds, while

orthoquinone forms can contribute to cross-linking (cohesive) bonds.[89] Furthermore, adhesive properties are generated through irreversible covalent bonds with organic substrates or reversible π-π interactions between synthetic polymers and coordination with metal oxides.[105] On the other hand, cohesive bonds are formed with multivalent metal ions through reversible complexation or with amine and thiol functional groups present in the amino acids of the byssal thread, thanks to Michael-type additions and Schiff base reactions.[106]

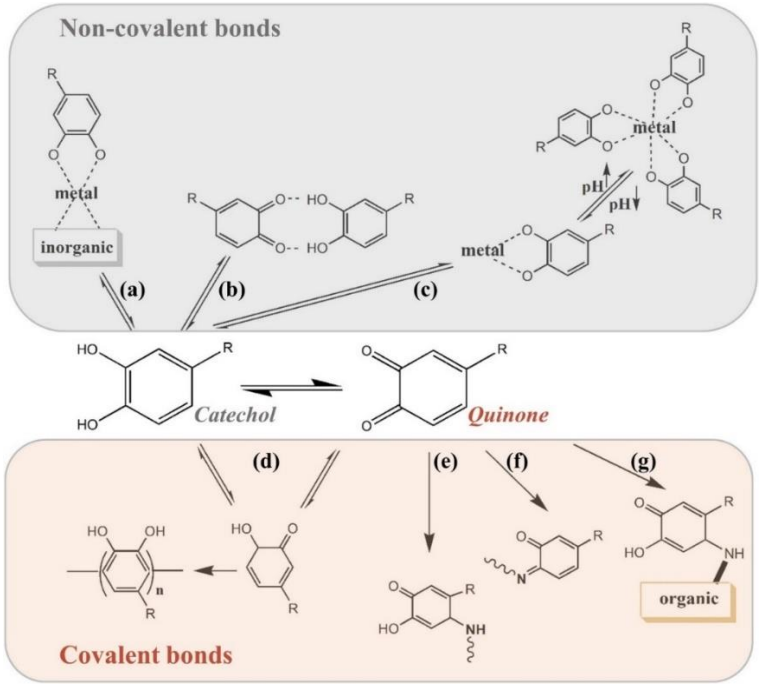

Figure 6. The most relevant reactions of catechol and quinone groups. Catechols are capable to form non-covalent bonds by: (**a**) reversible adhesion to inorganic materials (metal ions or metal oxide surfaces); (**b**) hydrogen bonding between catechols and quinones; and (**c**) reversible complexation with a metal ion. Quinones predominantly form covalent bonds by: (**d**) self-coupling of the semiquinone radical; and strong irreversible (**e**) Michael-type addition with amine (or thiol) group; (**f**) Schiff base reaction with amine (or thiol) group; and (**g**) adhesion to organic (amine-functionalized) surface.[92]

As a result, these molecules have attracted the attention of numerous research groups, precisely because they can be exploited for various applications in the field of regenerative medicine and tissue engineering, to improve the mechanical integration of the bioengineered tissue to the tissues surrounding the regenerating wound. This property, as far as skin wounds are concerned, has also been exploited to produce bioadhesives that can instantly stop wounds bleeding.[107] In this context, exploring adhesive injectable hydrogels regarding their tissue interaction and antibacterial properties unveils a promising avenue. Moreover, delving into polysaccharide-based hydrogels presents an opportunity to mitigate the limitations of conventional wound dressing techniques and high-dose antibiotic administration. This direction is crucial, given the drawbacks associated with systemic antibiotic use, such as adverse effects and the growing concern of antibiotic resistance due to improper prescription and poor patient adherence to therapy.[108] Among the polysaccharides most commonly used in biomedicine, of particular interest is Gellan Gum (GG) an anionic exopolysaccharide consisting of repeated tetrasaccharide units of D-glucose, D-glucuronic acid, D-glucose and L-rhamnose, produced by the aerobic microbial fermentation of *Sphingomonas elodea*.[109–112] The natural form of this polymer has an L-glyceryl substituent on the third carbon of the 3-linked D-Glc residue and, in some repetitive units, an acetyl group on the anomeric carbon of the same residue.[113] Such substituents can be removed from the repetitive structure with a thermal treatment with alkali,[114] in fact, GG is often sold in this deacetylated state (**Figure 7**).

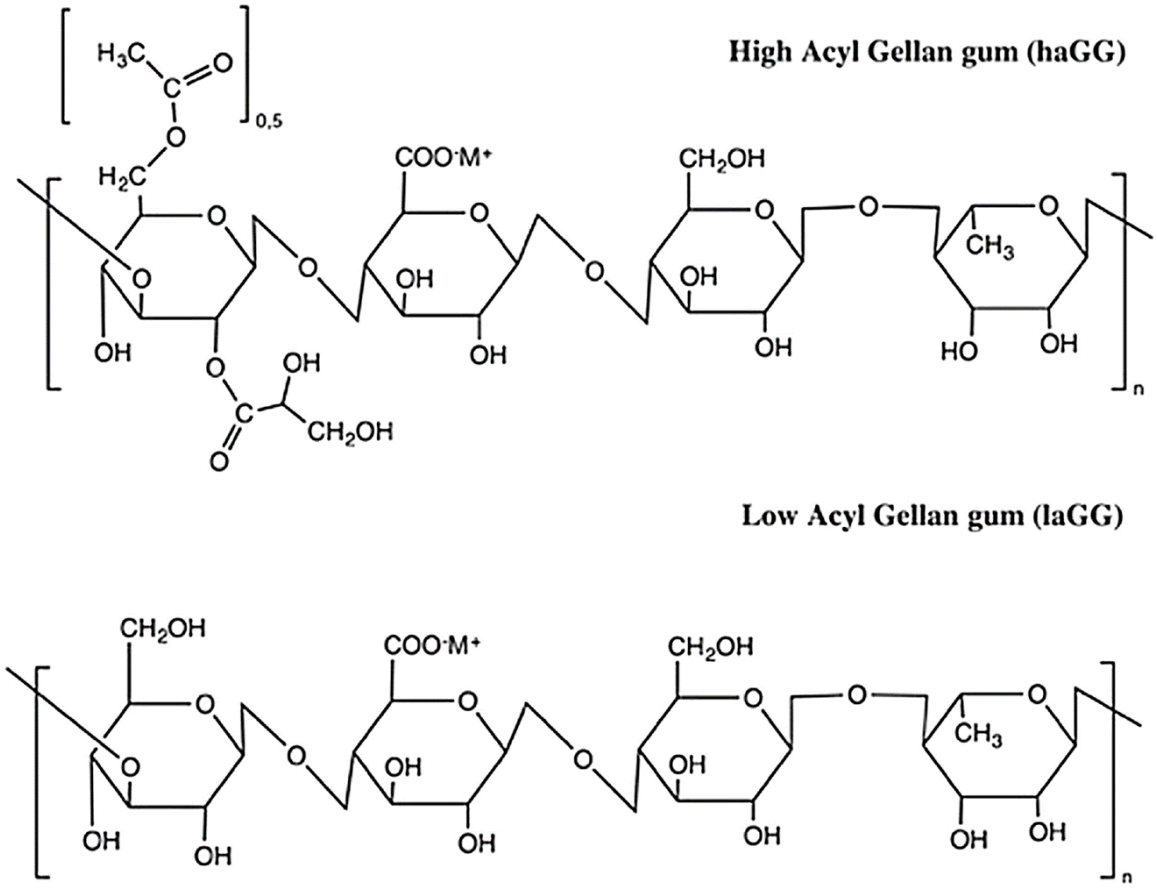

Figure 7. The structure of high and low-acyl form of gellan gum.[115]

GG was mainly used in the food industry due to its ability to form transparent hydrogels that are more resistant to heat and acid solutions than other polysaccharide hydrogels. It has also been used as an alternative to gelatine in the manufacture of products acceptable to vegetarians and religions that prohibit the use of mammalian materials.[116,117] In the last decade, GG has gained much importance in the biomedical field due to its special chemical-physical characteristics that are exploited to easily obtain physical hydrogels.[118] The aqueous dispersions of GG show a thermoreversible sol-gel transition due to the conformational change of the polysaccharide chains from a *random coil* to a *double helix* caused by the lowering of the temperature (**Figure 8**).[119]

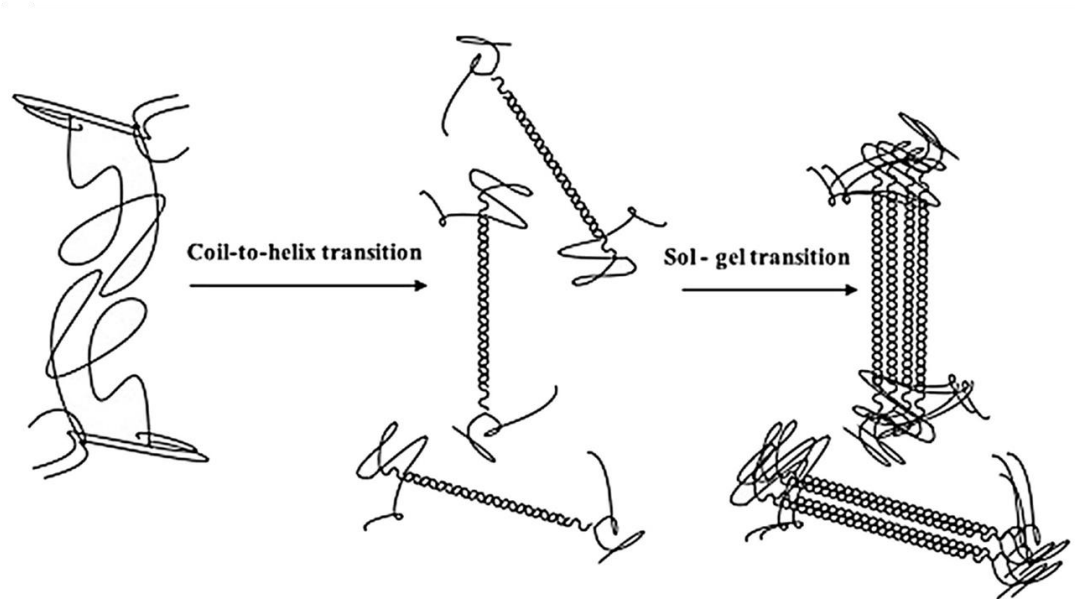

Figure 8. Conformational change of GG polysaccharide chains from *random coil* to *double helix.*[118]

The presence of metal cations induces the association of helices, allowing the formation of physical hydrogels with excellent biocompatibility, bioadhesion and biodegradability properties.[120] In particular, divalent cations allow the formation of GG hydrogels with better mechanical properties than those obtained in the presence of monovalent cations. This aspect is responsible for the main limitations associated with the use of GG-based hydrogels, as they gradually lose their structural integrity in vivo due to the exchange of divalent cations with monovalent cations present in the physiological medium.[121–123] Obviously, the rate at which this weakening occurs depends on the hydration of the tissue being analysed. For this reason, several chemical modifications of GG have been proposed with the common aim of modifying the chemical-physical properties of the polysaccharide and obtaining GG-based hydrogels with better stability under physiological conditions.[124] The degree of acylation also influences the strength of the resulting network; when GG is acylated it forms soft,

elastic, transparent and flexible gels, whereas deacetylation results in stiff, non-elastic and brittle gels.[111]

Xanthan gum (XG) is a pivotal microbial polysaccharide. Its discovery traces back to the 1950s when Allene Rosalind Jeanes made the breakthrough at the United States Department of Agriculture, USA.[125] The green light from the FDA (Fed. Reg. 345376) in 1969, deeming it a secure polymer, opened the doors for xanthan's deployment as a potent thickening agent and stabilizer across numerous food products.[126] XG boasts remarkable characteristics including strong water solubility, exceptional biocompatibility, and a high molecular weight exo-polysaccharide configuration featuring intricately branched polymer chains.[127,128] Its natural anionic structure comprises a recurring unit formed by a pentasaccharide, encompassing D-glucose, D-mannose, and D-glucuronic acid, in a molar ratio of 2:2:1. The primary XG backbone mainly assumes a linear β-(1–4)-D-glucose structure, akin to cellulose chains, while the side chain is essentially an amalgamation of terminal β-D-mannose linked to D-glucuronic acid via β-(1–4) in a pattern that further connects to D-mannose through α-(1–2) (**Figure 9**).[129–133] The presence of acetate and pyruvate groups, their proportions varying non-stoichiometrically based on bacterial strain production, fermentation conditions, and subsequent chemical alterations, further enriches the structure of XG.[132,134–136] When stabilizing counterions are present, they shield the internal charge interactions within the molecule. This results in the compact folding of sidechains against the backbone, forming a highly structured helix with a distinct five-fold helical molecule which is essentially stabilized by the non-covalent bond. This ordered structure significantly increases the stiffness of the material compared to its disordered 'random coil' form. When xanthan adopts this helical state, its stiffness is remarkable, exhibiting a persistence length of over 100 nanometers, positioning it among the most rigid biopolymers known.[137] The reversible

order-disorder conformational transition of the secondary structure of XG can be induced by altering the temperatures and the ionic strength. The disorder form is basically favored by high temperatures and low salt concentrations.[137–139] Meanwhile, the coil-helix transition temperature mainly depends on the content of acetate and pyruvate groups, ionic strength, pH, and polymer concentration.[132] XG is recognized for its complete biodegradability within a mere 2 days, owing to its natural origin. However, its similarity to cellulose in terms of structural composition makes it resistant to typical cellulose activity. The side chains of three sugar units in xanthan gum act as a protective barrier against enzymatic degradation. Interestingly, only the disordered form of xanthan gum is susceptible to cleavage by fungal cellulases, whereas the ordered helical structure remains unaffected. The tri-saccharide side chains of XG are likely to be a barrier to enzymatic attack.[129,140] The synthesis of XG is believed to be similar to the synthesis of exo-polysaccharide by other Gram-negative bacteria and generally produced by Xanthomonas, which present many different strains, as for instance, *X. arboricola, X. axonopodis, X. campestris*, *X. citri*, *X. fragaria, X. gummisudans, X. juglandis, X. phaseoli, X. vasculorium*.[126] *X. Campestris*, a plant-associated bacterium, is the most commonly pathovar employed for industrial production of xanthan gum.[141–143]

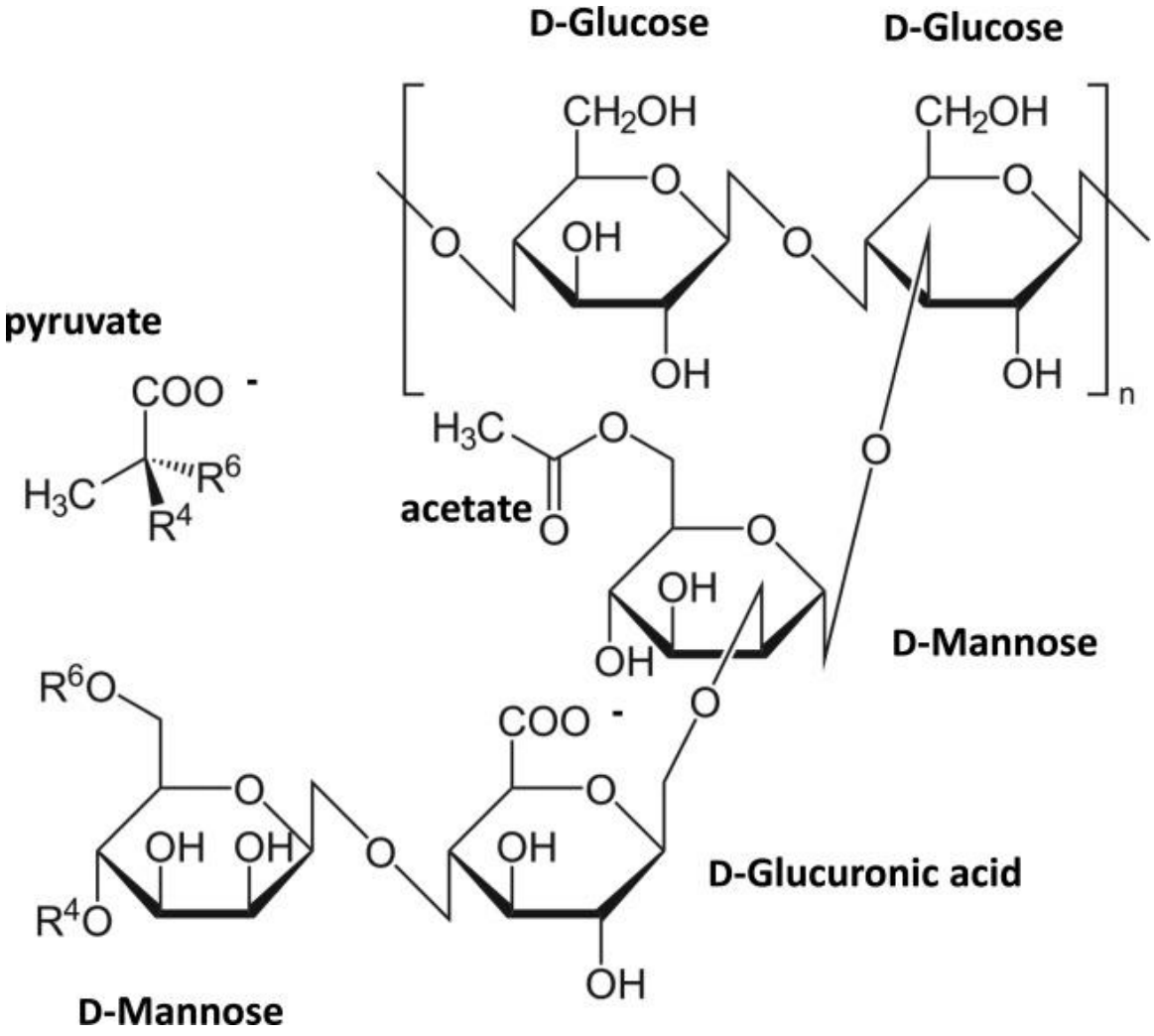

Figure 9. Representation of the chemical structure of xanthan gum repeating unit. Na^{+}, K^{+}, and Ca^{2+} are the most frequent counter-ions stemming from fermentation process.[142]

Xanthan gum has found extensive application in the food industry owing to its multifaceted properties. Firstly, it excels as an efficient thickener, demonstrating heightened solution viscosity even at low concentrations.[144] Secondly, it exhibits pseudoplastic behavior in aqueous solutions, facilitating processes such as mixing, pumping, filling, and pouring.[144] Thirdly, it maintains stability over a wide pH range, temperature variations, and fluctuations in ionic strength. Lastly, it remains stable under shear forces during processing and

packaging.[142] Notably, xanthan gum chains can form physical networks with bivalent cations, a complex arrangement involving two disaccharide units from the main chain and O-acetyl and pyruvyl residues from side chains. This leads to intramolecular cross-linking and chain contraction, as evidenced by conductometric, viscometric titrations, and nuclear magnetic resonance spectroscopy.[142] The XG solution is stable over a broad range of temperatures (up to 90 °C), salt concentrations, and pH (2–11).[145] These superior properties of XG resulted in being used for biomedical applications (e.g., drug delivery and tissue engineering) apart from industrial applications.[130] XG has recently received considerable attention as a biomaterial of choice for the fabrication of tissue scaffolds, particularly for extracellular matrix (ECM) tissue engineering applications. The success of regenerating damaged tissue depends on creating a three-dimensional microenvironment within XG-based scaffolds that promotes optimal cell-matrix interactions. This involves a delicate interplay between surface chemistry, nanotopology and mechanical stiffness.[146] XG itself naturally adopts a mild gel-like structure through its double helical conformations, induced by the presence of specific divalent cations. However, to achieve the desired mechanical strength and other relevant properties, the stiffness and stability of XG can be tailored by synergizing it with other biomaterials or reinforcements. To illustrate this concept, a schematic representation of the integration of XG with additional components and/or polymers in tissue engineering applications is presented in **Figure 10**.

Figure 10. Schematic representation of the use of XG with other components and/or polymers for tissue engineering applications.[129]

1.2.2.2 Antibacterial and stimulus-responsive systems

Given the aforementioned points, it is crucial for a hydrogel intended for treating skin wounds to possess antibacterial properties. The possibility of using hydrogels to deliver drugs with antimicrobial activity to the wound bed has been extensively investigated in recent years.

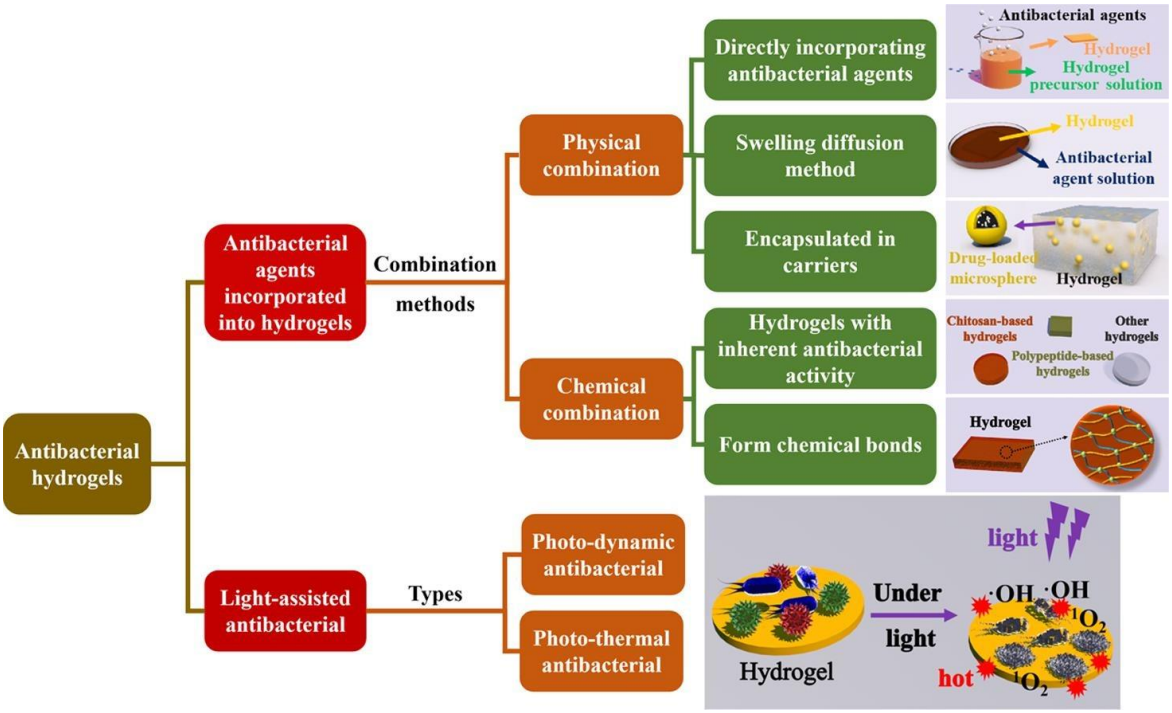

Figure 11. Methods of producing hydrogels with antibacterial activity.[42]

As already mentioned above, these hydrogels have the ability to include molecules with antibacterial activity, creating excellent delivery systems. They improve the pharmacokinetic and pharmacodynamic properties of drugs compared to traditional formulations by inducing a sustained release of the drug, which can be controlled by several mechanisms, including diffusion, swelling, chemical reactions and endogenous or exogenous stimuli. The application of these therapeutic systems to skin wounds allows the localized release of the antibiotic at the site of the infection so that the damaged area can be treated specifically, reducing systemic absorption of the drug and consequently side effects.[108,147] Depending on the preparation method adopted, the drug molecules may be physically incorporated or chemically bound to the hydrogel (**Figure 11**). The preparation of hydrogels in which the drug is physically loaded can be achieved by direct incorporation of the drug, by swelling or by encapsulation of the antibacterial agent in carriers.[42] The direct

incorporation method is simple and fast and consists of dissolving or dispersing the drug in the polymer dispersion, which then forms the hydrogel. For example, Qu et al. prepared an injectable hydrogel with antibacterial and antioxidant activity capable of accelerating the tissue repair process by promoting angiogenesis, collagen deposition and granulation tissue formation. The hydrogel was obtained by mixing oxidized hyaluronic acid functionalised with aniline tetramer (OHA-AT) with carboxyethyl chitosan (CEC) and loading it with amoxicillin by the direct incorporation method. In vitro studies on S. aureus and E. coli confirmed the excellent antibacterial performance of the hydrogel due to the release of amoxicillin.[148] Swelling incorporation, on the other hand, involves swelling a xerogel with a solution of the drug to promote its diffusion within the three-dimensional network.[149] However, drug molecules loaded into the hydrogel by either method tend to be rapidly released, resulting in a time-limited antibiotic effect that cannot be controlled from the outside.[150–152] To overcome these problems, the drug can be encapsulated in carriers (microparticles, nanoparticles, micelles) that are incorporated into the hydrogel. This allows for a slower release of the drug, resulting in a prolonged antibacterial effect.[42] Alternatively, drug molecules can be chemically bound to the hydrogel matrix. This avoids the problems typical of hydrogels physically loaded with the drug, such as rapid drug release, nanoparticle aggregation in the absence of suitable stabilizers, and poor duration of antibacterial activity due to the rate of drug diffusion.[153] Although, as discussed above, various methods can be used to control the release of antibiotics from hydrogels, these strategies do not overcome the problem of antibiotic resistance. In fact, many microorganisms have developed defence mechanisms that make them insensitive to the action of most antibiotics currently in use. It is, therefore, necessary to develop systems with "non-specific" antimicrobial activity, i.e. not strictly linked to the release of a specific antibiotic molecule, but activated by an electromagnetic stimulus. As shown in **Figure 12**, such a stimulus can generate the

production of reactive oxygen species (ROS) within the drug system or stimulate the release of heat from the system itself. These two mechanisms of action are known as "photodynamic antibacterial activity" (PDA) and "photothermal antibacterial activity" (PTA), respectively, and the therapies based on them are known as "photodynamic therapy" (PDT) and "photothermal therapy" (PTT). In both cases, the walls of pathogenic microorganisms are destabilized and destroyed.[42]

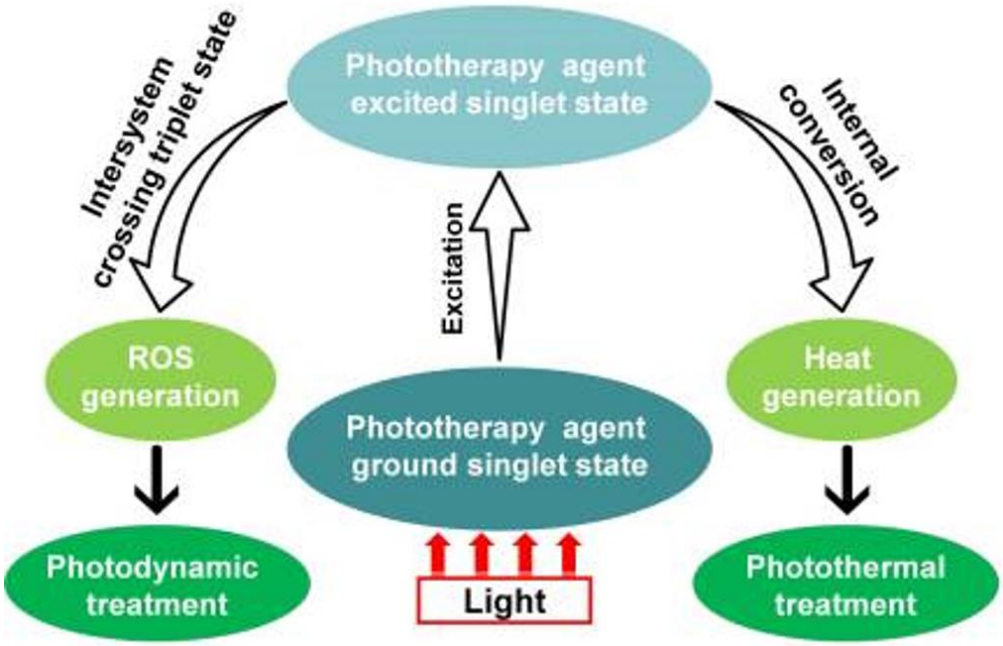

Figure 12. Mechanism of action of PDT and PTT.[42,154]

PDT involves the use of a photosensitive agent capable of absorbing light by switching to an excited state and transferring the energy to surrounding oxygen molecules, leading to the formation of ROS.[108,155] ROS induce the death of the micro-organisms colonizing the wound by two main mechanisms: one is to alter the permeability of the membrane, facilitating the escape of cellular contents and preventing the proper metabolic activity of the bacterium, through the oxidation of intracellular proteins, and the other is to induce DNA degradation,

producing oxidized products.[156] A distinction can be made between first and second-generation photosensitizers. First-generation PS are excited at wavelengths below 650 nm, which fall in the red part of the visible spectrum and are characterized by poor tissue penetration of light. Second-generation PS absorbs light at wavelengths longer than 630 nm, which are in the near-infrared (NIR). This allows the light to penetrate deeper into the tissue, producing a more intense photodynamic effect. Many chemical compounds have been used in PDT: acridine, anthraquinone, hypericin, psoralen, porphyrin, chlorine, bacteriochlorine, and 5-aminolevulinic acid derivatives.[108] Mai et al. developed a hydrogel with photodynamic antibacterial activity capable of promoting skin regeneration in infected burns. PDA was achieved by incorporating a photosensitive agent, represented by sodium sinoporphyrin (DVDMS), into a hydrogel based on carboxymethyl-chitosan (CMCS) and sodium alginate (SA), which also encapsulated poly(lactic-co-glycolic acid) (PLGA) nanospheres loaded with basic fibroblast growth factor (bFGF). ROS generation was measured using the green singlet oxygen sensor (SOSG), the reagent was mixed with both the free sodium sinoporphyrin and the hydrogel and irradiated at a power of 10 J/cm^2. The concentration of ROS produced was measured by fluorescence and it was seen that the fluorescence intensity increased with increasing concentration of DVDMS and hydrogel. The hydrogel shows a higher fluorescence intensity that persists over time than the free photosensitive agent, in fact, the free sodium sinoporphyrin shows no fluorescence signal after 6 hours. This is probably due to the aggregation of the free DVDMS molecules induced by the formation of π-π stacking interactions in the aqueous medium, reducing its capacity to absorb electromagnetic radiation, whereas the three-dimensional network of the hydrogel prevents the aggregation process of the porphyrin molecules, generating a high and stable fluorescence intensity over time. The reactive oxygen species generated, such as hydroxyl radical (•OH) and singlet oxygen ($^1O_2$), cause oxidation of cellular macromolecules and are

primarily responsible for the photodynamic antibacterial activity. *In vivo* studies have shown that hydrogels can promote tissue repair through inhibition of bacterial growth and biofilm formation, control of inflammation, collagen deposition and rapid re-epithelialization.[157] The photothermal therapy exploits the localized increase in temperature in the area to be treated which causes direct damage to the microorganisms.[158] Photothermal antibacterial activity can be imparted to hydrogels by incorporating photothermal agents such as gold nanoparticles (AuNPs) or silver nanoparticles (AgNPs), graphene oxide (GO), or polydopamine (pDA) into the hydrogel.[159,160] These nanomaterials are able to absorb NIR light at wavelengths between 700 and 1400 nm and convert it into heat.[161] The heat generated locally by photothermal agents damages bacterial membranes, increasing their permeability and inducing the denaturation of proteins and cytoplasmic enzymes. This cell death mechanism makes PTT effective not only against planktonic bacteria but also against bacteria that form sessile colonies, such as the biofilms mentioned above.[162] It also allows spatio-temporal control of the temperature increase, does not damage healthy tissue and does not induce resistance mechanisms in microorganisms.[162] Bacteria die at temperatures above 55°C due to the denaturation process of *heat shock proteins*. Wang et al. developed an injectable system obtained by incorporating MnO_2 *nanosheets* into a chitosan-based hydrogel functionalized with caffeic acid for the treatment of melanoma and the healing of wounds infected with multi-drug resistant (MDR) bacteria. Chitosan is a natural, biodegradable, biocompatible, non-immunogenic polymer with intrinsic antibacterial activity, but with poor tissue adhesion and no stimulus-sensitive ability to release bioactive molecules.[163,164] Functionalisation with caffeic acid, a molecule with a catechol structure, gives the chitosan good adhesion to tissues and allows it to cross-link via covalent bonds after MnO_2-mediated oxidation. In this system, the MnO_2 *nanosheets* also act as photothermal agents, allowing a localized temperature increase of up to 49.7°C after

irradiation at a wavelength of 808 nm, which can be used for PTT.[40] An excellent photothermal agent is polydopamine (pDA), obtained by oxidative polymerisation of dopamine, a neurotransmitter with important functions in the nervous, renal and cardiovascular systems.[165,166] pDA is generally produced through an oxidative self-polymerisation process under weakly alkaline conditions as shown in **Figure 13**.[167]

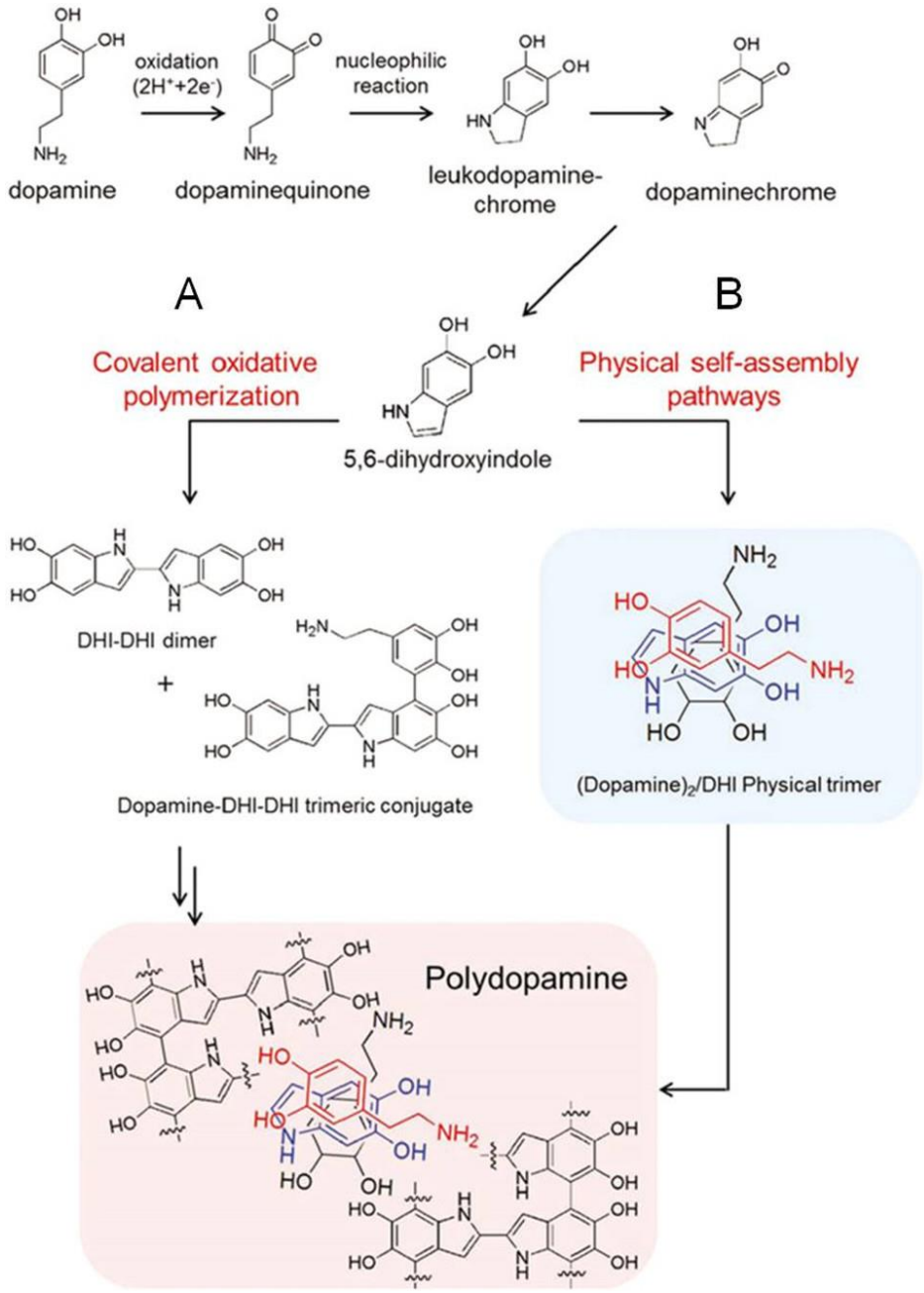

Figure 13. pDA synthesis pathways: (**A**) covalent bond-forming oxidative polymerization and (**B**) physical self-assembly of DA and DHI.[167]

The series of reactions leading to pDA begins with the oxidation of dopamine to dopamino-quinone. The latter, after deprotonation of the amine group, undergoes the Michael addition reaction leading to the formation of an intermediate which, upon oxidation, gives rise to dopamino-chrome. Through an intramolecular rearrangement mechanism, dopamino-chrome leads to the formation of DHI (5,6-dihydroxyindole).[168,169] DHI, either through a process of covalent oxidative polymerization or through physical interactions with free dopamine, leads to the formation of pDA (**Figure 13**), which takes the form of colloidal particles.[170] DHI, either through a process of covalent oxidative polymerization or through physical interactions with free dopamine, leads to the formation of pDA, which takes the form of colloidal particles (*pDA shell/coating*). The pDA-coating not only improves the chemical properties of these materials but also provides a multifunctional and smart platform.[167] Indeed, pDA nanostructures have numerous unsaturations that make them susceptible to nucleophilic attack by molecules containing amine or thiol functional groups. In addition, the presence of benzene rings allows the adsorption of drugs with aromatic structures through the formation of π-π stacking or hydrogen bonds.[171] A high photothermal conversion capacity has been found in systems containing pDA, which is thought to be related to its ability to absorb NIR light at 808 nm, allowing light to penetrate deep into tissues while reducing absorption by biological tissues, thus avoiding toxic effects. The photothermal conversion efficiency is~ 40%, higher than other materials such as carbon nanoparticles.[167,172] In a study, pDA nanoparticles were functionalized with PEG-SH and vancomycin (pDA-PEG-Van) for the photothermal treatment of MDR bacterial infections (**Figure 14**). Once delivered to the site of infection, the nanoparticles adhere to the bacterial surface by forming hydrogen bonds with the D-alanine residue on the bacterial wall. In this way, when exposed to NIR light, each nanoparticle acts as a single heat source, inducing a

powerful antibacterial effect at low power. This results in a local temperature of approximately 44°C, limiting the toxic effects on surrounding tissues.[173]

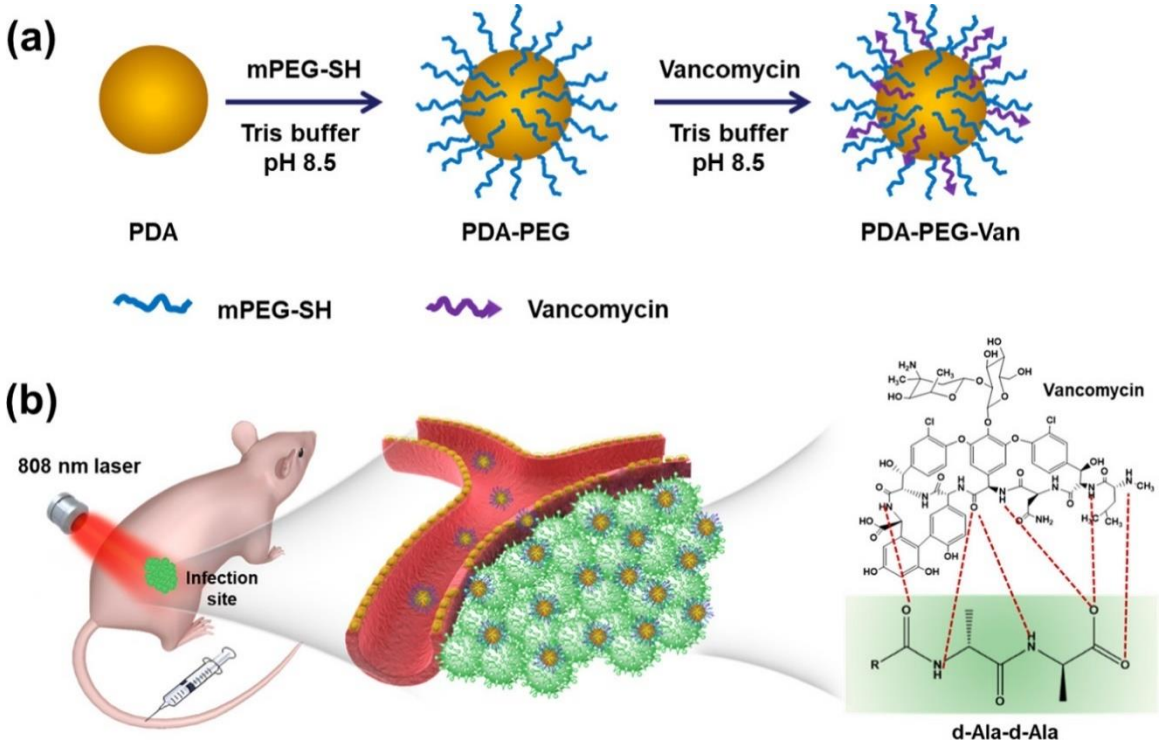

Figure 14. (**a**) Functionalization of pDA nanoparticles with PEG-SH and Vancomycin. (**b**) Photothermal antibacterial effect generated by pDA-PEG-Van nanoparticles under NIR light.[173]

Another example is the work of Fan et al, who used pDA nanoparticles functionalized with meganin I, an antimicrobial peptide, and showed that under NIR irradiation at 808 nm, an increase in temperature of up to 45°C was able to induce death of microorganisms while enhancing the antimicrobial effect of the peptide.[174] Zhu et al. prepared D-α-tocopherol polyethylene glycol succinate polylactide (TPGS-PLA) nanoparticles loaded with docetaxel and coated with pDA. The coating was used to conjugate the nanoparticles with galactosamine to enable site-specific targeting and enhance the antitumor activity of the NPs.[175] The pDA is also used as a *surface-coating* of metallic inorganic nanoparticles, such as gold and iron or non-metallic nanoparticles.[176] Black et al. prepared pDA-coated gold

nanoparticles via the polymerization reaction of dopamine on NPs in TRIS buffer (pH 8.5), which were then functionalized with anti-EGFR antibodies for tumor-specific imaging and photothermal therapy.[177] Thanks to its structure and chemical composition, pDA has found wide application in biomedicine due to its various properties: it imparts adhesiveness to tissues, has a high reactivity and ability to bind drugs, photothermal conversion ability, antioxidant/pro-oxidant, antibacterial activity, pH-responsiveness, biocompatibility and biodegradability.[167,178] These properties have generated a growing interest that has led to the use of pDA in the development of biomaterials for the treatment of various pathologies such as cancer, diabetes, bacterial infections and Parkinson's disease (**Figure 15**).[176]

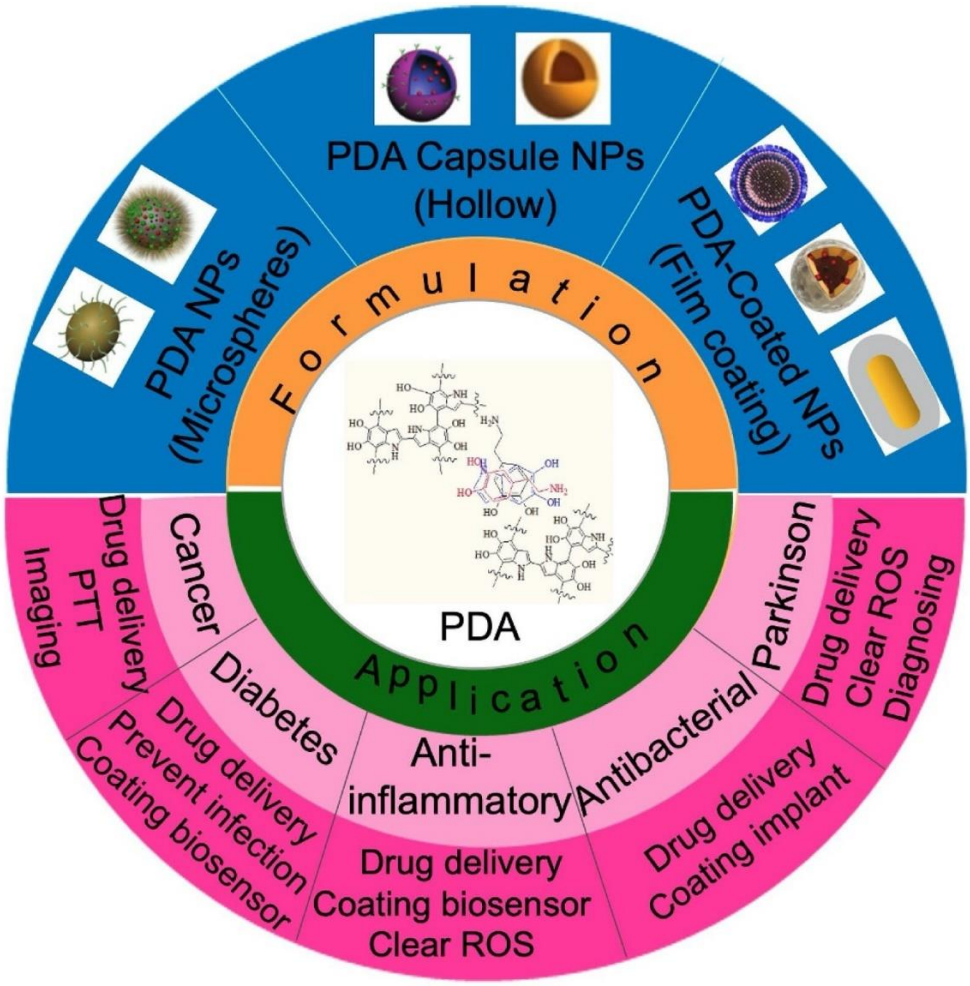

Figure 15. Schematic diagram of different types of polydopamine materials and their applications in biomedicine.[176]

Jiang Chang et al. designed a multifunctional composite hydrogel consisting of dopamine-conjugated γ-glutamic acid and adipic acid dihydrazide (γ-PGA-DA-ADH) obtained by oxidized dextran (Odex)-mediated crosslinking, in which copper-calcium silicate (Cu-CS) and pDA (pDA/Cu-CS hydrogel) were incorporated to obtain the so-called "*hot ion effect*", which synergistically combines the antibacterial activity of Cu^{2+} ions and the photothermal conversion ability generated by pDA. The photothermal conversion efficiency was evaluated by irradiating the pDA/Cu-CS hydrogel and comparing it with the control hydrogel (without pDA). It was shown that after NIR irradiation (808 nm) at a power of 0.8 W/cm^2 for 5 minutes, the temperature increased from 20 °C to 60 °C, indicating that the hydrogel had an excellent photothermal effect. The composite hydrogel was shown to have excellent antibacterial activity, inhibiting the growth of MDR-microorganisms, E. coli and, through in vivo results, the ability to promote tissue regeneration, collagen deposition and angiogenesis (**Figure 16**).[179]

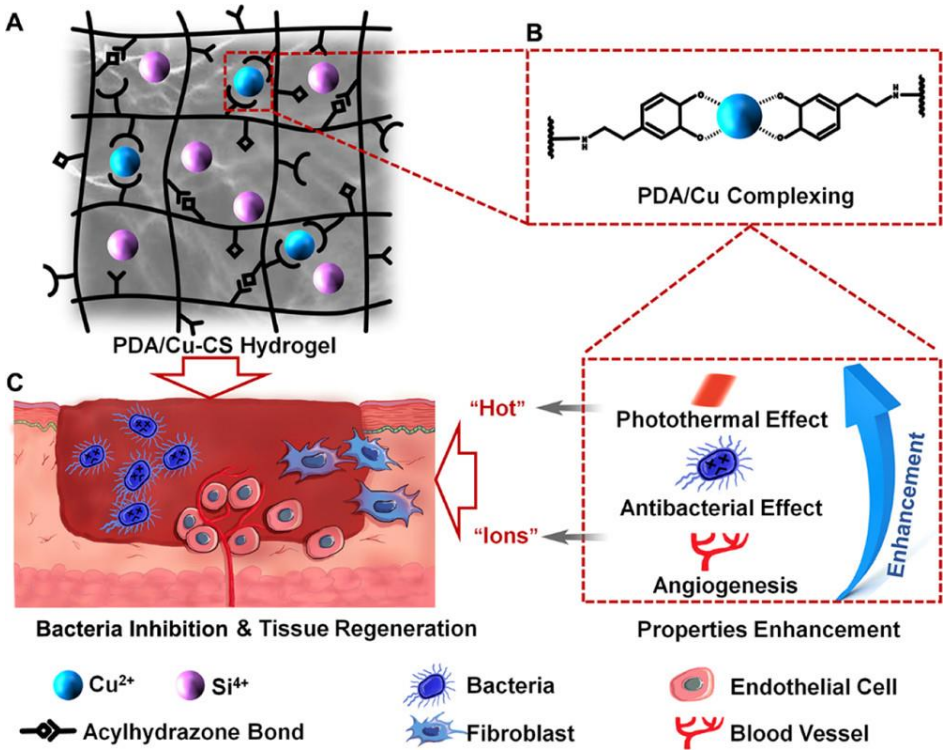

Figure 16. Design and application of the pDA/Cu-CS composite hydrogel. (**A**) Structures of prepared composite hydrogel networks. (**B**) Complexation of pDA and Cu ions (pDA/Cu complexing) endows the composite hydrogel with enhanced photothermal performance, antibacterial property and angiogenesis. (**C**) Composite hydrogel with "*hot ions effect*" for highly efficient bacterial inhibition and accelerated tissue regeneration for infectious wound healing.[179]

Y. Liang et al. instead prepared a multifunctional hydrogel with antibacterial activity based on chitosan and dopamine-functionalised gelatin (GT-DA/CS), in which pDA-coated carbon nanotubes (CNT-pDA) were incorporated. The gelatin was functionalised with dopamine at the carboxyl groups using the classical reaction with ethyl-dimethyl-aminopropyl carbodiimide (EDC) and N-hydroxysuccinimide (NHS). GT-DA/CS/CNT hydrogel was prepared by mixing GT-DA/CS dispersion and CNT-pDA dispersion, gelation was induced by dopamine self-polymerization process in the presence of H_2O_2 and horseradish peroxidase (HRP) (**Figure 17**). Doxycycline was incorporated into the hydrogel to provide

an antibacterial effect. The hydrogel has been shown to promote complete tissue repair resulting in wound closure and has been shown to have both antioxidant and adhesive properties due to the chemical and physical interactions that pDA and dopamine form with the proteins present in the wound site. Once applied, the hydrogel isolates the wound from the external environment and induces a haemostatic effect. The pDA-coated carbon nanotubes have the ability to absorb NIR light and convert it into thermal energy, creating a photothermal antibacterial effect that promotes the regeneration of damaged tissue.[41]

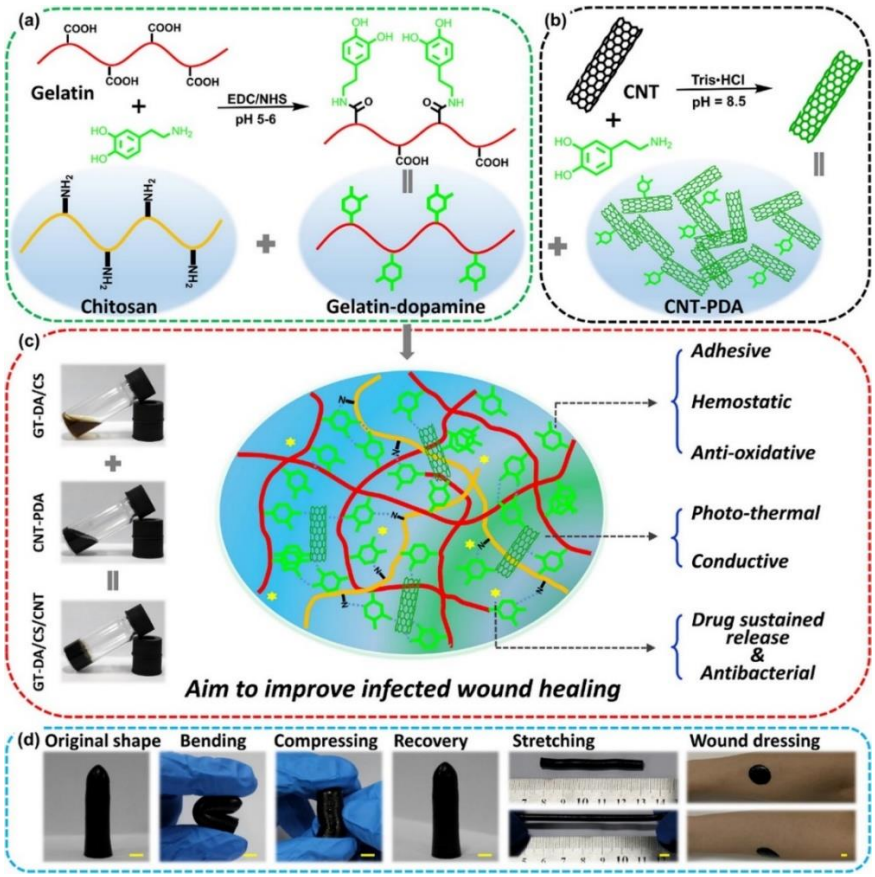

Figure 17. Preparation scheme of the GT-DA/CS/CNT-based hydrogel. Synthesis scheme of the GT-DA polymer (**a**), of the CNT-pDAs (**b**), and of the GT-DA/CS/CNT hydrogels (**c**). Original, bending, compressing and stretching shape representations and the application as a wound dressing. Scale bar: 5 mm. (**d**).[41]

The use of multifunctional injectable hydrogels with properties such as tissue adhesion, antibacterial activity, stimulus responsiveness and mechanical strength is desirable for a wide range of applications. As mentioned above, the interesting aspect of PTT is that, in addition to its direct antimicrobial activity, it has the ability to enhance the antimicrobial activity of molecules to which many bacteria have developed resistance. For this reason, many antibiotics that are now considered ineffective could be used again by exploiting the adjuvant effect of PTT. Infections caused by multi-resistant Gram-negative bacteria are characterised by high morbidity and mortality. Of particular concern are infections caused by *P. aeruginosa*, an opportunistic pathogen that has become increasingly difficult to eradicate due to its high level of antibiotic resistance. Furthermore, adaptive antibiotic resistance of *P. aeruginosa* is a recently characterized mechanism, including biofilm-mediated resistance and the formation of multidrug-tolerant cells, and is responsible for the persistence and recurrence of infections. There is an increasing need for the discovery and development of alternative therapeutic strategies for the treatment of *P. aeruginosa* infections.[180] Polymyxins are old antibiotics that had fallen out of use due to their side effects, but difficulties in producing new antibiotics and the emergence of antibiotic resistance in Gram-negative bacteria have led to a re-evaluation of their use as “last resort” antibiotics.[181] Polymyxins possess considerable therapeutic potential as they are effective against four of the six multi-resistant Gram-negative bacteria, the so-called ESKAPE (Enterococcus faecium, Staphylococcus aureus, Klebsiella pneumoniae, Acinetobacter baumannii, Pseudomonas aeruginosa, and Enterobacter). Polymyxin B and E are applied clinically.[182] Polymyxin E (colistin) is a mixture of two peptides, polymyxin E1 (colistin A) and polymyxin E2 (colistin B). Both have a ring of 7 amino acids to which a side acyl chain is attached to the N-terminal residue, the only difference being the acyl moiety, we find 6-methyl-octanoic acid and 6-methyl-heptanoic acid in polymyxin E1 and polymyxin E2

respectively.[182–188] Polymyxin E is available as colistin sulphate (for topical and oral use) and colistimethate sodium (for injection and inhalation).[189] Both polymyxin E and polymyxin B have the same mechanism of action and the same applications, however, polymyxin B has lower therapeutic efficacy and greater toxic effects.[182,190]They exert their bacteriostatic effect by damaging the bacterial cell membrane; their main target is lipopolysaccharide (consisting of three domains, lipid A, oligosaccharide and O-antigen), the main component of the outer membrane of Gram-negative bacteria.[191,192] The positively charged polymyxins and the negatively charged lipopolysaccharide (LP) form electrostatic interactions. This leads to a destabilization of the bacterial membrane with the introduction of the acyl chain of the antibiotic into the hydrophobic domain of the LP, represented by lipid A. By increasing the permeability of the bacterial membrane, the polymyxin penetrates into the periplasmic space where it forms interactions between the outer and inner surfaces and promotes the exchange of anionic phospholipids, creating an osmotic imbalance that induces the death of microorganisms.[193,194] The clinical use of polymyxins is mainly limited by their nephrotoxic and neurotoxic side effects (dose-dependent effects). To reduce the toxicity of polymyxins, it is necessary to develop controlled release and targeted therapeutic systems to reduce the dose and frequency of administration.[195] Topical administration of polymyxins is mainly limited by their low activity due to the conditions of the tissue and wound microenvironment (hydrolysis, oxidation, pH, proteolysis) and their minimal residence time at the site of application. Hydrogels, nanofibres and polymeric membranes can improve the chemical-physical stability of these antibiotics and prolong their release. These biodegradable systems are suitable for topical application in the treatment of infected skin lesions.[1,196–198] In recent years, various compounds with antimicrobial activity have been proposed, including carbon nanomaterials such as graphene, carbon nanotubes, fullerenes

and various forms of diamond, as well as antimicrobial peptides (APs), metal nanoparticles (NPs) and antimicrobial polymers or dendrimers.[199–203]

1.2.2.3 Silver nanoparticles

Several research teams have devoted their attention to the analysis of the antimicrobial properties of metal nanoparticles of silver (Ag), zinc oxide (ZnO), gold (Au), copper (Cu), and ferrous oxide (FeO).[204] In recent years, silver nanoparticles (AgNPs) have gained considerable attention in the field of skin wound treatment due to their promising antibacterial properties and reduced toxicity. Silver has been used for thousands of years to treat wounds and burns.[205] Although the use of silver salts as an antimicrobial agent declined with the discovery of antibiotics, AgNPs have now emerged as bactericides of great potential.[204] The use of silver has been limited by the cytotoxicity of silver ions. However, nanotechnology has facilitated the production of silver particles with higher efficacy against bacteria and, more importantly, lower toxicity toward eukariotic cells. AgNPs are of particular interest due to their ability to interact with bacterial cell membranes and increase oxidative stress through the release of Ag^+ ions. These nano-sized particles have a high surface-to-volume ratio, which allows for increased exposure to bacteria and therefore effective antimicrobial action. The antibacterial activity of AgNPs can be ascribed to several mechanisms of action. The oxidation of the particles in aqueous solution leads to the formation of Ag^+ ions, which have the ability to bind to the sulphhydryl or phosphoric groups present in the membrane or bacterial wall.[206,207] This interaction causes the denaturation of proteins essential for bacterial survival, contributing to the antibacterial effect of the AgNPs (**Figure 18**).[204]

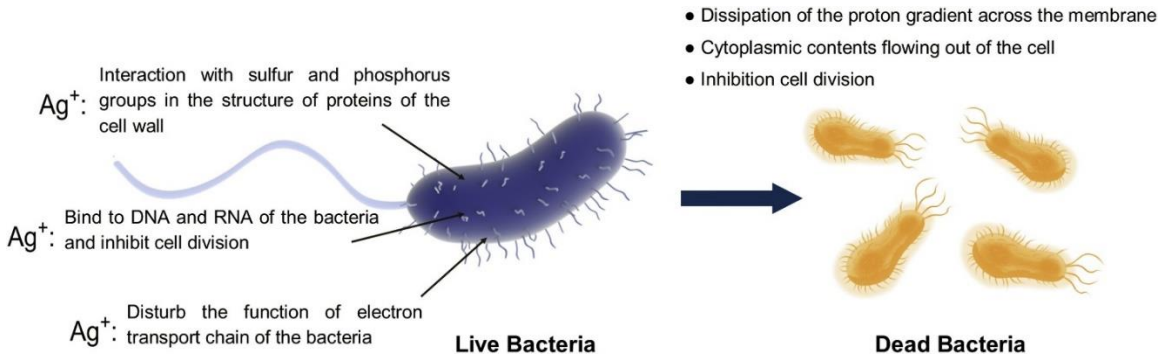

Figure 18. Antibacterial mechanisms of Ag^+ ions released by AgNPs.[204]

Another mechanism could be that these ions penetrate the ion channels that act on the ribosome and manage to inhibit the expression of the enzymes responsible for the production of ATP, leading to the death of the microorganism.[204,208] Ag^+ ions could also bind to negatively charged parts of the bacterial membrane through electrostatic interactions, creating pores that allow the cytoplasmic contents to leak out of the cell, resulting in a dissipation of the proton gradient across the membrane and ultimately cell death. Furthermore, the possible entry of Ag^+ ions into the bacterial cell could also have an effect on the function of the electron transport chain. The ions could also interact with bacterial DNA and RNA, leading to inhibition of cell division. Ionic silver would also stimulate the formation of reactive oxygen species (ROS), which have the ability to oxidize the proteins present in the mitochondria and thus also affect lipids and DNA, causing the rupture of the cell membrane and the death of the bacterium.[208] Several parameters can influence the activity of AgNPs, whether they are intrinsic properties such as size, shape and coating, or parameters attributed to the medium, including the presence of oxidizing species or other potential ligands for silver.[204,209,210] The use of AgNPs ranging in size from 1 to 100 nm has been reconsiderated in recent years for their diverse potential biomedical applications, especially thanks to their antimicrobial activity against approximately 650 microorganisms

(gram-negative and gram-positive bacteria, fungi and viruses).[204] Various approaches have been used to prepare AgNPs. These can be divided into physical and chemical methods. Physical methods mainly involve the irradiation of solutions containing soluble silver salts (such as $AgNO_3$) with γ or UV rays, while chemical methods involve the use of reducing agents. The chemical methods are the most widely used because they are highly efficient in terms of the amount of product obtained and because they produce nanoparticles of a few nanometres in size, which are stable in water and in organic solvents.[208,211] However, most of the reducing agents used to produce AgNPs, such as hydrazine or sodium borohydride ($NaBH_4$), are toxic and polluting. Therefore, the synthesis of metallic silver using these substances is unsustainable and carries risks related to the possibility of finding these substances, even in traces, in the final product. For this reason, green production methods have been developed in recent years using non-toxic reducing agents of natural origin.[204,212] AgNPs are colloidal particles that are hydrophobic and tend to aggregate and lose their antimicrobial properties due to their high surface energy and van der Waals forces.[213,214] Stabilising them with water-dispersible polymers is therefore essential. These polymers act as coating agents, adsorbing onto the surface of the nanoparticles and preventing aggregation both during the synthesis phase and during in vivo administration. The nucleation phase, which is responsible for the formation of nanoparticles, can be controlled by varying experimental parameters. These parameters include the choice of reducing agent, precursor concentration (often a silver salt such as $AgNO_3$), pH and temperature (**Figure 19**).[215]

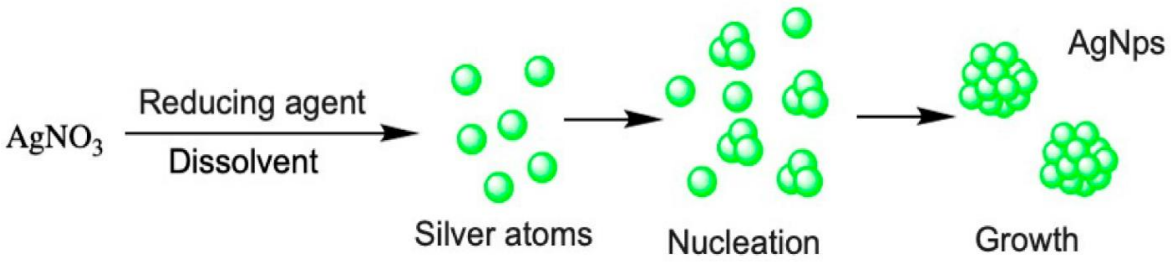

Figure 19. Synthesis steps of AgNPs by chemical reduction.[231]

Upon reduction of Ag^{+} to Ag^{0}, the initially clear $AgNO_3$ solution turn to colored dispersion, adopting a vivid yellow-orange hue. UV-Vis spectroscopy analysis uncovers the distinctive surface plasmon resonance band indicative of silver nanoparticle creation, typically observable within the 400 to 420 nm range.[216] The rate of the reaction increases when a strong reducing agent is employed, in contrast to a gentler reducing agent. This aspect acquires more interest considering the correlation established between the formation rate of AgNPs and their size, revealing an inverse relationship.[217,218] The effectiveness of the antimicrobial properties is significantly reduced when AgNPs form aggregates. Typically, synthetic polymers such as polyvinylpyrrolidone or polyvinyl alcohol are used as capping agents. Recently, however, many research groups have proposed the use of natural polymers, mainly plant-derived or biosynthesized polysaccharides. These natural polymers play a dual role as both reducing and capping agents.[219] These polymers can form coordination bonds with Ag^{+} ions present in the solution, facilitating their reduction, and act as protective colloids once the nanoparticles are generated.[220] The antimicrobial ability of these polymeric nanocomposites is strongly influenced by several factors such as particle size, distribution, degree of aggregation and interaction with the stabilizing polymer. As stabilizing polymer, some polysaccharides have been used, such as agarose, cellulose, starch, chitin, chitosan, dextran, sodium alginate, pectin, guar gum, hyaluronic acid or gellan gum.[215] Agarose was

one of the first polysaccharides used to optimize the production of silver nanoparticles (AgNPs). Chen and colleagues demonstrated that by using agarose as a capping agent, it was possible to modulate the dimensions of AgNPs by varying key parameters such as reaction temperature, $AgNO_3$ concentration, agarose amount and reaction time. As part of this study, the researchers functionalized agarose-stabilized nanoparticles with an antimicrobial peptide and successfully demonstrated that the combined action of the two agents enabled the creation of a biocompatible system characterized by pronounced antimicrobial properties, which in turn accelerated the healing process in infected wounds. In a series of in vivo experiments, the elimination of infection led to the observation of reactivated processes such as collagen synthesis and angiogenesis.[212] In contrast, in the study by Seo et al, sodium alginate was used as a protective colloid during the synthesis of AgNPs. The investigations carried out showed that the metallic nanoparticles exhibited a negative zeta potential due to the adsorption of the polysaccharides on their surface. In this case, sodium alginate provided both steric and electrostatic stabilization. However, it should be noted that in this research, the preparation of AgNPs was carried out using $NaBH_4$, a potentially polluting reducing agent.[221] On the other hand, in the work of Shao and colleagues, sodium alginate acted as a capping agent for the synthesis of AgNPs through an environmentally friendly approach using ascorbic acid as a reducing agent. In this scenario, nanocomposite sponges with antimicrobial activity were obtained by lyophilization.[221] Alginate is therefore considered to be an excellent stabilizing agent for AgNPs, which can be generated in situ using the polysaccharide to produce fibers, films and sponges. Hydrogels are a primary category of systems being investigated for the stabilization and application of silver nanoparticles (AgNPs) to skin lesions. Due to their viscous nature, these systems are proving to be highly effective in stabilizing nanoparticles and facilitating their easy application to the wound surface. In addition, they can be used both to control the release of AgNPs or Ag^+ ions and

as carriers for the simultaneous delivery of other bioactive molecules such as anti-inflammatory agents or growth factors that support the healing process.[222–225] Considering that polysaccharides are the preferred polymers for the preparation of biomedical hydrogels and that they have been proposed as reducing and coating agents for the synthesis of AgNPs, it is understandable that several research groups have focused their efforts on the development of polysaccharide-based hydrogels containing these metallic nanoparticles. Li et al. developed a dopamine-functionalized hyaluronic acid derivative to enable *in situ* reduction of silver ions, resulting in an antibacterial hydrogel loaded with AgNPs. Experimental results demonstrated the biocompatibility of the hydrogel and its excellent antibacterial properties against both Gram-positive (*S. aureus*) and Gram-negative (*E. coli*) bacteria. In addition, the hydrogel accelerated wound healing in an animal model within 12 days.[226] Other particularly interesting studies focus on the production of hydrogels derived from polysaccharides loaded with AgNPs, which confer intrinsic antibacterial properties to the material, as in the case of chitosan. Masood et al. developed a chitosan and PEG-based hydrogel for the treatment of skin wounds. In this study, the polysaccharide acts both as a reducing agent to enable in situ formation of AgNPs and as a natural antibacterial polymer. The authors demonstrated its efficacy in treating skin wound infections in vivo by cross-linking a dispersion of chitosan, AgNPs and PEG with glutaraldehyde.[227] Conversely, Diniz et al. have produced a hydrogel by combining sodium alginate and gelatin to facilitate the formation and stabilization of AgNPs. Studies in mice showed that the resulting system accelerated the rate of skin wound healing.[228] Dhar et al. have synthesized AgNPs using glucose as a reducing and stabilizing agent. These nanoparticles have been shown to be highly stable under changes in pH and electrolyte concentrations, highlighting the robustness conferred by the properties of glucose on the particles produced. In vitro diffusion studies using AgNPs hydrogels on the skin of rats, it emerged that even at low doses, a significant

concentration of nanoparticles can penetrate inside bacterial cells. Importantly, these AgNPs dispersions did not demonstrate toxicity to mouse embryonic fibroblasts (NIH/3T3), suggesting a possible use of glucose-stabilized AgNPs for topical treatments.[229] Recent researches in the eco-friendly production of AgNPs are trying to minimize the use of reducing agents such as $NaBH_4$. An intriguing approach is the use of catechol groups for on-the-spot silver reduction. These groups have a low reduction potential and are easily oxidized, providing the electrons necessary for the reduction of the Ag^+ ions. An example of a molecule containing catechol groups is dopamine, known for its reducing properties which have been exploited for the synthesis of AgNPs. During the oxidation process, the catechol groups lose two electrons and transform into a dopa-quinone structure which binds to the surface of the AgNPs. The alkylamine portion remains outside, contributing to the stabilization of monodisperse nanoparticles.[230,231] Fullenkamp et al. have developed a hydrogel based on a PEG dendrimer functionalized with dopamine end groups, promoting the formation of AgNPs without the use of toxic reducing agents. The oxidizable properties of the catechol groups not only provide the electrons necessary for the reduction of silver but also favor the cross-linking of the system, creating bonds between the oxidized end portions.[95] Xiang et al. have prepared a copolymer of polycarboxybetaine-co-dopamine-methacrylamide containing repeating units with a zwitterionic functional group alternating with dopamine units. This copolymer (PCBDA) can be used to functionalise the surface of medical gauzes with a thin film of hydrogel to favour the formation of AgNPs. This research group has shown that this polymer is able to prevent bacteria from adhering to the gauze thanks to the electrical charges of the carboxybetaine unit, while the repetitive dopamine units allow AgNPs to easily form on the gauze, giving it antimicrobial activity (**Figure 20**).[232]

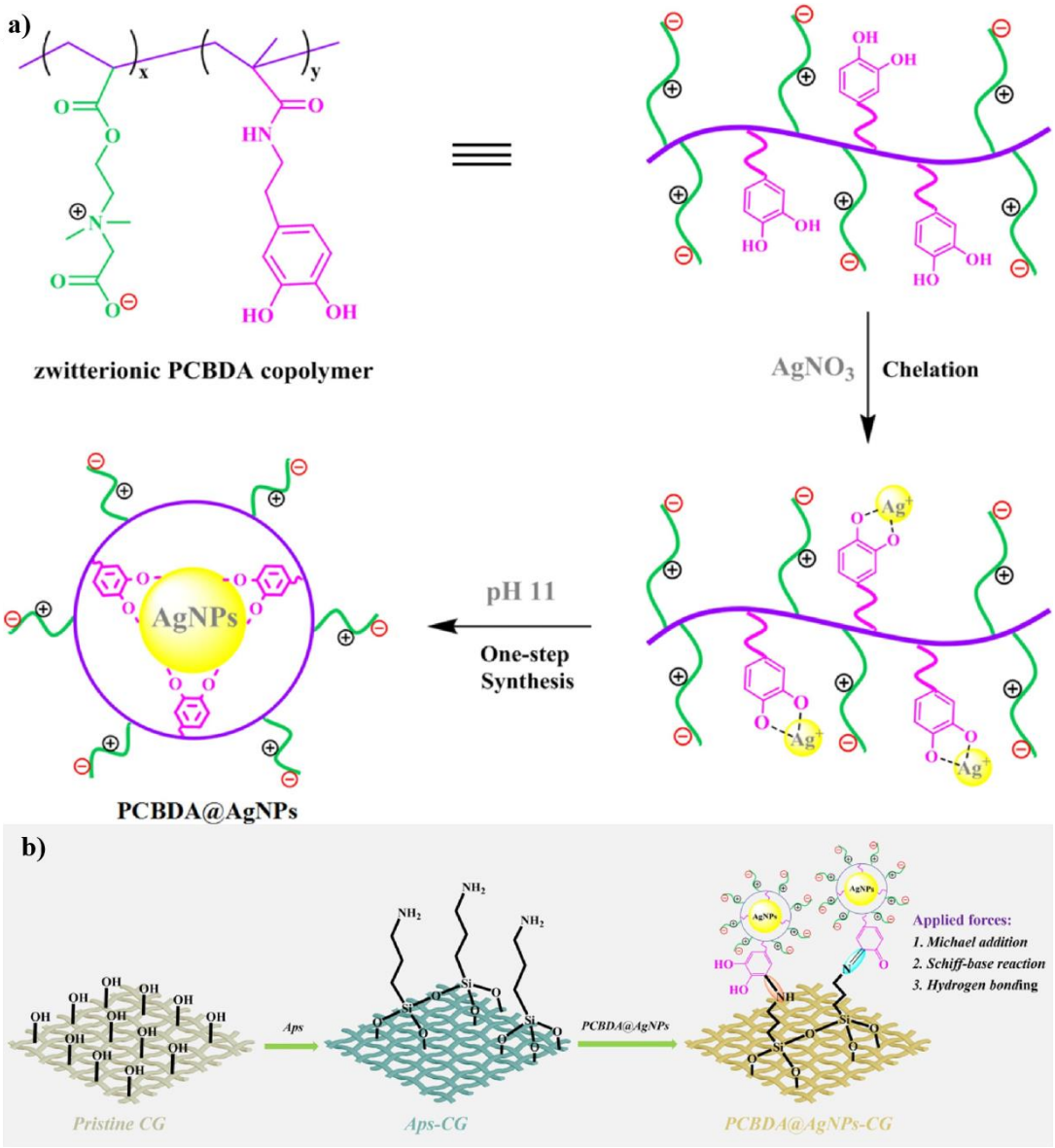

Figura 20. Schematic representation of PCBDA@AgNPs synthetic pathway (**a**) and PCBDA@AgNPs-CG decoration processes (**b**).[232]

Another important feature for designing a multifunctional wound healing system is the radical scavenging capability. Molecules containing catechol groups, as already mentioned during the discussion on polydopamine, have the ability to act as radical scavengers. Cao et al. evaluated the redox properties of catechol-modified chitosan-mimetic melanin-mimetic

films by applying a reverse electrochemical engineering method using a honeycomb gold electrode coated with a catechol-chitosan film. This method simultaneously measures the electrochemical current associated with the oxidation of ABTS, 2,2′-azino-bis(3-ethyl-benzothiazolin-6-sulphonic acid), considered a standard reagent for the study of free radical scavenging activity, and the optical absorbance of the $ABTS^{+\bullet}$ radical, formed during oxidation. That diffuses from the electrode surface into the catechol-chitosan film and can be easily measured spectrophotometrically. In this way, the radical scavenging activity of the film itself can be measured (**Figure 21**).[233]

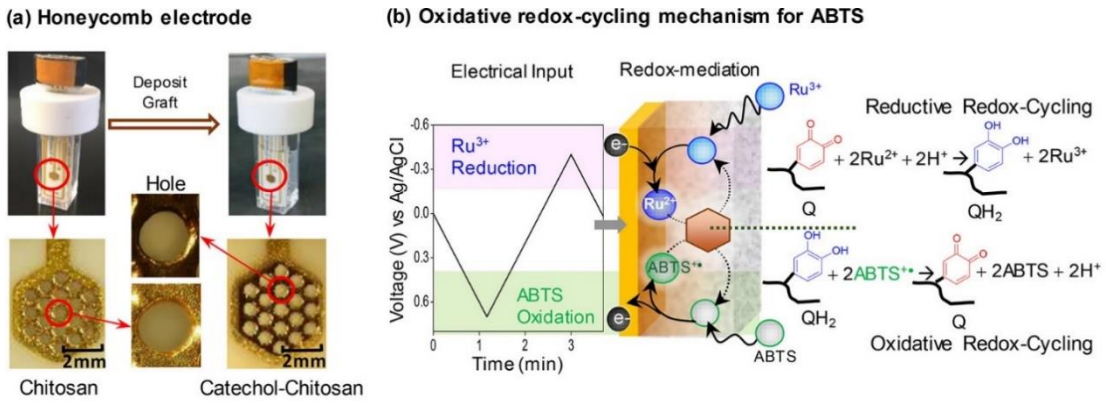

Figura 21. (**a**) Images of the chitosan and catechol-chitosan coated honeycomb electrode used for spectro-electrochemical sensing. (**b**) Scheme illustrating the thermodynamically controlled oxidative and reductive redox cycle reactions that allow the mediators to exchange electrons with the catechol-chitosan film (under oxidizing conditions, the radical $ABTS^{+\bullet}$ is generated).[233]

Hydrogels as previously mentioned, are very useful for wound treatment, they can be exploited to incorporate AgNPs allowing their diffusion in situ. Many studies are aimed at the production of injectable hydrogels, i.e. systems capable of gelling in situ so as to adapt to the shape and size of the skin lesion.[234,235] But the use of microparticulate systems

(microgels) is also very interesting. These particles are able to swell in the wound bed and could be particularly suitable for homogeneous coating of the entire surface. Thanks to their micrometric dimensions, the surface area in contact with the skin is greater than that of classical dosage forms such as hydrogels and can be exploited to achieve a faster, but still controlled, release of the bioactive agent. Many research groups have produced microparticles (MPs) decorated with AgNPs by extrusion. For example, prepared composite Mps consisting of a polyelectrolyte complex of N,N,N-trimethyl chitosan (TMC) and sodium alginate containing AgNPs. The hydrogel MPs efficiently allowed the release of Ag^+ ions, protecting and inhibiting the aggregation of AgNPs. Antimicrobial tests have shown that the concentration of MPs/AgNPs administered can be modulated to provide an amount of Ag^+ ions necessary to kill *Escherichia coli* cells that is not cytotoxic. In this case, 61% of the charged AgNPs were released in an aqueous solution at pH 7.4 and oxidized to Ag^+, while 39% remained in the MPs matrix.[236] Azizi et al. also developed bio-nanocomposites based on a κ-carrageenan matrix containing AgNPs obtained through an ecological biosynthesis process. The produced MPs bio-nanocomposites showed a lower swelling capacity compared to MPs consisting exclusively of pure κ-carrageenan hydrogels. This property was influenced by the porosity of the hydrogel networks. Furthermore, studies evaluating the release of Ag^+ ions from MPs bio-nanocomposites of κ-Ca/AgNPs have shown an excellent and sustained control of the release process, which follows a Fickian diffusion model. The release was adequately described by an exponential power law, the intensity of which depends on the amount of AgNPs present in the composites. It was observed that a higher amount of AgNPs within the MPs was associated with the formation of agglomerations of closely spaced particles. This configuration gave rise to anion-anion electrostatic repulsive forces, the effect of which altered the release mechanism. This change was attributed to the relaxation of the polymer network. The slow release of the Ag^+ ions

showed considerable efficacy in the control of bacteria such as *S. aureus*, *MRSA*, *P. aeruginosa* and *E. coli*. It is particularly interesting to note that the cytotoxicity tests showed an acceptable toxicity for the κ-Ca/AgNPs bio-nanocomposite hydrogels. This result suggests a promising pharmacological potential for such materials.[237] Yadollahi et al. have produced polymeric microspheres (MPs) based on chitosan (CH) and containing silver nanoparticles (AgNPs). The aim of this study was to demonstrate the efficacy of this new type of nanocomposite microspheres as an innovative system for controlled drug delivery, as shown in **Figure 22**. The CH/Ag nanocomposite microspheres showed a increase in swelling ability, together with more pronounced antibacterial properties than microspheres made exclusively from pure chitosan. This improvement was attributed to the presence of AgNPs. Silver nanoparticles have also been shown to have the potential to prolong the drug-release process from microspheres. This effect was attributed to an increase in the distance that the drug must travel to diffuse from the microparticle into its environment. Based on these results, it is possible to consider these nanocomposite microspheres as possible promising candidates for the implementation of controlled drug delivery systems.[238]

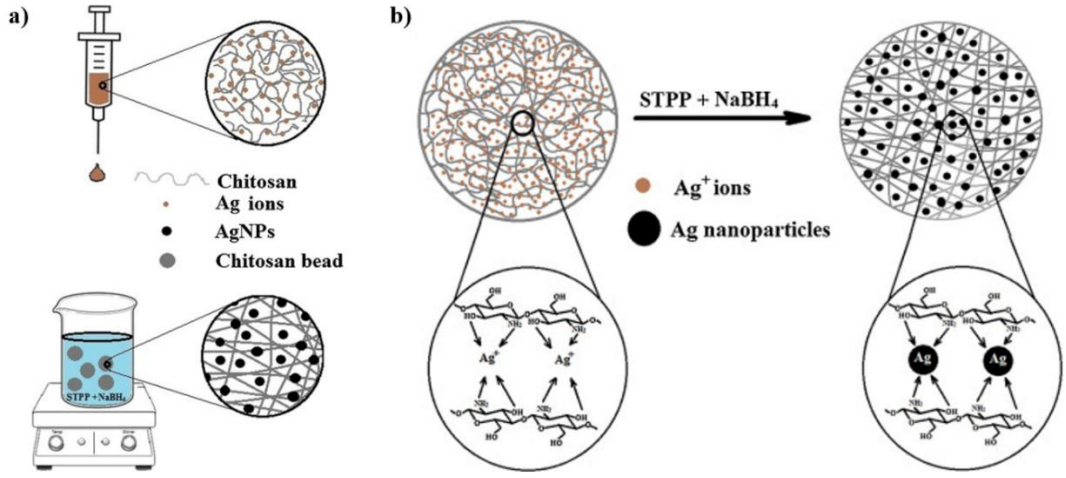

Figura 22. MPs preparation of CH/Ag nanocomposite hydrogels (**a**) and interactions of chitosan with Ag^+ ions and AgNPs (**b**).[238]

Zhou et al. have prepared AgNPs-loaded microparticles in situ using a hydroxyapatite/alginate (HAp/Alg) compound, by the double emulsion method. The microparticles resulting from this nanocomposite combination exhibited a homogeneous distribution of AgNPs within their structure (as shown in **Figure 23**). The microparticles showed remarkable compatibility with antibacterial activity against both *E. coli* and *S. aureus*.[239]

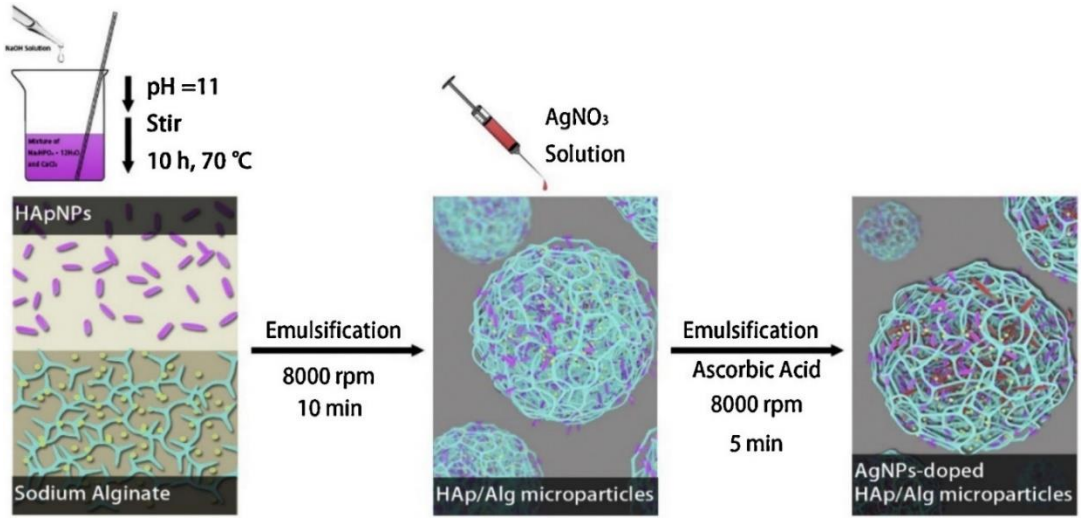

Figure 23. Synthesis of HAp/Alg nanocomposite microparticles with AgNPs by double-emulsion method.[239]

Yang et al. have produced composite microparticles of chitosan (CH) loaded with silver nanoparticles (AgNPs) using the microfluidic method (**Figure 24**). These nanocomposite particles, observed under the microscope, had a spherical, intact and solid surface. Elemental mapping at the microstructure level (EDS) confirmed the presence and uniform distribution of silver atoms (Ag^0) within the MPs. In the UV-Vis spectra of the composite microparticle dispersions, a peak at 410 nm was detected, which is characteristic of nanoscale silver

nanoparticles. These composite microparticles were shown to be effective in inhibiting the growth of bacteria such as *E. coli*.[240]

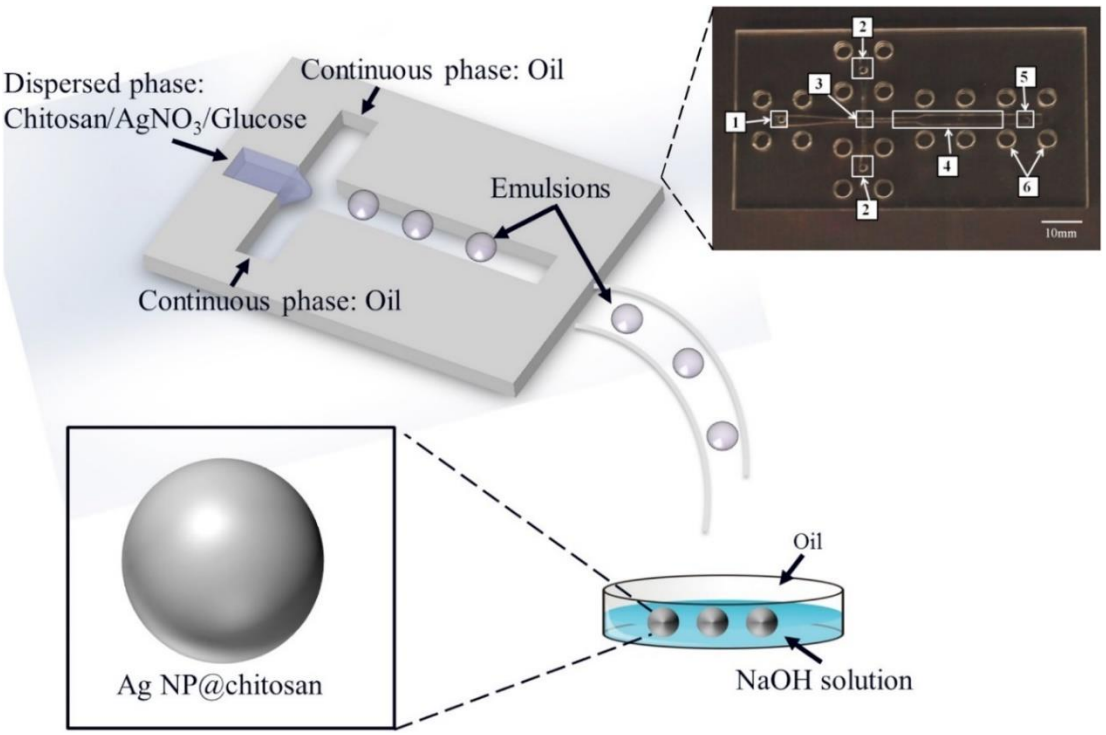

Figure 24. Schematics of the production of the chitosan composite microparticles loaded with AgNPs by microfluidic method.[240]

Dilshad et al. also have presented an effective chemical reduction method for the synthesis of well-defined AgNPs and AgMPs. The study showed that some compounds, such as citric acid and maleic acid, act as stabilizers of nano- and micro-particles and affect their size and shape.[241] These substances may contribute in part to enhancing the antimicrobial and anticancer potential of silver particles, but may also contribute to the antioxidant activity of nanoparticles by scavenging or trapping free radicals (**Figure 25**). The effectiveness of silver nanoparticles (AgNPs) in neutralizing free radicals has long been demonstrated, in addition to using the ABTS assay, mentioned above, also through the use of the DPPH assay.[242] In

addition to that, under this situation, the antioxidant efficacy of the particles is further enhanced by the bio-capping agents (maleic acid and citric acid) which adsorb on the surface of the nanoparticles. These agents possess intrinsic antioxidant activity due to their ability to form complexes with metals through the chelation process.[241,243]

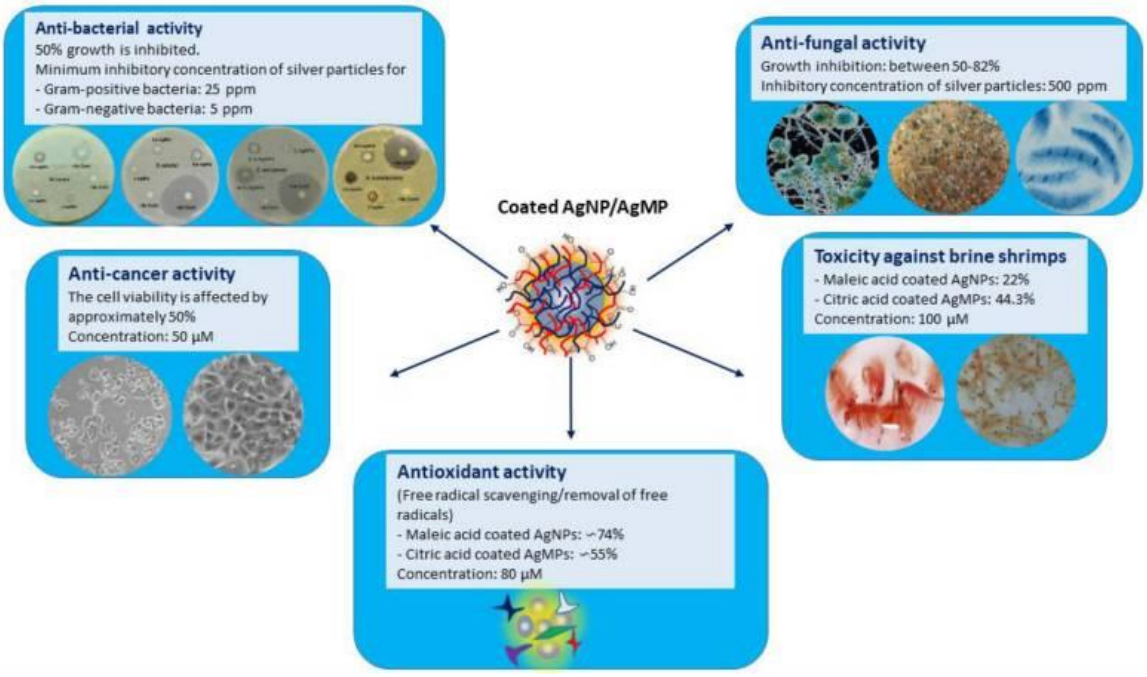

Figura 25. Activities shown by microparticles coated with AgNPs/AgMPs.[241]

The above-mentioned techniques make it possible to produce composite microparticles with silver nanoparticles (AgNPs), which have exceptional properties for various biomedical applications. However, their reproducibility is not always guaranteed, and they require long production times, which limits their adaptability on an industrial scale-up. Among these techniques, spray drying is widely cited in the literature for the preparation of microparticles. This method is particularly suitable for heat-sensitive compounds and for the encapsulation of nanostructures. One of its strengths is the ability to control critical aspects such as particle size, reproducibility and reliability. It is also a continuous process that can be adapted for

industrial scale-up. The main process is spray drying, in which a polymer solution containing the active ingredient or metal nanoparticles is sprayed into a drying chamber. The small droplets formed are converted into solid microparticles by the use of heated air, which rapidly evaporates the solvent. A notable advantage of this method is that the resulting microparticles are usually free of organic solvents, unlike other preparation processes which, if used, can result in the presence of toxic solvent contaminants in the finished product.[244,245]

1.2.2.4 Dendrimer or Hyperbranched polymers with antibacterial activity

Continuous research and development in the field of chemistry has opened up new perspectives in the design and synthesis of compounds with antibacterial properties. The aim of developing new antimicrobials is not only to ensure efficacy against bacteria but also to prevent the emergence of bacterial resistance.[246] One group of substances that has attracted increasing attention in this context are antimicrobial peptides (APs), a broad range of molecules active against bacteria, capsular viruses, protozoa and fungi. Synthesized on ribosomes and encoded by genes, APs are a key element of the innate immune system of all animal organisms. APs are relatively small (consisting of 10-50 amino acids), amphiphilic and cationic-charged peptides that fold into amphipathic structures and interfere with the plasma membranes of target cells through destabilization and/or permeation processes.[247–251] Their multi-directional mode of action allows APs to prevent the emergence of acquired resistance by bacteria.[252] Despite the interesting potential of APs as an alternative to conventional antibiotics due to their low tendency to generate antimicrobial resistance, they have certain limitations. These limitations are due to their peptide nature and result in reduced bioavailability and poor proteolytic stability, factors that have hindered clinical progress to date. To overcome these challenges, various modifications have been used to

develop synthetic analogues capable of mimicking the properties of APs.[253,254] The main model for these modifications remains natural APs, with a focus on their physicochemical properties related to membrane activity, such as positive charge and amphiphilicity. Antimicrobial polymers (AMPs) have emerged as one of the most promising synthetic strategies to emulate these properties.[255] AMPs can exhibit antibacterial activity due to their intrinsic chemical structure, which includes quaternary ammonium groups, alanine and polylysine, or they can be used as a base to enhance existing antibiotics activity. As shown in **Figure 26**, the design of AMPs is based on the chemical models provided by APs.[255]

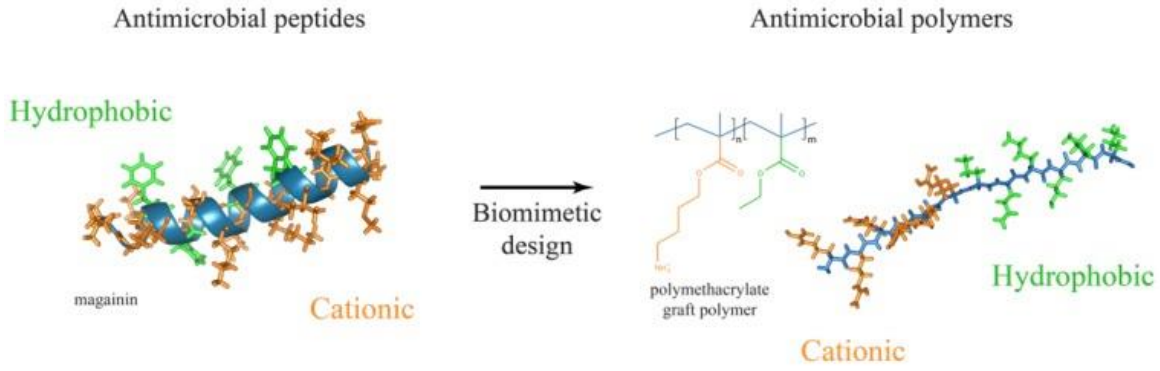

Figura 26. Structural similarities between antimicrobial polymers (AMPs) and antimicrobial peptides (APs).[256]

Advances in the research of antimicrobial polymers, both natural and synthetic, have led to a growing interest among researchers in the further development of amphiphilic polymer structures with antimicrobial properties.[256] The characteristics of polymer structures and their physicochemical properties, such as molecular weight, polymer architecture, amphiphilic ratio and molecular arrangement, are factors that can influence the antimicrobial potency and selectivity of materials.[257] An ideal amphiphilic antibacterial polymer with a cationic moiety, low molecular weight and low lipophilicity could exhibit effective

antibacterial activity against Gram-positive bacteria while having a minimal effect on human erythrocyte lysis, i.e. < 4% hemolysis at a specific minimum inhibitory concentration (MIC).334 Locock et al in 2014 highlighted how the combined effect of specific pendant functional groups can alter the potency, selectivity and mechanisms of synthetic polymer AMPs. Empirical evidence has shown that optimizing the degree of hydrophobicity and cationic strength is crucial for amphiphilic polymers to achieve maximum antibacterial activity and minimal red blood cell hemolysis.[259] For example, polyurethanes mimicking APs with a lower ratio of the hydrophobic region and higher cationic strength have shown higher bactericidal activity and lower hemolysis rate.[260] When comparing cationic amine- and guanidine-copolymers, the latter of low to moderate molecular weight and hydrophobicity showed higher antimicrobial activity against *S. epidermis* and lower toxicity toward red blood cells.[258] On the other hand, self- or biodegradation of polymers is an essential aspect in the selection of suitable antimicrobial materials.[257,261] The degradability properties of antimicrobial materials prevent or minimize undesirable complications associated with the prolonged persistence of materials in the human body or the environment. A controlled polymer degradation rate, achieved through monomer composition and amine functionality, could allow precise control of the duration of antimicrobial activity.[262,263] Dendrimers are a class of molecules whose name derives from 'dendron', meaning 'tree', due to their distinctive branched structure (**Figure 27**). Dendrimers are hyper-branched polymer molecules that are characterized by a geometrically almost perfect three-dimensional architecture and a unique set of surface functionalities that provide them with unique properties that make them very different from linear polymers. They have a central core to which monomer branches are anchored to form a polymeric structure; these branches develop from the core, resulting in a globular conformation with a size between 2 and 5 nm. Each of these branches is called a generation (G1, G2, G3, etc.). The greater the

number of generations, the greater the number of terminally branched and exposed functional groups available for conjugation with other molecules, including small-molecule antibiotics.[264] The relationship between generations and the presence of peripheral groups is directly related to charge presentation, making dendrimers versatile for both therapeutic and imaging applications. The synthesis of drugs and targeting moieties is closely related to the characteristics of the terminal functionalities. These functionalities provide a perfect solution for coupling different copies of a drug and/or ligand to the periphery of dendrimers. The interaction between a dendrimer with multiple ligands on its surface and a target with multiple receptors results in a significant increase in the affinity between the dendrimer and the cell.[265] The presence of multiple ligands conjugated to a dendrimeric scaffold can therefore transform the structure into a high-affinity molecule. The chemical branches of dendrimers can be modified for solubility and degradability to enhance biological properties of interest.[266] The globular structure of dendrimers allows the formation of coexisting nano-districts, giving distinct properties between the core and the periphery. This opens up the possibility of encapsulating active molecules within the dendrimers themselves. The dendrimer technology is able to overcome some limitations of traditional pharmaceutical formulations, such as efficient cellular entry, reduced uptake by macrophages, targeting ability, and facilitation of passage through biological barriers via transcytosis. In addition to their role as molecular transporters, dendrimers can possess intrinsic bioactive properties and can be used to modify materials to obtain hybrid materials. Cationic dendrimers have attracted constant interest from the scientific community due to their ability to cross cell membranes via endocytosis and their exposed positive charges, which give them antibacterial ability.

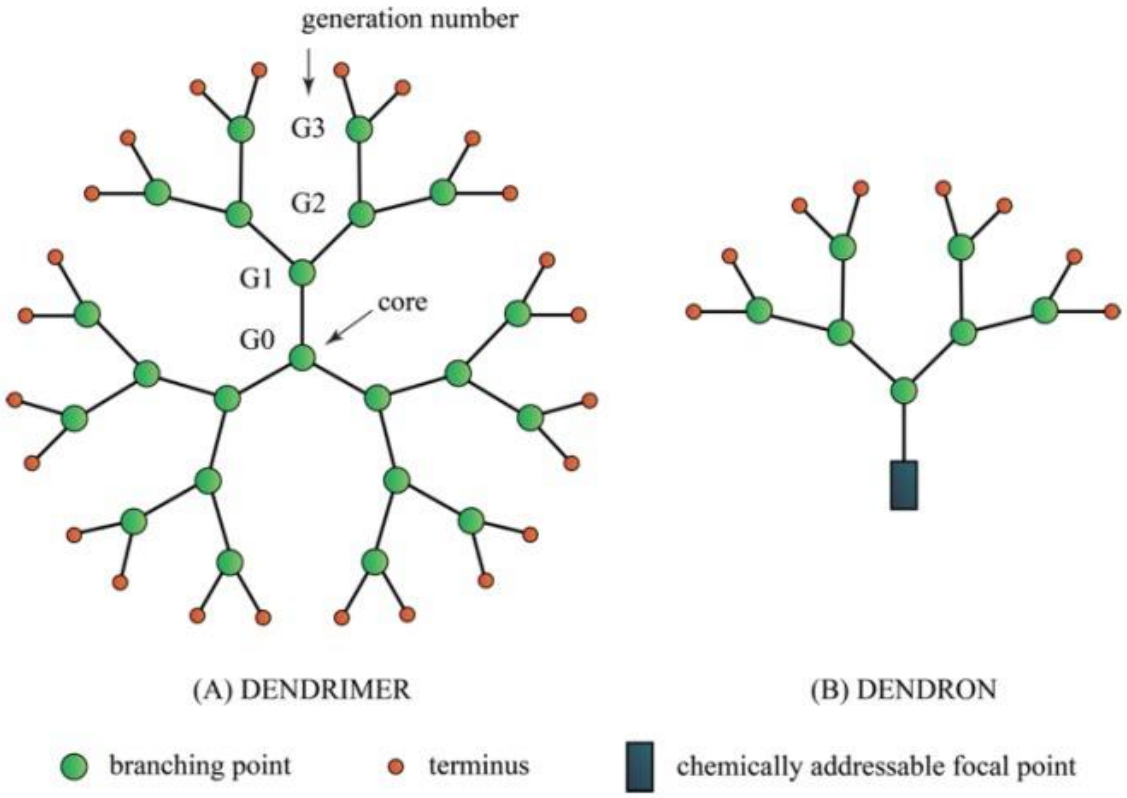

Figure 27. Typical structure of a dendrimer (**A**) and a dendron (**B**), from which it derives.[267]

Different synthetic strategies that can be applied are summarised in **Figure 28**. The synthesis of dendrimers is often based on a repeated sequence of robust organic reactions, where each successive reaction results in a higher dendrimer generation, at least doubling both the molecular weight and the number of peripheral groups. Tomalia and Newkome were among the first authors to independently report the complete synthesis and characterization of dendrimers, known as 'true dendrimers' and 'cascade molecules' respectively.[268,269]

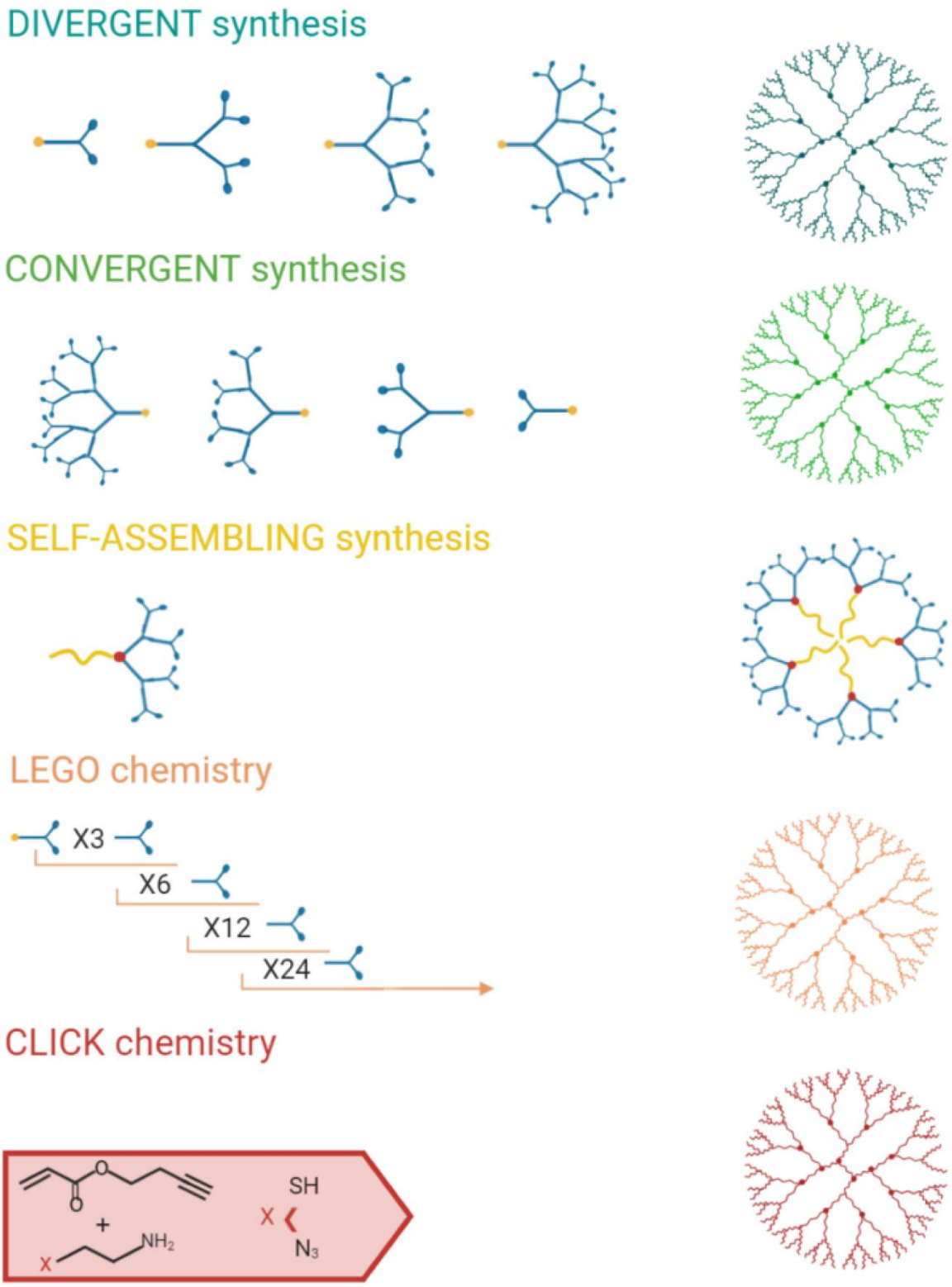

Figure 28. Synthetic strategies exploited in the development of dendrimers.[270]

Among the most commonly used dendrimers in biological applications are those based on poly(amidoamine) (PAMAM) and polypropylene imine (PPI) (**Figure 29**). Tomalia was the first to commercialize poly(amidoamine) (PAMAM) dendrimers. Initially studied as drug delivery vehicles, cationic poly(amidoamine) (PAMAM) dendrimers were later evaluated for their antimicrobial properties.[271,272] The antimicrobial activity of such dendrimers is closely linked to multivalency effects resulting from their tree-like structure and, in particular, the abundant presence of active fractions. Both cationic and amphiphilic dendrimers exert antimicrobial activity by disrupting the membrane of the pathogen.[273,274]

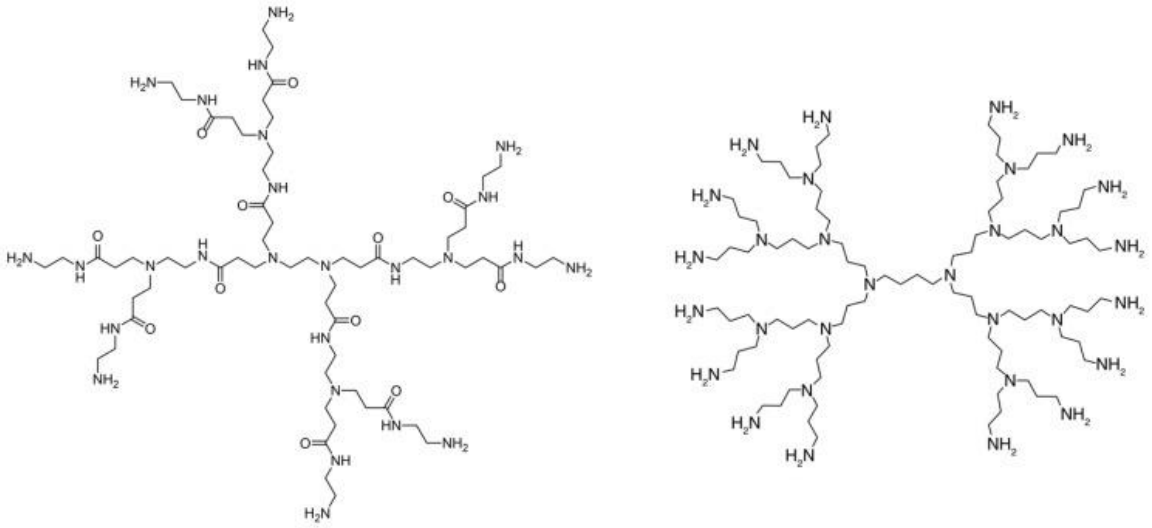

(a) Polyamidoamine dendrimer G1 (b) Polypropyleneimine dendrimer G3

Figure 29. Structures of dendrimers based on polyamidoamines (PAMAM) (**a**) and polypropylene imine (PPI) (**b**), common dendrimers for biological applications.[270]

The antibacterial efficacy is intrinsically linked to the electrostatic interaction between the positive charges of the dendrimers and the negative bacterial surface, as well as the progressive weakening of the bacterial membranes and the destruction of the lipid bilayer.[275] Therefore, as with other antimicrobial agents, the multivalency of positive charges plays a

key role in the antimicrobial activity of dendrimers. Those with higher generations have proven to be particularly effective as highly active biocidal agents.[276] Among dendrimers, polyamidoamine (PAMAM) dendrimers have been the most extensively studied, and those of the third generation or higher with amine end groups (PAMAM-NH_2) have shown marked cytotoxic toxicity, which has limited their use as antibacterial agents in in vivo settings.[277] Attempts to chemically modify PAMAM-NH_2 dendrimers helped to reduce their toxicity but resulted in a decrease in antibacterial activity.[278] In contrast, lower-generation PAMAM-NH_2 dendrimers exhibit broad antimicrobial activity, excellent therapeutic efficacy and relatively low cytotoxicity without inducing bacterial resistance.[279] However, cationic dendrimers are toxic to mammalian cells, and in order to maintain the antibacterial effect with a significant reduction in toxicity to eukaryotic cells, nitric oxide (NO)-releasing dendrimers were developed.[280,281] The synergy of NO and cationic dendrimers led to a reduction in the concentration of cationic dendrimers while maintaining satisfactory antibacterial activity and reducing toxicity to mammalian cells (**Figure 35**). Modification of the cationic amine groups of PAMAM with PEG chains showed a drastic reduction in toxicity problems without reducing the antimicrobial capacity.[282] De Queiroz et al. conjugated polyglycerol dendritic acid (PGLD) with chitosan to obtain PGLD-chitosan dendrimers capable of overcoming bacterial proliferation of *Staphylococcus aureus* and *P. aeruginosa*.[283] Fourth-generation poly(propyleneimine) dendrimers with their maltose-modified surface (schematically shown in **Figure 30**) were evaluated for their antibacterial activity against the Gram-positive bacteria *S. aureus* and *S. epidermidis*; and against the Gram-negative bacteria *E. coli*, *P. aeruginosa* and the yeast *C. albicans*. Dendrimers showed the greatest antimicrobial activity against *S. aureus*.[284]

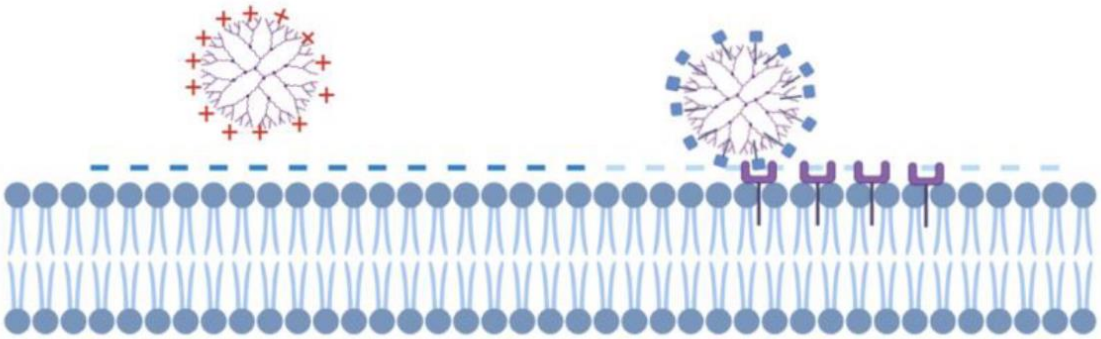

Figure 30. Cationic dendrimers and maltose-conjugated dendrimers, whose antimicrobial activity is linked to electrostatic interaction and consequent permeabilization of bacterial membranes, or interaction with specific receptors on the host cell membrane.[270]

Mofrad et al. have demonstrated the efficacy of the dendrimer G3-poly-amidoamines (G3-PAMAM) against seven species of both Gram-positive and Gram-negative bacteria. Interestingly, a higher sensitivity was observed in *Salmonella* species, while a lower sensitivity was found in *Klebsiella* species. The authors suggested that differences in bacterial membrane composition contribute to the different barriers against dendrimers entering the bacteria.[285] Furthermore, Pires et al. demonstrated the effective antimicrobial activity of the peptide dendrimers G3KL against multiresistant *Acinetobacter baumannii* and *Pseudomonas aeruginosa*.[286] It is of utmost importance to evaluate the biological compatibility and cytotoxic potential of compounds when assessing their suitability for pharmaceutical and biomedical applications. The cytotoxic effects of PAMAM dendrimers have been investigated in several mammalian cell lines.[287–290] Byrne et al. reported that amine-functionalized PAMAM dendrimers exhibited severe long-term toxic effects

compared to acute effects in a long-term exposure study.[289] The toxic mechanism leading to cell death was confirmed to be the accumulation of dendrimers in cellular tissues.[290] The reduced biocompatibility of amine-functionalized PAMAM dendrimers could be attributed to their polycationic nature and accumulation in cells or tissues due to their slow degradation.367 Chemically, this slow degradation can be attributed to the presence of the amide interior of the dendrimers, which is both hydrolytically stable at physiological pH and enzymatically stable in vivo. The latter property presents a challenge to researchers seeking to make structural modifications to create a new generation of self-immolating dendrimers that degrade in response to specific stimuli.[292] Due to these limitations, there is growing interest in the use of biodegradable dendrimers as a non-toxic alternative. In this context, a new family of cationic dendrimers, the polyester dendrimers based on 2,2 bis(hydroxymethyl)propionic acid (bis-MPA), have emerged as a promising alternative to the dendrimers described above, due to their structural versatility, good cytotoxic profile and their degradation to non-toxic substances (**Figure 31**).[293–295] Fadel et al. conducted an in-depth analysis to investigate the relationship between biodegradation and cytotoxicity of bis-MPA dendrimers, taking into account their generation and surface groups, in comparison to PAMAM dendrimers with hydroxyl and amine functionalities. This study showed that hydroxyl group dendrimers were not toxic, whereas those with a cationic charge, such as PAMAM dendrimers, were cytotoxic. In addition, bis-MPA dendrimers with hydroxyl functionality showed greater susceptibility to degradation at pH 7.5 than under more acidic conditions such as pH 4.5. The degradation process was found to occur via a depolymerization mechanism, with hydrolysis of the ester linkages initially progressing from the periphery inwards towards the dendrimeric core.[296] Again, the amine-functional bis-MPA dendrimers decorated with β-alanine were evaluated for their antimicrobial activity and degradation profile.[297,298] The hydrolytic evaluation showed a rapid degradation by

removal of β-alanine groups at physiological pH.[298] Although traditional bis-MPA dendrimers offer a wide range of desirable properties to meet the needs of applied research in biomedical applications, it should be considered that their hydrolytic depolymerization process at pH 7 could be a limiting factor in contexts where stability is preferred for conjugation purposes or to ensure sustained performance in a physiological environment.

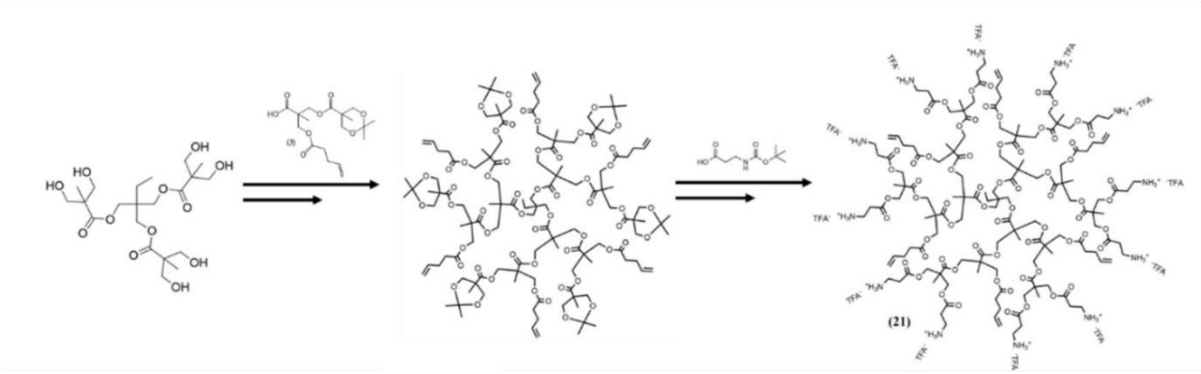

Figure 31. Schematic illustration of the synthesis route for bifunctional dendrimers with alkenes and ammonium groups.[299]

One strategy to improve the cytotoxicity profile of these dendrimers is to combine them with other compounds, such as other polymers or polysaccharides. One example is provided by Fan et al. who designed antibacterial hydrogels based on the self-assembly of the cationic polyester bis-MPA dendrimers described above and carboxylated cellulose (CNF) nanofibrils. Hydrogels of G3 and G4 dendrimers showed 100% killing efficiency against Gram-positive and Gram-negative bacteria. They also showed high biocompatibility with cells due to the role of CNFs in slowing the release of toxic cationic dendrimers.[297] To further overcome these limitations, in a recent work, Namata and collaborators presented a new family of amino-functionalized bis-MPS dendrimers that manage to maintain internal structural integrity even at high pH (**Figure 32**). Indeed, the modification of the outer layer

showing Cysteamine-functionality increases the hydrolytic stability at various physiologically relevant pHs compared to the previously reported β-alanine derivatives.[298,299] An alternative depolymerization mechanism was observed for this novel dendrimer. In contrast to β-alanine-functionalized bis-MPA dendrimers, the loss of the first functionalized bis-MPA moiety at the periphery was followed by a bis-MPA group in the inner layer rather than a gradual loss in the surface layer. The increase in stability was accompanied by an increase in antibacterial activity against both Gram-positive and Gram-negative planktonic bacterial strains. Surprisingly, despite the considerable toxicity often associated with cationic systems, this new class of dendrimers has been shown to be non-toxic at the concentrations at which they exhibit activity against bacteria.[300]

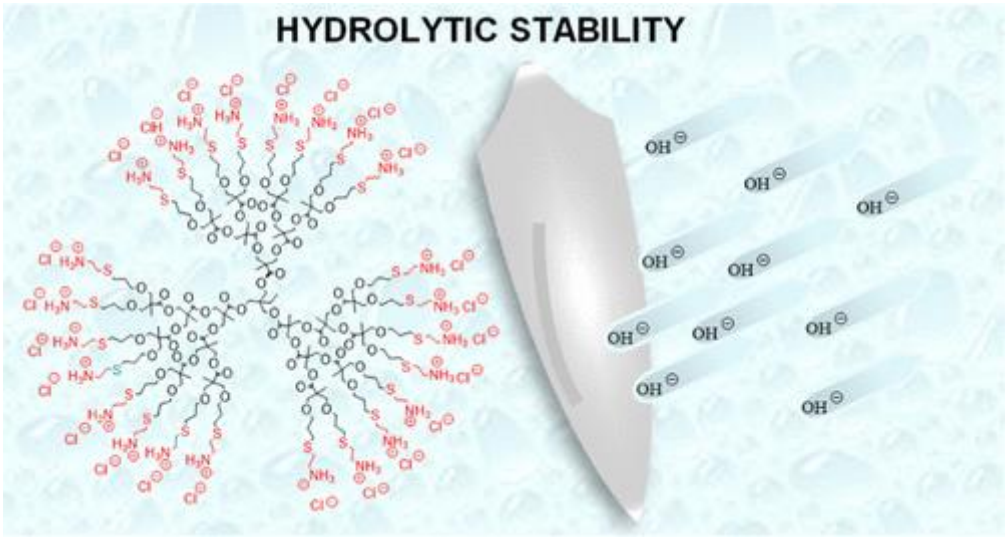

Figure 32. New class of highly stable bis-MPA dendrimers at high pH.[300]

Another family of dendrimers that has been studied in recent years is that developed by Sanz dell'Olmo et al. These are carbosilanic polyphenolic dendrimers decorated with ferulic, caffeic and gallic acids. The results obtained by spectrophotometric and electrochemical techniques confirmed that the dendritic polyphenols had higher antioxidant activities than

the free polyphenols. The formation of the dendrimer and the type of acid significantly influenced the antioxidant activity and antibacterial properties. In particular, G1-(Gallic)$_4$ appeared to be the most promising candidate with a MIC_{50} of 4 ppm against S. aureus and 16 ppm against E. coli.[301] Rodríguez-Prieto et al. demonstrated the antibacterial activity of several dendritic carbosilane molecules containing N-heterocyclic silver(I) carbenes and their precursors. The effect of parameters such as topology, generation, hydrophobicity and presence of silver ions was studied, confirming the crucial role of the lipophilic-hydrophilic balance. Furthermore, the in-depth study aimed at elucidating the mode of action of *Bacillus subtilis* identified the cell envelope as the main target. Taken together, this work highlights the potential of cationic imidazolium dendrimers or Ag(I)-NHC metallodendrimers in the fight against bacterial infections.[302]

2. Aim of the dissertation

The challenge in developing therapeutic systems for the treatment of chronic skin wounds is to address the negative effects that these difficult-to-heal wounds have on patients' quality of life. Wounds that fail to heal, due to the absence of a protective barrier, are easily subject to infections, which further delay healing and pose a growing threat to global health due to the emergence of antibiotic resistance. Furthermore, at the site of the wound, the persistent inflammatory state is worsened by the excessive release of oxygen free radicals (ROS) and proteolytic enzymes by the cells of the immune system, which attempt to eliminate pathogens that have infiltrated the wound itself. This prolongs or even blocks the healing process, leaving patients in a debilitating state requiring lengthy treatments that place a burden on the healthcare system. Among the most studied strategies in recent years to find an ideal treatment for chronic wounds, are antibacterial injectable hydrogels based on polysaccharides, synthetic polymers, or hybrid biomaterials. The former presents various advantages, mainly linked to biocompatibility, biodegradability, and low cytotoxicity. Synthetic biomaterials are above all interesting for their chemical versatility and low production cost. Hybrid biomaterials therefore represent the right compromise and allow obtaining multifunctional systems with synergistic characteristics, due to the properties of both components. Hydrogels, based on the starting biomaterials, can be designed in such a way as to have certain functions and activities. Therefore, multifunctional and smart systems must be used, i.e. capable of responding to certain external or internal stimuli and which have activities suited to the application's requirements, such as antimicrobial activity or/and radical scavenging capacity, if it is a question of treating the infected wound. Among the various natural polymers, Gellan Gum (GG) and Xanthan Gum (XG) have shown

considerable potential as usefull starting materials, such as to allow their wide application in the biomedical field. The starting molecular structures of polymers allow for easy functionalization with new functional groups, which allow their subsequent use in the formulation of injectable and multifunctional hydrogels.

The diversity and intricacy of wounds require a spectrum of individualized and personalized therapeutic strategies. While extensive research and studies have been undertaken in the realm of wound healing, the array of skin lesions, spanning from acute to chronic wounds, present unique complexities that demand equally diverse and innovative solutions. For instance, wounds exhibiting resistance to long-term healing, such as chronic pressure ulcers or diabetic wounds, require pioneering treatments that surpass conventional methodologies. Additionally, the susceptibility to infection, presence of impaired tissues, and the emergence of antibiotic resistance emphasizes the critical need for the development of sophisticated therapeutic approaches. Despite significant progress in medical technology and research on biomimetic materials, the requirement remains for the development of highly adaptable and versatile systems, capable of responding to varied conditions and stages of wound healing. Innovation is pivotal in augmenting the speed and efficacy of the healing process, concurrently mitigating the risks of complications and enhancing the quality of life for patients. Ongoing research continues to underscore the essentiality of a profound understanding of wound dynamics and the tailored development of solutions to address these challenges. This Ph.D. thesis highlights that, despite progress, there is considerable potential for innovation and the creation of new strategies based on the development of biomaterials for wound treatments. For this reason, the main aim of this Ph.D. thesis was to design and synthesize new semi-synthetic derivatives of the aforementioned polysaccharides to obtain multifunctional, smart scaffolds capable of conveying the latest generation antimicrobial

agents. From a functional point of view, given the potential application in infected skin wounds, the formation of dynamic bonds and self-healing hydrogels was the basis of the investigation of this Ph.D. thesis to provide the obtained hydrogels with adjustable mechanical properties and chemical stability. In particular, hydrogels have been obtained by forming imine bonds between biomaterials having aldehyde groups and amino groups. The Schiff Bases react, even in mild conditions, reversibly, allowing the hydrogels to recover their structures and functions. The dynamism of this bond favors the process of injection of the hydrogel into the site of the infected skin wound with subsequent deposition of the hydrogel following the irregular perimeters of the wound. A criticism of wound healing bandages is their poor adhesion to tissues. L-3,4-dihydroxyphenylalanine (Dopamine) is an amino acid present in mussel adhesive proteins (MAP), secreted by marine mussels, which are able to build complexes of byssal threads and adhesive plates to firmly anchor their bodies on all surfaces. It is for this reason that, in addition to designing injectable hydrogels, during all the work carried out during the Ph.D. period, particular attention was paid to the use, as a functional group, of dopamine as a group capable of providing the biomaterial for tissue adhesion. Mussel-inspired polymers were therefore obtained. As regards the antimicrobial aspect, the research carried out during this Ph.D. period was characterized by a crescendo, gradually using increasingly innovative and alternative materials to the common antibiotics incorporated into the aforementioned mussel-inspired injectable hydrogels. In particular, the first works focused on the use of classic antibiotics, such as Ciprofloxacin and Colistin, which are still among those antibiotic molecules against which not all pathogenic bacterial strains have yet developed resistance. The use of these antibiotics inside hydrogels, which represent a classic and specific attack strategy against bacteria, was however accompanied by the presence of a biomaterial capable of exerting a non-specific antibacterial activity, polydopamine (pDA). The pDA is a polymer obtained through the self-

polymerization of dopamine, which has the ability to convert light at a certain wavelength (in the infrared spectrum, 810 nm) into heat and thus exerts a photothermal antimicrobial activity (APTT). The evolution and development of advanced therapeutic systems for the treatment of wounds have placed an increasing emphasis on finding solutions that not only promote healing, but also combat infections without relying exclusively on antibiotics. The need to reduce dependence on antibiotics derives mainly from the increase in bacterial resistance, a phenomenon caused in part by the excessive and unregulated use of antibiotics themselves. As a result, there is growing interest in developing therapeutic wound healing systems that can fight infections without resorting to traditional antibiotics. Subsequently, an approach was adopted that aimed to develop systems that were able to prevent and treat infections effectively even without the use of antibiotics. By exploiting new technologies and advanced materials, we tried to obtain systems that not only could promote wound healing, but were also able to fight infections in a targeted and specific way. developing hybrid hydrogels through the use of cationic polyester dendrimers, hybrid hydrogels containing metal nanoparticles, such as green-synthesized in situ silver nanoparticles (AgNPs). The use of microcapsules and microspheres offers significant advantages, such as the protection of the encapsulated substances and the possibility of prolonged treatments by injection or directly spraying them into the wound site.[303] The approach of developing biodegradable microparticles via the spray drying method shows promise in the context of wound healing. In order to reduce the toxicity associated with high concentrations of antibiotic molecules, metal nanoparticles (etc.), it is desirable to develop a formulation that allows a controlled and prolonged release, exceeding the effectiveness of traditional microspheres or hydrogels alone. An injectable hydrogel incorporating nanocomposite microspheres could uniformly coat the wound site and conform to its shape after injection.

In this context, it is hypothesized that, within such a system, the nanoparticles should initially diffuse from the microsphere matrix and subsequently from the hydrogel network to be released into the wound bed. This gradual release could reduce cytotoxicity related to high concentrations of bioactive substances. The goal of obtaining a system capable of controlling and minimizing side effects, especially toxicity, represents a challenge in research to ensure a safe and effective treatment for wounds.

With this aim, initially, new gellan gum (GG) derivatives were synthesized for the subsequent formulation of injectable hydrogels. In particular, in a first work, in order to improve the performance of gellan gum, the effect of reducing the molecular weight as a function of the alkaline hydrolysis times of the polysaccharide was first studied. Indeed, although there were several studies describing the characterization of low molecular weight GG products, these mainly investigated the rheological properties of aqueous dispersions.[304–306] However, a study on the correlation of the rheological properties of different low molecular weight GGs with the physicochemical properties of the derived ionotropic cross-linked hydrogels was missing. The low molecular weight GG products were obtained by alkaline hydrolysis of a high molecular weight GG by varying the reaction times and keeping the temperature constant. The aim of this work was to investigate whether the drastic reduction in the molecular weight of GG still allowed the obtaining of thermotropic products that could be cross-linked, exploiting the ionic strength of the external medium. Furthermore, we aimed to study the influence of molecular weight on the main physicochemical characteristics of GG hydrogels.

Subsequently, in a second work, we used the lowest molecular weight GG_{24} as a starting Gellan Gum in the form of tetrabutylammonium salts, $GG_{24}TBA$, to obtain an amino derivative of GG with low acyl content, called GG-EDA, which shows superior viscoelastic

properties and chemical versatility compared to the starting macromolecule, which had already been synthesized in our research group.[112] In particular, in this work, a hydrogel was developed GG-EDA-based nanocomposite cross-linked via Michael-type addition using 4-arm polyethylene glycol functionalized with vinyl sulfone (4-VS-PEG) as a cross-linking agent in the presence of polydopamine (pDA) nanoparticles. As previously mentioned, pDA gave photothermal properties to the hydrogel, providing it with non-specific antimicrobial activity against bacteria. pDa also undergoes nucleophilic attack by the pendant amino groups of GG-EDA during the gelation process, thus taking an active part in the production of hydrogels with superior viscoelastic properties, hydrolytic resistance, and photostability. In this work, ciprofloxacin, chosen as a model drug due to its broad antimicrobial spectrum (it is active against both Gram-positive and Gram-negative bacteria) and its low minimum inhibitory concentration (MIC),[307] was incorporated into the hydrogel-containing pDA.

The GG_8 and GG_{24} derivatives were also used later, in the form of tetrabutylammonium salts, GG_8-TBA and GG_{24}-TBA, for the subsequent functionalizations of the polysaccharide itself, inserting as groups polyethylene glycol and dopamine pendants. obtaining, respectively, GG_8-DAPEG and GG_{24}-DA-PEG. GG_8-DA-PEG was used to develop injectable hydrogels, resulting from the electrostatic interactions formed between the polymer and colistin sulfate, a polypeptide antibiotic active against Gram-negative bacteria. The hydrogel was then loaded with pDA. The pDA has colloidal dimensions which could favor its diffusion from the hydrogel causing the system to lose its photothermal properties. To overcome this problem, microparticles were therefore produced, based on GG_{24}-DA-PEG, which were functionalized with a pDA shell and then incorporated into the hydrogel to make it responsive to NIR light, conferring photothermal properties. It was thus possible to obtain multifunctional systems, with rapid shape adaptability, rapid self-healing, and tissue

adhesion, which simultaneously exert a non-specific antioxidant and antimicrobial action, due to the pDA present on the surface of the microparticles, and a specific antimicrobial action, thanks to the presence of the antibiotic, the release of which is accelerated thanks to the response to the NIR stimulus, applied to the site of the infected skin wound. Few articles reported that colistin enhanced the effect of APTT on bacteria by disrupting bacterial membranes. But it is known to work by enhancing antibacterial photodynamic therapy (APDT).[308] Strengthened by this knowledge, we hypothesized that the use of systems capable of responding to NIR by incorporating Colistin could also offer a significant advantage in enhancing the antibacterial action due to pDA, acting not only against Gram-negative strains but also against Gram-positives. The bactericidal effect was tested on planktonic forms of Pseudomonas aeruginosa, which can be considered a model of serious and difficult-to-eradicate infections in humans.[309] A further step forward has been made, using a synthetic dendrimer synthesized by the research group of Professor Michael Malkoch of the Royal Institute of Technology in Stockholm as an antibacterial agent. The objective of the work was to develop a new hydrogel platform with tunable viscoelastic properties to safely deliver multifunctional cationic polyester dendrimers. We produced hybrid hydrogels composed of the antibacterial cationic dendrimer TMP-G2-alanine[298] and low molecular weight Gellan-Gum, GG_8, functionalized with dopamine, GG-DA. By exploiting the polyanionic nature of GG, we demonstrated that it is possible to obtain physical hydrogels simply by mixing the polysaccharide dispersion with the cationic dendrimer. The obtained physical hydrogels could be further cross-linked with $CaCl_2$ solution to obtain solid double-cross-linked hydrogels. The presence of pendant catechol moieties on the polysaccharide backbone allows additional interactions with the dendrimer, such as Schiff Base and Michael addition, after dopamine oxidation. This made it possible to obtain injectable hydrogels with self-healing and adhesive properties. Overall, we demonstrated that the physicochemical and

viscoelastic characteristics of hydrogels are related to the precise hybridization of multifunctional cationic polyester dendrimers and dopamine-functionalized Gellan Gum and can be easily modulated by changing the conditions of the external medium thanks to the sensitivity of GG and the presence of catecholic portions. Despite numerous technological advances, there is still a need to develop systems capable of producing stable silver nanoparticles (AgNPs) through simple methods that make them preservable and easily administered to the site of infected wounds. For this reason, in another work, we used the same derivative of the GG used previously. The GG having pendant catechol portions, GG-DA, which, in this case, in addition to having the dual function of reducing and stabilizing agent in the synthesis process of AgNPs, could be processed through the spray drying process to obtain nano-in micro AgNPs doped particles (AgNPs@MPs) which, thanks to the sensitivity to the ionic strength of GG, were stable in saline media. As a proof of concept, AgNPs@MPs were incorporated into injectable hybrid hydrogel scaffolds, to achieve a nano-in-micro-in-macro system. Injectable hydrogels were produced by forming dynamic imine bonds between oxidized xanthan gum (OXG) and amine-terminated linear-dendritic hyperbranched block copolymer (HB10K-G5-alanine).

Chemical-physical characterization was carried out on all the polymeric derivatives obtained during this Ph.D. to validate the successful derivatization with the functional groups. Rheological analyses were conducted to evaluate the viscoelastic, shear thinning, and self-healing properties of the hydrogels. Everything was also documented macroscopically, using photographic and video media. The morphology of the samples and the incorporation of any microparticles or nanoparticles within the hydrogels were evaluated by SEM and TEM. Through hyperthermia studies, the photothermal conversion efficiency and photostability of samples responsive to NIR light were studied. In order to study the potential antibacterial

activity of the hydrogels, preliminary in vitro release studies of the antibiotics were conducted, in the first cases, but also a leaching-out study in the case in which the antibacterial agent was represented by the cationic dendrimer. To demonstrate the improvement in the bioadhesion properties of the hydrogels following the functionalization of the polymers with dopamine, ex vivo adhesion tests were carried out on pig skin. The hydrogels were also characterized for their antioxidant profile by colorimetric assays indicative of the radical scavenging activity. The cytocompatibility of the hydrogels was tested using various cell lines, including human dermal fibroblasts (HDF), mouse monocyte cells (RAW 264.7), keratinocytes (HaCAT) while the antibacterial properties were evaluated against S. aureus, E. coli and P.aeruginosa. Therefore, by rapidly killing bacteria and having an effective antioxidant effect, these engineered hydrogels could be good candidates for accelerating the healing of infected wound.

3. Results and Discussions

3.1 Physicochemical and rheological characterization of different low molecular weight gellan gum products and derived ionotropic crosslinked hydrogels

3.1.1 Basic hydrolysis and characterization of GG products

Basic hydrolysis is a well-known method used to reduce GG molecular weight in order to obtain derivatives that can be dispersed in water at relatively high concentrations without resulting in too viscous solutions, still maintaining ionotropic and thermos-rheological properties such as those of native GG. Here, with the aim to obtain low molecular weight products, GG was hydrolyzed in drastic conditions, dispersing it at a concentration of 1% w/v in NaOH 0.1 N solution maintaining a constant temperature of 50 °C. By changing the reaction time, we obtained 4 products with different low molecular weights and PI, listed in **Figure 33**.

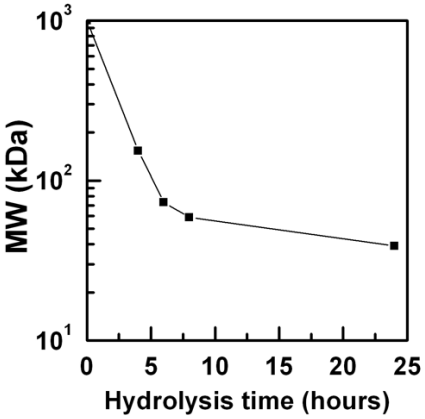

Sample	MW (kDa)	PI	Yield %
GG_4	153(±7.8)	3.03(±0.16)	65
GG_6	73(±2.1)	2.8(±0.52)	75
GG_8	59±(4.3)	2.4(±0.23)	70
GG_{24}	39±(4.5)	1.7(±0.27)	77

Figure 33. Reduction of GG molecular weight as a function of basic hydrolysis time. The table report molecular weights, polydispersity index and yield % of obtained samples

From the data reported, it is possible to notice that PI decreases proportionally with the MW, meaning that the hydrolysis process uniforms the size of degraded macromolecular chains. Considering that the starting GG has a MW of 1000 kDa (product supplier information) it is clear that the hydrolysis occurs mainly during the first 6 hours, since the MW is reduced by an order of magnitude, and became slower after this time until 24 h. The product named GG_{24} resulted to be water-dispersible even at room temperature and until a concentration of 5% w/v, while for higher concentration it needs higher temperatures (³50 °C). For all the other products it was possible to produce aqueous dispersions with concentrations ranging from 5% to 10% w/v by means of oven incubation at 80°C. Interestingly, all the hydrolysis products resulted to be freely dispersible in dimethyl sulfoxide at 50°C and at a concentration of 1% w/v producing a clear dispersion already after 1 hour of magnetic stirring. This aspect is interesting since the poor dispersibility of high molecular weight GG in this organic solvent often brings to the necessity of producing its tetrabutylammonium salt to perform chemical functionalizations that cannot be performed in an aqueous environment.[310,311] Although this procedure is simple to conduct, it still requires several time-consuming steps that could be bypassed using GG with lower molecular weights

3.1.2 Hydrogels characterization

Among the physicochemical properties of GG aqueous dispersions, thermotropic behavior is particularly interesting since allows a thermally reversible coil-to-helix transition triggered by the temperature decrease that leads to the formation of physical hydrogels at room temperature. Several studies demonstrate that this transition is promoted with increasing molar mass, concentration of the starting dispersion and cations presence.[304–306] High molecular weight GG aqueous dispersions form stable physical hydrogels at a temperature below 40 °C even at low concentrations. How is possible to notice from **Figure 34**, aqueous dispersions at 5% w/v for all the obtained low molecular products show the typical thermotropic behavior of GG, since during the cooling process a sensible increase of both storage (G′) and loss (G²) modulus can be observed. For all the investigated samples the temperature at which G′ reaches the plateau is below 40 °C with no significative changes between different samples. G′ values at low temperature decrease proportionally with the sample molecular weight (with no significative differences between GG_6 and GG_8) demonstrating that, at this concentration, the coil-to-helix aggregation for longer macromolecular chains leads to the formation of a major number of junction zones which in turns determine the obtainment of stiffer physical hydrogels.

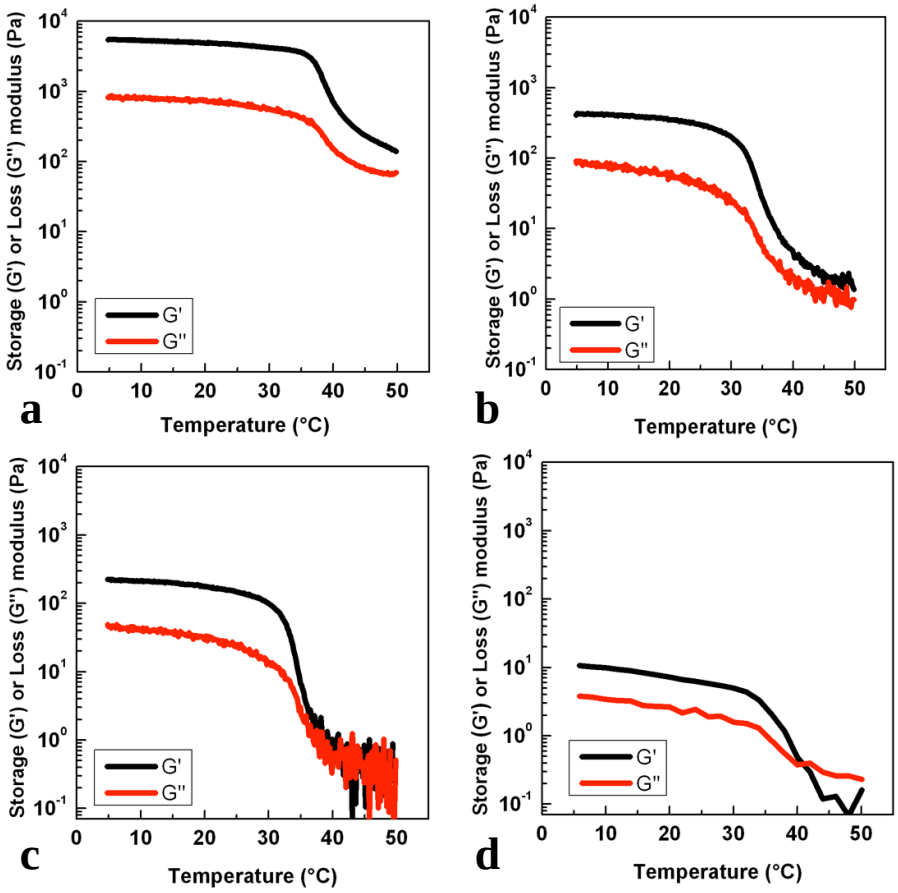

Figure 34. Temperature dependence of storage modulus (G) and loss modulus (G″) during cooling process for hydrolysis product GG_4 (**a**), GG_6 (**b**), GG_8 (**c**) and GG_{24} (**d**) dispersed in water at 5% w/v. Experiments were performed at 0.5 Hz and 1% of strain.

At room temperature, GG_{24} aqueous dispersion (5% w/v) forms a loose hydrogel that does not flow under the influence of gravity, following the inversion of the test tube but begins to flow when slightly disturbed. Interestingly, this dispersion maintains its ionotropic properties since it forms a stable hydrogel when in contact with DPBS pH 7.4 or with $CaCl_2$ 0.1M aqueous solution. Clearly, cations induce the establishment of coordination bonds that strengthen the hydrated three-dimensional network. Overall, this behavior is particularly

interesting from the perspective of developing injectable biomedical systems whose gelation is induced by contact with physiologic fluids. Molecular weight and molecular weight distribution influence the rheological behavior of polymer solutions. Normally in rheological analysis, small amplitude oscillatory shear (SAOS) is used to research the linear viscoelastic region, which however fails in characterizing the material structure, processing, applications, and functions. The rheological properties of hydrolyzed GG samples here produced were investigated using the large amplitude oscillatory shear (LAOS) technique to provide an explanation of the microstructural differences between different molecular weight GG. To describe these proprieties LAOS technique was found to be very sensitive to explore the polymer interactions in a non-linear viscoelastic regime. In the linear viscoelastic regime (LVE), the storage and loss moduli, G′ and G″, respectively, are nearly parallel indicating LVE behavior with a decrease in both moduli as the molecular weight decreases. As the strain increases, reaching the critical strain, samples undergo a transition where G' decreases suddenly as the strain increases, while G^2 first increases and then decreases. This behavior is defined as weak strain overshoot (LAOS type III) [312] and it is shown in the GG_4, GG_6, and GG_8 samples. As illustrated in **Figure 35** the samples with higher molecular weight require a smaller critical strain to disrupt the equilibrium microstructure than those with lower molecular weight. This can be due to the balance between the formation and the destruction of the network junctions [313]. The formation of weak interactions stabilize the double helix and this causes a more evident strain overshoot behavior. Tong et al. used the LAOS technique to show the microstructural differences between HA and LAGG [314]. They showed a more pronounced strain overshoot behavior for HA gellan gum with respect to LAGG due to the stabilization of the double helix structure due to the presence of glycerate group in HA gellan gum.

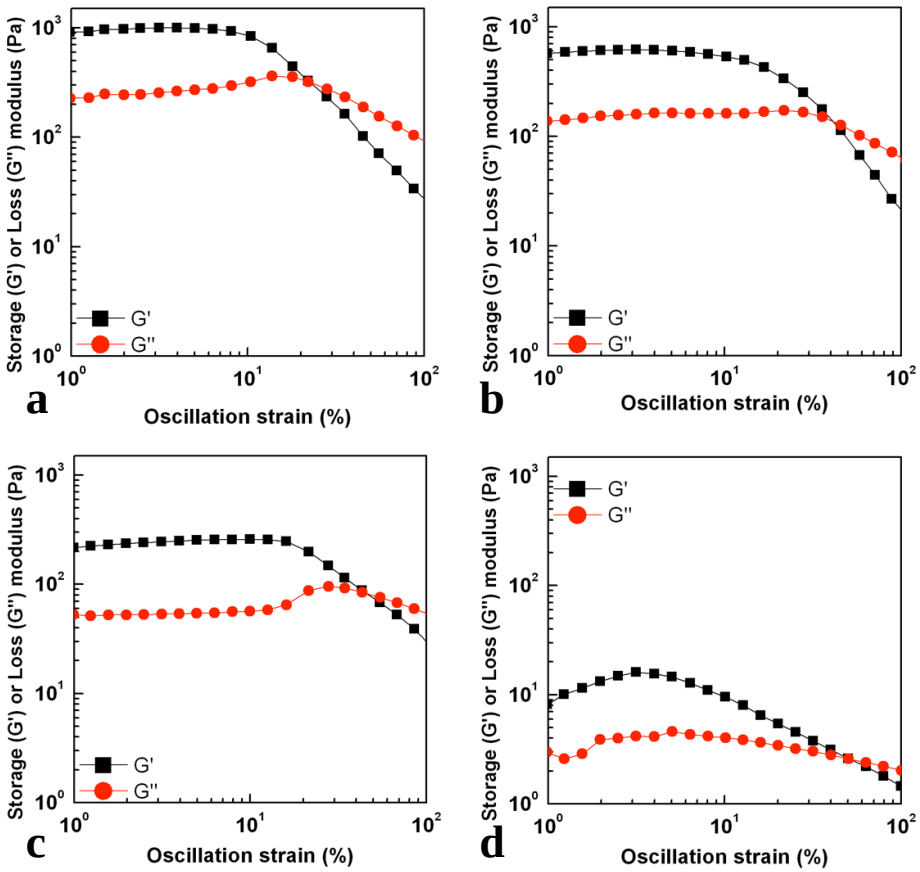

Figure 35. Strain sweep experiments performed at 0.1 Hz for hydrolysis products GG_4 (**a**), GG_6 (**b**), GG_8 (**c**), and GG_{24} (**d**) dispersed in water at 5% w/v.

In high molecular weight samples the chains, in aqueous solutions at 25°C, assume a helix conformation and chains are highly extended due to the electrostatic repulsion from the charged groups on the side chains. When a deformation is applied, the molecules may align and up to a certain strain G″ slightly increases. When a large deformation is applied, over the critical strain, the complex structure is destroyed, after which the polymer chains align with the flow field, and G″ decreases. The relative intensity of the overshoot and the strain value at maximum G'' decrease with the increase in molecular weight. Indeed, this behavior is more evident for GG_8 while it is less pronounced for GG_4 and GG_6 (**Figure 35**) showing

the strong impact of the molecular weight on the samples microstructure interactions. It can be probably explained assuming that as the molecular weight increases chains are forced together to be closest and the electrostatic repulsion can be stronger than the capacity to form weak interactions resulting in a faster disruption of the microstructure for GG_4 and GG_6 compared to GG_8.

The molecular weight highly influences the coil-to-helix transition during gelation. In particular, the transition is promoted with increasing molar mass. Considering the GG_{24} sample, double helix formation occurred as shown in thermo-rheological analysis (**Figure 34d**) and as already studied by Ogawa et al.[315] They evaluated the effect of molar mass on the coil-to-helix transition concluding that the lowest molar mass below which no helix is formed at 25 °C in aqueous solutions with 25 mmol NaCl, lies between Mw=32×10^3 and Mw=17×10^3, i.e. below the molecular weight of GG_{24}. Although the double helix is obtained the molecular weight may be too low to stabilize the double helix. This may cause a continuous rearrangement of the microstructures during oscillatory shear leading to a slight increase of both moduli at low strain % for GG_{24}. When the critical strain is reached the chains align with the flow and both moduli decrease. To summarize, molecular weight largely impacts the balance between microstructure interactions. Ionotropic crosslinking was studied by inducing the samples gelation in the presence of two different amounts of $CaCl_2$. For these analyzes samples were dispersed in MilliQ water and the salt solution was added to the hot polymeric dispersion. The GG concentration in this case was set to 2% w/v (lower compared to the just described rheological analyzes) to avoid quick and inhomogeneous gelation that can occurs in the concentrated hot dispersion following the addition of the salt solution.

It is possible to notice from **Figure 36,** G' values decrease as the molecular weight of GG decrease and shows an increment in accordance with the $CaCl_2$ concentration confirming

that all the obtain hydrolysis products retain the typical ionic strength of high molecular weight GG.

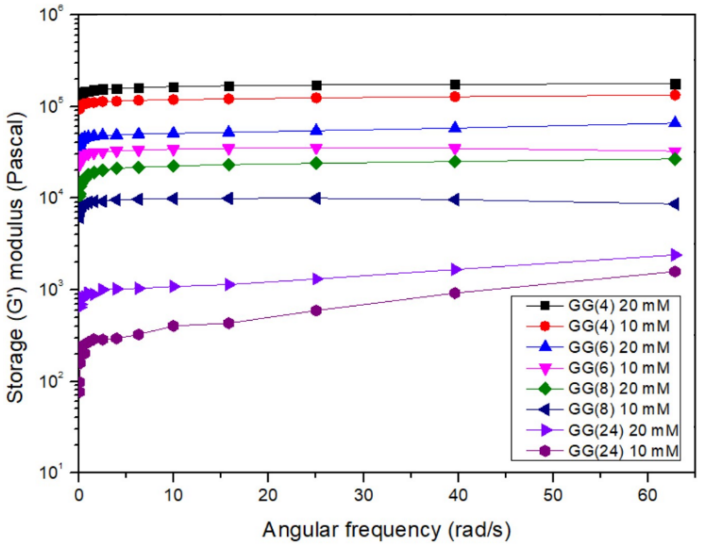

Figure 36. Elastic moduli (G') obtained from frequency sweep rheograms performed at 1 % of strain on GG ionotropic crosslinked hydrogels with different $CaCl_2$ concentration.

For morphological, physicochemical and rheological studies crosslinked samples were produced by curing the temperature-induced hydrogels (obtained from 5% w/v aqueous dispersion) with $CaCl_2$ 0.1M solution. Obtained samples were fractured in the swollen state and freeze-dried to investigate the morphology of xerogels by SEM studies.

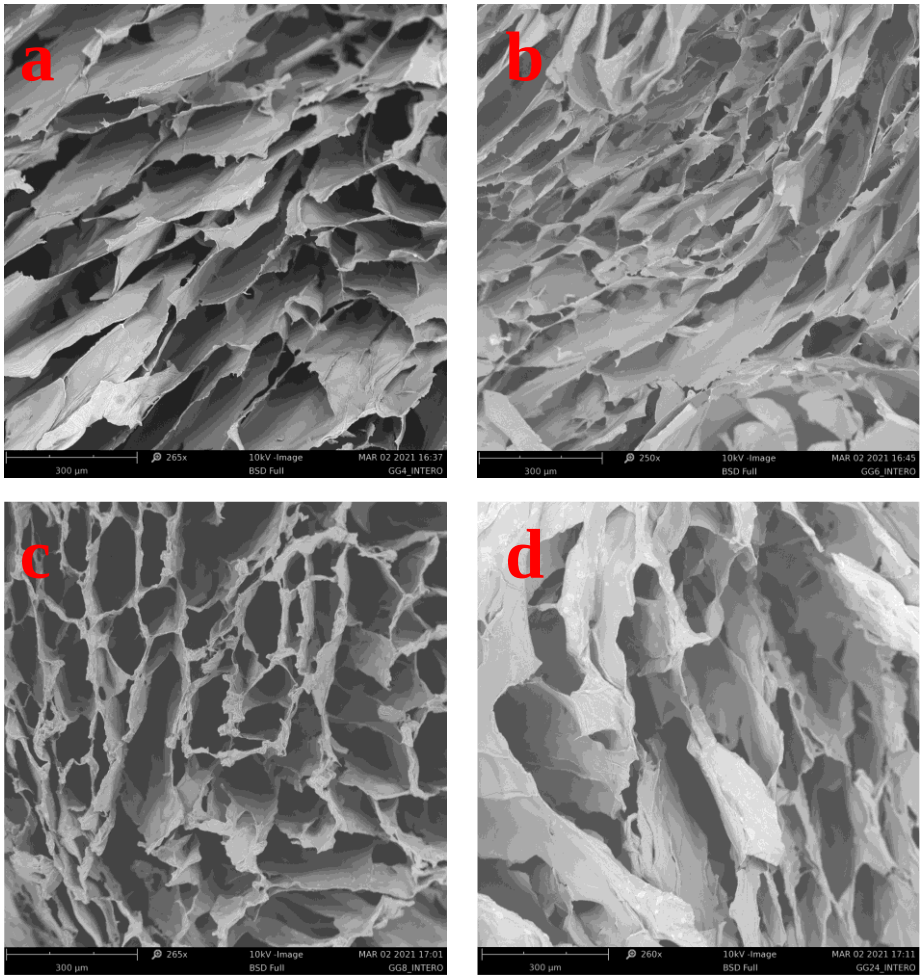

Figure 37. SEM images of freeze-dried hydrogel obtained by the ionotropic crosslinking of 5% w/v aqueous dispersion of GG_4 (**a**), GG_6 (**b**), GG_8 (**c**) and GG_{24} (**d**).

Figure 37 reveals that, as it was predictable, all the freeze-dried products show a highly porous structure even if a less compact structure with larger pores is observable for GG_{24}. These data are in accordance with those obtained from swelling studies that, besides to reveal that all the investigated sample show a high capacity of incorporate aqueous medium, demonstrate that GG_{24} hydrogel, due to the less dense network, swells significative more

compared with hydrogels produced starting from products with higher molecular weight (**Figure 38a**).

The release of dextran-FITC loaded into the ionotropic crosslinked hydrogels demonstrates that the diffusion of the labelled polysaccharide is quicker from the hydrogel obtained from GG_{24} likely because of the higher hydration of the polymeric network. No significative differences in the diffusion rate were observable from hydrogels obtained from GG_4, GG_6 and GG_8 (**Figure 38b**).

All the samples reach the swelling equilibrium at 37 °C after 24 h of incubation (no significative differences were observed in the samples weight after 48 hour).

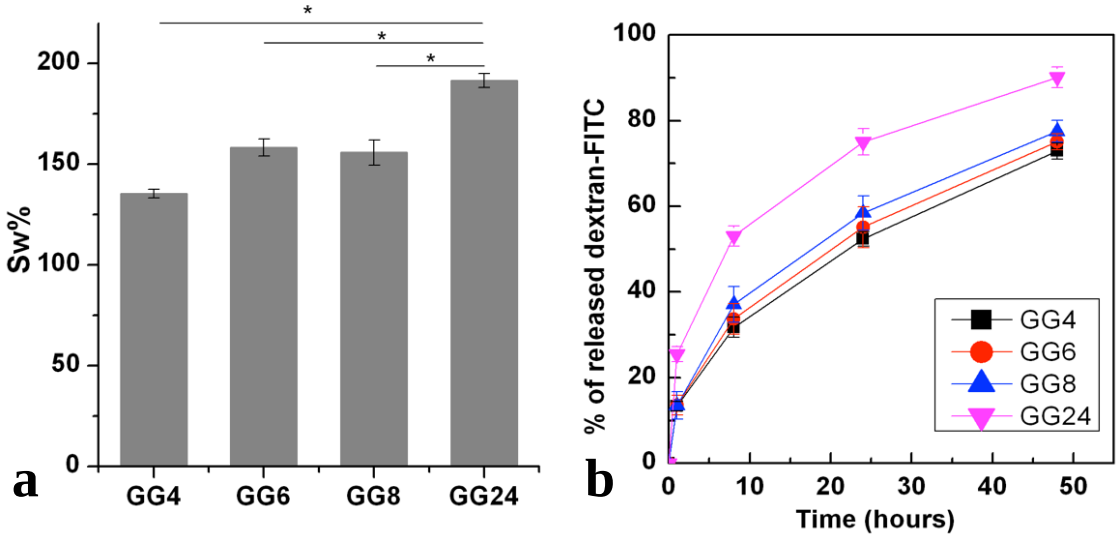

Figure 38. Swelling % of ionotropic crosslinked low molecular weight GG hydrogels incubated for 24 hours in DPBS pH 7.4 at 37°C (**a**), release of dextran- FITC from hydrogels (**b**).

At scheduled incubation times, the viscoelastic properties of ionotropic crosslinked hydrogels were also investigated by means of rheology tests performed in frequency sweep.

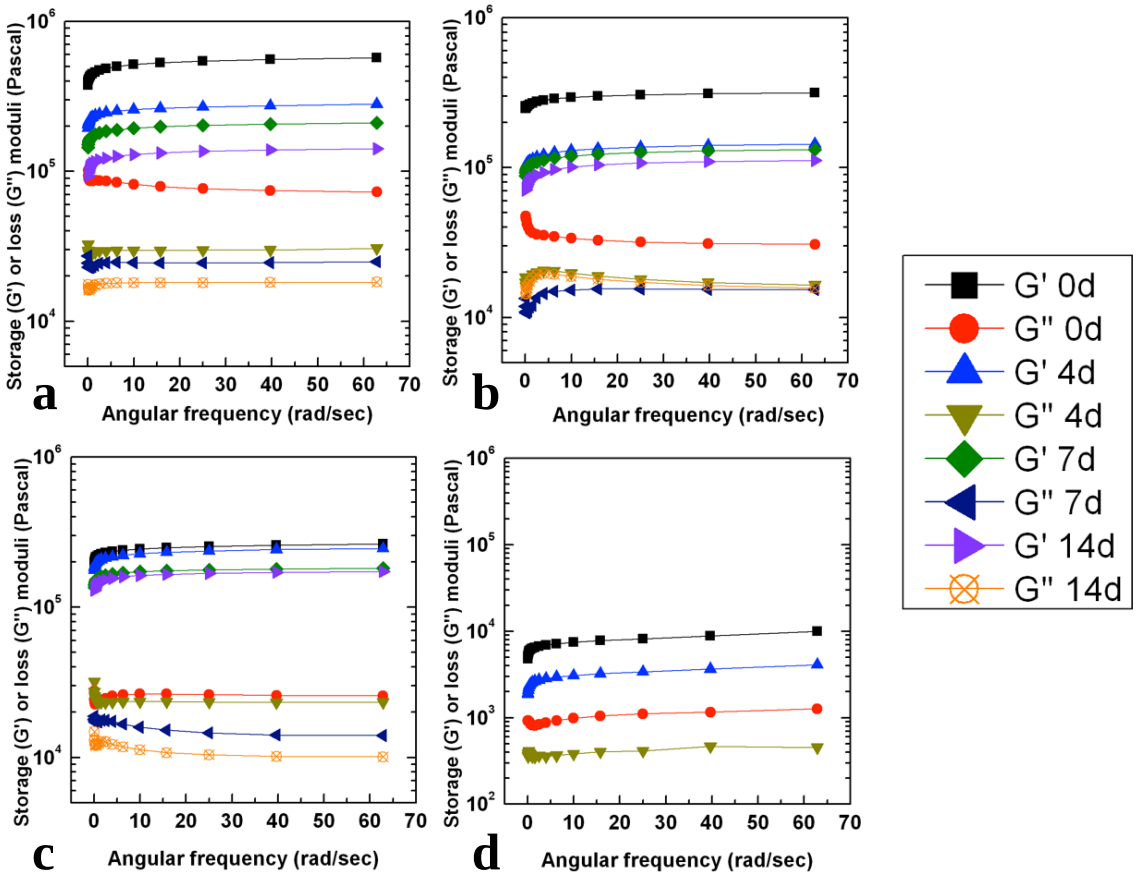

Figure 39. Frequency sweep rheograms performed at 1 % of strain for GG_4 (**a**), GG_6 (**b**), GG_8 (**c**) and GG_{24} (**d**) ionotropic crosslinked hydrogels incubated for different times in DPBS pH7.4 at 37°C.

The curing with $CaCl_2$ 0.1M for 1 hour allows the formation of stable physical hydrogels, which can be easily handled. These samples were incubated in DPBS pH 7.4 to mimic the physiologic conditions where the exchange of calcium ions with monovalent one causes the loosening of the hydrogel structures. Rheological analyses were conducted at scheduled time points to measure the effect of calcium depletion on the elastic properties of samples with the aim to investigate if this effect can be influenced by the polysaccharide starting molecular weight. As shown in **Figure 39**, the value of samples G′ modulus, measured soon after the

ionotropic crosslinking procedure, decreases as the molecular weight of sample decreases in accordance with what already observed in previous analyzes. A decrement in the G′ values was observed for all the investigated samples as the incubation time increases demonstrating that Ca^{2+} loss causes the loosening of the polymeric network. It is possible to notice that, except for GG24, after 14 days of incubation, G' value is similar for GG_4, GG_6 and GG_8 and show values around 10^5 Pascal. These results can reflect the hydrogel stability. Macroscopically, except from hydrogels obtained starting from the product with the lower molecular weight (GG_{24}), samples retain their structural integrity during all the investigated time points, while hydrogels obtained with the GG_{24} product start to appear fragmented already after one week of incubation and was not possible to handle them to perform a repeatable rheological analysis (**Figure 40**).

Figure 40. GG_{24} (**on the right**) and GG_8 (**on the left**) ionotropic crosslinked hydrogels after 1 week of incubation at 37°C in DPBS pH 7.4.

Cytocompatibility tests were performed using MC3T3-E1 pre-osteoblastic cells, chosen as a model cell line. All the investigated samples and all the concentrations tested showed no toxic effects after 24 hours of incubation confirming their cytocompatibility (**Figure 41**).

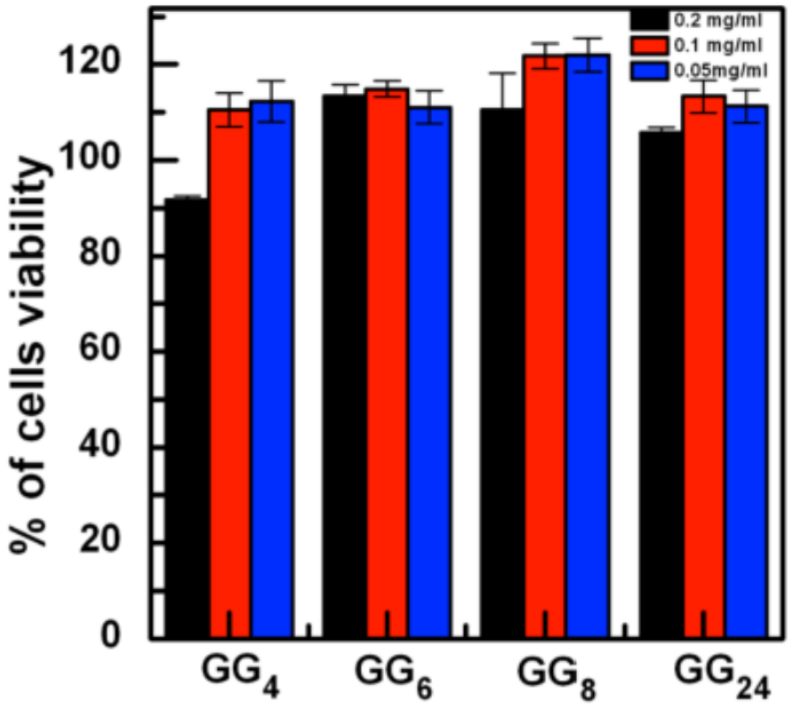

Figure 41. Viability of MC3T3-E1 preosteoblastic cells cultured for 24 h in the presence of GG degradation products at different concentrations. Viability is expressed as % compared to untreated cells.

By dispersing GG hydrolysis products at a concentration of 2.5 w/v it was possible to obtain at room temperature fluid systems that can be easily loaded onto 1 mL syringe and mixed with the cell suspension to produce cells encapsulated hydrogels. Upon mixing, the culture medium induces an increase in the viscosity of the dispersions into the syringe due to partial gelation of the systems. In any case, it was still possible to easily extrude the cell containing hydrogel into the culture wells. Encapsulated cells were cultured for 24 hours and then treated with live and dead fluorescence staining kit that allows observing both viable (green) and dead (red) cells (**Figure 42**). In all the investigated hydrogels no dead cells were

observable, confirming that neither the encapsulation process nor the material itself has a negative effect on the cell viability (**Figure 41**).

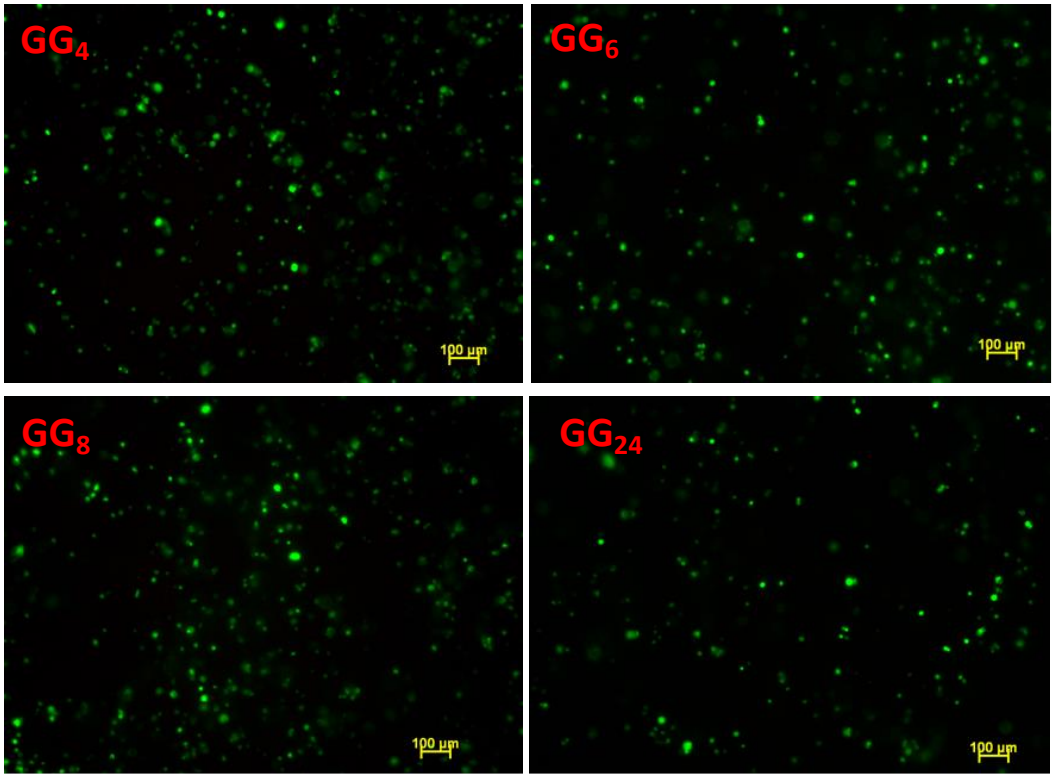

Figure 42. Live/dead staining of MC3T3-E1 preosteoblastic cells encapsulated into GG products after 24 hours of culture.

3.2 Ciprofloxacin releasing gellan gum/polydopamine based hydrogels with near-infrared activated photothermal properties

3.2.1 Synthesis of GG-EDA

The pendant primary amino groups were inserted on the polymeric backbone of the GG with a chemical procedure similar to that already described to functionalize hyaluronic acid with alkyl amines and used to insert alkyl chains in the same GG.[311,316,317] The initial GG was degraded under alkaline conditions (for 24h hours), as previously described, to allow its complete deacetylation and to obtain a derivative with a lower molecular weight which forms less viscous dispersions than the starting polysaccharide and therefore easier to handle and study. The functionalization procedure, shown in **Figure 43**, involves the activation of primary hydroxyl groups of the glucosidic residues of GG with 4-NBPC and the subsequent reaction with EDA.

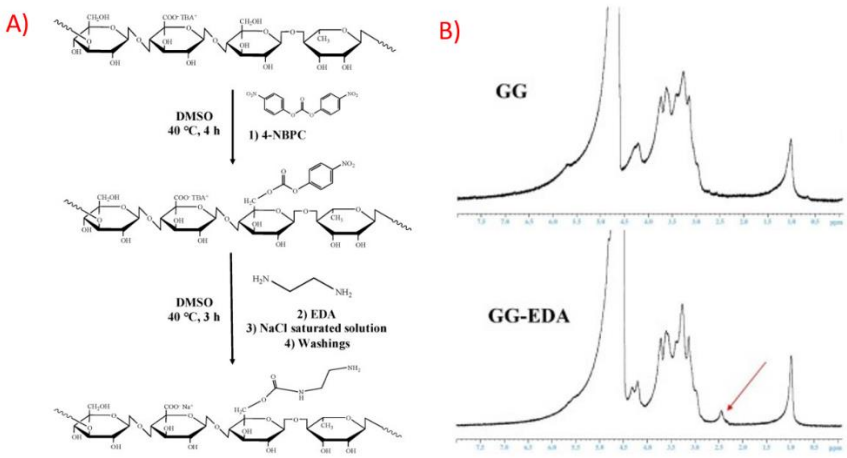

Figure 43. Schematic representation of chemical steps used to synthetized GG-EDA **(A)**, ^{1}H-NMR spectra of GG and GG-EDA (**B**).[112]

The insertion of pending EDA groups was evaluated by ^{1}H-NMR analysis, by comparing the GG-EDA and GG spectra. **Figure 43B** shows the GG-EDA ^{1}H NMR spectrum with a new peak at δ 2.5 (indicated by the red arrow) assigned to the methylene protons near the free amino group of EDA. The $DD_{EDA\%}$ was calculated with the analysis of the GG-EDA ^{1}H-NMR spectrum, by comparing the integral of the peak at δ 2.5 with that at δ 1 (3H, s, of the -CH_3 of rhamnose), resulting equal to 43 ± 3 mol%.

3.2.2 Hydrogels production, rheological and physicochemical characterization

The insertion of pendant amine groups in the GG polysaccharide backbone generates the formation of a polyampholyte with superior viscoelastic features compared to the parent macromolecule. At physiologic pH, the physical interactions between GG-EDA protonated basic groups and carboxylate groups contribute to stabilize the three-dimensional hydrated network that GG aqueous dispersions form as a result of the temperature-induced sol-gel transition. [112] Besides, amine groups increase the macromolecule chemical versatility and make it possible to crosslink the derivative through the establishment of covalent bonds with crosslinker-bearing electrophilic moieties that can undergo nucleophilic addition under mild reaction conditions. [318–320] Chemical hydrogels are generally more mechanically stable, easily handled and, depending on the chemical bonds between the macromolecules, more resistant to both hydrolytic and enzymatic degradation compared to physical ones. Covalent bonds between the macromolecules allow to retain the internal microporous structure as well as sample shape and size after the freeze-drying process. The possibility to obtain a stable xerogel is not of secondary importance in the development of a wound bandage since it makes possible to produce a device possibly sterilizable through different techniques that

can be stored for long periods and can be easily cut and reshaped based on the area where it needs to be positioned.

Vinylsulfone functionalized 4-arm PEG is an example of the just described crosslinker that here was used to crosslink GG-EDA. PEG has been chosen because of its plasticizer properties, [321,322] that can be useful to decrease the brittleness typical of polysaccharide derived hydrogels. The crosslinking reaction between the hydrophilic macromolecules occurs spontaneously in aqueous environment without the use of activating agents due to the well-known Michael type addition between GG pendant free amino groups and vinylsulfone terminal double bonds of 4-arm PEG (**Figure 44a**).

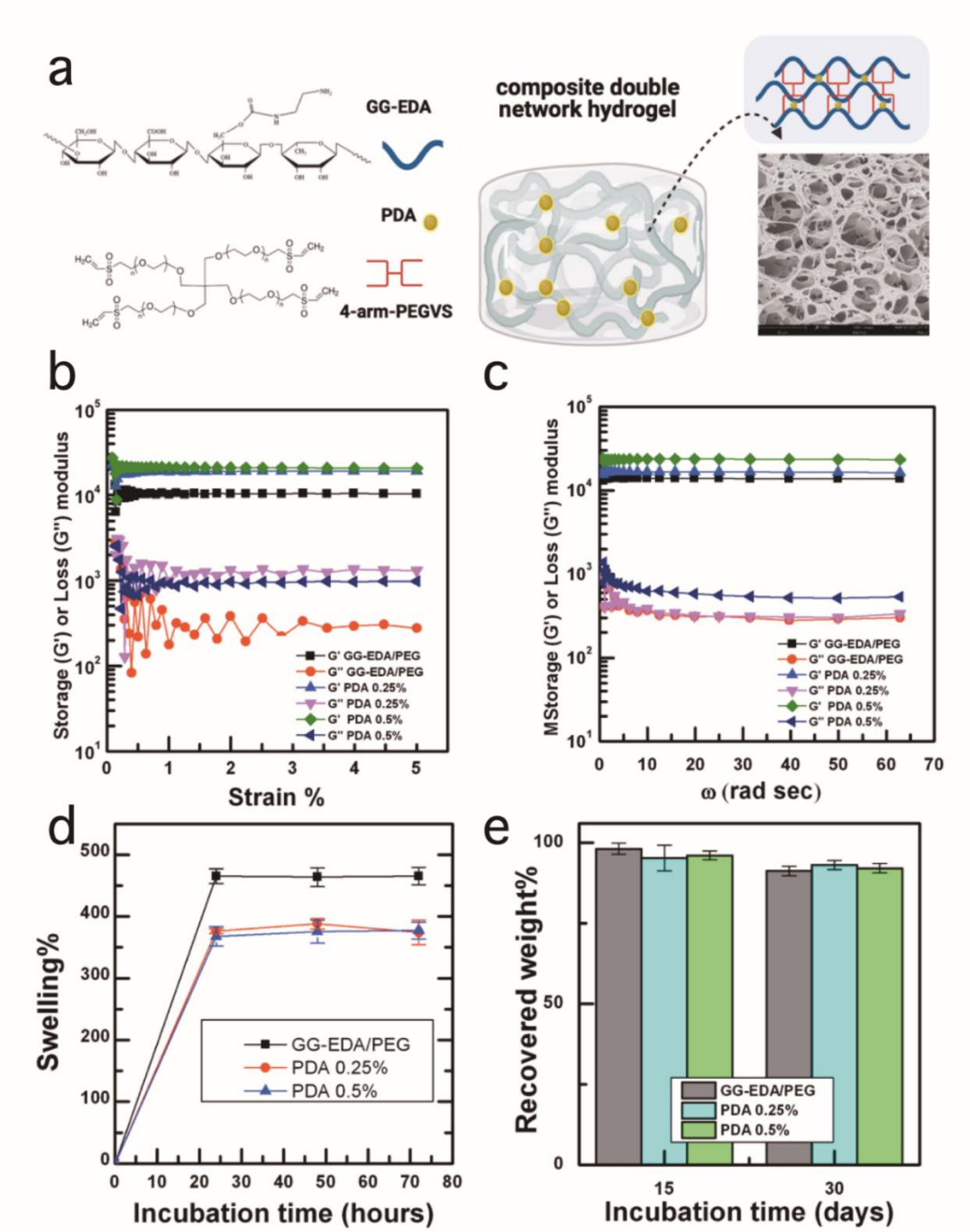

Figure 44. Schematic representation of the crosslinking process and SEM image of GG-EDA/PEG/pDA 0.5% freeze-dried hydrogel (**a**). Rheograms of composite and pDA free hydrogels obtained in amplitude (**b**) and oscillation (**c**) frequency**.** Hydrogels swelling (**d**) and hydrolytic resistance (**e**) behavior.

Already after 3 minutes the system undergoes a drastic loss of fluidity observable through the inversion tube test confirming that the reaction takes place quickly due to the high temperature (80 °C) needed to obtain a fluid homogeneous GG-EDA aqueous dispersion. pDA doped hydrogels were prepared simply by adding the particles dispersion in the gel forming solution. No significative differences in the gelation time were observed between pDA containing and pDA free samples. On the dried state samples appear macroscopically as soft sponges with defined shape while on the micrometric scale they show a highly porous structure (**Figure 44a and 45**).

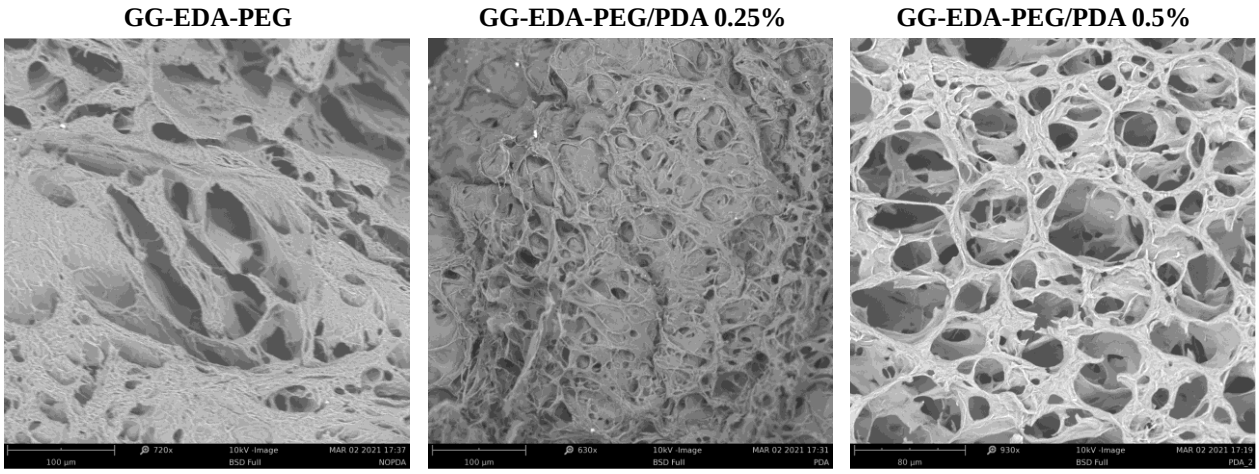

Figure 45. Scanning electron microscope images of GG-EDA-PEG based hydrogels.

pDA nanoparticles have electrophilic nature and can undergo Michael type addition as well as vinylsulfone moieties [323]. Thus, considering the high excess of pendant amino groups compared to 4-arm PEG double bonds, it is likely to suppose that pDA nanoparticles take part actively to the gelation process acting not only as a nanostructured dopant but also as crosslinking agent.

Interestingly, this hypothesis seems to the confirmed by rheological tests, peformed in *amplitude* and *oscillation sweep,* that show an increment of storage modulus in the

nanocomposite hydrogels attributable to the higher amount of chemical bonds established in these samples (**Figure 44b,c**). DSC analysis conducted on pDA free and pDA containing hydrogels confirm the structuring effect of organic particles visible from the slight shift in the GG degradation temperature peak of the thermograms as reported in the **Figure 46**.

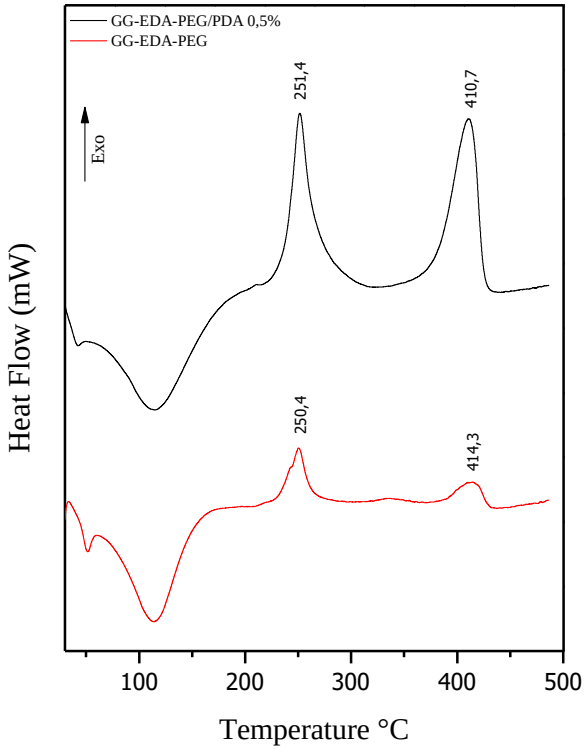

Figure 46. DSC curves of GG-EDA-PEG/pDA 0.5 % (black) and GG-EDA-PEG (red). Differential scanning calorimetry (DSC) performed by using a DSC/TGA 131 EVO (by SETARAM Instuments). Each DSC measurement was performed under nitrogen atmosphere with a flow of 1 ml min^{-1}, using about 10 mg of dried sample placed into an aluminum crucible. The heating rate applied was: 10 °C min^{-1}, 30−500 °C.

Swelling studies (**Figure 44d**) further corroborate this result since, how is possible to notice from the graph in figure 1 d, pDA free hydrogel swells significantly more($p>0.05$) than

nanocomposite samples due to the less dense polymeric network. In any case, all the investigated samples show an high capacity to incorporate the aqueous medium which reflect their potential ability to seize once in vivo the wound exudate which contain many nutrient that favors bacterial growth and leads to skin maceration.[324] Physical ionotropic crosslinked hydrogels, produced by treating of GG aqueous dispersion with divalent cations such as Ca^{2+}, due to the exchange with monovalent cations contained in the physiological medium, gradually lost their structural integrity once administered in vivo.[122,123] For this reason, GG has been functionalized with different moieties that enable its chemical crosslinking or retard the hydrolytic process for the derived hydrogels.[311,317,325,326] In the development of a wound treating system this aspect is of crucial importance since the device has to maintain its structural integrity during the treatment to maintain its barrier function and avoid frequent dressing changes that would damage the newly formed tissue.[327] As reported in **Figure 44e**, the chemical hydrogels obtained by crosslinking GG-EDA with vinylsulfone derivatized 4-arm PEG, showed high hydrolytic resistance in physiological conditions at 37°C showing only a slight loss on weight after 30 days of incubation. Despite the higher swelling % of the pDA free samples, no significative differences are observable with the nanocomposite hydrogels meaning that the hydrolytic resistance is mainly attributable to the crosslinking between the macromolecules.

3.2.3 Characterization of photothermal properties, production of ciprofloxacin medicated hydrogels and drug release studies

Hydrogels photothermal effect was visualized using IR thermal camera by capturing images after irradiating the samples with NIR laser at 810 nm for different time intervals. How it was predictable, pDA free hydrogel did not show photothermal properties while pDA

containing samples showed a temperature increase proportional to the irradiation time (**Figure 47a**). The local rise in temperature above 50 °C can causes damages to the host tissues and cells so much so that nowadays hyperthermia is a commonly accepted technique for the ablation of solid tumors.[320] For this reason, when the localized heating process is needed to eradicate the infection in a wound, to avoid severe tissue damages on the healing tissue, it is of crucial importance to finely control the space-time heat release. In other words, ideally the system could quickly "turn on" to generate heat locally, to affect the bacteria viability on the wound bed and eventually onto the implanted material itself, then cool down just as quickly to avoid the destabilization of the surrounding tissues. It is worth to notice that using a power density of 8 W cm^{-2}, it was possible to reach high temperatures (up to 50 °C) already after 100 sec of irradiation for GG-EDA-PEG/pDA 0.5% sample thus confirming the remarkable photothermal features of this hydrogel. Thermal images also show that the rise in temperature is highly localized as it possible to notice from the color change moving from the sample center (the irradiated area) to the closer surrounding areas. Measurements conducted on the external medium with optic fiber are more suitable to investigate the temperature of the hydrogels surrounding environment that shed light to the effectively exchanged heat and give information on the temperature reached by the tissues eventually in contact with samples. It is possible to notice for **Figure 47b** that there is a strong pDA dose-dependent photothermal effect. In particular a strong heating process is observable for GG-EDA-PEG/pDA 0.5% that rises the external medium temperature by 35 °C and brings the temperature in the culture well up to 55°C (the starting sample temperature was 20 °C) after 125 sec of irradiation. The same irradiation process for GG-EDA-PEG/pDA 0.25% sample causes a milder photothermal effect since the maximum rise in the temperature reached was 20°C. To the light of these results, we decide to use GG-EDA-PEG/pDA 0.5% for further characterization studies. The possibility to easily control the sample temperature

by changing the irradiation time and/or the laser power density is highly desirable to get a complete control over the heating process that ensure to operate safely reaching temperatures that could affect the stability of the microbial colonies, assisting as example the effect of the released antibiotics, without causing damages in the healing tissue. Moreover, after the irradiation, hydrogel must retain its photothermal effect to ensure that the treatment can be repeated with the same efficiency for several times without the need to replace the dressing. This would make possible to perform cycles of irradiation also after the complete release of the antibiotic occurs to minimize the risk of wound re-colonization. Photothermal stability tests were conducted irradiating GG-EDA-PEG/pDA 0.5% sample for 5 consecutive cycles with different laser power densities. How it was predictable, the rise in temperature is proportional to the irradiation power (**Figure 47c**). It is possible to notice that the photothermal effect is kept constant during the consecutive cycles regardless of the laser power density used. In fact, after 5 cycles of irradiation no significative temperature changes were observed for the same power density. Clearly, since the photothermal effect is due to the presence in the sample of pDA nanoparticles, their depletion from the hydrogel should cause a gradual loss of its capacity to generate local heat after consecutive treatments. Considering their colloidal nature, it is reasonable to suppose that, if freely dispersed in the hydrogel, pDA nanoparticles would be released from the sample through a diffusion process that could be exacerbated from the hyperthermic effect occurring during the irradiation. On the contrary, the photothermal stability observed for the GG-EDA-PEG/pDA 0.5% hydrogel further corroborates the hypothesis that pDA nanoparticles take an active role in the crosslinking process and are firmly anchored in the hydrated three-dimensional network through stable covalent bonds.

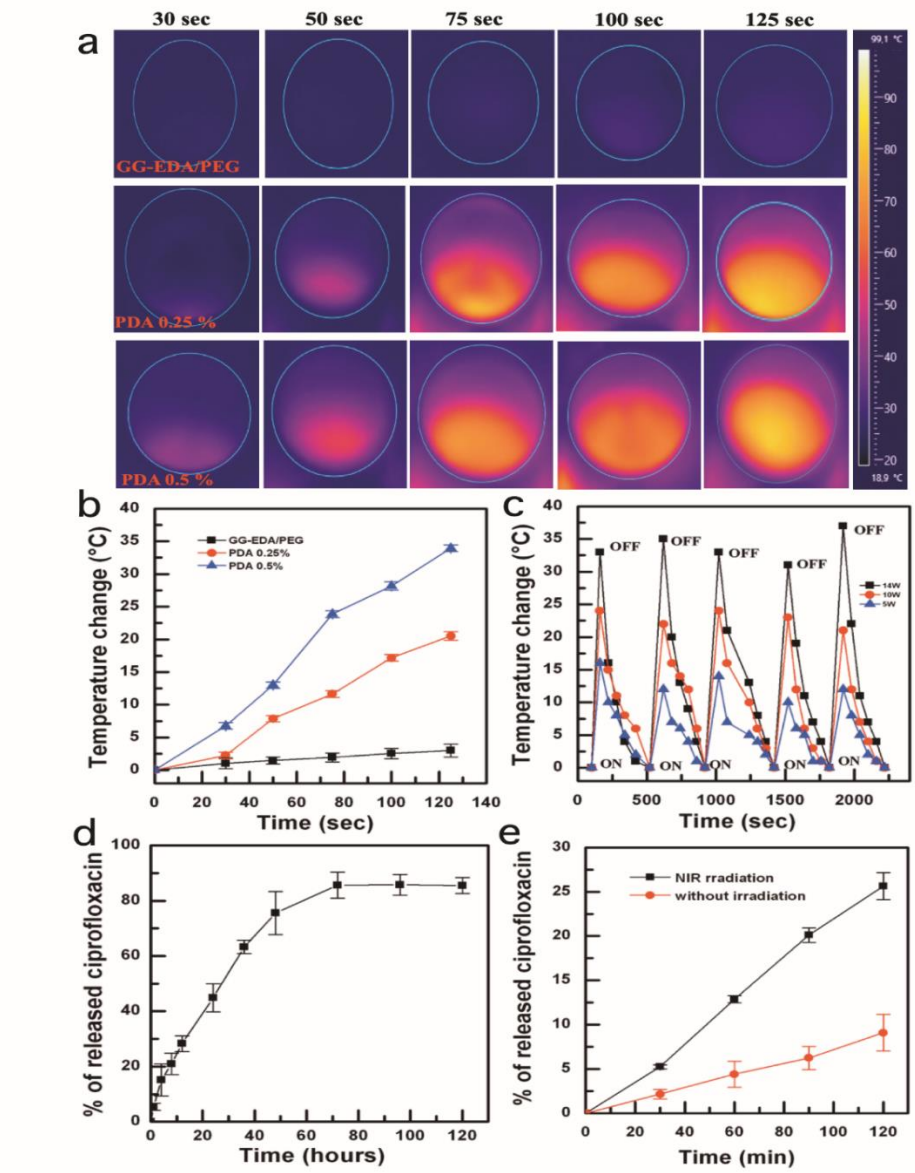

Figure 47. Infrared thermal images of a 24-well plate containing DPBS pH 7.4 embedded hydrogels under 810 nm laser exposure (8 W cm^{-2}) for different time intervals (**a**). Temperature variation, tested with optic fiber, of the external medium as a function of irradiation time (8 W cm^{-2}) (**b**) Data shown as mean ± s.e.m. Photothermal stability test conducted with 5 on-off irradiation cycles on GG-EDA-PEG/pDA 0.5% sample at different laser power densities (**c**). Cumulative release of ciprofloxacin from GG-EDA-PEG/pDA 0.5% hydrogel incubated in DPBS pH 7.4 at 37°C (**d**). Effect of the irradiation at 810 nm at (80 sec 8 W cm^{-2}) on the ciprofloxacin release from GG-EDA-PEG/pDA 0.5% sample. Data shown as mean ± s.e.m.

Only GG-EDA-PEG/pDA 0.5% gelling dispersion was used to prepare medicated samples because of the better photothermal properties compared to the other investigated hydrogels. Ciprofloxacin hemisuccinate salt was prepared by spray drying in the presence of polyvinyl pyrrolidone as a stabilizer to obtain freely water soluble microparticles (**Figure 48**) that can be dissolved in the gelling polymeric dispersion. For the drug containing system no macroscopic differences, compared with the ciprofloxacin free samples were observed in the gelation time evaluated with the inversion tube test.

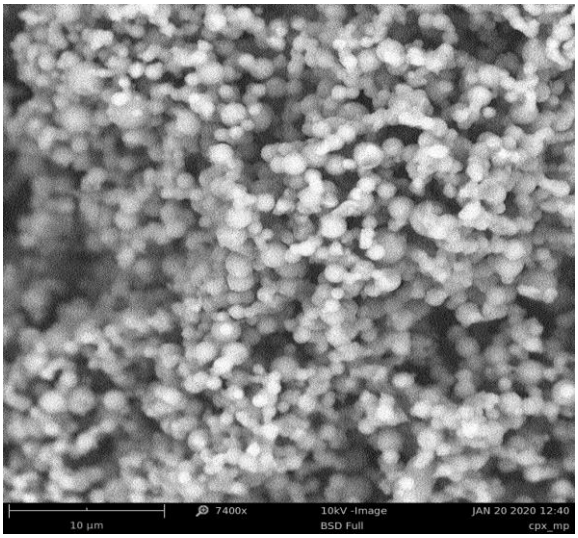

Figure 48. Ciprofloxacin hemisuccinate microparticles obtained by spray-drying produced by using the Buchi Nano B 90 HP spray dryer.

In physiological conditions ciprofloxacin is released gradually from GG-EDA-PEG/pDA 0.5% hydrogel and its release is complete after 72 (**Figure 47d**). The controlled diffusion from the hydrogel it is likely influenced by the presence of ionic interactions between the antibiotics and GG polymeric backbone. One of the advantages of the synthetic approach used to produce GG-EDA is the maintenance of underivatized carboxylic groups that could

be exploited in this case as anchorage sites for the antibiotic. In fact, in its salt form ciprofloxacin can establish ionic interactions with GG carboxylate group through the positive charge onto the piperazine nitrogen.[328] Still, ciprofloxacin interacts with aromatic portion of pDA nanoparticles trough π-π interactions that enhance the hydrogel capability to retain the antibiotics. NIR irradiation boosted the release of the antibiotic after 4 consecutive treatments as shown in **Figure 47e**. This typical behavior has been already described in the literature for the release of active agents from NIR activated bulk materials and nanosystems.[329,330] Considering that GG shows a marked inverse correlation between temperature and viscoelastic properties, it is likely to suppose that the rise in temperature, besides to accelerate the diffusional release of the solute from the hydrogel, causes a destabilization in the three-dimensional network that results in an enlargement of the polymeric meshes that could facilitate the drug removal from the sample.

3.2.4 In vitro cytocompatibility and antimicrobial effect

Primary HDF were chosen as cell model to investigate the cytocompatibility of produced hydrogels. During the experiment samples were taken in indirect contact with HDF by means of inserts that avoid physical damages to the cells. Both the cells viability and their proliferative activity were not influenced by the presence of the hydrogels in the culture environment as demonstrated by the metabolic activity assay (MTS) results reported in **Figure 49a**. In fact, no significative differences were observed in the metabolic activity of cells cultured in the presence of all tested hydrogels compared with the control. Live/dead staining assay allows to qualitatively investigate simultaneously the presence of both viable (green stained) and dead (red stained) cells by using different fluorescence probes. No dead cells were observable in the presence or not of all the investigated hydrogels with cells that

maintain their typical spindle-like shape (**Figure 49b**). For simplicity, only images relating to the cells grown in contact with GG-EDA-PEG/pDA 0.5% are shown). Moreover, it was possible to visually ascertain that cell proliferation activity between day 3 and day 7, as demonstrated by the increased number of viable cells in the culture well, that remains unchanged regardless of the presence of hydrogels.

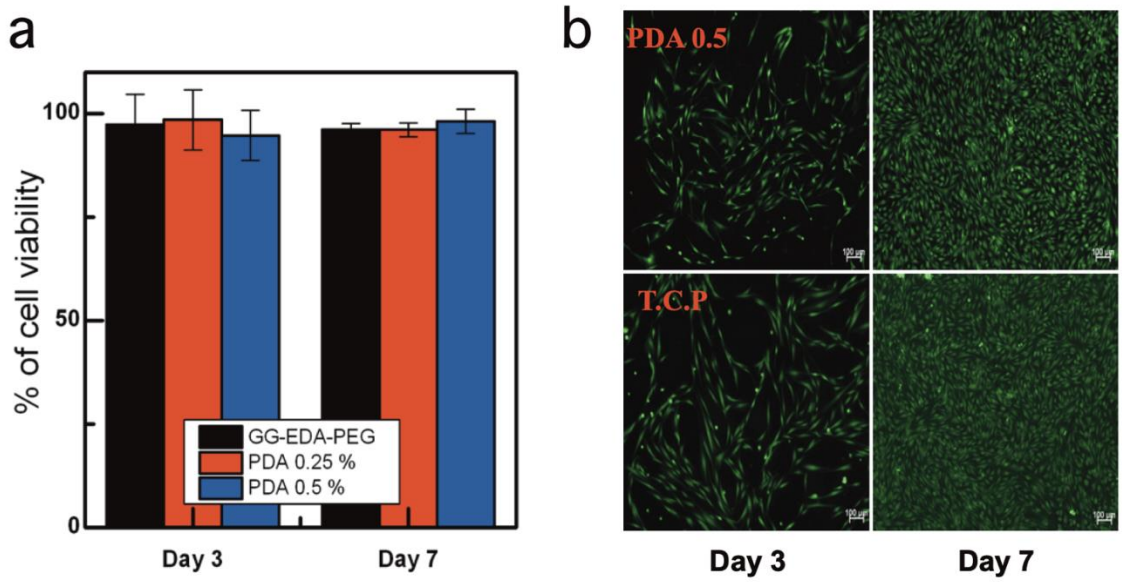

Figure 49. Cytocompatibility study for GG-EDA-PEG, GG-EDA-PEG/pDA 0.25%, and GG-EDA-PEG/pDA 0.5% on human dermis fibroblasts (HDF) by MTS assay: viability was assessed by culturing the cells in the presence or not (T.C.P) of samples after 1 and 7 days **(a)**. Live/dead assay fluorescence images of HDF cultured in the presence or not of GG-EDA-PEG/pDA 0.5% hydrogel after 3 and 7 days of culture **(b)**.

Antimicrobial experiments were conducted using GG-EDA-PEG/pDA 0.5% hydrogel on *S. aureus* (Gram-positive pathogen) and *P. aeruginosa* (Gram-negative pathogen) as they represent two of the pathogens that frequently cause local infections and are listed by the WHO as "antibiotic-resistant priority pathogens" that pose the greatest threat human

health.[331] The released ciprofloxacin hemisuccinate resulted to be effective against both tested bacteria, even if, how it is possible to notice from **Figure 50a**, a more marked antimicrobial effect was observed for P. Aeruginosa. In fact, after 24 hours of culture for both free drug and for the NIR treated medicated hydrogel, a complete sterilization occurred while a drastic decrement of the CFU, compared with the control (growth kinetic), was observed in the wells with the unirradiated medicated hydrogels. This clearly can be ascribed to the higher amount of released drug in the NIR treated sample in accordance to the release experiments results. A strong CFU reduction was also observed for S. Aureus even if in this case no significative differences were observed treating the samples with NIR. For this reason, the experiment for the Gram-positive pathogen was repeated by treating the samples with 4 consecutive irradiation cycles. **Figure 50b** shows that the repeated hyperthermic effect carried out a synergistic antimicrobial effect potentiating the activity of ciprofloxacin hemisuccinate. It was interesting to notice that NIR treated samples showed very few CFU and in some cases completed sterilization occurred. It should be also noticed that NIR treatment determinates a significative decrement of the growth kinetics already after one irradiation cycle also for the drug free samples and for both tested strains. This is interesting since it would enable, once in vivo, to continue the irradiation treatment also after the complete release of the drug payload occurred to avoid eventual wound re-infection.

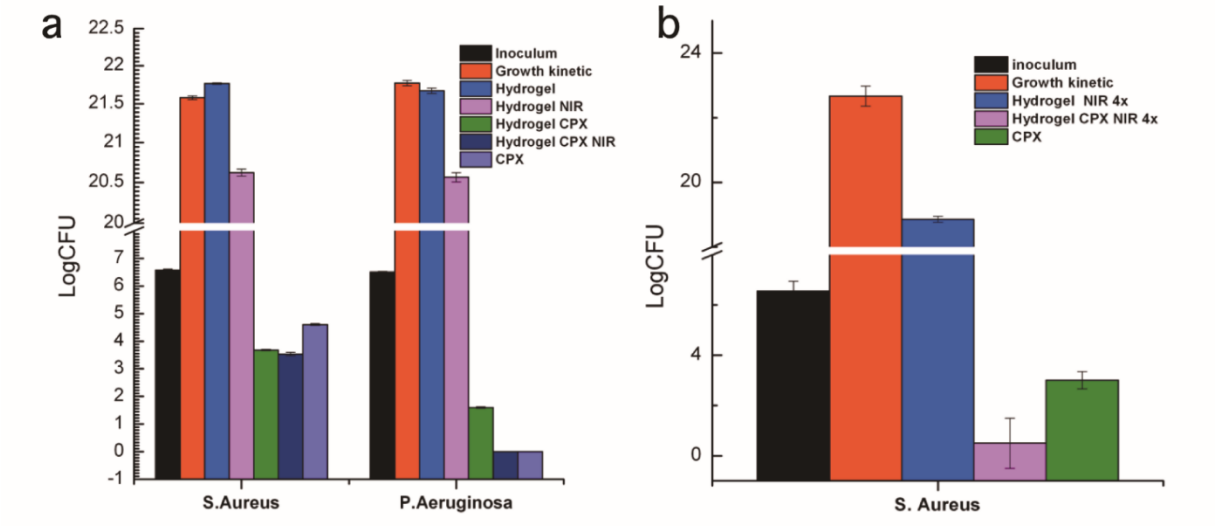

Figure 50. Antimicrobial effect of GG-EDA-PEG/pDA 0.5% hydrogel (containing or not 30 μg of drug) with and without 810 nm NIR laser exposure (80s, 8W cm^{-2}) and free ciprofloxacin hemisuccinate against *S. aureus* and *P. aeruginosa* (**a**), antimicrobial effect of GG-EDA-PEG/pDA 0.5% (containing or not 30 μg of drug) with 4 consecutive cycles of irradiation at 810 nm (being each cycle 80s and 8W cm^{-2}) against *S. aureus* (**b**).

3.3 Near-infrared light-responsive and antibacterial injectable hydrogels with antioxidant activity based on a Dopamine-functionalized Gellan Gum for wound healing

3.3.1 Synthesis and characterization of GG-DA-PEG

High molecular weight Gellan Gum was degraded in alkaline conditions as previously reported,[332] to obtain derivatives with a lower molecular weight that form less viscous aqueous dispersions than the starting polysaccharide and therefore easier to handle and study. In particular, high molecular weight GG was hydrolyzed dispersing it at a concentration of 1% w/v in NaOH 0.1 N solution, maintaining a constant temperature of 50 °C. By changing the reaction time (8 and 24h), we obtained two products, named respectively GG_8 and GG_{24}, based on the hydrolysis times, having respectively MW of 59±(4.3) and 39±(4.5) (kDa).

Tetrabutyl (TBA) ammonium salt was prepared as elsewhere reported to obtain organic solvent dispersible derivatives.[317] The functionalization procedure, described and shown in **Figure 51A**, is similar to that already described by our research group to functionalize GG with alkyl amines[112,311,317] and involves the activation of primary hydroxyl groups of GG glucosidic residues with 4-NBPC and the subsequent reaction with DA and PEG. These groups have been inserted into the polymeric backbone to give to the final derivative respectively greater tissue adhesiveness and to increase its water dispersibility.

This particular, chemical procedure was used to maintain unfunctionalized GG carboxylic group in the final products in order to avoid the loss of the ionic strength sensitivity. This is particularly important considering the low molecular weight of starting polysaccharide. DA groups linked to GG_8 and GG_{24} was determined by ^1H NMR analysis (in D_2O) of both GG_8-DA-PEG and GG_{24}-DA-PEG comparing the peak at δ 6.8 attributable to the protons in the

aromatic group of the dopamine (-CH_2-) with the peak at δ 1.10 attributable to the methyl group of gellan gum (-CH_3 of rhamnose portion of GG). The degree of molar derivatization in dopamine (DD_{DA}mol%) was determined by ^{1}H-NMR analysis. The products were also qualitatively characterized by FT-IR analysis and Uv-vis spectroscopy. The ATR-FTIR analysis confirms, as shown in **Figure 51B**, the functionalization of the GG polymeric backbone. In particular, the formation of the C=O ester bond is confirmed by the presence of the peak at 1752 cm^{-1}; the formation of the carbamate bond was confirmed by the appearance of the amide band II at 1531 cm^{-1} [311]. Furthermore, the presence of the peaks at 1112 cm^{-1} and 845 cm^{-1} in the spectrum of the derivative GG_8-DA-PEG are attributable respectively to the stretching -COC- and to the -CH group (peaks present and characteristic of the PEG spectrum).[333]

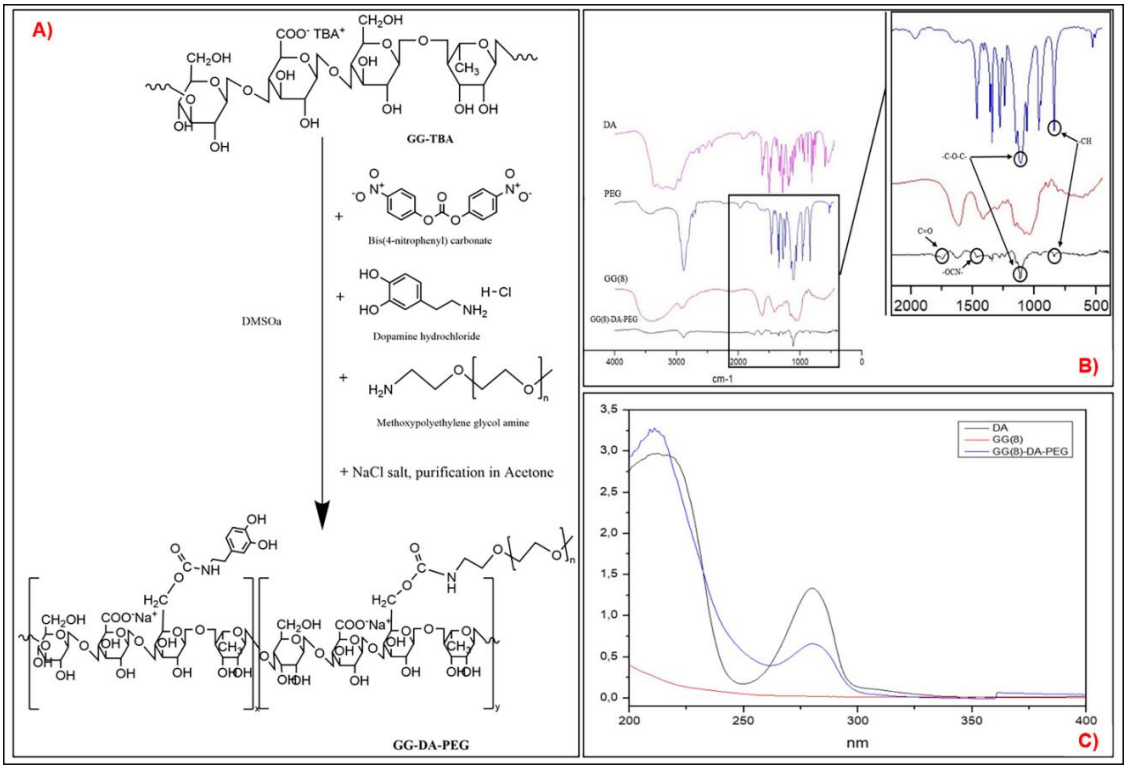

Figure 51. Synthesis scheme of GG (8)-DA-PEG and GG (24)-DA-PEG derivatives (**A**). ATR-FTIR (**B**) and Uv-vis spectra (**C**).

Learmonth and collaborators developed DA modified GG via standard amidation procedures employing high molecular weight GG demonstrating that the insertion of pendant catechol groups influences the viscoelastic behavior of the final product.[334]

The same reaction was carried out using GG_{24}-TBA and GG_8-TBA as a starting polymer to obtain two derivatives with different physicochemical properties. The insertion of pending DA and PEG groups was evaluated by ^{1}H-NMR analysis. The spectra obtained from the two polymers at different molecular weights did not show significant differences. **Figure 52** shows the GG_8-DA-PEG ^{1}H-NMR spectrum with peaks at δ 6.5 and δ 6.8 (indicated by the arrow) attributable to the three aromatic DA protons. The degree of functionalization in DA was equal to 14% ± 1.4 mol% and was calculated by correlating the integral of aromatic protons peaks with the integral of the single peak at δ 1.10, attributable to the protons belonging to the -CH_3 group of the GG rhamnose. On the contrary, the peak at δ 3.5, attributable to the methylene protons of the PEG chains, does not allow to calculate the DD% in PEG since it overlaps numerous peaks of the pyranoside protons (δ 3.1-4) of the GG. The functionalization of GG with dopamine was also confirmed by UV analysis (**Figure 51C**), in fact the dispersion of GG_8-DA-PEG at 0.2% shows an absorption peak at 280 nm typical of dopamine, which instead does not appear in the spectrum of GG_8.

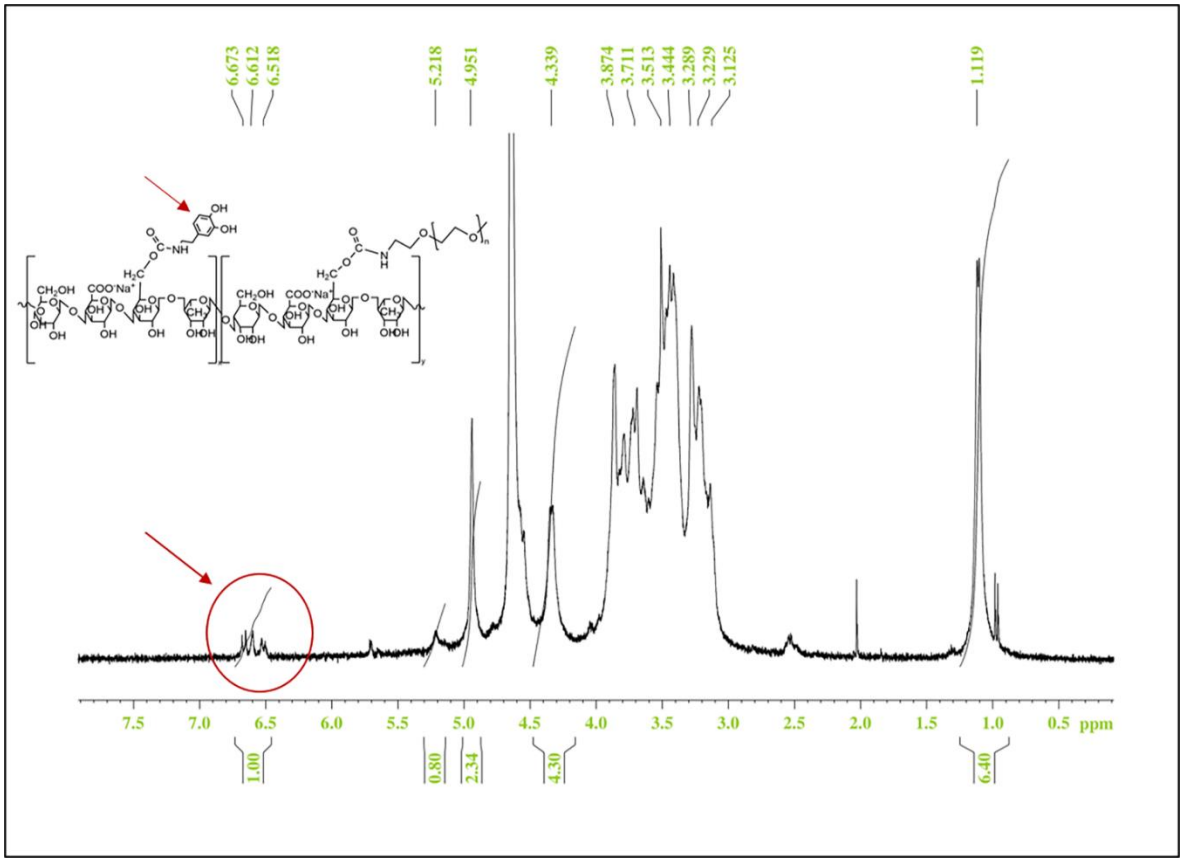

Figure 52. ^{1}H-NMR of the GG_8-DA-PEG derivative.

The effects of the functionalization of GG with dopamine and PEG were observed macroscopically by studying the dispersibility in water of the obtained products. Both derivatives allow to obtain clear water dispersions under mild heating condition (40°C for 10 minutes) and at a concentration of 5% w/v. Interestingly, after cooling down to room temperature, derivatives dispersions remain fluids on the contrary of the unfunctionalized GG. It is reasonable to suppose that PEG pendant chains can cause a perturbation of the *coil-to-helix* transition process responsible for the typical temperature induced gelation of the GG aqueous dispersion thus, facilitating the mixing with Colistin sulfate solution and obtain injectable hydrogels later. Nevertheless, both derivatives dispersions were still sensitive to the ionic strength of the surrounding medium as, when injected into DPBS pH 7.4, they

undergo a rapid gelation process. The higher molecular weight derivative, GG_8-DA-PEG, allows to obtain structured and compact hydrogels while the lower molecular derivative, GG_{24}-DA-PEG, forms fragmented hydrogels. on the whole, the reduction of the molecular weight of GG and the functionalization made to the macromolecule allow to overcome one of the most important limitations of the native polysaccharide which is linked to the difficulty in obtaining, at room temperature, fluid dispersions capable of gelling once in vivo.

3.3.2 Production and characterization of microparticles (MPs@pDA)

To produce a system capable of having a non-specific antimicrobial effect by means of a photothermal activity and an antioxidant action capable of removing the high production of ROS typical of the wound environment, it was decided to incorporate polydopamine into a hydrogel. Since, due to its colloidal size, the pDA could easily diffuse from the hydrogel to the administration site, causing the system to lose its photothermal and radical-scavenger properties, it was decided to allow the polymerization of dopamine on the surface of polymeric microparticles, produced starting from the GG_{24}-DA-PEG derivate, which could be easily dispersed within the gel forming polymer dispersion favoring the retention of the pDA within the delivery system. This specific derivative was chosen, because thanks to its low molecular weight it allows to obtain, at concentrations lower than 1% (w/v), aqueous dispersions that are fluid enough to be spray dried to obtain microstructures. The microparticles were obtained with a weight yield equal to 78.3% ± 6.5% with respect to the starting polymer. From the images acquired by optical microscope and scanning electron microscopy (SEM) it is clear that the microparticles obtained have an average diameter of 0.83 μm. The microparticles appear spherical and with a smooth surface (**Figure 53**).

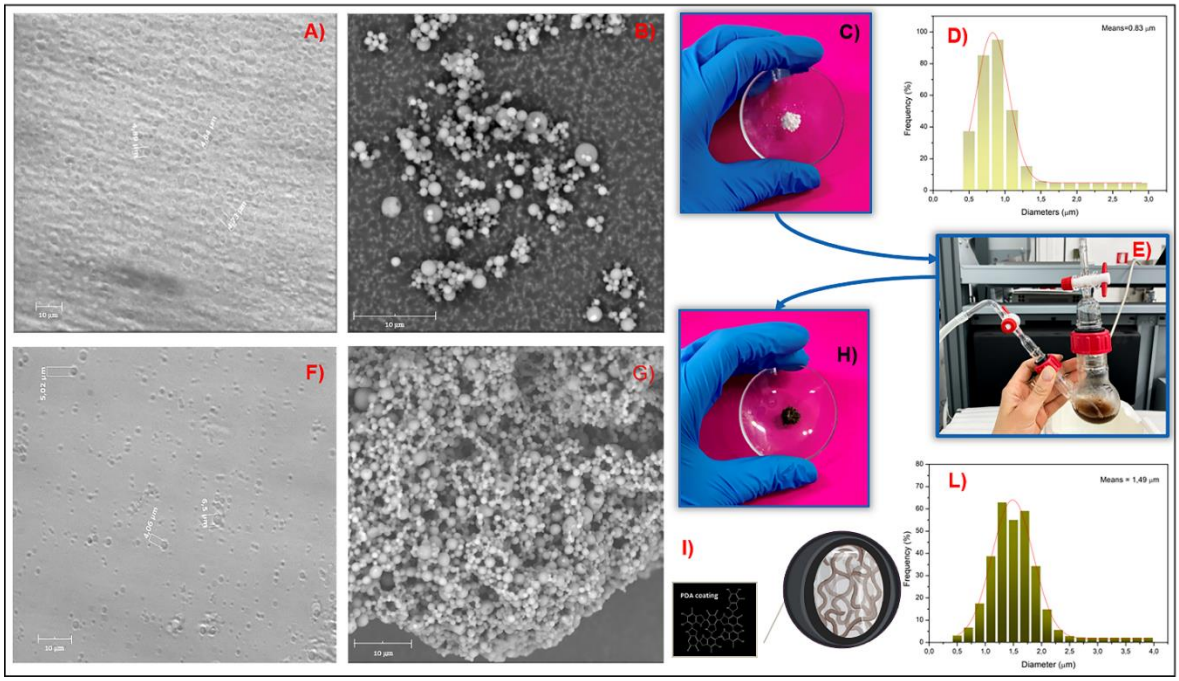

Figure 53. Images of microparticles of GG (24)-DA-PEG acquired by optical microscope (**A**), SEM analysis (**B**) and macroscopic image (**C**); dimensional distribution of MPs (**D**); image of dopamine oxidative polymerization reaction (**E**); MPs@pDA images acquired by optical microscope (**F**), SEM analysis (**G**) and macroscopic image (**H**); schematic representation of MPs@pDA (**I**); dimensional distribution of MPs (**L**).

Dopamine following oxidation, which can be catalyzed by the basic environment or by the presence of oxygen, generates a dark-colored amorphous polymer that tends to deposit on any type of surface, forming a surface coating. Obtained microparticles were used as a scaffold on which the polymerization of dopamine took place. The oxidative polymerization reaction was carried out by adding the dopamine solution to the microparticles previously dispersed in $CaCl_2$ 1M insufflating oxygen into the reaction mixture. The choice of the reaction solvent served to avoid the swelling and dispersion of the microparticles which instead occurs in water (not shown). Obviously, Ca^{2+} ions induce the ionotropic crosslinking of GG_{24}-DA-PEG allowing the MPs to retain their structure during dopamine

polymerization. The formation of the pDA coating on MPs is favored by the presence of dopamine in the GG_{24}-DA-PEG derivative, since not only dopamine tends to polymerize with itself in the reaction medium, but also tends to polymerize with dopamine exposed on the MPs of GG_{24}-DA-PEG. The microparticles with the polydopamine coating were named MPs@pDA and the yield was about 55% ± 3% with respect to the initial mass of the microparticles. The particles obtained, due to the presence of the pDA on their surface, acquire a dark color as shown in **Figure 53G**. From observation under an optical microscope and SEM, there is a slight increase in the percentage of particles with larger dimensions (**Figure 53F and 53G)**. This is an indication of the dopamine polymerization process on their surface, in fact the average diameter, as you can see from the **Figure 53L** is 1.49 µm.

3.3.3 Production and characterization of hydrogels: SEM analysis, rheological studies

Since, following ionotropic gelation, the GG_8-DA-PEG derivative allows to obtain compact hydrogels with a well-defined structure, this derivative has been used to produce medicated hydrogels with an antibiotic active against Gram negative pathogens. In particular, it was decided to exploit the presence of the carboxylated groups of the glucuronic acid residues of GG_8-DA-PEG to form, in water at pH 7, an ionic pair with the protonated amino groups of an antibiotic with a polypeptide structure, such as colistin sulphate. Therefore, colistin was loaded by exploiting the polyelectrolyte interactions between its positively charged and the negatively charged of GG_8-DA-PEG [335]. Two hydrogels were prepared using two different concentrations of the GG_8-DA-PEG polymer, 2% and 3% (w/v), and a fixed concentration of colistin sulfate, 2.5% (w/w) with respect to the polymer. The hydrogels were prepared simply by mixing an aqueous dispersion of the polysaccharide derivative with a solution of colistin sulfate and following mixing it was possible to observe

the immediate formation of the physical hydrogel, as demonstrated by the tube inversion test (**Figure 54**). Although the formation of the ion pair causes a drastic increase in the viscosity of the aqueous dispersions of GG_8-DA-PEG, the hydrogels obtained, thanks to the reversible nature of this interaction, have a certain fluidity which allows them to be loaded and extruded from a syringe (**Figure 58E**).

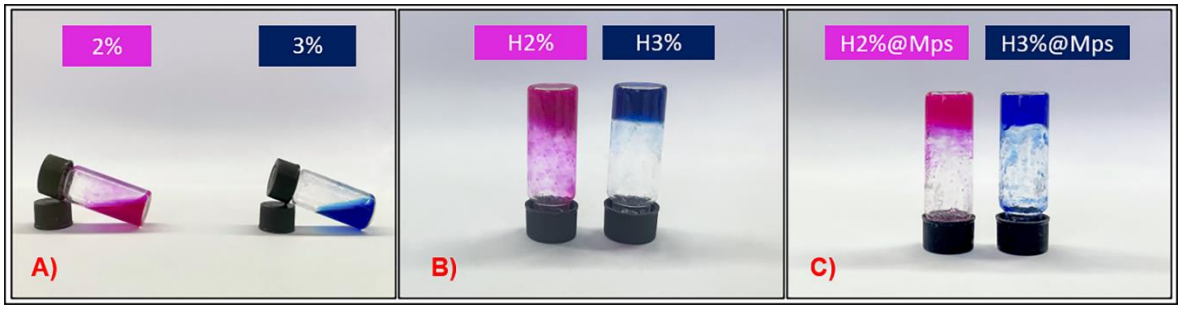

Figure 54. Tube inversion test. Images of the dispersions of GG_8-DA-PEG at 2% (w/v) (on right) and at 3% (w/v) (on left) (**A**); hydrogels formed following the addition of a solution of colistin sulphate, H2% (on left) and H3% (on right) (**B**); hydrogels formed following the addition of MPs@pDA and a solution of colistin sulphate, H2%@MPs (on left) and H3%@MPs (on right) (**C**). The samples in which the polymer concentration was 2% w/v were stained with Rhodamine, while the 3% w/v samples were stained with Azure II.

The same medicated hydrogels were also produced by incorporating the MPs@pDA, dispersed in the aqueous dispersions of GG_8-DA-PEG before the addition of colistin sulfate. Different weight ratios have been tested between GG_8-DA-PEG and MPs@ pDA and it has been seen that a quantity of microstructures equal to 15% (w/w) with respect to the weight of the polymer is the maximum value that allows to maintain the fluidity of the polymer dispersion and not to modify the gelation after the addition of the drug solution (**Figure 54C**). Beyond these concentrations, the microparticles strongly reduce the fluidity of the

aqueous dispersion of GG_8-DA-PEG and induce the formation of non-homogeneous hydrogels. Therefore, four different hydrogels were produced, indicated by different abbreviations as shown in **Table 1.**

Table 1. Hydrogels containing 2.5 % w/w colistin sulfate prepared using different amount of GG_8-DA-PEG and MPs@pDA

Sample	% w/v GG_8-DA-PEG	% w/w colistin sulfate	% w/w
H2%	2	2.5	0
H3%	3	2.5	0
H2%@Mps	2	2.5	15
H3%@Mps	3	2.5	15

Through SEM analysis it is possible to observe the highly porous structure of the H3%@MPs hydrogel and the presence of the MPs@pDA incorporated between the meshes of the three-dimensional network, also demonstrated by observation under an optical microscope (**Figure 55 A, B, C**).

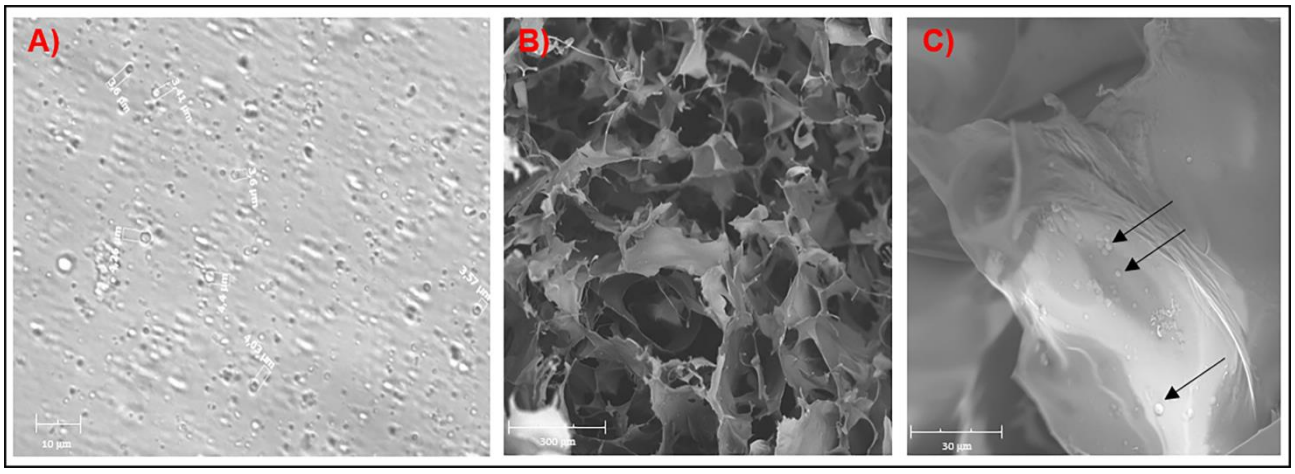

Figure 55. Optical microscope (**A**) and SEM (**B** and **C**) images of H3%@MPs hydrogel.

From the oscillation amplitude studies, all hydrogels showed a viscoelastic behavior dependent on strain%, i.e. the typical behavior of dynamic (physical) gel networks, as shown in **Figure 56**. In particular, for low strain % values, G' is greater than G", indicating that the system does not flow but behaves like a solid when subjected to slight mechanical perturbations. On the contrary, for high strain % values, G" becomes larger than G' indicating that the system begins to flow after flow point (the point where dynamic storage modulus and loss modulus intersect). This behavior is typical of physical gels, where there are reversible bonds between macromolecules that must be broken before allowing the gel to flow freely. G' value of the hydrogels increases as the polymer concentration increases and for the same concentration it is greater in the hydrogels containing the MPs@pDA. This denotes that the microparticles contribute to increasing the compactness of the hydrogels. However, analyzing the flow points obtained for the various hydrogels, we realize that the presence of the microstructures decreases the strain% value beyond which the systems begin to flow. In particular for hydrogels without MPs@pDA, H2% and H3%, the flow point value does not show significant differences and is 164% and 167% respectively, while for hydrogels with MPs@pDA, H2%@MPs and H3%@MPs, the values are 130% and 69% respectively. In particular, in Figure 5 we see that the point of flow has shifted to the left as we load the microparticles into the H3% hydrogel. This result provides a clear indication of the fluidity and, in turn, injectability of the developed hydrogels.

The results also indicate that after the incorporation of MPs@pDA into the polymer matrix, less force would be required to inject it and the injection pressure can be controlled by varying the loading level of the reinforcements [336]. This means that, if on the one hand the microparticles contribute to obtaining more "rigid" hydrogels, on the other hand in the phase

of mechanical perturbation, they allow the hydrogel to flow earlier (at lower strain stresses) probably because they interpose themselves between the polymer chains.

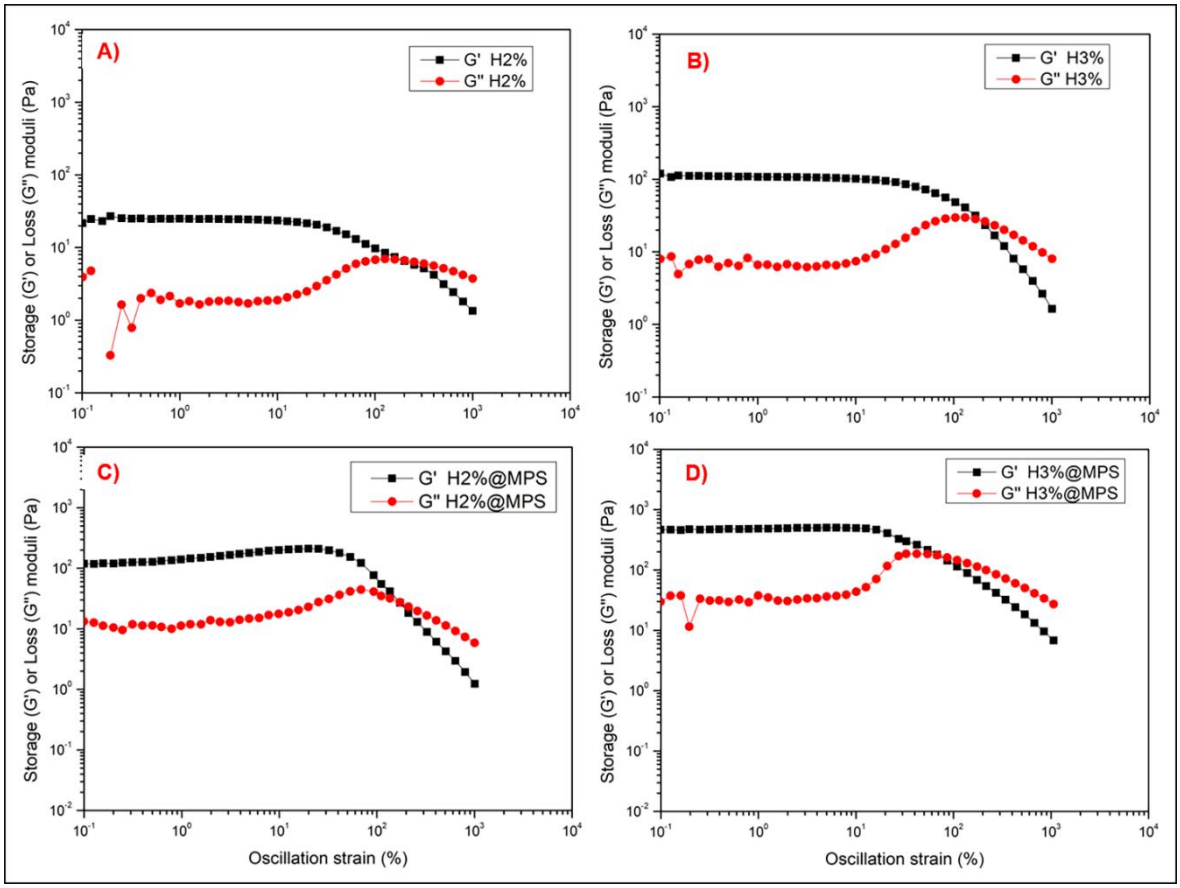

Figure 56. Oscillation amplitude studies of H2%, H3%, H2%@MPs and H3%@MPs hydrogels.

Flow sweep studies reported in **Figure 57** show that, proportionally to the increase in the concentration of the polymer, there is a slight increase in the initial viscosity at low shear rate values, which is equal to approximately 40 and 550 Pa*s for H2% and H3% respectively, for a shear rate of approximately 0.1 s^{-1}. The introduction of MPs@pDA in both hydrogels results in an increase in the initial viscosity, which is approximately 420 for H2%@MPs and 1010 Pa*s for H3%@MPs. The viscosity trend is comparable for all the hydrogels that have shown a marked decrease in viscosity as the speed with which shear stress is applied

increases, up to a minimum value beyond which the viscosity remains almost constant, thus confirming the pseudoplastic behavior of hydrogels.

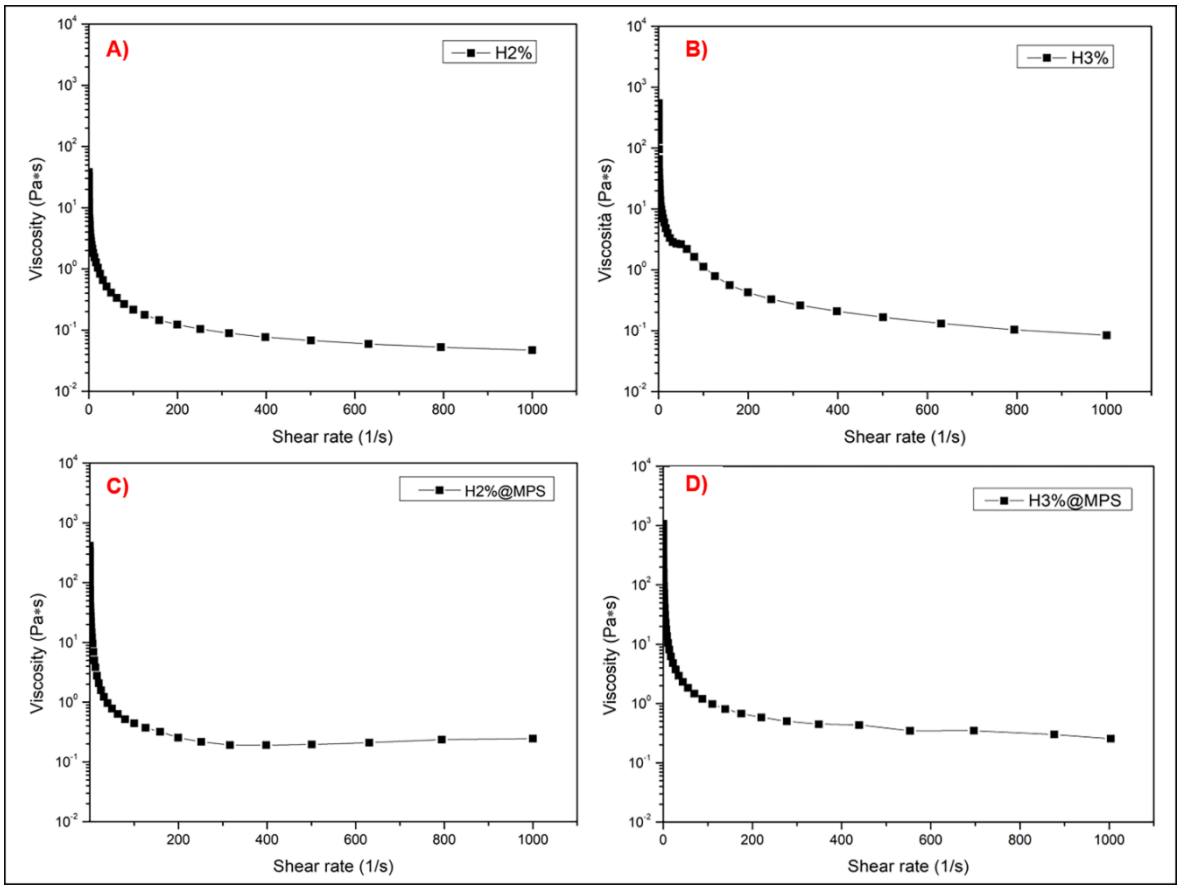

Figure 57. Flow sweep studies of H2%, H3%, H2%@MPs and H3%@MPs hydrogels.

These hydrogels therefore exhibit a shear thinning behavior (**Figure 57**), which represents the ease with which the polymer chains are able to align in the direction of application of the shear stress. In fact, as the shear rate increases, a decrease in the viscosity of the system is observed due to the breakdown of intermolecular bonds which occurs when the polymer chains begin to flow over each other. This rheological property is an important feature of injectable systems and is an indication of the ease of extrusion of the same from the needle of a syringe.

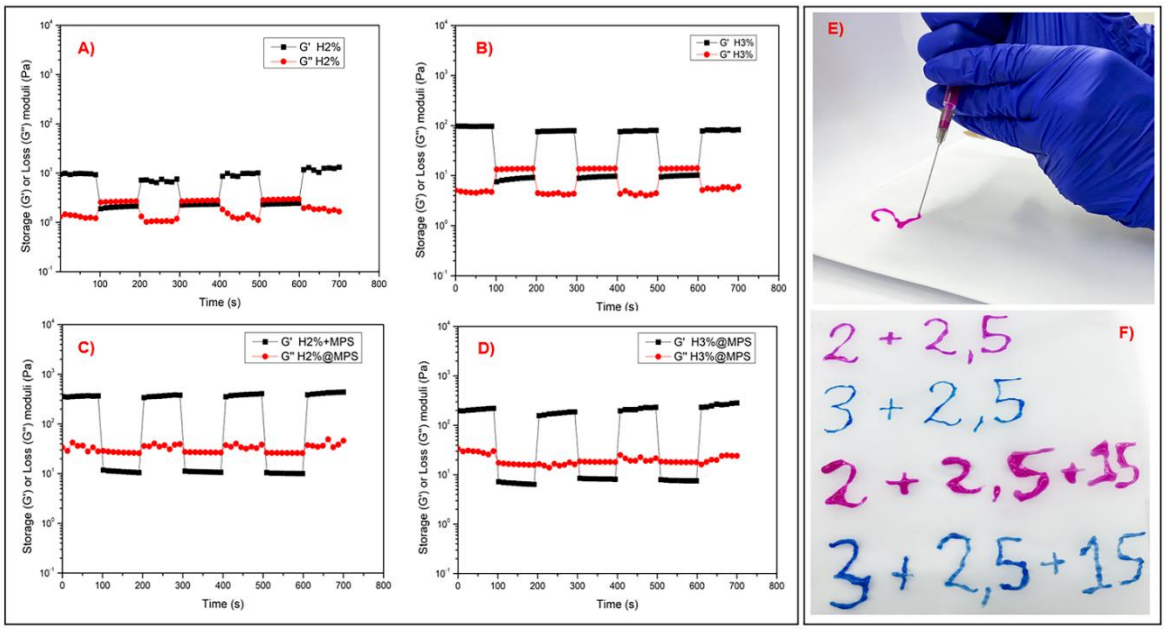

Figure 58. Recovery time studies of H2% (**A**), H3% (**B**), H2%@MPs (**C**) and H3%@MPs (**D**) hydrogels. The injectability of hydrogels observed macroscopically by extruding them through a 21 G needle (**E**,**F**).

The injectability of the obtained hydrogels was assessed through rheological studies in the recovery time regime (**Figure 58**), in which the samples are alternatively subjected to a low and high strain%. To facilitate injectability, the viscosity of the hydrogel must decrease as the shear stress increases (pseudoplastic behavior); on the other hand, once the effort applied when the hydrogel is ideally injected into the wound site has ceased, it must recover its initial viscosity as soon as possible and regain its initial physicochemical properties, assuming the shape of the injection site. The rheological analysis of recovery time has shown that all hydrogels show good recovery in the different low-high (1% -500%) strain% cycles applied. As for the H2% hydrogel, by applying a high strain, a rapid reduction of G' from ~ 10 Pa to ~ 1 Pa was observed; when a strain of 1% was applied again, the G' recovered 100% of the initial value and this trend was also maintained in subsequent cycles. The hydrogel H3%,

showed a reduction of the G' value from ~ 100 Pa to ~ 10 Pa, also in this case the hydrogel showed a 100% recovery of both G' and G" within a few seconds after strain-induced failure, which was reproducible over additional strain cycles. As for the H2%@MPs and H3%@MPs hydrogels, the presence of the MPs@pDA did not affect the recovery of the two modules through the low strain-high strain cycles, although variations of G' and G" did occur compared to hydrogels prepared without the microparticles. The H2%@MPs and H3%@MPs hydrogels have higher initial G' values, as shown previously in the oscillation amplitude analyses. In particular, the H2%@MPs hydrogel showed a reduction of G' from ~ 500 Pa to ~ 10 Pa while the hydrogel H3%@MPs showed a reduction of G' from ~ 200 Pa to values <10 Pa.This rheological study made it possible to confirm what it was possible to observe macroscopically, i.e. that the systems are injectable and it is also possible to "write" by injecting them (**Figure 58E-F**).

This is a demonstration, on the other hand, of the ease of extrusion of hydrogels from a syringe, due to the dynamic and reversible bonds that make up the hydrogel scaffold break when subjected to stress. On the other hand, it indicates that once the applied effort is finished, the system does not deform, rather it recovers its initial structural integrity, since the bonds are reformed when the effort is removed. Therefore, hydrogels likely have some self-healing character, suggesting that the hydrogel once injected into the wound site could take its shape and resist mechanical deformations induced by patient shocks or movement.

3.3.4 Hyperthermia studies

The photothermal conversion efficiency of the hydrogels, resulting from the high absorption of NIR at a wavelength equal to 810 nm by the MPs@pDA, has been studied through irradiation studies carried out at different irradiation powers by monitoring the variation of

temperature within 10 minutes. The presence of MPs@pDA gives the hydrogels strong photothermal properties that are not affected by the concentration of GG_8-DA-PEG. In fact, as can be seen from the graphs shown in **Figure 59A**, by irradiating the H2%@MPs and H3%@MPs hydrogels at a power of 0.74, 1.48 and 1.85 W/cm^2, an increase in the temperature in the surrounding medium (DPBS pH 7.4) is obtained, observed after 10 minutes, equal to 10, 12 and 15 °C respectively. It is evident that even hydrogels without MPs@pDA show, albeit to a lesser extent, a certain ability to develop heat following irradiation. This behavior is probably due to the oxidation of the catechol groups of dopamine which leads to the formation of structures similar to melanin.[337]

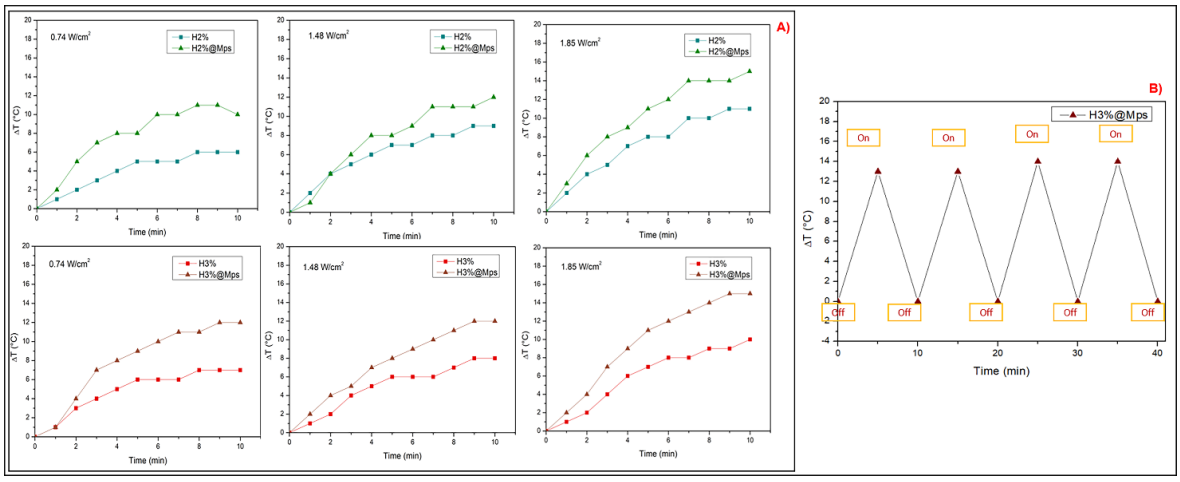

Figure 59. Photothermal conversion efficiency of the hydrogels, after irradiating at a power of 0.74, 1.48 and 1.85 W/cm^2 (**A**). Photostability study of H3%@MPs studied by irradiation-cooling cycles (5 minutes for irradiation and 5 minutes for cooling) at a power of 1.48 W/cm^2 (**B**).

A photostability study was also performed by operating consecutive cycles of irradiation. The assay was performed by carrying out four 10-minute irradiation-cooling cycles (5 minutes for irradiation and 5 minutes for cooling) at a power of 1.48 W/cm^2. Since no significant differences were observed in the ability to develop heat as a function of sample concentration, only the results obtained for H3%@MPs sample have been here reported. As

can be seen from **Figure 59B**, a comparable temperature rise/fall is recorded in the surrounding medium after each heating and cooling cycle. This result demonstrates that the hydrogel, once subjected to irradiation cycles at predetermined times, is able to maintain the photothermal conversion capacity over time, inducing a controlled increase in temperature, which can be exploited to enhance the antimicrobial effect of the colistin.

3.3.5 Drug release studies

Thermostability studies have amply demonstrated that Colistin remains stable at 37 °C [338]. For this reason, it was chosen to irradiate the hydrogels to study the release of the antibiotic only at 1.48W/ cm^2 for 5 minutes, because in the temperature in the well in other cases could be too low or too high, reaching temperatures above 37 °C (increases up to 9 points in ΔT). It is also known that Colistin is very stable in water, but less stable in isotonic phosphate buffer at 37 °C [339]. So, but as time passes and the temperature increases the polypeptide structure begins to denature and this would cause an inefficiency in our system.

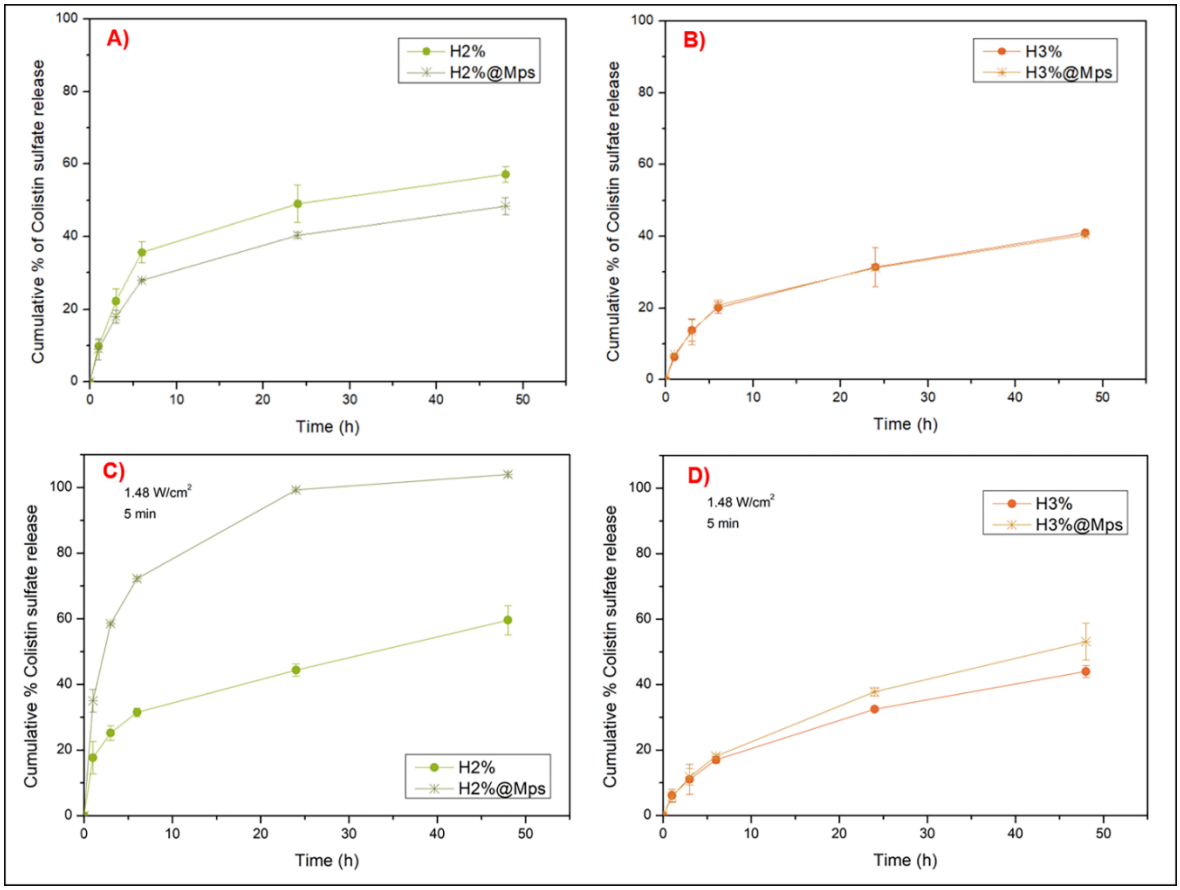

Figure 60. Release study of colistin sulphate from H2% and H2%@MPs (**A**), H3% and H3%@MPs (**B**) hydrogels in DPBS pH 7.4 without NIR irradiation; from H2% and H2%@MPs (**C**), H3% and H3%@MPs (**D**) hydrogels in DPBS pH 7.4 after NIR irradiation.shoud be inserted here.

As shown in **Figure 60**, comparing the release profiles of H2% and H2%@MPs hydrogels it is evident that the antimicrobial peptide forms bonds with the pDA present on the microstructures, in fact the release is slowed down in the presence of MPs@pDA. The same thing is not visible when comparing the H3% and H3%@MPs hydrogels, which showed a comparable release profile. Probably, in this case, the greater compactness of the hydrogel masks this interaction effect with the MPs@pDA. On the other hand, the increase in the temperature in the well after NIR irradiation determines an increase in the quantity of drug released as a function of time, as it favors the diffusion of the drug through the hydrogel

network. As it can be seen, in fact, after 48 hours, 100% of the colistin sulphate is released from the H2%@MPs hydrogel, while the maximum quantity released by the hydrogel itself, when not subjected to NIR light, was about 48%. Similarly, after 48 hours ~ 51% of the drug is released from the H3%@MPs hydrogel after NIR irradiation, while the percentage of colistin released from the corresponding non-irradiated hydrogel is 40%. Lower release is also observed for 3% (w/v) samples. Also, although an increase in the amount of drug released in the sample is observed with MPs, this increase is less marked than with 2% (w/v) hydrogel. The drug release appears to be less affected by the effect of NIR, certainly because H3%@MPs is more compact. In the initial phase of the study there is a rapid release of colistin sulphate, while after the first 6 hours the colistin is released more slowly from each hydrogel. Probably the initial increase in temperature induces a rapid diffusion of the colistin sulphate molecules, in particular in the H2%@MPs and H3%@MPs hydrogels. In these systems the MPs@pDA partially takes over the colistin, making it more available to diffuse in the medium, the remaining amount of colistin incorporated between the hydrogel meshes, instead, is characterized by a slower release.

3.3.6 *In vitro* evaluation of antioxidant activity

The antioxidant capacity of the GG_8-DA-PEG polymer over time and of the MPs@pDA at different concentrations was tested by evaluating the free radical scavenging properties through the DPPH and the $ABTS^{\bullet+}$ assays. The absorption spectra UV of $ABTS^{\bullet+}$ and DPPH assays are showed in **Figures 61** and **62**.

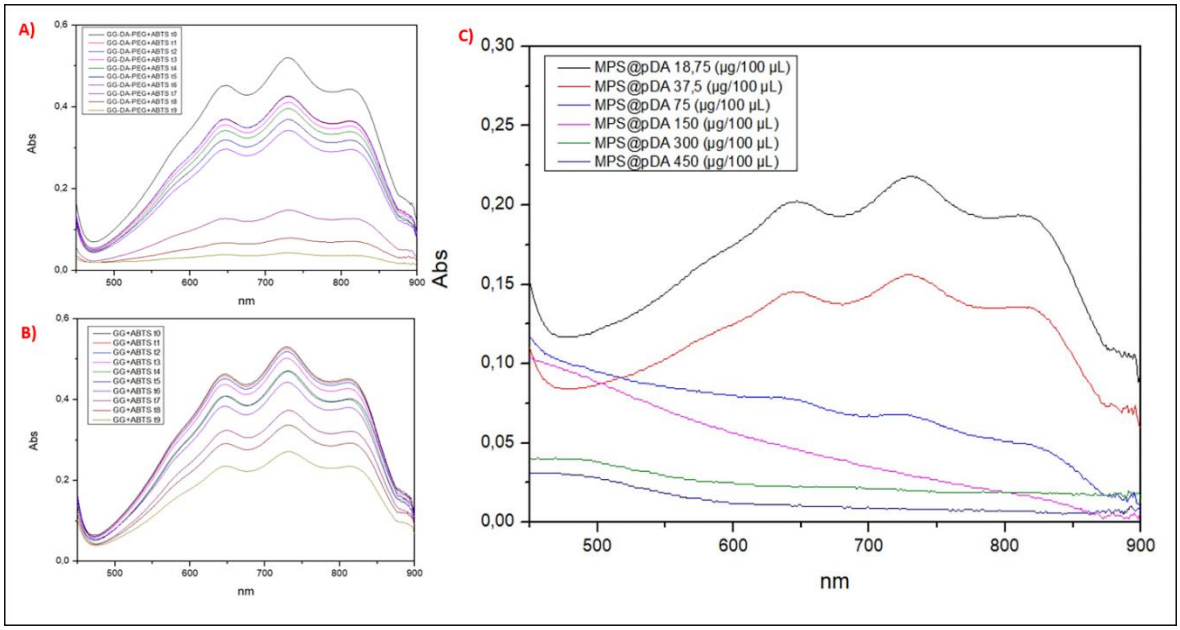

Figure 61. Absorption Uv-Spectra of ABTS$^{\bullet+}$ assay of GG_8-DA-PEG (**A**), GG_8 (**B**) at set times and MPs@pDA at different concentrations (**C**).

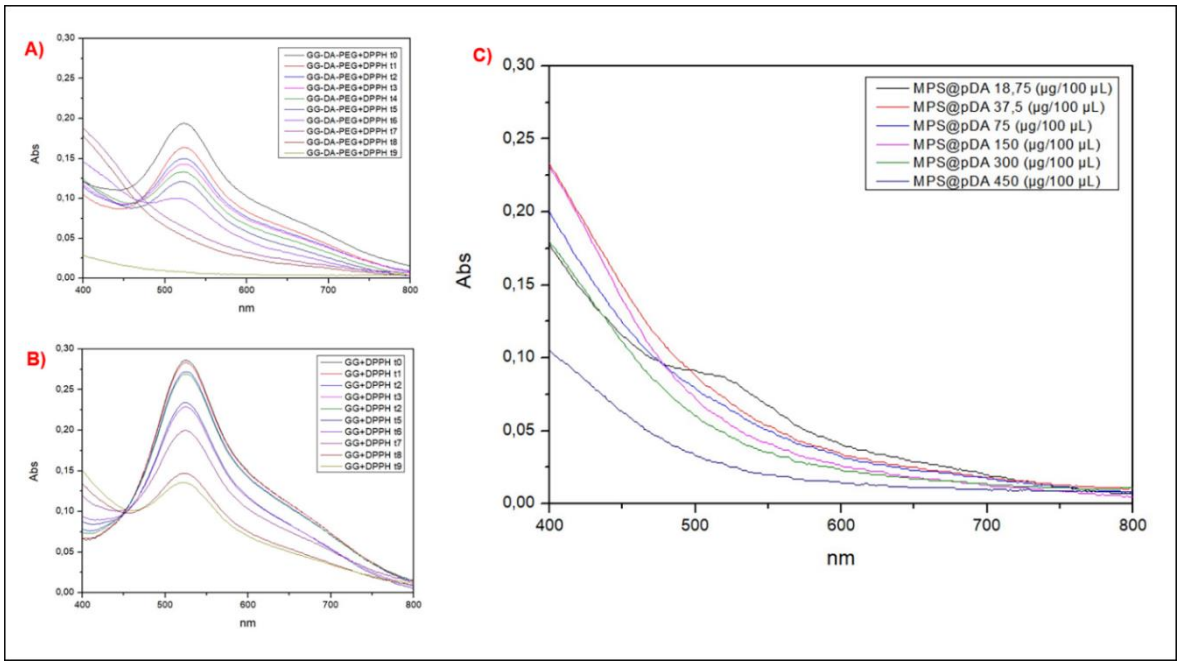

Figure 62. Absorption Uv-Spectra of DPPH assay of GG_8-DA-PEG (**A**), GG_8 **(B)** at set times and MPs@pDA at different concentrations (**C**).

The results of the $ABTS^{\bullet+}$ assay shown in **Figure 63A** demonstrated that, after 72 hours of incubation, the samples with the GG_8-DA-PEG have a scavenging ratio of about 90%. As can be seen in the graph, it is evident that the insertion of dopamine in the polymeric backbone allows to increase the radical scavenger activity of the starting GG_8, which instead after 72 hours was able to eliminate up to 40% of radicals [340].

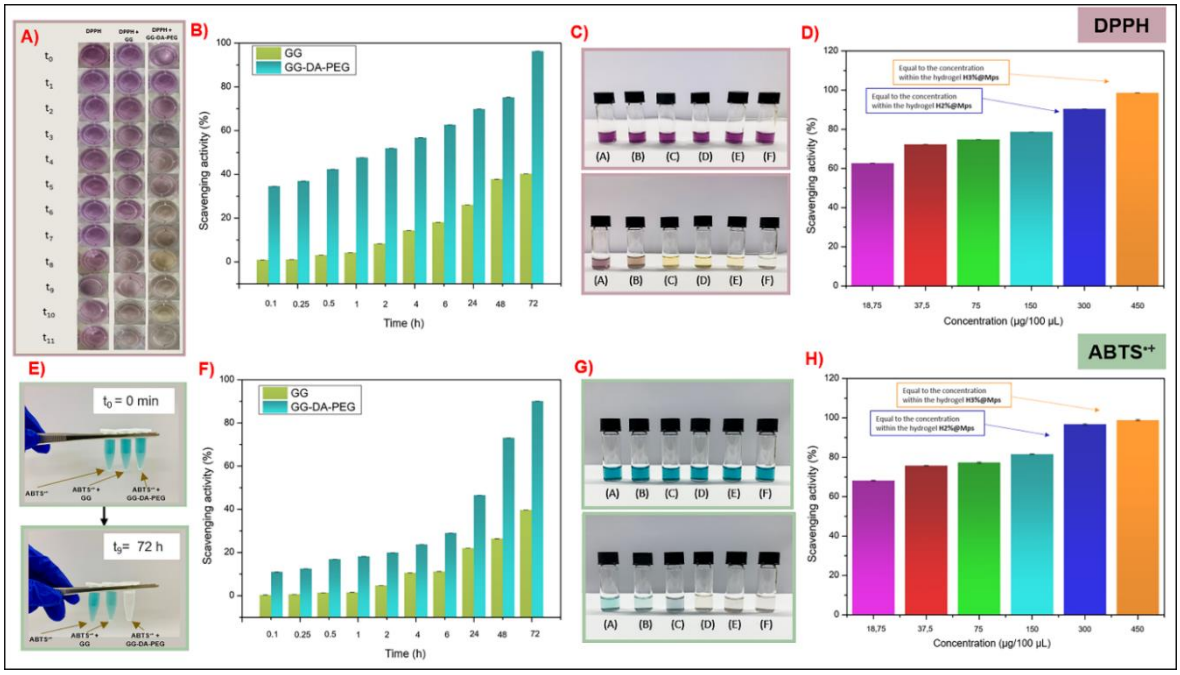

Figure 63. Radical scavenging activities of GG_8-DA-PEG and GG_8 (**A-B**) and of MPs@pDA (**C-D**) measured by DPPH assay. Radical scavenging activities of GG_8-DA-PEG and GG_8 (**E-F**) and of Mps@pDA (**G-H**) measured by $ABTS^{\bullet+}$ assay.

As expected, MPs@pDA have a dose-dependent antioxidant capacity, in fact, as the concentration increases, the ability to eliminate radicals increases. Specifically, the samples at concentrations corresponding to those present in the H2%@MPs and H3%@MPs hydrogels immediately eliminate 96% and 98% of $ABTS^{\bullet+}$ free radicals, respectively (**Figure 63C-D**). Likewise, the results of DPPH scavenging established a similar trend in

Figure 63. After 72 hours of incubation, the samples with the polymer dispersion have a scavenging ratio of about 96%. It can be seen that, also in this case, the MPs@pDA at the concentrations corresponding to the quantities present in the hydrogels H2%@MPs and H3%@MPs immediately eliminate respectively 90% and 100% of the DPPH free radicals. These data therefore demonstrate that the MPs@pDA added to the polymer dispersion of GG_8-DA-PEG for the production of the hydrogels significantly improve and strengthen the intrinsic antioxidant capacity of the dopamine-modified polysaccharide over time, as the radical scavenging effect of the microstructures is immediate allowing a complete elimination of ROS.[341] This is important because a hydrogel thus produced could perform its antioxidant capacity during the initial phase of the wound healing process, which proved our preliminary hypothesis.

3.3.7 Adhesion test

An adhesive hydrogel promotes the closure of the flaps of a wound, stops bleeding by inducing a hemostatic effect and reduces the loss of gas and liquids from the tissue, allowing an adequate healing process of the damaged tissue. In order to demonstrate the macroscopic adhesiveness of the hydrogel, conferred by the presence of dopamine on the backbone of the polysaccharide derivative and by the pDA coating on the microparticles, *ex vivo* studies were performed using porcine skin samples [342]. The study was conducted by placing the hydrogel between two layers of skin and subsequently forcing the separation of the two layers with the aid of weights of 20, 50, 100 and 200 g (**Figure 64**). The GG_8 polymer was used as a control. A further check was carried out by carrying out the test on the dispersion of GG_8-DA-PEG at 3% (w/v) only. It has been observed that all hydrogels, H2%, H3%, H2%@MPs

and H3%@MPs keep the two layers of skin adhered up to 100 g in weight. On the other hand, when a weight of 200 g is attached to one of the two layers of skin, the two layers separate. The polymer dispersion alone has been shown to keep the two layers of skin adhered up to a weight of 100 g, this confirms the fact that the presence of dopamine strengthens the adhesive properties of the starting polysaccharide. The sample with GG (8) has instead shown to have milder adhesive capacity, in fact the two layers of skin remain adherent for weights of 20 and 50 g and when the weight of 100 g is used, the two layers of skin separate.

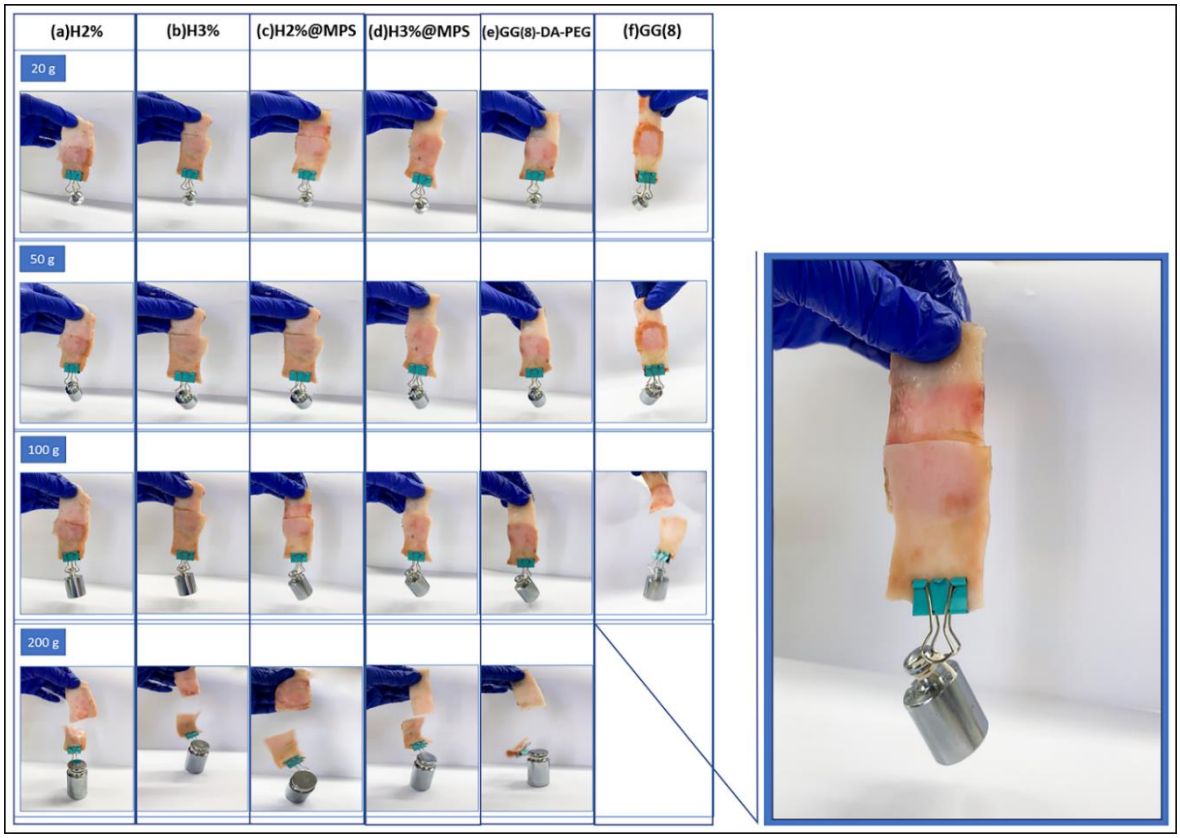

Figure 64. Adhesion test *ex vivo* adhesiveness tests were performed by placing the hydrogels H2% (**a**), H3% (**b**), H2%@MPs (**c**) and H3%@MPs (**d**) and the dispersions of GG_8-DA-PEG at 3% (w/v) (**e**) and GG_8 at 3% (w/v) (**f**) between two layers of porcine skin and forcing their subsequent separation with the aid of 20, 50, 100 and 200 g weights.

3.3.8 Cytocompatibility studies

Primary HDFs were used as model cells to study the cytocompatibility of hydrogels. During the experiment, H2%@MPs and H3%@MPs hydrogels were injected directly into CellCrown insert (Sigma-Aldrich) to avoid direct contact with HDF to avoid physical damage to the cells.

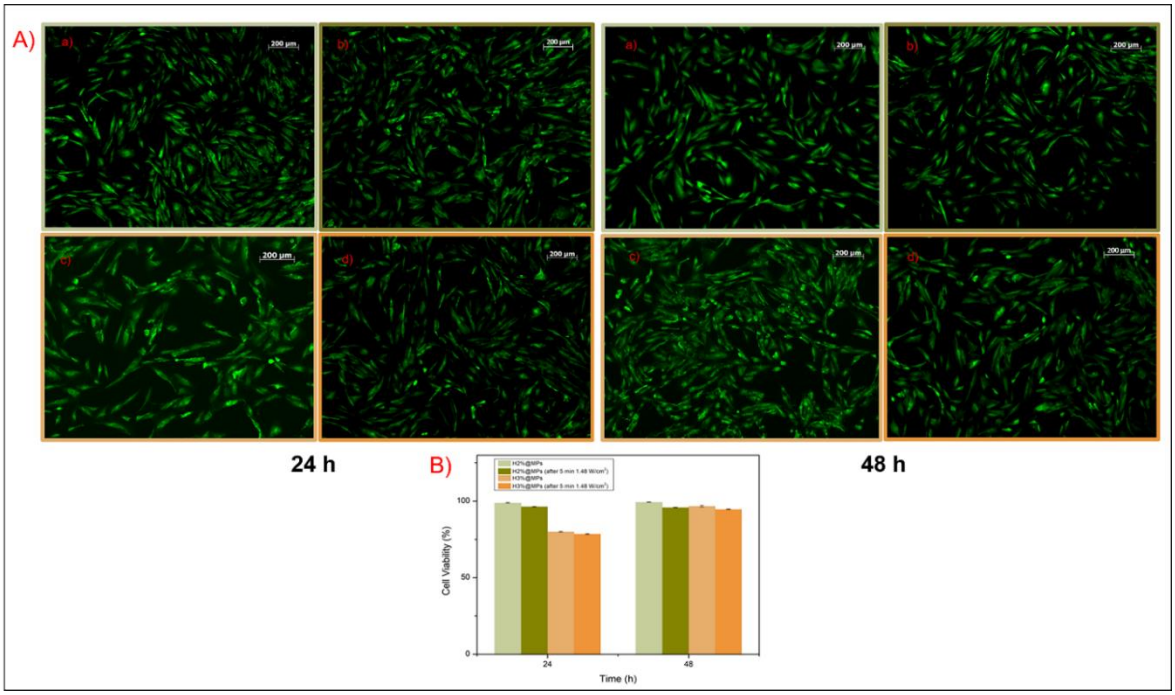

Figure 65. (**A**) MTS assay doing after 24h (left) and 48h (right) of **a)** H2%@MPs not irradiated, **b)** H2%@MPs after laser exposure (5 min, 1.48 W/cm^2), **c)** H3%@MPs not irradiated and **d)** H3%@MPs after laser exposure (5 min, 4 W). (**B**) Cell viability % as a function of time after incubation with H2%@MPs not irradiated, H2%@MPs after laser exposure (5min, 1.48 W/cm^2), H3%@MPs not irradiated and H3%@MPs after laser exposure (5 min, 1.48 W/cm^2).

In **Figure 65B** the cell viability of HDF is shown, influenced by the presence of hydrogels, as demonstrated by the results of the metabolic activity test (MTS). No significant differences were found in the metabolic activity of cells in culture in the presence of

H2%@MPs hydrogels up to 48 hours of culture, while for H3%@MPs hydrogels, cells remain alive after 48 hours up to 70% of the control. Through the live/dead staining test it was possible to qualitatively observe the presence of viable (green colored) and dead (red colored) cells using different fluorescence probes. It is evident that the cells retain their typical spindle-like shape (**Figure 65A**). As appears evident, in confirmation of the MTS test described above, no dead cells were observed both in the absence and in the presence of H2%@MPs and H3%@MPs hydrogels both after 24 and 48 hours.

3.3.9 *In vitro* evaluation of antibacterial activity

Antibacterial activity of H2%, H3%, H2%@MPs and H3%@MPs hydrogels, was preliminarily evaluated in terms of diameter of zone of inhibition of free-living bacterial growth against reference strains *P. aeruginosa* ATCC 15442, without and after NIR irradiation (1.48 W/cm^2, 5min). All hydrogel showed a strong antibacterial activity, demonstrated by the formation of an inhibition halo in all samples >15mm (**Figure 66** and **Table 2**). In particular, the hydrogel prepared incorporating microparticles (MPs@pDA) (15% w/w) were more active against *P. aeruginosa* respect to hydrogel without microparticles. Specifically, the hydrogel H3%@MPs showed the highest antimicrobial activity, with inhibition zone diameter of 18.6 mm (**Table 2**). A slight improvement in activity was observed for all samples after NIR irradiation respect to samples without NIR. Particularly, the sample H3%@MPs irradiated resulted the most active against tested strain, see **Figure 66** and **Table 2**.

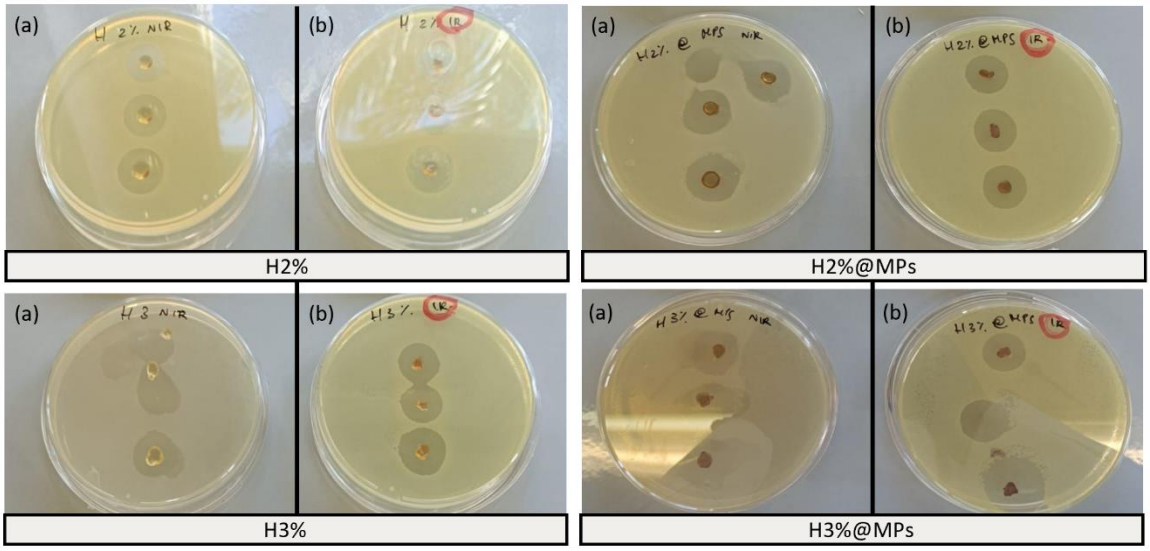

Figure 66. Inhibition zone diameter of the hydrogels H2% and H3% (**samples on the left**), or hydrogel with MPs@pDA, H2%@MPs and H3%@MPs (**samples on the right**), against *P. aeruginosa* ATTC 15442, without and after NIR irradiation (**a, b** respectively).

Table 2. Inhibition zone diameter (mm) of non-irradiated and irradiated (1.48 W/cm^2, 5min) hydrogel samples against *P. aeruginosa* ATTC 15442.

Sample	% w/v GG_8-DA-PEG	% w/w Colistin sulfate	% w/w
H2%	2	2.5	0
H3%	3	2.5	0
H2%@MPs	2	2.5	15
H3%@MPs	3	2.5	15

The antimicrobial investigation has been continued by focusing on the most active sample H3%@Mp, extending the antibacterial activity evaluation also against *Staphylococcus aureus* ATCC 25923. The inhibition of planktonic growth of two pathogens was evaluated by the count of viable bacterial cells and expressed as units forming colonies (CFU/mL) after 2; 4; 6 and 24 hours of incubation of tested microorganisms in the presence of H3%@MPs not irradiated or after NIR irradiation (1.48 W/cm2, 5min). The growth control bacterial counts (not treated) ranging from around 3.2 x 10^7 to 2.8 x 10^8 CFU/ml (*P. aeruginosa*) and from 1.3 x 10^8 to 1.5 x10^9 CFU/ml (*S. aureus*) at different tested time (**Figure 67**). The effect of NIR light exposure was very significant for *P. aeruginosa* at 2 and 4h with a log reduction of 1.7 and 1.9 respectively. At 6 and 24 h a dramatic reduction of the viable counts of *P. aeruginosa* in the presence of the sample H3%@MPs (both irradiated and not irradiated) was observed (**Figure 67A**). In the case of viable counts of *S. aureus* (**Figure 67B**) a slight inhibition of growth was observed only in the case of the irradiated microparticles, with a maximum log reduction equal to 1 after 24h.

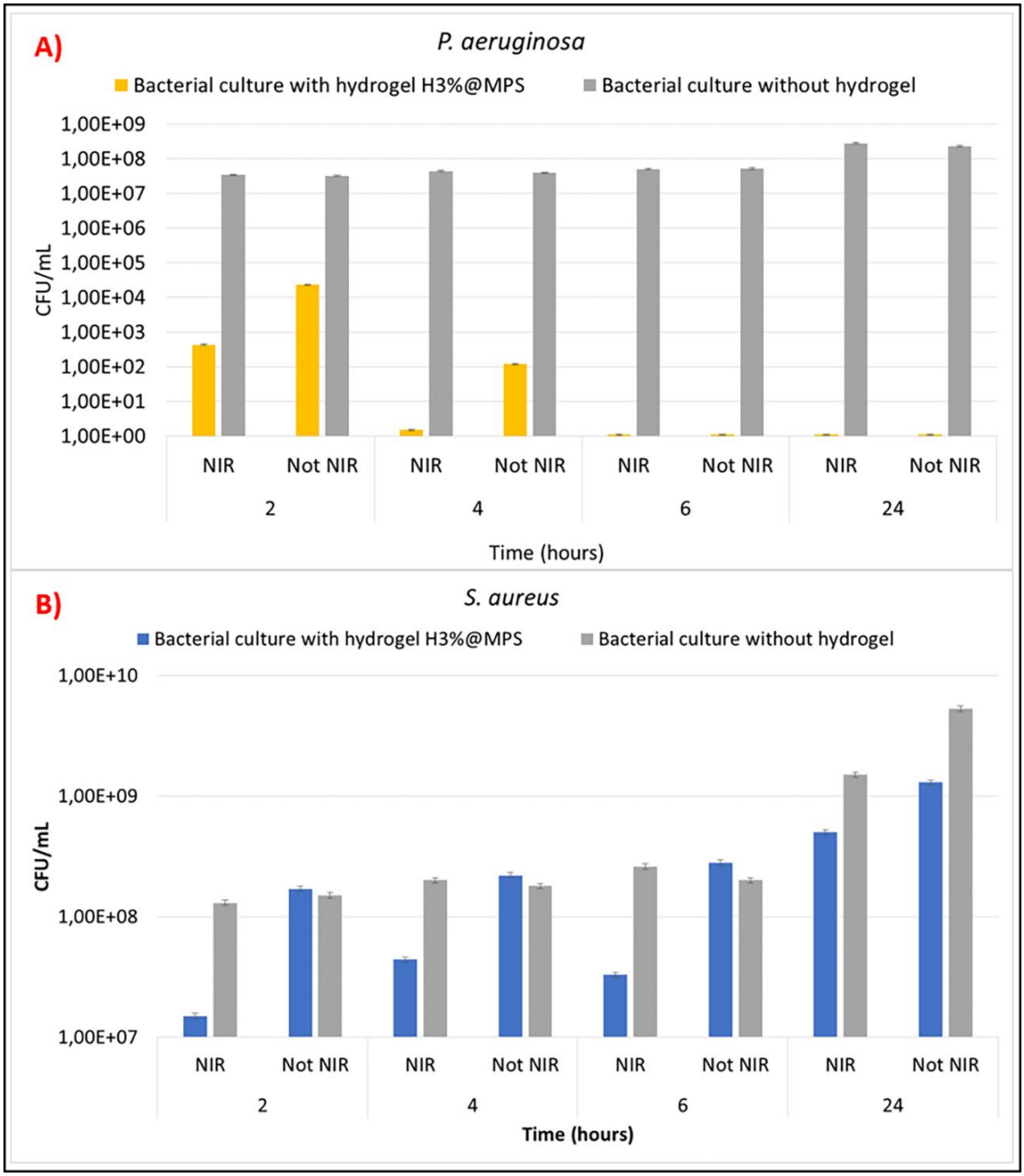

Figure 67. Antibacterial activity against *P. aeruginosa* ATTC 15442 (**A**) and *S. aureus* ATCC 25923 (**B**) of H3% hydrogel prepared incorporating microparticles (H3%@MPs), without (not NIR) and after NIR irradiation (1.48 W/cm^2, 5 min). Histograms show the colony forming units (CFU/ml) of bacterial strains obtained by viable plate counts method at different incubation times (2, 4, 6 and 24 hours).

3.4 Antibacterial broad-spectrum dendritic/gellan gum hybrid hydrogels with rapid shape-forming and self-healing for wound healing application

3.4.1 Hybrid Hydrogels production

The development of multifunctional wound dressings based on antibiotic-free hydrogels that efficiently promote the eradication of infection of damaged tissues is crucial to address existing healthcare challenges. An attractive materials solution that we hypothesized is the development of a novel platform of hydrogels that combines the unique properties of natural-derived biomaterial and AMP-mimicking dendritic polymers. Consequently, we explored the hybridization of anionic GG-DA together with the non-toxic and antibacterial cationic TMP-G2-alanine polyester dendrimer.[298] The functionalization procedure of GG with DA, described and shown in **Figure 68**, is similar to that already described and involves the activation of the primary hydroxyl groups of the glucosidic residues of GG with 4-NBPC and the subsequent reaction with DA.[343] The degree of molar derivatization in dopamine (DD_{DA}mol%) was evaluated by ^{1}H-NMR analysis (**Figure 68B**) of GG-DA, comparing the peak at δ 6.8, attributable to the protons in the aromatic group of the dopamine (-CH_2), with the peak at δ 1.10, attributable to the methyl group of Gellan Gum (-CH_3 of rhamnose portion of GG). The degree of functionalization in DA was equal to 36 % ± 1.6 mol%. The ATR-FTIR analysis confirms, as shown in **Figure 68C**, the functionalization of the GG polymeric backbone. In particular, the formation of the C=O ester bond is confirmed by the presence of the peak at 1750 cm^{-1}; the formation of the carbamate bond was confirmed by the appearance of the amide band II at 1528 cm^{-1}.[311]

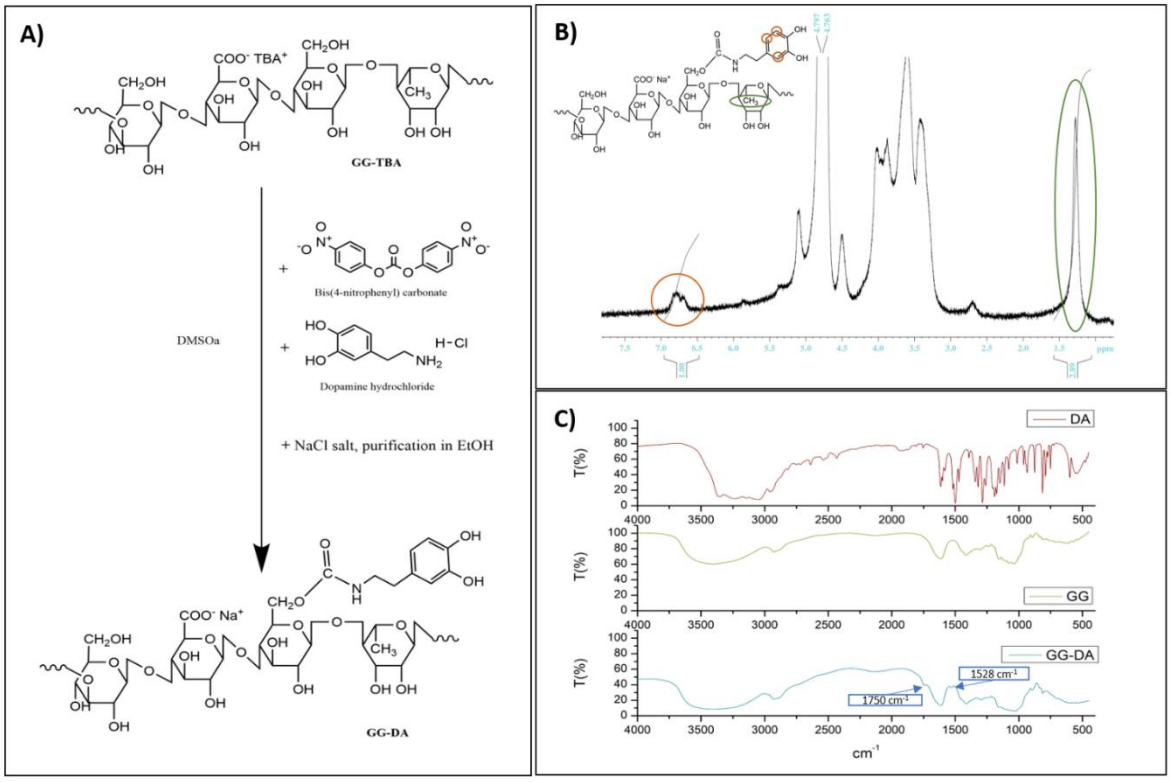

Figure 68. Scheme of synthesis of GG-DA derivate (**A**), ^{1}H-NMR (**B**), and FT-IR spectra (**C**).

Initial mixing of GG-DA and TMP-G2-alanine in aqueous conditions resulted in fragile and fragmented polyelectrolyte complex hydrogels. A strategy was therefore required that goes beyond simple ionic interaction and towards well-structured hybrid hydrogels with improved viscoelastic properties suited for biomedical applications.[344] More specifically, the strategy was reinforced by implementing a dual-crosslinking approach by combining ionic self-assembly of the networks with a subsequent curing step in 0.1M $CaCl_2$ at 4°C for 1h. The hydrogels, referred to as “solid" or "sol" hybrid hydrogels, with enhanced modulus were produced straightforwardly by simultaneous injection of the two-component solutions of GG-DA and TMP-G2-alanine into different molds, for example, a cylindrical mold, and then immersed in 0.1 M $CaCl_2$. Three-dimensional cylindrical hydrogels with dual crosslinks

were obtained, first via physical ionic interactions between NH_3^+ of the dendrimer and COO^- of the GG-DA polymer and then reinforced through ionotropic crosslinking of GG-DA with divalent Ca^{2+} ions which are interposed between the carboxyl groups represented on gellan gum chains (**Figure 69A**). Indeed, the proposed dual-crosslinked strategy improves the viscoelastic performance of the designed hydrogels. To detect the impact of crosslinking induced by Ca^{2+} ions on modulus, a rheological assessment of the hydrogels was conducted by comparing the crosslinking gelation process. For comparison, two representative hydrogel systems were produced and evaluated. In total, four different hydrogels were developed by mixing the precursors i.e. two H1 (no $CaCl_2$) and H3 (no $CaCl_2$), and two more, H1 ($CaCl_2$) and H3 ($CaCl_2$) that were finally immersed in 0.1 M $CaCl_2$ for 1h. To detect the effect of ion-induced crosslinking, the rheological profile of hydrogels based on GG-DA and TMP-G2-alanine was evaluated by comparing the crosslinking procedures, using only physical crosslinking or dual-crosslinking with 0.1M $CaCl_2$.

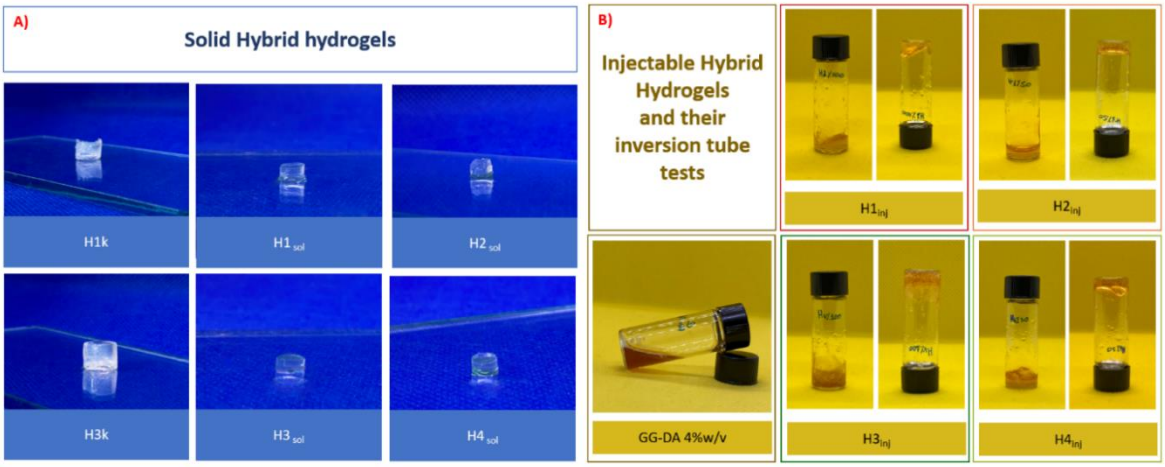

Figure 69. Pictures of different hybrid hydrogels produced. Control, solid (**A**), and injectable (**B**) hybrid hydrogels.

Frequency sweep analyses in **Figure 70** revealed an order of magnitude higher G' and G" values for the hydrogels with reinforced crosslinking with $CaCl_2$. These findings supported our initial hypothesis in which Ca^{2+} crosslinking with available pendant carboxylic groups further enhanced the modulus of the hybrid hydrogels. All solid hydrogels were then produced following the identified procedure.

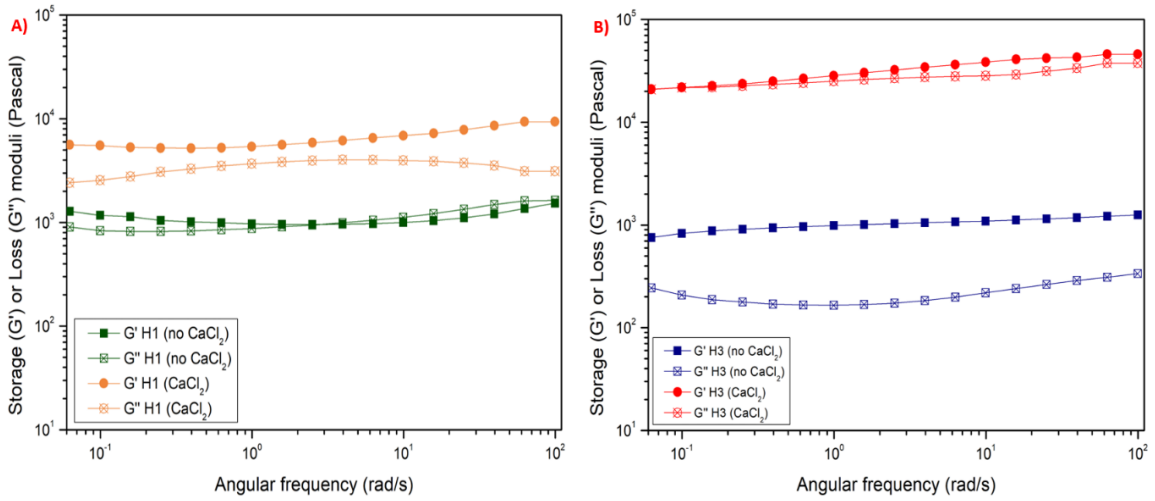

Figure 70. Frequency sweep analyses of solid hybrid hydrogel double-crosslinked ($CaCl_2$) compared to hybrid hydrogels without ionotropic crosslinking (no $CaCl_2$). (**A**) G' and G'' of H1 with or without curing in 0.1 M $CaCl_2$, and (**B**) G' and G'' of H3 with or without curing in 0.1 M $CaCl_2$.

To further capitalize on the modularity of the proposed two-component hybrid hydrogels platform we further explored the feasibility to generate injectable hydrogels, referred to as injectable or inj hybrid hydrogels. Antibacterial hydrogels with injectable, remodeling, and self-healing properties can perfectly fill uneven wounds as on-demand topical hydrogel solutions for accelerated infectious wound healing.[345] In this context, and in contrast to the Ca^{2+} crosslinking strategy, the oxidization of the pendant dopamine into dopa-quinone at elevated pH of 8.5 followed by mixing with TMP-G2-alanine dendrimer facilitated the

development of injectable hydrogels. From the point of view of wound applicability, hydrogels would be readily oxidized in air and under oxidative conditions, which are also closely associated with bacterial colonization and lead the wound to approach an alkaline pH.[346] The systems were found extrudable from a syringe and post-injection of the mixture resulted in "soft" and homogeneous injectable hydrogels (**Figure 79B**). These hydrogels are reinforced with a new set of crosslinking mechanisms, such as the imine bond by Shiff Base and Michael addition, which together with the non-covalent physical bonds present in the already formed polyelectrolyte complex, give these injectability and self-healing properties.[347] The formation of both solid and injectable hybrid hydrogel types is shown in the scheme in **Figure 71.**

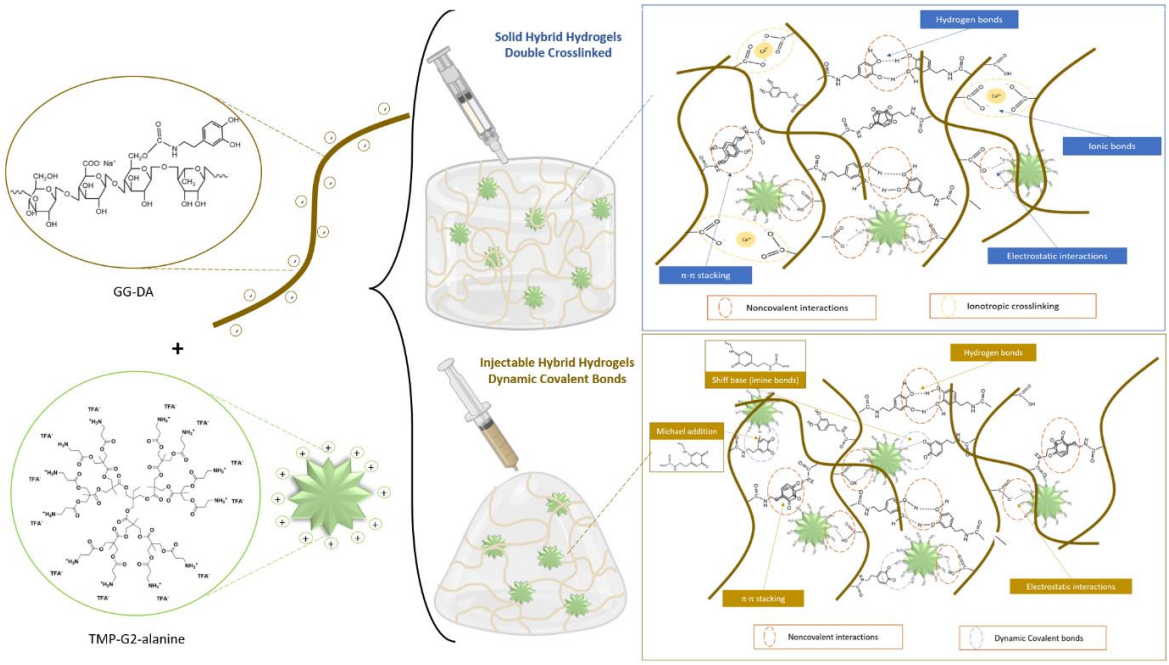

Figure 71. Schematic diagram describing the formation of solid hybrid hydrogels (above) and injectable hybrid hydrogels (below).

3.4.2 Characterization

FTIR analysis was used to determine the presence of dendrimers within both hybrid hydrogels. In **Figure 72A**, representative spectra of two hybrid hydrogels, $H1_{sol}$ and $H1_{inj}$ (3%w/v GG-DA and 100%w/w TMP-G2-alanine with respect to GG-DA) are shown in comparison with the spectra of TMP-G2-alanine, GG-DA, and the H1k (3%w/v GG-DA alone in 0.1M $CaCl_2$), produced from GG-DA alone. The peaks at 1733 cm^{-1} and 1667 cm^{-1} are characteristic of the C=O due to the carbonyl ester and of the deformation vibration peak of $–NH_2$ in the dendrimer. Both peaks were observed in the spectra of the solid and injectable hybrid hydrogels H1 as well as for the pure dendrimer sample. Swelling of hybrid hydrogels was evaluated for up to 48 hours in which the injectable hydrogels showed higher swelling behavior than the solid hydrogels, **Figure 72C, and 72D**. Additionally, the injectable hydrogels exhibited a two-fold swifter swelling capacity reaching a plateau after 4 h compared to the solid hydrogels that required 8 h. The values are shown in **Table 3**. The swelling capacity of the control hydrogels and solid hybrid hydrogels was studied for up to 48h. However, the structural integrity of the injectable hydrogels was compromised after 24 h, and swelling data were collected within that time frame. The control hydrogels, H1k and H2k, elucidated lower swelling capacity than hybrid hydrogels. This could be reasoned to the formation of more compact polymer networks based on ionic crosslinks between the available carboxylate groups of GG-DA and the divalent Ca^{2+}. For the hybrid systems, hydrogels with the lowest percentages of both GG-DA and TMP-G2-alanine, called H2, noted the highest swelling percentage (after 24h, ~1267% for the solid and ~1768% for the injectable). This can be compared to the compared to H3 reaching ~1145% for the solid and ~1438% for the injectable hydrogels after 24h. With over 10-fold water swelling capacity these hydrogels have the potential to scavenge skin wound exudate that contains nutrients

necessary for bacterial growth and lead to skin maceration.[324] **Figure 72B** shows the SEM image of the section of lyophilized $H1_{sol}$. The image of the dehydrated hydrogel shows a spongy-like porous network. This typical structure could promote swelling, interactions with biological fluids, and gaseous exchanges.

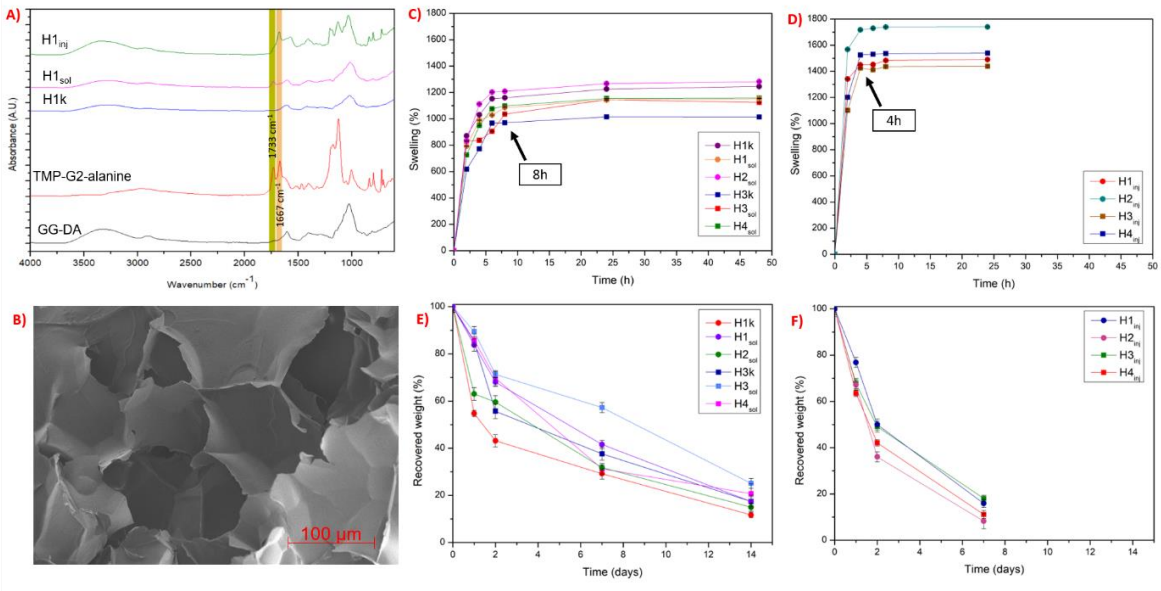

Figure 72. Characterization of the hybrid hydrogels. (**A**) FT-IR of representative solid, injectable, and control hydrogels, TMP-G2-alanine, and GG-DA. (**B**) SEM image of the $H1_{sol}$ as a representative sample. Swelling behavior of solid, control (**C**), and injectable (**D**) hydrogels. Hydrolytic degradation of solid, control (**E**), and injectable (**F**) hydrogels.

In **Figure 73** there are also the SEM analyses of the hydrogels $H1_{inj}$, and H1k, which have similar structures to the previous hydrogel. The degradation properties of wound dressing materials are important as it is essential to meet the skin's requirements in remodeling and inducing morphogenesis to form new tissues.[348] A degradation study was carried out both in terms of recovered weight% compared to the original weight and also in terms of viscoelastic

properties over time. Amplitude and frequency sweep rheological degradation study was performed in phosphate-buffered saline (PBS pH 7.4) at 37 ° C.

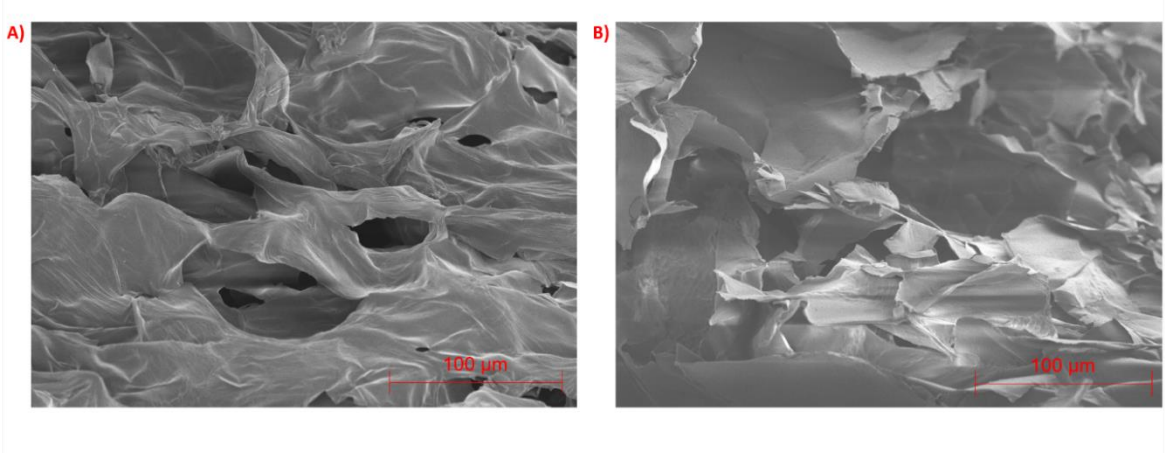

Figure 73. SEM images of the $H1_{inj}$ (**A**), and H1k (**B**) hydrogels as representative samples.

The injectable hydrogels degraded faster, reaching less than 50% of their original weight within 2 days (**Figure 72F**), than the solid hydrogels that required 7 days for 50% loss of their original weight (**Figure 72E**). In general, all solid and control hydrogels could be recovered for up to 14 days, while injectable hydrogels were completely degraded. The solid hydrogel with the highest polymer and dendrimer content, $H3_{sol}$, showed greater degradation resistance than all hybrid hydrogels with ~60% weight recovered after 7 days (**Table 3**). From the amplitude sweep rheograms, after each time of incubation, it can be seen that the Storage modulus (G') and the Loss modulus (G'') decrease, confirming that the networks undergo degradation as shown in **Figure 74-75**.

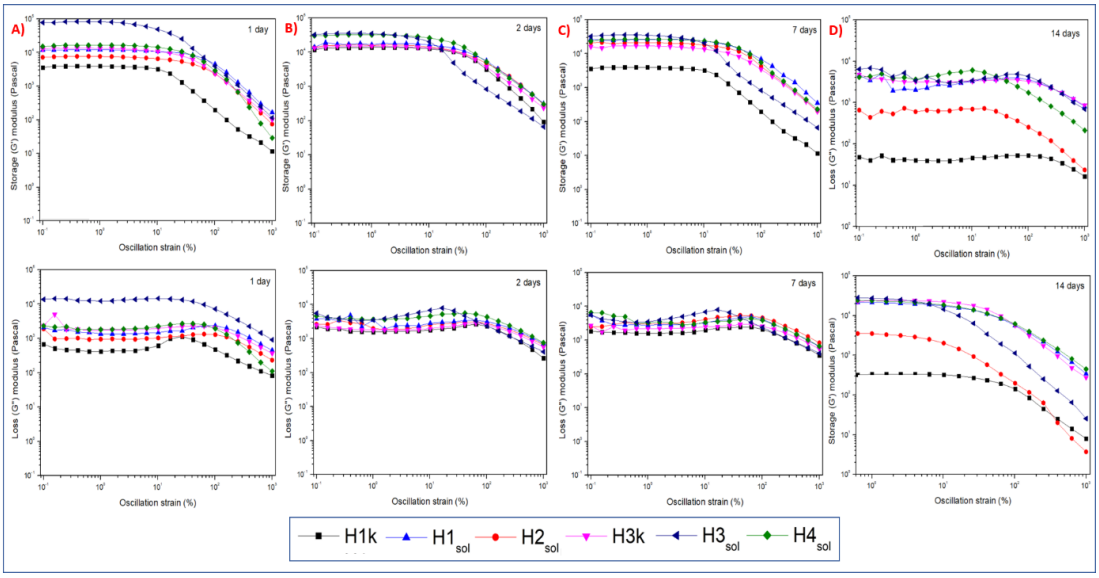

Figure 74. Amplitude sweep analyses of solid hybrid hydrogel at 1 day (**A**), 2 days (**B**), 7 days (**C**), and 14 days (**D**) of incubation in PBS (pH 7.4) at 37°C.

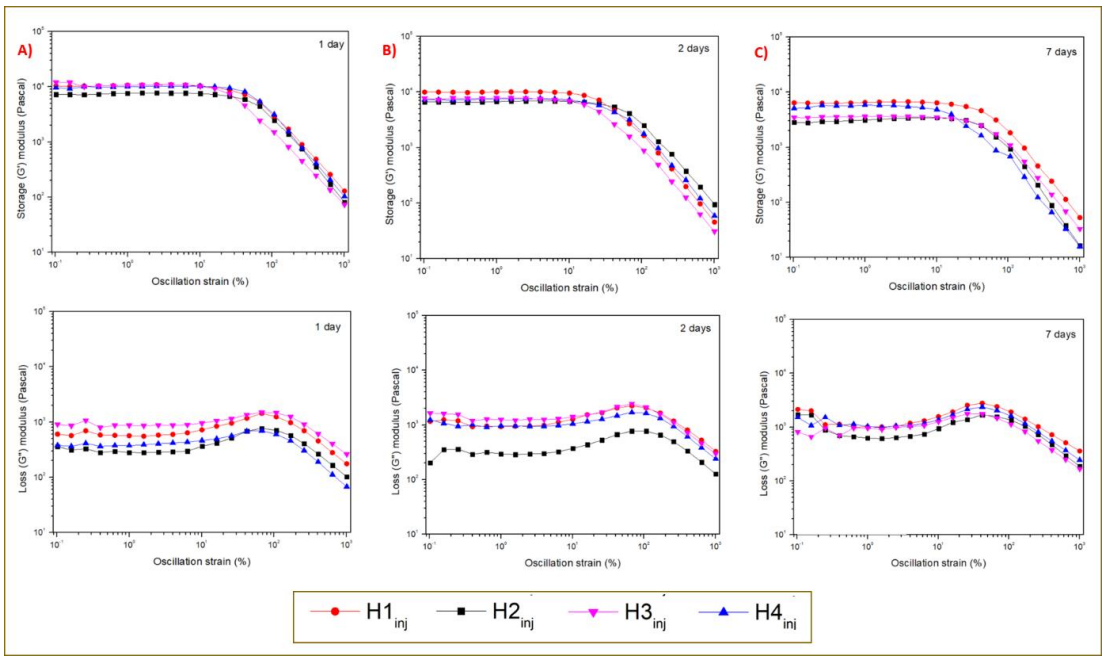

Figure 75. Amplitude sweep analyses of injectable hybrid hydrogel at 1 day (**A**), 2 days (**B**), and 7 days (**C**) of incubation in PBS (pH 7.4) at 37°C.

Furthermore, from frequency sweep rheograms, the decrease in the elastic behavior is probably attributable not only to the degradation and release of the dendrimer but also, in

the solid hydrogels, to the possible depletion of calcium from the three-dimensional structure (**Figure 76-77**).

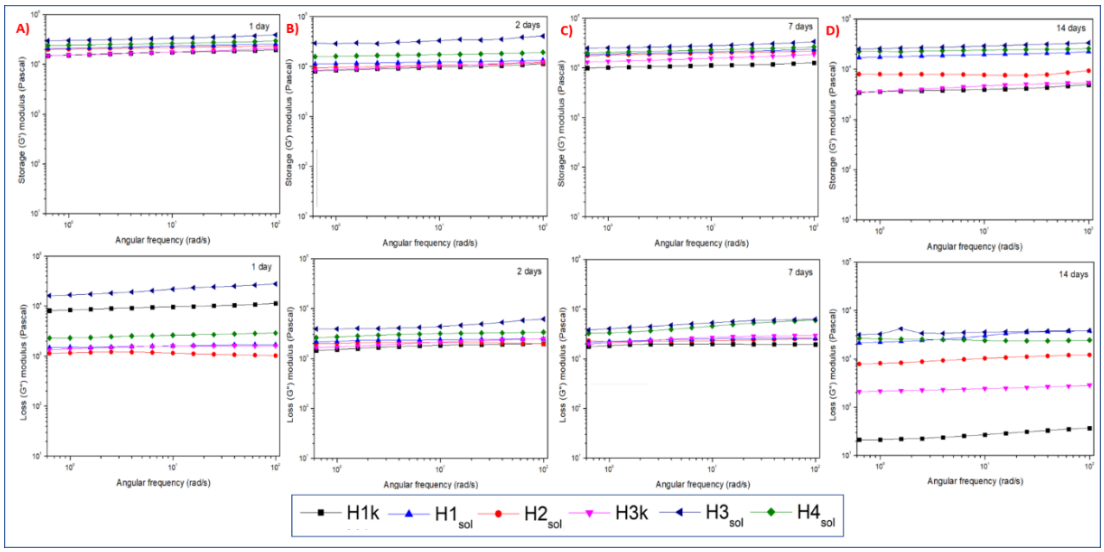

Figure 76. Frequency sweep analyses of solid hybrid hydrogel at 1 day (**A**), 2 days (**B**), 7 days (**C**), and 14 days (**D**) of incubation in PBS (pH 7.4) at 37°C.

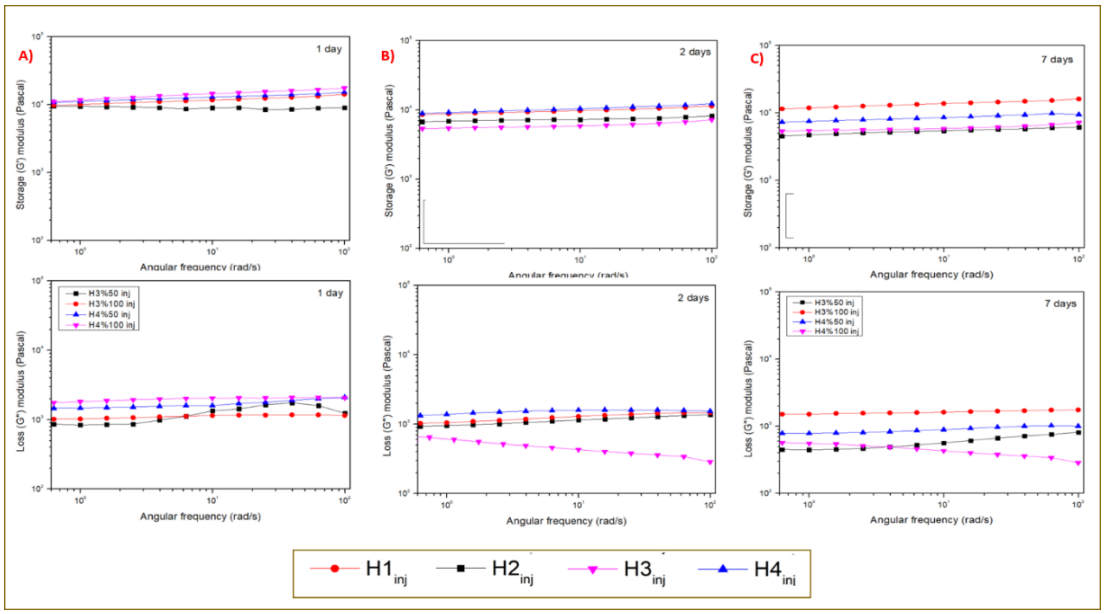

Figure 77. Frequency sweep analyses of the injectable hybrid hydrogel at 1 day (**A**), 2 days (**B**), and 7 days (**C**) of incubation in PBS (pH 7.4) at 37°C.

Overall, the collected data indicates that the hybrid hydrogels possess adjustable properties and by varying the concentrations of the two biomaterials different degradation rates are obtained. Hydrogels produced using these two materials could potentially be administered to treat infection in the first few days after injury to allow the healing process to resume.

A leaching-out study of the dendrimer and both the hybrid hydrogels were conducted in PBS solution (pH 7.4) at 37 °C. As shown in **Figure 78**, the MALDI-TOF spectrum of pure TMP-G2-alanine dendrimer with a single peak at 2058 m/z was compared with the spectra of the hybrid solid (**Figure 78A**) and injectable hydrogels (**Figure 78B**) at different time point. Multiple peaks at lower m/z were detected and that could be correlated to fragmented dendrimers that diffused out from the hydrogels. This suggests that the ionically integrated dendrimers undergo hydrolysis, through de-esterification of the peripheral beta-alanine groups, that in turn facilitate their detachment from the networks prior to release in PBS solution. Based on the analysis of MALDI peaks, the dendrimer lost its monodisperse integrity by fast losing of the peripheral β-alanines.[298] **Figure 78C** showed part of the representative degradation products, with the increase of time, Bis-MPA also de-attached from the dendrimers. Compared with $H3_{sol}$, degradation products from $H3_{inj}$ showed lower molecular weights and more loss of Bis-MPA, suggesting that the dendrimers are more stable and protected by $H3_{sol}$ hydrogels. No significant structural or leaching differences were detected in the spectra after 4 hours for the $H3_{sol}$ hydrogel. A similar observation was found for $H3_{inj}$, which shows the presence of peaks correlated to dendrimer fragments after 4, 6, and 8 hours. In contrast to the solid hybrid hydrogels, the dendrimers leached from the $H3_{inj}$ undergo accelerated degradation including the decomposition of the dendritic skeleton.

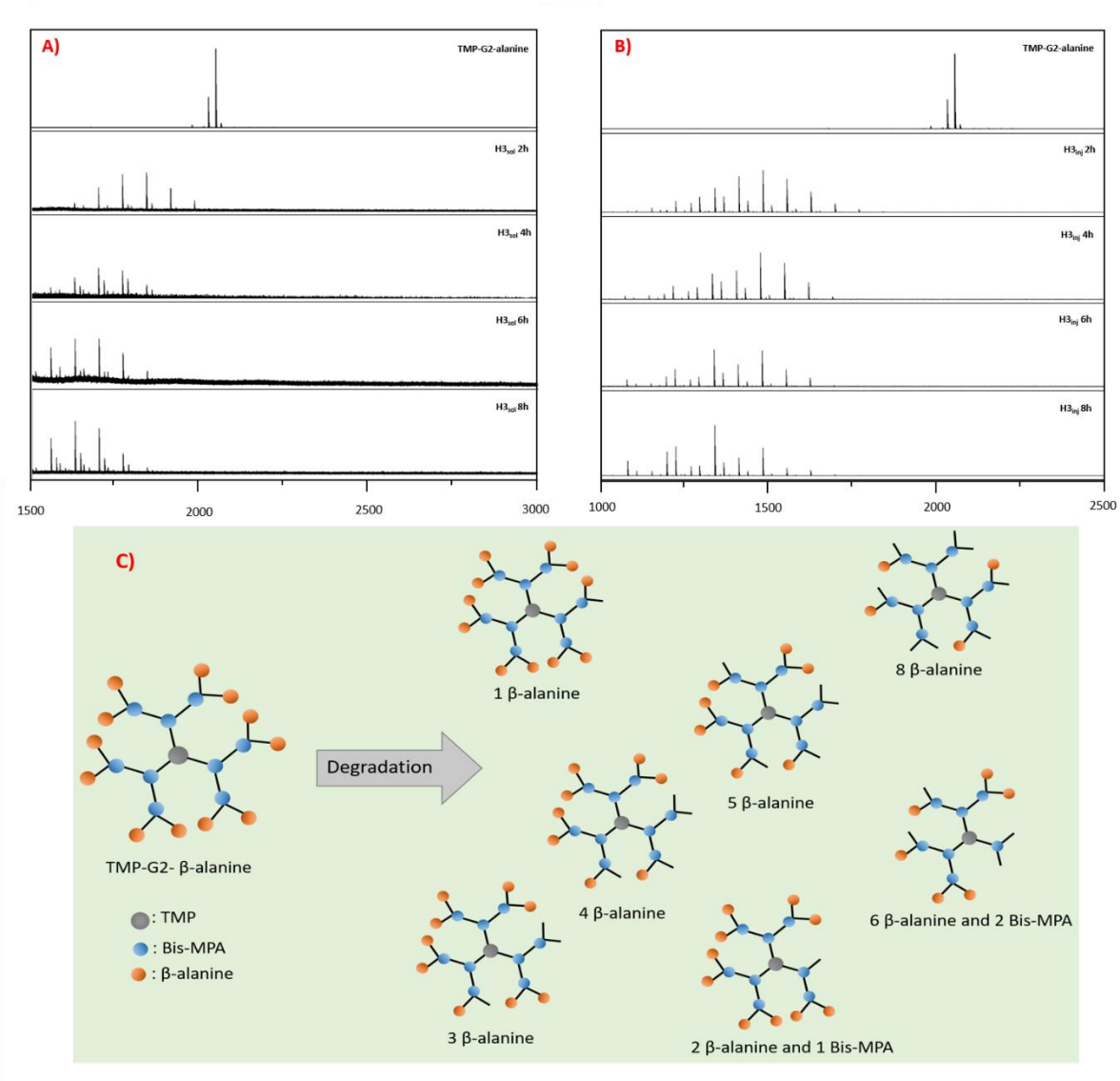

Figure 78. MALDI-TOF spectra of hybrid hydrogels. Representative spectra of leaching of TMP-G2-alanine from H3 solid hydrogel (**A**) and injectable hydrogel (**B**) after 2, 4, 6, and 8 hours in PBS at 37°C, (**C**) part of the degradation products based on the MALDI-TOF spectra.

These tunable hydrogels exhibited good viscoelastic strength and modulus comparable to human soft tissues.[349] The rheological properties of all hybrid hydrogels were thoroughly investigated by frequency sweep analyses. **Figure 79E-F** shows the storage modulus (G') and the loss modulus (G'') of the solid hydrogels, while **Figure 79G-H** shows the moduli of

the injectable hydrogels as a function of frequency. All hybrid and control hydrogels displayed G' higher than G'' in the studied frequency range, indicating that the hydrogels behaved as viscoelastic solids. The moduli of the solid hydrogels, $H3_{sol}$ (G' ~ 21.0 kPa and G'' ~ 20.8 kPa) and $H1_{sol}$ (G' ~ 5.6 kPa and G'' ~ 2.4 kPa) were noted higher than the control hydrogels, H3k (G' ~ 9.0 kPa and G'' ~ 6.4 kPa), and H1k (G' ~ 3.7 kPa and G'' ~ 3.1 kPa). Concerning the same mass ratio between GG-DA and TMP-G2-alanine, the solid hydrogels exhibited higher G' and G'' than their injectable counterpart. For example, $H3_{sol}$ G' ~ 21.0 kPa and G'' ~20.8 kPa and $H3_{inj}$ G' ~ 2.1 kPa and G'' ~0.3 kPa (all other data are included in **Table 3**).

Table 3. Summary data of swelling, degradation, and rheological of hydrogels.

			Amplitude sweep			Frequency sweep		Flow sweep	Recovery time			
Sample	**Swelling plateau (%)**	**Recovered weight (%) after 7 days**	**G' (kPa)**	**G'' (kPa)**	**Cross-point strain %**	**G' (kPa)**	**G'' (kPa)**	**Viscosity (Pa*s)**	**G' (kPa) (1% strain)**	**G'' (kPa) (1% strain)**	**G' (kPa) (500% strain)**	**G'' (kPa) (500% strain)**
H1k	1160	30	9.9	3.8	19.5	3.7	3.1	-	-	-	-	-
H3k	970	35	51.4	10.8	12.6	9.0	6.4	-	-	-	-	-
$H1_{sol}$	1085	45	12.2	9,0	4.4	5.6	2.4	-	-	-	-	-
$H2_{sol}$	1210	32	3.8	2.3	19.5	3.8	3.2	-	-	-	-	-
$H3_{sol}$	1035	60	139.9	43.8	4.4	21.0	20.8	-	-	-	-	-
$H4_{sol}$	1100	30	10.9	7.4	19.5	4.8	4.2	-	-	-	-	-
$H1_{inj}$	1450	15	0.3	0.1	144.3	0.4	0.06	1825	0.4	0.06	0.02	0.03
$H2_{inj}$	1720	8	0.1	0.03	144.3	0.5	0.03	545	0.2	0.05	0.001	0.009
$H3_{inj}$	1420	18	3.0	0.5	144.3	2.1	0.3	1965	1.6	0.3	0.01	0.06
$H4_{inj}$	1525	10	0.2	0.03	216.8	0.6	0.07	865	0.5	0.1	0.009	0.01

The increased moduli are reflected by stronger intermolecular interactions in which the TMP-G2-alanine dendrimer enables the production of more tightly crosslinked three-dimensional networks at the same concentration of GG-DA. It is also important to stark

contrast in moduli between the hybrid hydrogels. In this case, an almost one order of magnitude in moduli difference between the solid hydrogel ($H3_{sol}$ with G' ~21.0 kPa) and the injectable hydrogel ($H3_{inj}$ with G' ~ 0.5 kPa). Regarding injectable hydrogels, the overall reduction in moduli is correlated to the crosslinking chemistry where quinone groups could form imine bonds, amine bonds, as well as physical interactions. The latter is intriguing mode-of-crosslinking that provided the hydrogels with shear-thinning and self-healing behavior. When a self-healing hydrogel is applied to the wound site, it will be able to withstand the external force due to displacement.[350] Preliminary amplitude sweep analyses of all hybrid hydrogels showed that initially, G' was higher than G''. As shown in **Figure 79A-D**, at the LVE (Linear Viscoelastic Region), G' and G'' had a constant value, while a decrease was observed as the strain increased. A cross-point between G' and G'' crossed was noted with increased strain, which indicates the critical point near which the hydrogel is in a state between solid and fluid. For the solid hydrogels, it is equal to a strain < 10^2 %, while for all injectable hydrogels, it is > 10^2 %. When the strain exceeded the critical strain point, G' dropped dramatically reaching values below G'' in which the hydrogel networks collapsed [351]. Visual examination after the analysis revealed that the solid hydrogels were fragmented and broken while the injectable hydrogels were found intact and in a flow state. The latter is in fact due to the self-healing behavior as confirmed by the analysis of recovery times, **Figure 80C**.

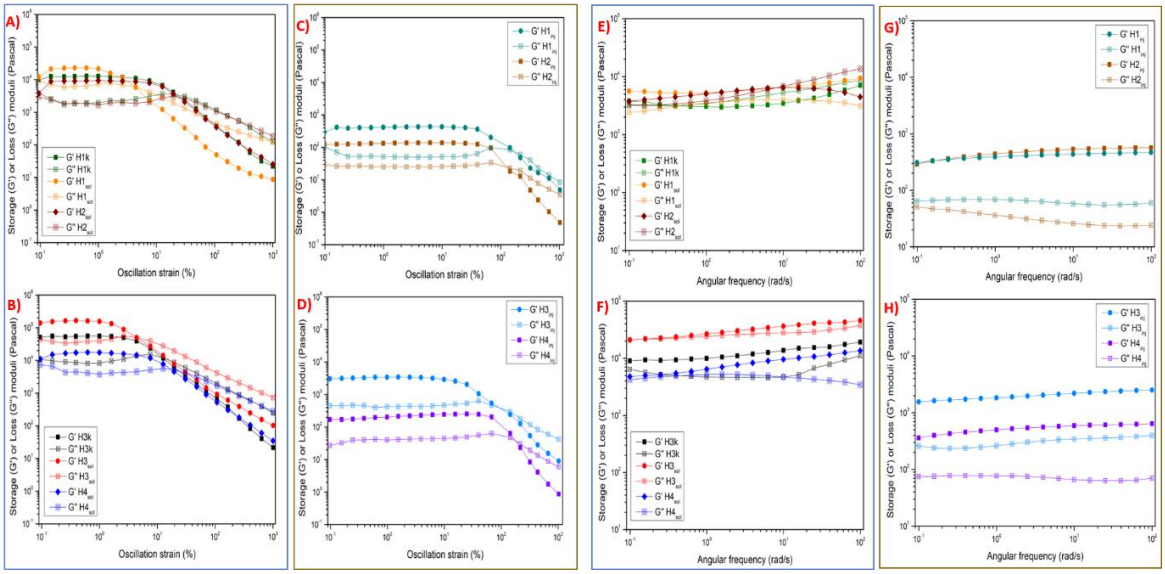

Figure 79. Amplitude sweep analysis of hybrid hydrogels. G' and G'' moduli of control, solid (**A, B**) and injectable (**C, D**) hydrogels. Frequency sweep analysis of hybrid hydrogels. G' and G'' moduli of control, solid (**E, F**) and injectable (**G, H**) hydrogels.

Furthermore, the hydrogels possessed shear-thinning properties which is a critical property for use as injectable solutions for topical application, as shown in **Figure 80A**. To corroborate the results of the amplitude sweep analyses, recovery time measurements were further performed to test the rheology recovery behavior of the injectable hydrogels. The recovery and collapse behaviors of the hydrogels could be alternately looped, demonstrating a rapid and efficient self-healing ability. Indeed, after successive cycles of 100 s each, all injectable hydrogels recovered to their original values. The oscillatory shear strain was changed from 1% to 500% and was maintained for 100 s at each cycle. G' dropped from high values ~230-1678 Pa ($H2_{inj}$-$H3_{inj}$) to low values ~2-23 Pa ($H2_{inj}$-$H3_{inj}$) and subsequently recovered to their original high values. As seen in **Figure 80C,** the same self-healing behavior was observed for G'', changing from high values ~49-309 Pa ($H2_{inj}$-$H3_{inj}$) to low

values ~8-66 Pa ($H2_{inj}$-$H3_{inj}$). These results suggest that all injectable hydrogels, independent of moduli, show rapid and almost full recovery after oscillatory shear deformation (**Figure 80D**). The self-healing behavior is also shown in **Figure 80B**, where it is noted that two pieces of the same hydrogel (one colored with Rhodamine B and one uncolored) if placed in contact and reform as a single piece.

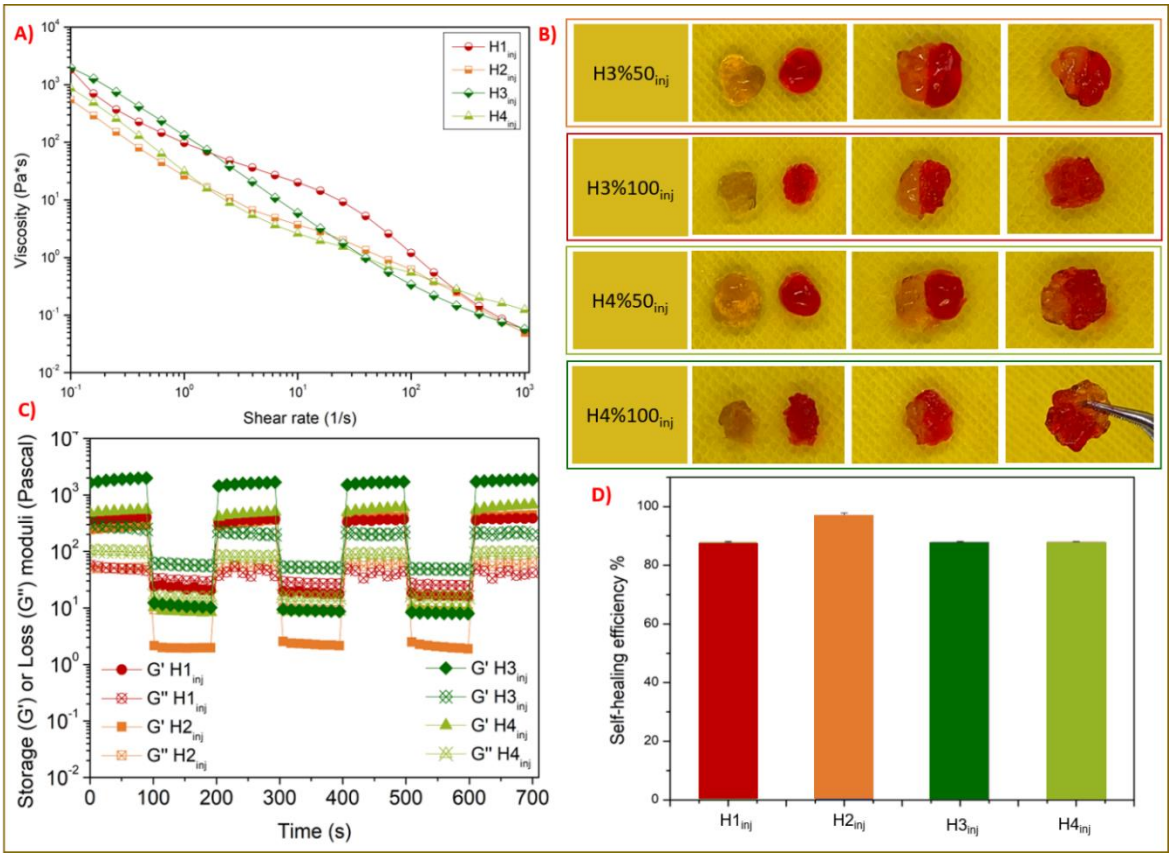

Figure 80. Shear-thinning and self-healing properties of the injectable hydrogels. Flow sweep analysis (**A**), macroscopic behavior of self-healing (**B**), recovery time analysis (**C**), and self-healing efficiency after seven cycles of recovery time analysis (**D**) of injectable hybrid hydrogels.

Obtaining a biomaterial with intrinsic tissue adhesive properties is advantageous as it would ensure permanence on the wound bed without it being washed away by biological fluids,

thus ensuring minimal compliance.[352] Hydrogel H1k, $H1_{sol,}$ and $H1_{inj}$ exemplify the adhesion to a wide variety of substrates. **Figure 81**. All hybrid hydrogels produced showed a similar ability to adhere to glass, plastic, metal, aluminum foil, wood and raw pig skin. The adhesive property of the hydrogels is probably due to the presence of cationic amino groups as well as catechol groups, as confirmed by the adhesion of the control hydrogels.[353] This confirms the uniqueness of the hybrids hydrogels as adhesive networks with potential use as coatings or implantable materials that could be applied directly into the wound without the need for additional fixation or other supports.

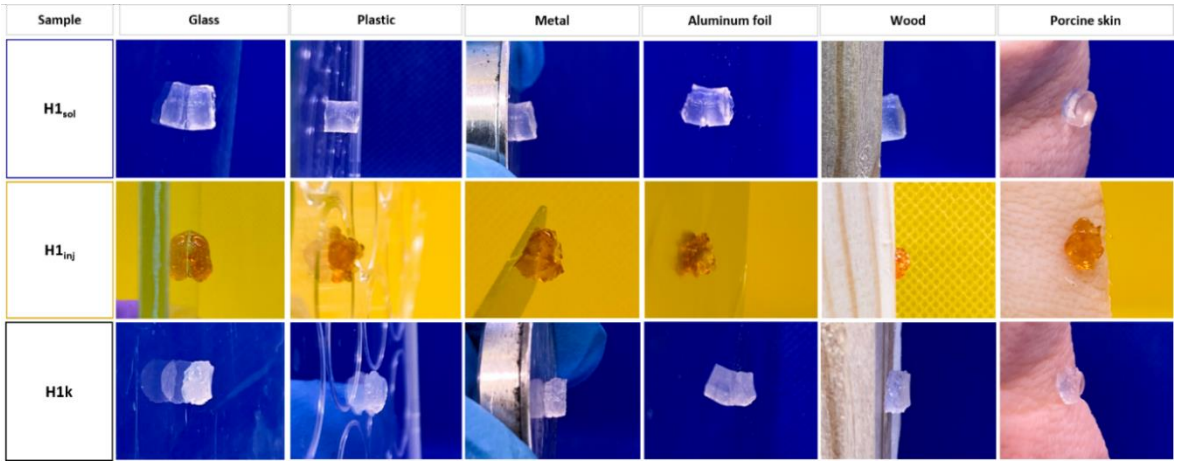

Figure 81. The adhesiveness of the hybrid and control hydrogels on different substrates.

3.4.2 Cytocompatibility of the hybrid hydrogels

Producing a suitable microenvironment in the form of cytocompatible hydrogels where cells can survive and grow for wound healing is one of the most important factors. Consequently, a study was performed on three different cell lines: Fibroblasts (HDFs), Keratinocytes (HaCaT), and macrophages (RAW 264.7). These cells are known to play important roles in normal skin wound healing and several studies detail their involvement in cellular therapy processes. HDFs are cells that directly deposit extracellular matrix proteins during the

healing process,[354,355] while HaCaT have the ability to form a large sheet of epidermis that improves wound closure and epithelialization.[354,356] Inflammatory signals trigger the proliferation and maturation of these two cell types, which are essential for wound healing.[357] Macrophages and monocytes (RAW 264.7) improve the healing rate of wounds.[358] A cytocompatibility test was performed by applying all hydrogels in direct contact with the three aforementioned cell lines (**Figure 82**).

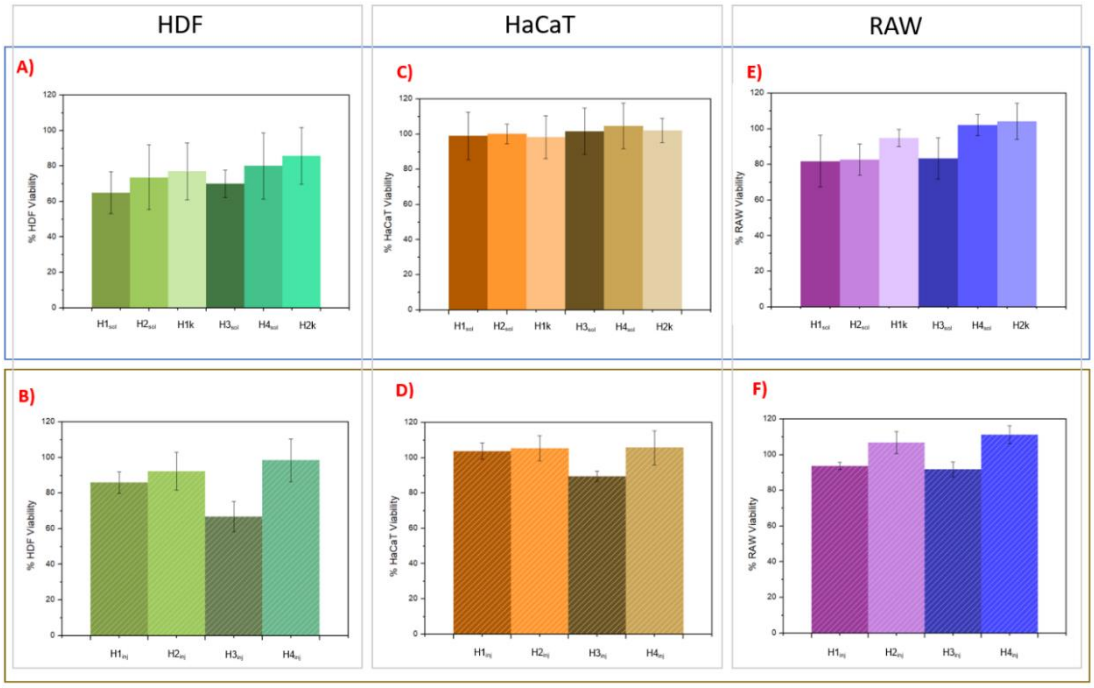

Figure 82. The cytocompatibility of the solid (**A**) and injectable (**B**) hybrid hydrogels tested with HDF cells; solid (**C**) and injectable (**D**) hybrid hydrogels tested with HaCaT cells, and solid (**E**) and injectable (**F**) hybrid hydrogels tested with RAW cells. All data are shown as a mean value ± SD (*n* =3).

For the control hydrogels without the presence of dendrimers, H1k, and H3k, the cytocompatibility was found good. In the case of the hybrid networks, the solid hydrogels

indicated good cytocompatibility in which $H4_{sol}$ and $H2_{sol}$ with a lower concentration of dendrimers showed overall higher cell viability compared to hydrogels with a higher concentration of dendrimers, $H3_{sol}$ and $H1_{sol}$. Similarly, for the injectable hydrogels, $H4_{inj}$ and $H2_{inj}$ exhibited overall higher cell viability than the hydrogels with increased concentration of dendrimers, $H3_{inj}$ and $H1_{inj}$. It should also be noted that the injectable hydrogels have slightly better cytocompatibility profiles than their solid counterpart. This is probably a production-related effect as the solid hydrogels required a pH increase of the precursor GG-DA > 8.5, to oxidize the catechol groups, before adding the TMP-G2-alanine. The presence of quinone in the hybrid hydrogels could promote the cells to withstand oxidative stress and thereof affect cell growth.[350] For both solid and injectable hydrogels, incubation with RAW and HaCaT cells showed better viability than HDF. For example, cell viability of $H4_{sol}$ in HDFs was 80%, HaCaTs of 105%, and RAW 264.7 of 102%; while with $H4_{inj}$ the HDF had a viability of 98%, the HaCaT of 106% and the RAW of 111%. These findings indicate that both solid and injectable H4 hydrogels are safe to use as they enhance cell proliferation of both RAW 264.7 cells and HaCaT cells and allow a good HDF viability. Neither solid nor injectable hydrogels possess cytotoxic effects towards HaCaTs, with viability around or greater than 100% in all cases, which formed a monolayer of cells after 24h co-incubation with hydrogels. Collectively, these hybrid hydrogels show great promise as skin wound dressings in which the cells maintain normal cell morphology, comparable to the cell-alone control, **Figure 83-85**.

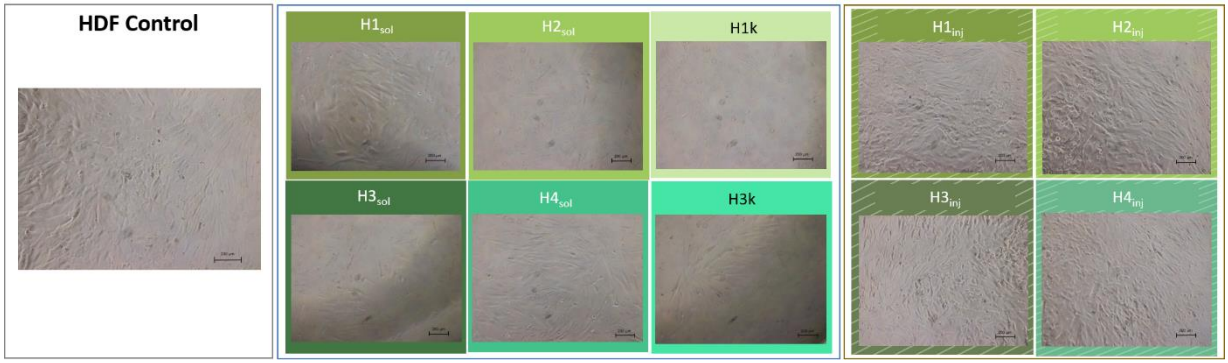

Figure 83. Cytocompatibility test. Images of HDF cells after 24 hours of incubation with all hybrid hydrogels.

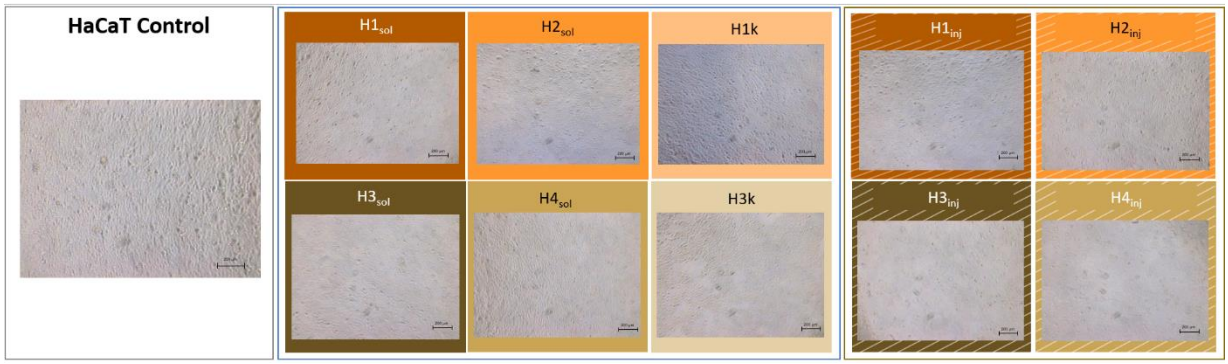

Figure 84. Cytocompatibility test. Images of HaCaT cells after 24 hours of incubation with all hybrid hydrogels.

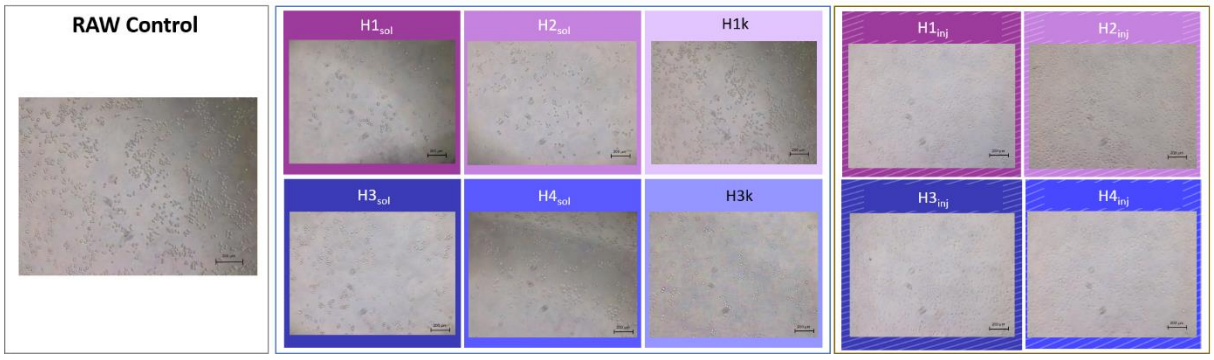

Figure 85. Cytocompatibility test. Images of RAW 264.7 cells after 24 hours of incubation with all hybrid hydrogels.

3.4.3 Antimicrobial studies of the hybrid hydrogels

The antibacterial property of the cationic dendrimer, TMP-G2-alanine, was investigated using MIC and MBC assays. Two types of bacteria were used in the study, *S. aureus* 2569 (Gram-positive) and *E. coli* 178 (Gram-negative).[359] The MIC and MBC values for the cationic dendrimer showed good antibacterial properties against both bacteria, **Table 4**. The results also detailed that higher dendrimer concentrations were required to kill *S. aureus* than *E. coli*, suggesting greater efficiency against Gram- than Gram+ strains. The MIC and MBC values of GG-DA are above 2 mg/mL, indicating that the pure polymer has no obvious antibacterial properties.

Table 4. MIC and MBC Values of TMP-G2-alanine and GG-DA.

Measurement	Sample	E.coli 178			S.aureus 2569		
		µg/mL	µM	NH_3^+ (µM)	µg/mL	µM	NH_3^+ (µM)
MIC value	TMP-G2-alanine	62,5	18,4	221	250	73,6	882
	GG-DA	>2000			>2000		
MBC value	TMP-G2-alanine	125	36,8	441	500	147,1	1765
	GG-DA	>2000			>2000		

All hybrid solid hydrogels exhibited antibacterial properties with inhibition zones visible on the agar plate against both *E. coli* 178 and *S. aureus* 2569, as shown in **Figure 86**.

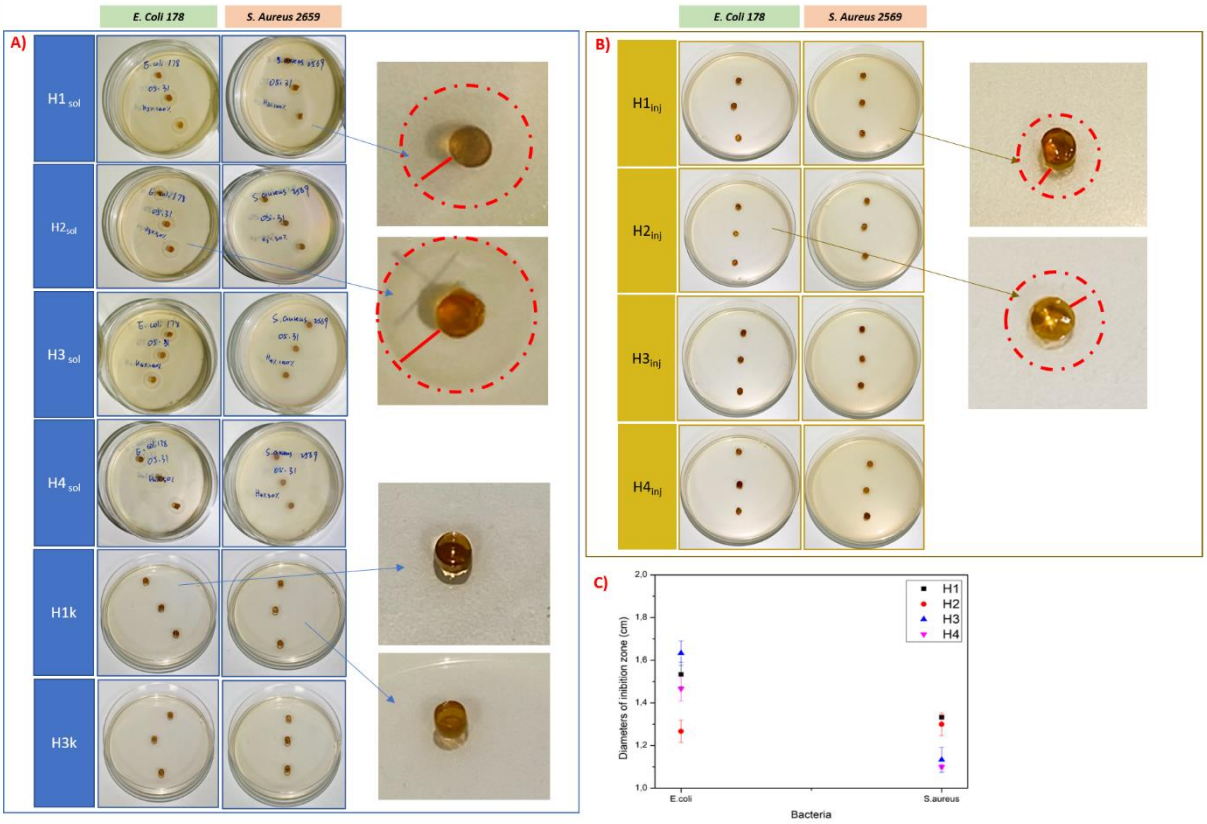

Figure 86. Disk diffusion test of control, solid (**A**), and injectable (**B**) hybrid hydrogels. Average diameters of inhibition zones of the hybrid solid hydrogels against *E. coli* and *S. aureus* (**C**).

The antimicrobial test in bacterial solution (10^5 CFU/mL) with the two bacterial strains demonstrated that both solid and injectable hydrogels possess good activity against both *S. aureus* and *E. coli*. The average diameters of the inhibition zones (**Figure 86**) were measured and showed that they were larger towards *E. coli*, indicating better antibacterial activity of the hydrogels against this strain, compared to *S. aureus*. In fact, for this other bacterial strain, the average diameter of the inhibition zones was lower for all the tested hydrogels. As expected, hydrogels containing higher amounts of dendrimer showed larger initiation zones. For *E. coli* the average diameter for $H3_{sol}$ was 1.65 cm, and for $H1_{sol}$ was 1.53 cm. The lower the concentration of dendrimer, the more the halo shrinks, in fact, the average diameter was

1.47 cm for $H4_{sol}$, while for $H2_{sol}$ was 1.27 cm. This changed when hydrogels were tested with *S. aureus* instead; in this case, the inhibition zones are comparable respectively for the hydrogels $H3_{sol}$ and $H4_{sol}$ (1.13 cm and 1.1 cm) and $H1_{sol}$ and $H2_{sol}$ (1.33 and 1.3). The control hydrogels didn't show inhibition zones. Even for the injectable hydrogels, it was impossible to observe the inhibition zones, probably because the dendrimer was more firmly bound to the polymer in the meshes of the three-dimensional network. In particular, solid hydrogels possessed a great sterilizing mode-of-action with 100% killing for both *S. aureus* and *E. coli* already after 4 h incubation. On the other hand, the injectable hydrogels showed a decreasing antibacterial activity over time (**Figure 87**). A plausible explanation is related to the dendrimers that are covalently bound within the networks which inhibit their leaching out compared with the solid hydrogels. This was confirmed by the inhibition zones and increased degradation of the dendrimer as corroborated by the leaching analyses, **Figure 78**. Similar to the dendrimer, the hydrogels with increased dendrimer concentration resulted in higher antibacterial activity. Hydrogels with higher concentrations of initial dendrimer showed higher killing efficiency of bacteria after 4 h. $H1_{inj}$ showed 100% of the killing of *E. coli* and $H3_{inj}$ of 98%; while $H1_{inj}$ killed 90% and $H3_{inj}$ 94% of *S. aureus*. The hydrogels with lower initial concentrations of dendrimer instead showed a lower killing efficiency of both bacterial strains after 4 h. $H2_{inj}$ showed a killing % of *E. coli* of 93% and $H4_{inj}$ of 96%; while $H2_{inj}$ killed 82% and $H4_{inj}$ 81% of *S. aureus*.

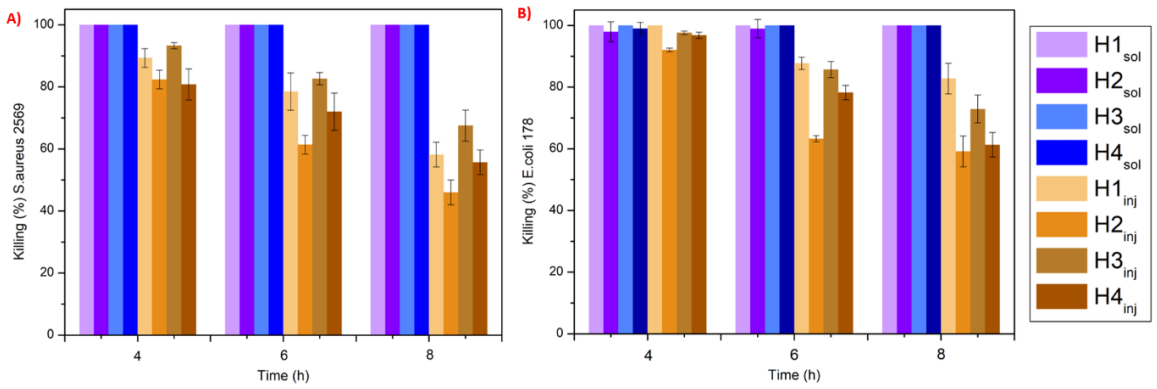

Figure 87. Antimicrobial activity of hybrid hydrogels against *S. aureus* 2569 (**A**) and *E. coli* 178 (**B**). All data are shown as a mean value ± SD (n =3).

3.5. In situ synthesis of silver nanoparticles and development of nano/micro-composite injectable hydrogel with antimicrobial activity

3.5.1 *In situ* synthesis and characterization of AgNPs

Catechol pendant moieties were inserted into the GG backbone by the reaction of dopamine with activated polysaccharide hydroxyl groups (reaction mechanism and characterization described in **Figure 68**, as reported.[360] GG-DA was used as a reducing and/or stabilizing agent for AgNPs synthesized *in situ*. The silver reduction process was conducted through two different approaches in aqueous conditions both in line with green synthesis fundamentals without using environmentally toxic reducing agents (Kajani et al. 2014). GG has already been used by Dhar and collaborators for the *in situ* production of AgNPs using the polysaccharide as the reducing and capping agent. In this work, in order to reduce silver ions, it was necessary to bring the pH of the polymeric dispersion containing the silver salt precursor to 11 and to keep the reaction at 95° C for 4 hours. These reaction conditions are quite harsh and can lead to an alkaline degradation of the polysaccharide.[229] Dopamine catechol groups can reduce Ag ions for the *in situ* formation of AgNPs in milder conditions. In this work, low molecular weight GG (59 kDa ± 4.3) with pendant dopamine groups enabled the complete reduction of Ag^{+} at pH 6 by exploiting the catechol oxidation in aqueous solution. The reducing and stabilizing effect of GG and GG-DA on the *in situ* synthesis of AgNPs was compared (**Figure 88**).

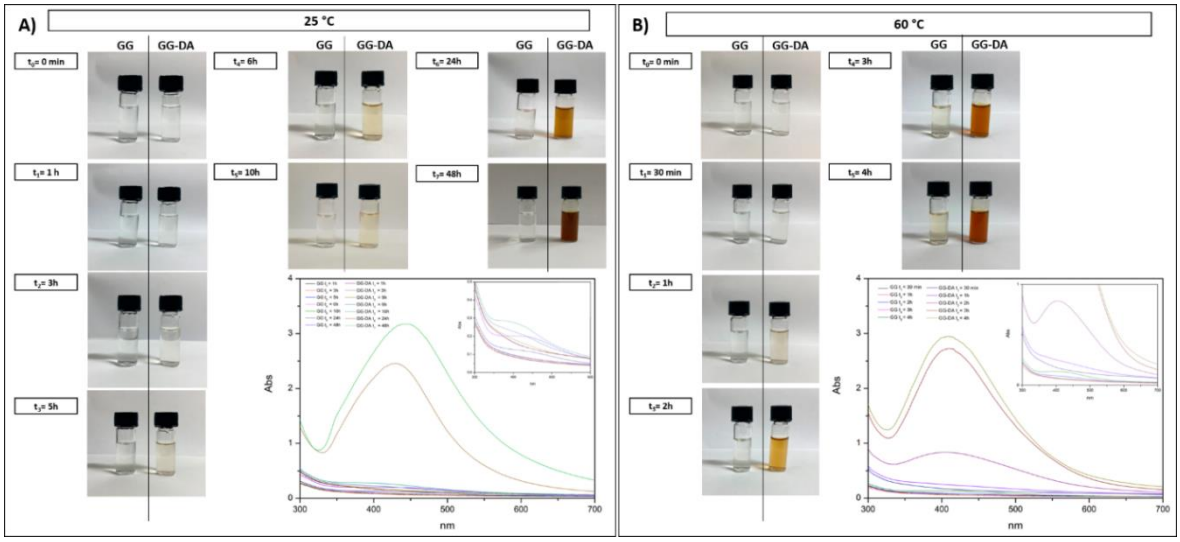

Figure 88. Comparative study of *in situ* green synthesis of AgNPs at 25 °C (**A**) and 60 °C (**B**).

GG-DA showed a faster color change, already after 5 h at 25 °C, as shown in **Figure 88A**. GG did not induce any significant change. This color change may be due to either dopamine oxidation or AgNPs formation. After 24 hours of incubation, the dispersion became dark brown. UV-Vis spectroscopic analysis confirmed the production of AgNPs with the appearance of an absorption peak at around 430-440 nm, a characteristic peak of surface plasmon resonance, which increases with increasing incubation time, indicating the *in situ* production of AgNPs. Temperature also played a role in the reaction, as higher temperatures (60°C) accelerate AgNP formation in both GG and GG-DA dispersions (**Figure 88B**), although again the presence of dopamine leads to a faster reaction. The UV-Vis spectrum of the GG-DA dispersion showed an absorption peak at around 410 nm after 2 hours of incubation. Similarly, a slight color change can be observed in the GG dispersion after 4 hours of incubation. In order to further accelerate the production of AgNPs, the reaction was conducted at higher temperatures (80 °C), and color change of the dispersion was noted upon the addition of $AgNO_3$ after 30 minutes of incubation (**Figure 89B, T-method**) when the

intensity of the orange color of the dispersion turned to light brown. The UV spectrum in **Figure 89C** shows the characteristic absorption peak at 410 nm. There was no significant color change in the GG/$AgNO_3$ dispersion after 30 minutes at the same temperature. From SEM images, it was possible to observe AgNPs as luminescent nanostructures within the lyophilized dispersion (**Figure 89D**). Changing the temperature of the dispersion is, therefore an advantageous since it allows to obtain the same results in much shorter times. It is interesting to notice that by increasing the reaction temperature from 25°C to 60/80°C, the absorbance peak typical of the plasmon resonance shifts toward lower wavelengths (430 nm to 410 nm). This shift could indicate the formation of smaller nanoparticles; in fact, the size of AgNPs is inversely proportional to the reduction rate of the Ag^+ ion.[216] Another green method is the UV radiation-induced synthesis of AgNPs, due to its simplicity, easy process control, temperature-independent reduction, homogeneous nucleation of nanoparticles, and no need to add reducing agents, so this method is also harmless and environmentally friendly. Furthermore, this method provides fully reduced metal nanoparticles, a highly pure and highly stable state. The UV irradiation method for the preparation of metal nanoparticles is of increasing interest and has shown enormous potential in both morphological control and particle size distribution.[362] It is however necessary, during the synthesis of AgNPs, to find a strategy to protect them from aggregation because when nanoparticles are dispersed in a solvent, Van der Waals forces and Brownian motion have important effects on their stability.[363] The combination of these forces results in the aggregation of nanoparticles. To improve the stability of nanoparticle dispersion in aqueous media, polymers or other modifiers such as surfactants play a fundamental role to generate repulsion between the nanoparticles and stabilize them.[364] In this case, catechol groups can contribute to stabilize the produced AgNPs coordination bonds. Based on what has been discussed, it was therefore

chosen to irradiate the dispersion of GG-DA/$AgNO_3$ with UV radiation (365 nm) for 30 minutes. **Figure 89B-C** shows the images and UV/Vis spectra of the reaction mixtures. The characteristic peak of AgNPs appears also in this case at 410 nm, which confirms the occurred in situ synthesis of the metal nanoparticles.

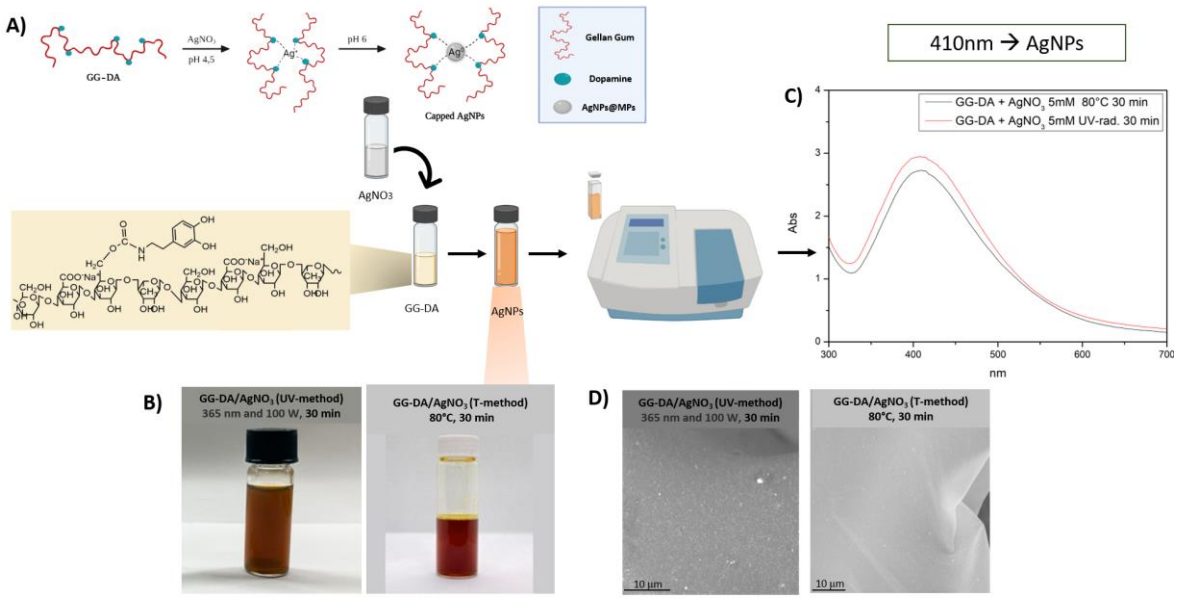

Figure 89. Scheme of *in situ* green synthesis of AgNPs (**A**); images of in situ synthesis of AgNPs (**B**); UV/Vis spectra of GG-DA/$AgNO_3$ dispersion (peak of surface plasmon resonance of AgNPs at 410nm) obtained with different synthetic approach (**C**); SEM analyses of the lyophilized dispersions (**D**).

3.4.2 Production and characterization of MPs and nano-into-micro AgNPs@MPs

The GG-DA/AgNP dispersions were converted into powder by spray drying technique thus obtaining nano-into-micro systems,[365] in which the AgNPs were loaded into polymeric microparticles, called AgNPs@MPs (T) and AgNPs@MPs (UV) (in which the terms T and UV in brackets indicate the method used for AgNPs synthesis). In this case, the use of low molecular weight GG as a starting molecule to produce GG-DA derivative is of crucial

importance to obtain a dispersion with sufficiently low viscosity that enables the spray-drying process. The advantages of producing a microparticulate powder rely on the possibility to obtain an AgNPs-doped stable simple handling system that can be directly administered onto the wound or can be dispersed in different vehicles that can cover the wound bed. The morphology and size distribution of the microparticles were investigated by SEM analysis shown in **Figure 90**. The mean diameters of obtained microparticles, calculated from SEM using ImageJ software, were almost comparable in all three cases (also in the microparticles without AgNPs produced as a control sample and called MPs). The results are for MPs 3.4 ± 0.3 µm, for AgNPs@MPs (T) 2.8 ± 0.7 µm and for AgNPs@MPs (UV) 4.0 µm ± 0.4.

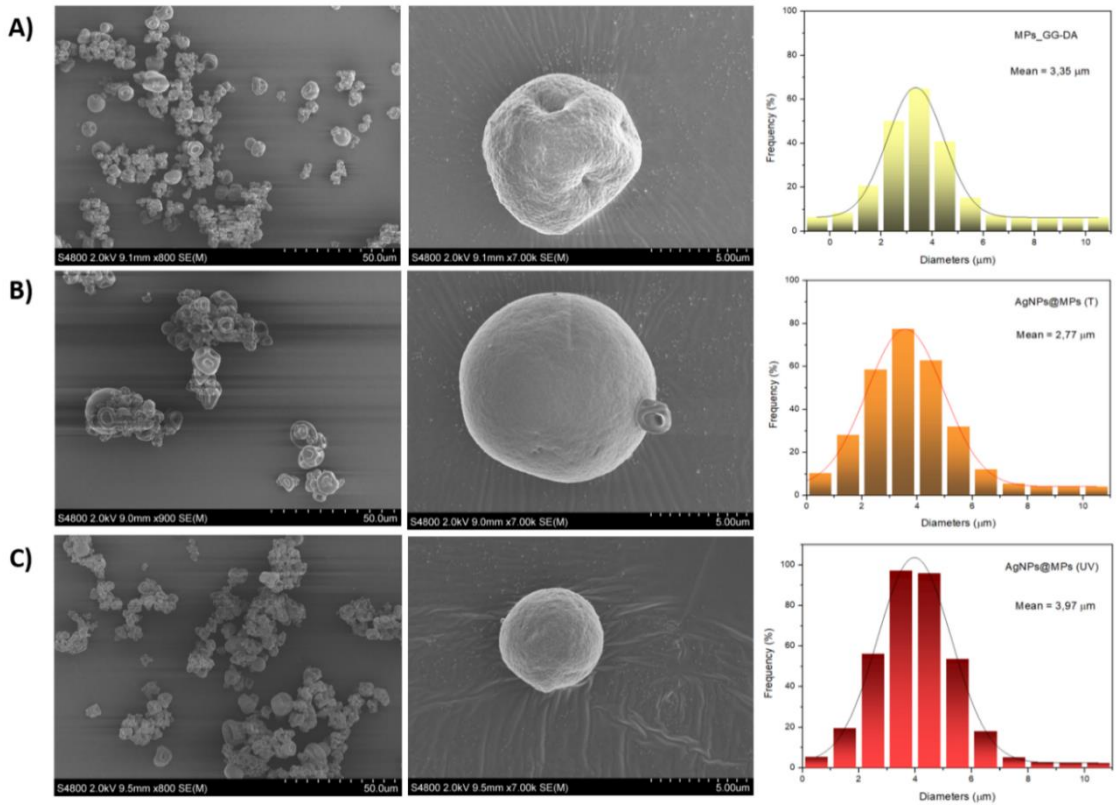

Figure 90. SEM and size distribution of MPs (**A**), AgNPs@MPs (T) (**B**), and AgNPs@MPs (UV) (**C**).

The FTIR spectra of AgNPs@MPs(T) and AgNPs@MPs (UV) shown in **Figure 91** were compared with that of empty MPs to identify potential functional groups that could have contributed to the *in situ* reduction process of silver ions (Ag^{+}) into silver nanoparticles (Ag^{0}). The FTIR spectrum of the MPs showed peaks around 2902, 1611, and 1411 cm^{-1} which correspond to the C-H stretching, C=C stretching, and C-H bending vibrations, respectively [366,367]. The peaks for the C-H stretching and C-H bending vibrations were shifted to 2886 cm^{-1}, and 1362 cm^{-1} in the AgNPs@MPs (T) spectrum and 2893 cm^{-1}, 1379 cm^{-1} in the AgNPs@MPs (UV) spectrum, respectively. The involvement of GG-DA polymer in the green synthesis and as capping agent of AgNPs was confirmed by peak shift [368]. Broad bands were found in all three spectra at 3310 cm^{-1} due to stretching vibrations of O-H (alcohol/catechol), this peak decreased in the spectra of AgNPs@MPs (T) (Abs: 0.1028) and AgNPS@MPs (UV) (Abs: 0.0762) spectra with respect to MPs (Abs 0.1489), after immobilization of the silver nanoparticles, indicating that the catechol group was responsible for the reduction process and/or the capping that took place [369]. A peak at 1294 cm^{-1} corresponding to stretching vibrations of C-O was present in the MPs spectrum, instead, it disappeared in the spectra of AgNPs@MPs (T and UV) [370]. The shoulder peak at 1725 cm^{-1} was found in the FTIR spectrum of MPs due to C=O stretching which was shifted to 1720 cm^{-1} in AgNPs@MPs (T) and to 1714 cm^{-1} in the spectrum of AgNPs@MPs (UV). Furthermore, there was not an excess peak in the range of 500-540 cm^{-1}, corresponding to the free metal ions of silver [371]. On the whole, the FTIR study confirms that GG-DA has a role as a reducing and/or capping agent, reducing Ag^{+} to Ag^{0} and stabilizing agent in the green synthesis of AgNPs.

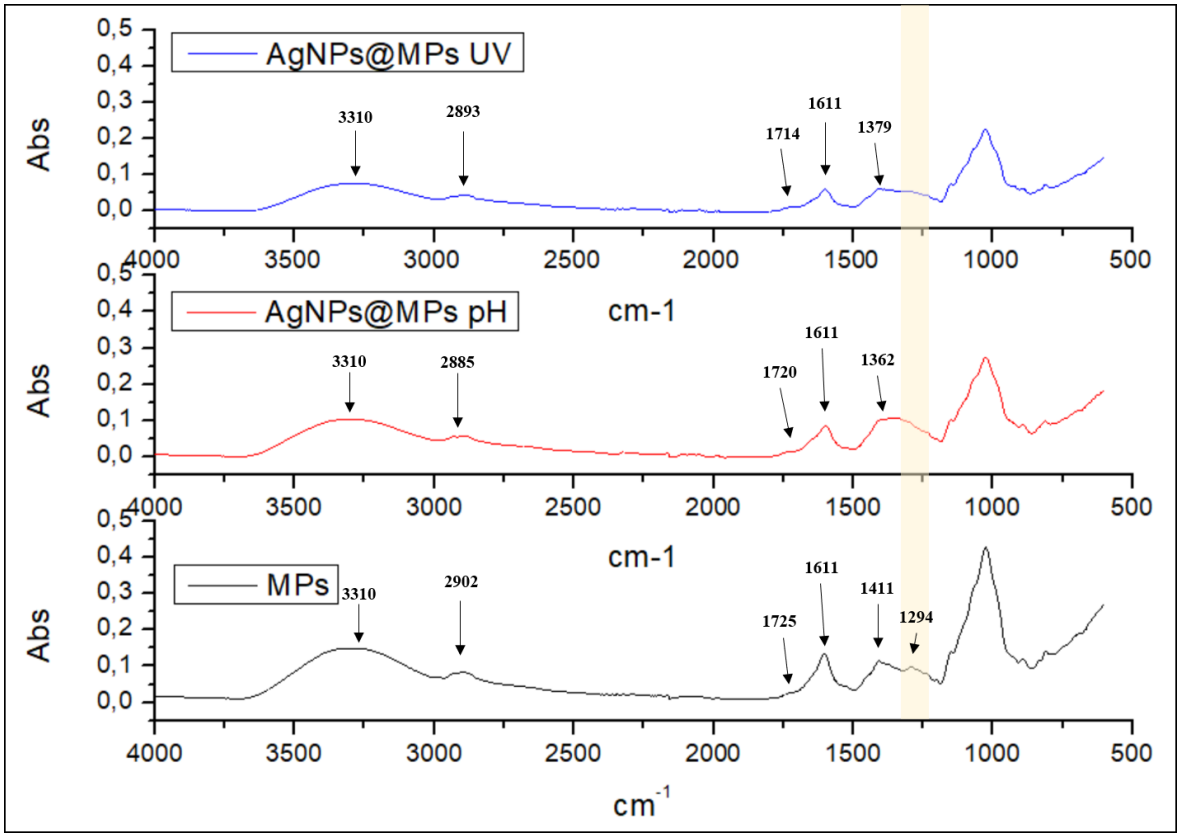

Figure 91. FTIR of MPs, AgNPs@MPs (T), and AgNPs@MPs (UV).

X-ray photoelectron spectroscopy (XPS) data for AgNPs@MPs (T) and AgNPs@MPs (UV), showing the levels of the Ag3d nucleus are shown in **Figure 92A** and the main quantitative results are summarized in **Table 5**.

Table 5. XPS $Ag3d_{5/2}$ metal data collected on AgNPs@MPs (T) and AgNPs@MPs (UV).

Sample	Signal	Binding Energy (eV)	Related Area (%)	Assignment
AgNPs@MPs (T)	$Ag3d_{5/2}$	368.3; 374.3	100%	Ag(0)
AgNPs@MPs (UV)	$Ag3d_{5/2}$	368.3; 374.3	100%	Ag(0)

Graphs in **Figure 92A** show two spin-orbit pairs of components, which were individuated in the Ag3d XPS spectrum. The main $Ag3d_{5/2}$ component is centered at 368.3 eV Binding Energy (BE) value and corresponds to metal silver atoms in the nanoparticles.[372] The second spin-orbit pair of small intensity at higher BE values ($Ag3d_{5/2}$ at 374.3 eV) is attributed to the more oxidized surface Ag bonded with an organic structure, indicating successful immobilization of silver nanoparticles (Ag^0) on GG-DA.[232,373]

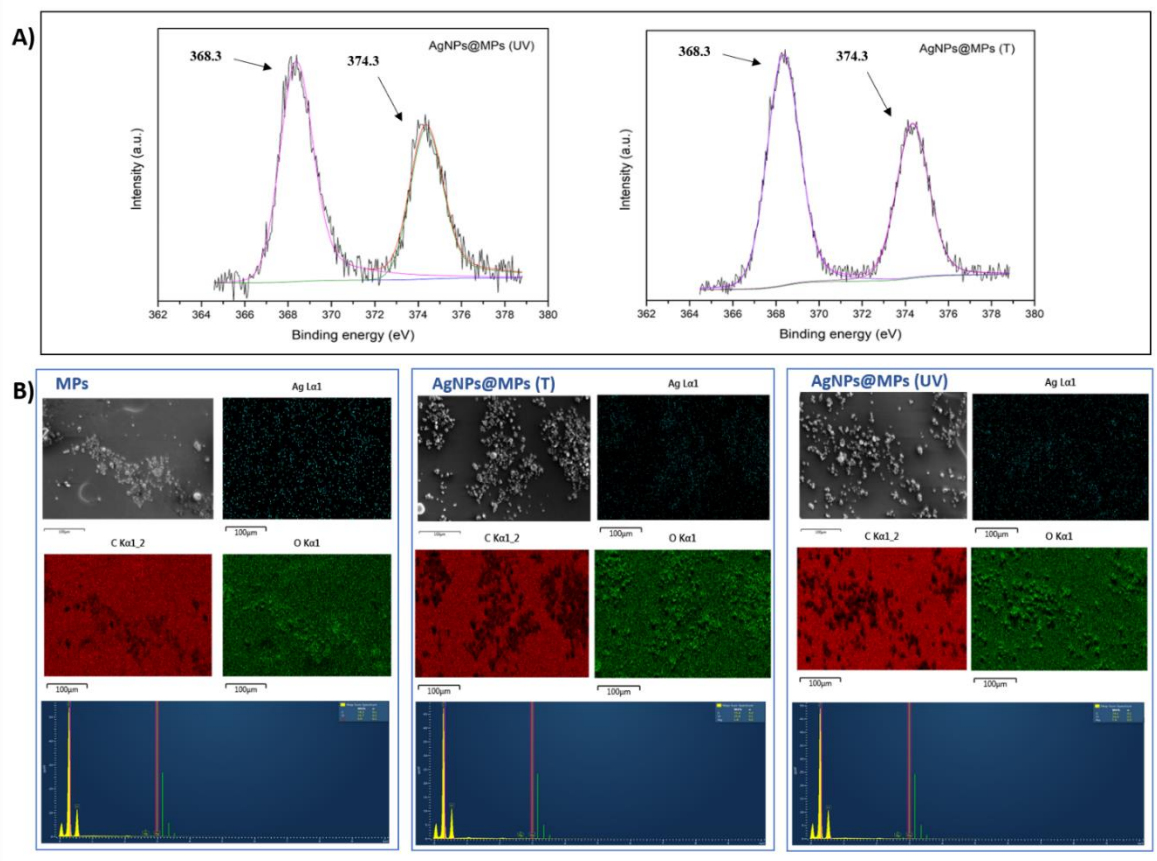

Figure 92. Ag3d spectra of silver nanoparticles in AgNPs@MPs (T) and AgNPs@MPs (UV) (**A**); and SEM-EDX of MPs, AgNPs@MPs (pH), and AgNPs@MPs (UV) (**B**).

The presence of silver nanoparticles in AgNPs@MPs (T) and AgNPs@MPs (UV) was confirmed by the EDX (Energy Dispersive X-ray Spectroscopy) distinct signal in the silver region of the spectrum (**Figure 92C**). The percentage of silver is shown in **Table 6**.

Table 6. Percentage of various elements observed in EDX analysis.

Sample	Element	Weight %	σ
MPs	C	74.3	0.1
	O	25.7	0.1
	Ag	**0.0**	**0.1**
AgNPs@MPs (T)	C	72.4	0.2
	O	25.8	0.1
	Ag	**1.9**	**0.2**
AgNPs@MPs (UV)	C	74.1	0.1
	O	24.9	0.1
	Ag	**1.9**	**0.2**

Transmission electron microscopy (TEM) images demonstrated the uniform distribution of AgNPs inside the AgNPs@MPs (T) and AgNPs@MPs (UV) as shown in **Figure 93**. Both types of AgNPs are spherical and have an average diameter of around 13 nm. As expected, and mentioned above, AgNPs (UV) were shown to be less polydisperse than AgNPs (T).

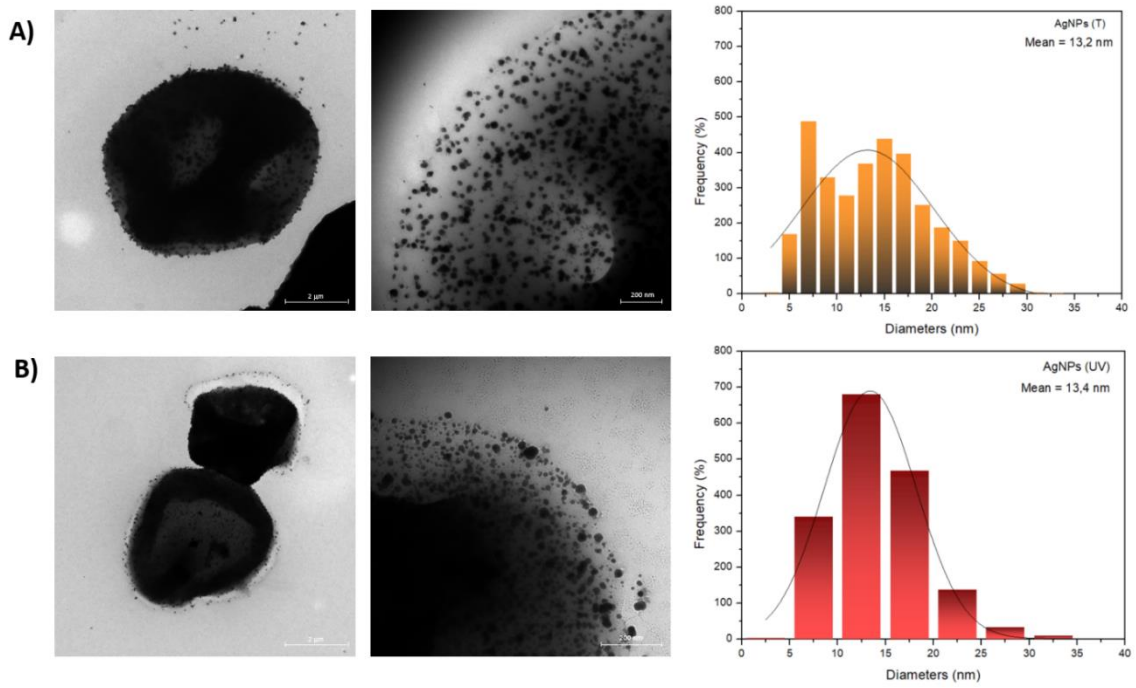

Figure 93. TEM images and size distribution of AgNPs@MPs (pH) (**A**), and AgNPs@MPs (UV) (**B**).

Experiments of microparticles mineralization and ICP/MS silver determination were also carried out to quantify the concentration of AgNPs present in the microstructures. The calculated amount was equal to 52±2 µg of Ag per 1 mg of AgNPs@MPs (T) and 44±4 µg of Ag per 1 mg of AgNPs@MPs (UV). AgNPs@MP were dispersed after a few minutes of incubation in water, making it impossible to visualize them under an optical microscope. On the contrary, as expected they show good stability in saline media.

In particular, a pre-treatment was carried out for 24 hours in DPBS pH 7.4 or in 1 M $CaCl_2$ at 4 °C. After this time, the MPs, the AgNPs@MPs (T), and the AgNPs@MPs (UV) were incubated at 37°C for 7 days in DPBS. These media were chosen because DPBS pH 7.4 represents the most common buffer used for biological purposes, while $CaCl_2$ is the medium of choice used for the ionotropic crosslinking of GG. From the microscope images, it was possible to notice that the microparticles maintain their spherical shape even after seven days of incubation for both pretreatment methods used. AgNPs@MPs (T), AgNPs@MPs (UV) and MPs showed comparable behavior, thus only images of AgNPs@MPs (T) were reported in **Figure 94**. These results demonstrated that ionotropic crosslinking with divalent ions is not strictly necessary to guarantee the stability of the produced microparticles.

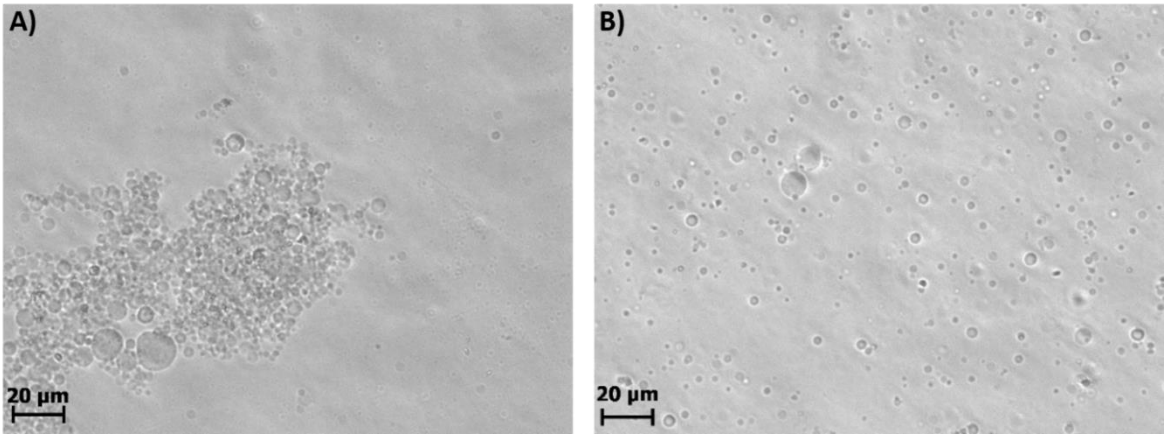

Figure 94. AgNPs@MPs (T) after seven days maintained at 37 °C in DPBS after pretreatment in DPBS **(A)** and 1 M $CaCl_2$ **(B)**.

3.5.3 Production and Characterization of Hydrogels

Being composed of hydrophilic polymeric networks, hydrogels are capable of hydrating wound areas and guaranteeing the presence of oxygen in the tissue.[344]

Polysaccharide-based hydrogels have been extensively investigated for wound healing applications because of their physicochemical properties and biocompatibility.[374–378] Here, with the aim to produce a model injectable hydrogel as a vehicle for the produced nano-into-micro antimicrobial particles we used oxidized xanthan gum (OXG), as an easily cross-linkable polysaccharide derivative. OXG was produced via sodium periodate reaction with Xanthan Gum. The oxidation degree of OXG was calculated to be 25.8% ± 0.2% by potentiometric titration of the NaOH/hydroxylamine hydrochloride solution, how described in the **5.5.5 paragraph**.

In the ^{1}H-NMR spectrum of OXG, obtained at 55 °C, shown in **Figure 95,** it is possible to note the presence of signals at 1.95 and 2.34 ppm, attributed to the groups present in the oxidized saccharide units. The signal at 9.44 ppm is instead attributed to the presence of aldehyde groups formed during the oxidation process.[379] HB10k-G5-alanine (synthesized based on previous work) was also chosen because of its degradability and interesting chemical versatility given by the presence of several terminal amine groups that upon protonation confer antimicrobial properties to the macromolecules.[380] These features in this case were exploited to perform the crosslinking with the oxidized polysaccharide via imine bond formation. This crosslinking mechanism guarantees a quick gelation of the system simply upon mixing the polymeric dispersions. The reversibility of imine bonds, stable at physiological pH, endows the hydrogel with interesting rheological properties, such as injectability and shape adaptability, particularly suitable for wound administration.

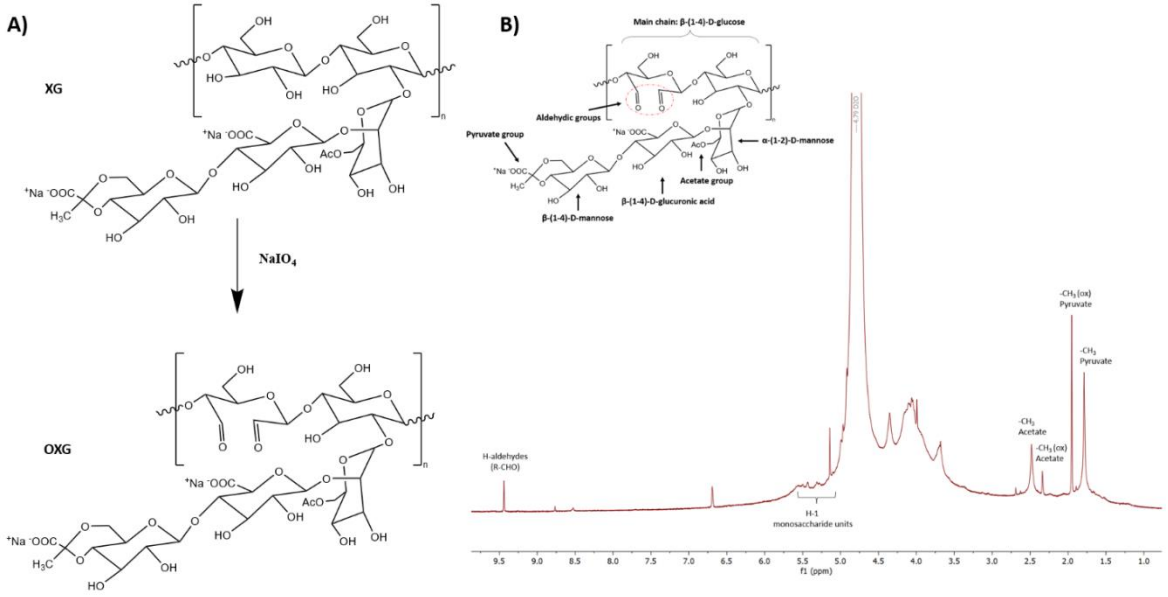

Figure 95. Scheme of preparation **(A)** and ^{1}H-NMR spectrum **(B)** of OXG.

As shown in **Figure 96**, two hydrogels were initially produced. The final weight percent of HB10k-G5-alanine relative to OXG was set as 1 and 0.5%w/w; the samples were then designated as XH_1 and $XH_{0.5}$, respectively. AgNPs@MPs (T and UV) were added to both hydrogels dispersing them in the OXG dispersion before the gelation. Four types of hydrogels were thus obtained. The names and concentrations are shown in **Table 10.**

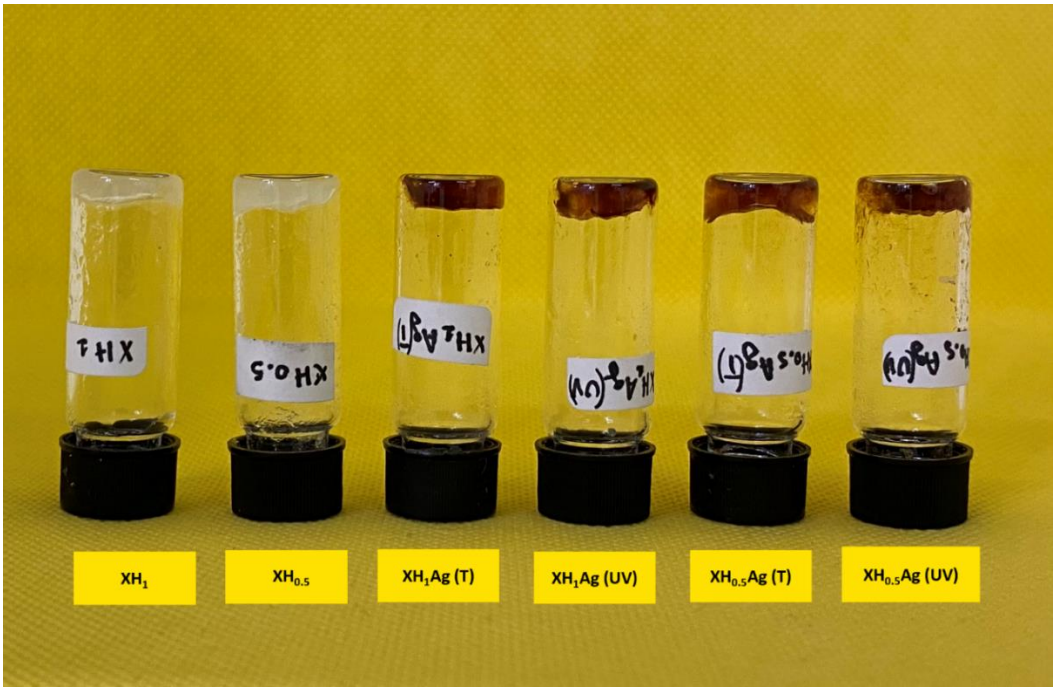

Figure 96. $XH_{0.5}$, $XH_{0.5}$-Ag(T), and $XH_{0.5}$-Ag(UV) hydrogels; XH_1, XH_1-Ag(T), and XH_1-Ag(UV) hydrogels formed.

Through the SEM analysis (**Figure 97**), it was possible to observe the presence of AgNPs@MPs incorporated between the meshes of the three-dimensional network of the XH_1-Ag(UV) hydrogel.

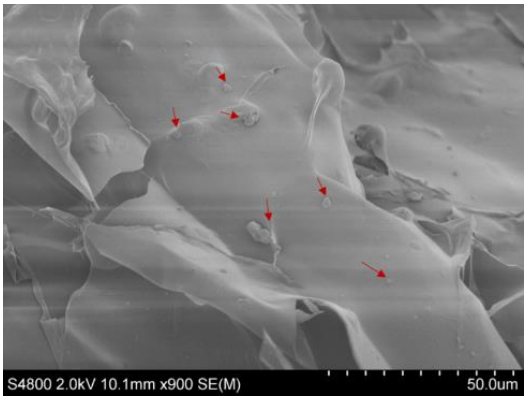

Figure 97. SEM image of XH_1-Ag(UV) hydrogel.

3.5.4 Rheological Characterization of hydrogels

The viscoelastic property of the obtained hydrogels was determined by oscillatory frequency sweep analyses. Nano-into-micro AgNPs@MPs obtained for T or UV-induced Ag reduction showed to affect similarly the hydrogels rheological behavior, as it was reasonable to assume (e.g. results obtained for $XH_{0.5}$-Ag(T) and $XH_{0.5}$-Ag(UV) and for XH_1-Ag(T) and XH_1-Ag(UV) were perfectly overlapped). For this reason, from now on, in this manuscript samples will be named $XH_{0.5}$-Ag and XH_1-Ag, $XH_{0.5,}$ and XH_1 (without microparticles). As shown in **Figure 98A and 99A**, for all hydrogels produced, the results showed G′ (Storage modulus) > G″ (Loss modulus) within 0.06-100 rad/s and G′ increased when the concentration of the OXG was twice as much as the HB10k-G5-alanine in the hydrogel mixture. Furthermore, it was also evident that the modulus increased when AgNPs@MPs were loaded into the hydrogel evidencing a known structuring effect that microparticles have on three-dimensional hydrated networks.[381]

Table 7. Summary data of rheological analyses of hydrogels.

	Frequency sweep		Oscillation amplitude sweep			Flow sweep	Recovery time			
Sample	G' (Pa)	G" (Pa)	G' (Pa)	G" (Pa)	Cross-point (strain%)	Viscosity (Pa•s)	G' (Pa) (strain % =1)	G" (Pa) (strain % =1)	G' (Pa) (strain % =500)	G" (Pa) (strain % =500)
XH_1	195±2,2	20±0,6	298±2,5	19±1,7	193±1,2	182±1,6	341±0,9	44±1,9	5±0,4	17±0,6
XH_1-Ag	280±1	80±3,3	2455±4,5	1170±1	42±1,4	1073±0,6	524±1	83±1,2	7±0,2	25±1,2
$XH_{0.5}$	30±3,7	6±0,9	111±1,2	25±0,9	193±0,7	75±1,3	73±0,6	20±1,3	2±0,3	8±0,7
$XH_{0.5}$-Ag	56±0,5	15±2,9	382±0,8	164±0,7	193±1	545±1,2	289±1,6	46±0,9	5±0,7	18±0,7

As shown in **Table 7**, XH_1 has higher moduli (G' and G") than $XH_{0.5}$, while XH_1-Ag has higher moduli than XH_1 and $XH_{0.5}$-Ag higher than $XH_{0.5}$. In **Figure 98B and 99B** the oscillation amplitude analysis demonstrated that all hydrogels exhibited a strain-dependent viscoelastic response. G' was independent of strain and was consistently greater than G" in the linear viscoelastic region (LVR: 0.1-10%), exhibiting the characteristics of viscoelastic materials.[382,383] At low strain % values, again, samples containing AgNPs@MPs showed higher G' and G", as reported in **Table 7**. The rheograms also showed the cross-point beyond which the G″ exceeds the G′, indicating that the hydrogel structure was collapsed, resulting in the gel-sol transition when the hydrogel starts to flow.[384] Macroscopically, the hydrogels were able to be extruded from a syringe needle and be injected and weathered in DPBS pH 7.4. The injectability of the material is related to its ability to remain homogeneous under pressure.[384] An important factor for injectability from the rheology data is the shear-thinning behavior.[385] The viscosity changes of the hydrogels at shear rates between 0.1 and 1000 1/s were measured to investigate the shear thinning properties. As shown in **Figure 98C** and **Figure 99C**, the viscosity of all the hydrogels decreased with increasing shear rates, suggesting that the shear thinning behavior of the hydrogels is due to the disruption of the reversible interactions in the network and the alignment of the molecules in the direction of the applied shear stress. At low shear rates (0.1 1/s), $XH_{0.5}$ had the lowest viscosity and XH_1-Ag had the highest viscosity. Viscosity, therefore, increased on increasing the ratio concentration between the polymers present in the hydrogel mixture, but also based on the presence of AgNPs@MPs. These results were therefore in agreement with the elastic modulus values. At high shear rates (1000 1/s), the viscosity of XH_1 was slightly higher than the viscosity of XH_1-Ag; while $XH_{0.5}$ has a lower viscosity than the corresponding hydrogel with the AgNPs@MPs, $XH_{0.5}$-Ag (**Table 7**).

From the cross-point values obtained through the oscillation amplitude analysis, it was possible to set the recovery time analysis (**Figure 98D** and **Figure 99D**), subjecting each hydrogel to 7 alternating deformation cycles (low strain% 1%, high strain% 500%). The shear-thinning analysis demonstrated the self-healing behavior of the hydrogels based on the rapid reform bonds following a break, once subjected to high strain%, and the good recovery of hydrogels in the different low-high strain % cycles applied.[386] Concerning the hydrogel with the AgNPs@MPs, $XH_{0.5}$-Ag, the presence of the nano/micro-structures did not influence the recovery of the two modules through the low-strain-high-strain cycles. There is no tendency to decrease healing efficiency after 7 cycles. The average value of the same in the 7 cycles observed is 87,0% ± 0.1 (**Figure 99E**). While for the XH_1-Ag hydrogel, the presence of AgNPs@MPs improved the self-healing capacity, reaching a % efficiency of 103,0% ± 0.2 (**Figure 98E**).

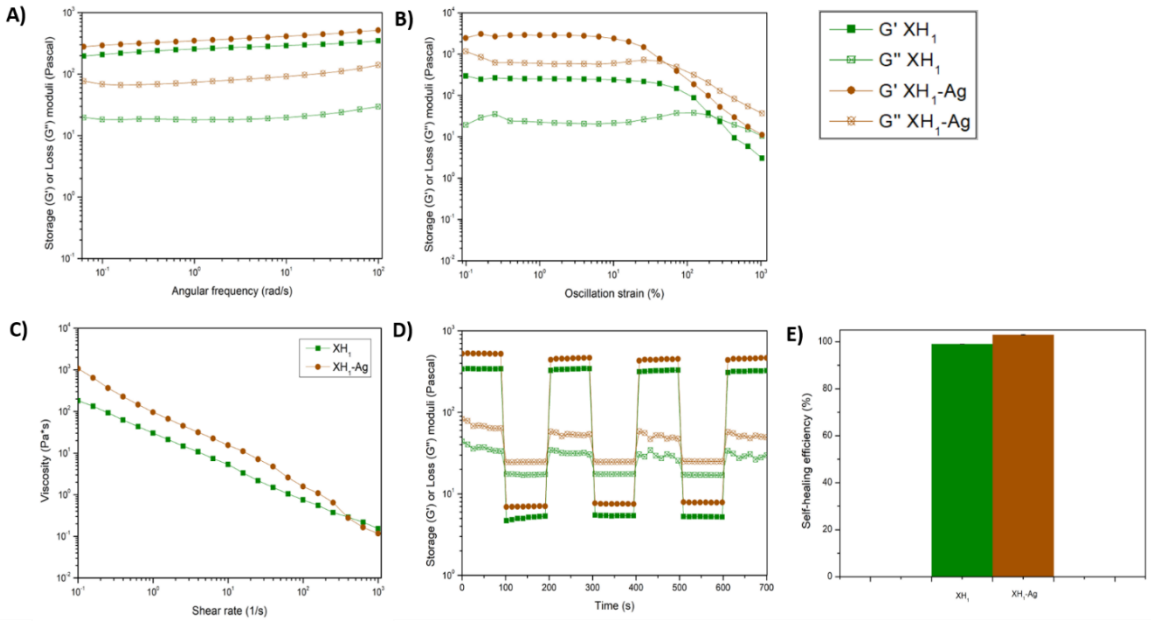

Figure 98. Frequency sweep (**A**), oscillation amplitude sweep (**B**), flow sweep (**C**), recovery time (**D**) rheological analyses; self-healing efficiency (**E**) of XH_1 and XH_1-Ag hydrogels.

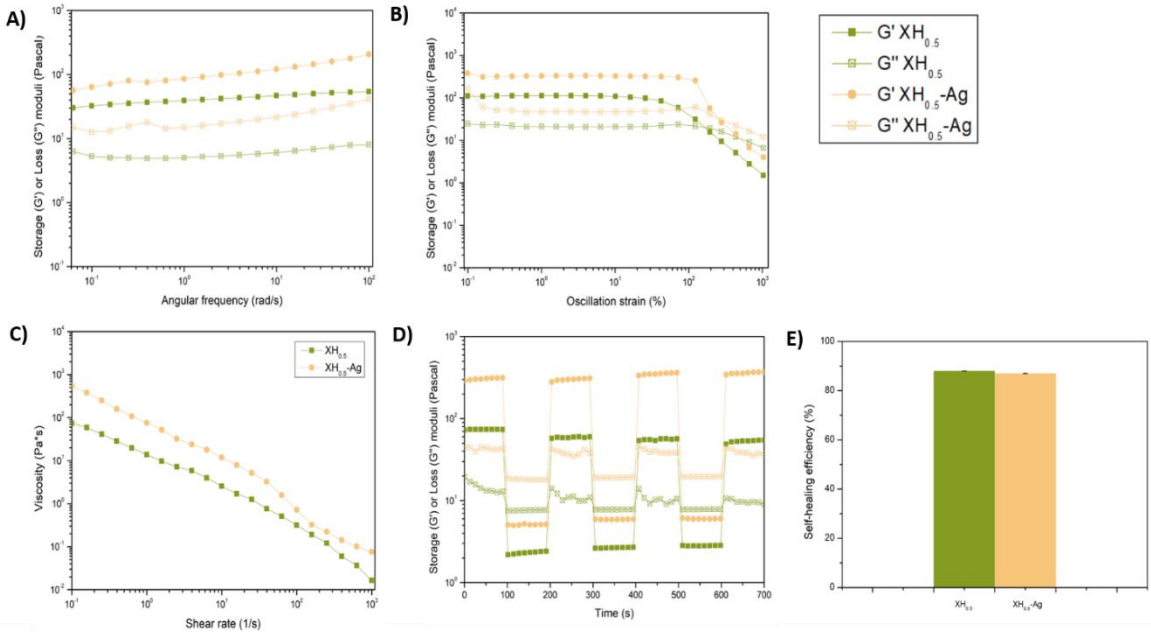

Figure 99. Frequency sweep (**A**), oscillation amplitude sweep (**B**), flow sweep (**C**), recovery time (**D**) rheological analyses; self-healing efficiency (**E**) of $XH_{0.5}$ and $XH_{0.5}$-Ag hydrogels.

3.5.5 $ABTS^{\bullet+}$ radical scavenging assay of microparticles and hydrogels

Reactive oxygen species (ROS) in the wound microenvironment impede cutaneous wound healing [387]. Therefore, the ideal dressing should possess antioxidant activity. To evaluate the antioxidant activity, the free radical scavenging efficiency of $ABTS^{\bullet+}$ was examined. The antioxidant activity was initially studied for MPs, AgNPs@MPs (T), and AgNPs@MPs (UV) at different concentrations. The graph in **Figure 100A** showed how MPs and both AgNPs@MPs (T and UV) at a concentration of 0.250 mg/ml can neutralize the radicals, this was also visible macroscopically in **Figure 100B**, where it can be noted the discoloration of the solution. The introduction of catechol groups in the GG backbone improved the antioxidant capacity of MPs.[343] But interestingly, even with the introduction of AgNPs into the system, the $ABTS^{\bullet+}$ scavenging activity was already higher at lower concentrations of 0.03125. We further evaluated the antioxidant activity of hydrogels using the same approach. As shown in **Figure 100C, D**, compared to the XH_1 control, the XH_1-Ag (UV) and XH_1-Ag (T) hydrogels were shown to have increased scavenging activity at set times and there are significant differences between samples containing AgNPs@MPs, compared to those without them. These results, therefore, revealed that the introduction of catechol groups and AgNPs can give the systems excellent antioxidant activity, as already reported in the literature.[388]

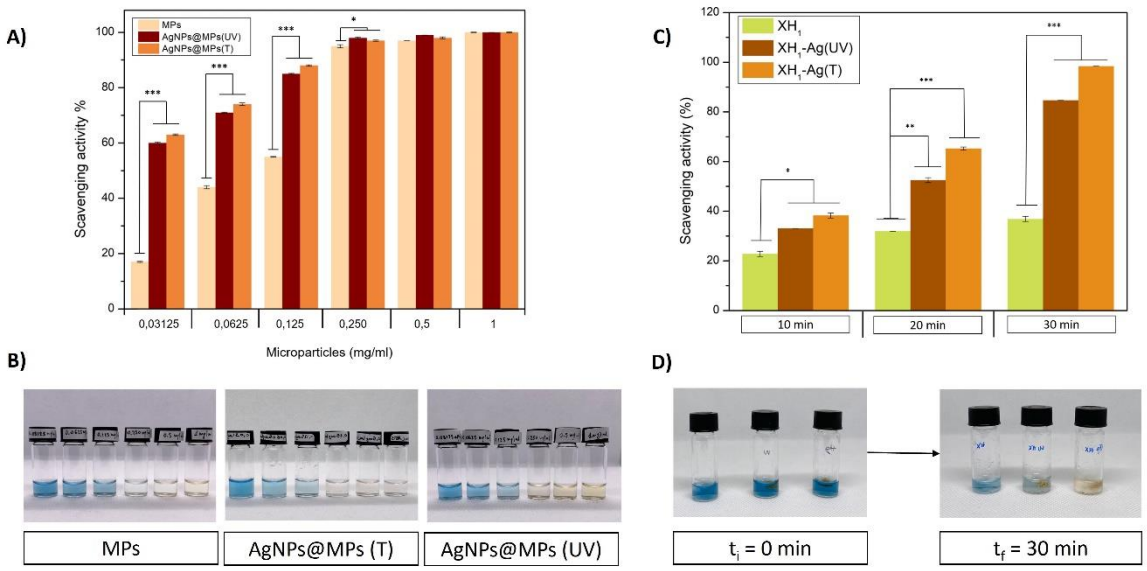

Figure 100. The $ABTS^{+}$ scavenging activity of MPs, AgNPs@MPs (UV), and AgNPs@MPs (T) (**A, B**); and of XH_1, XH_1-Ag (UV) and XH_1-Ag (T) hydrogels (**C, D**). All data are shown as a mean value ± SD (*n* =3); (* $p \leq 0,05$; ** $p \leq 0,01$; *** $p \leq 0,001$).

3.5.6 Cytocompatibility evaluation of the microparticles and hydrogels

An *in vitro* cytocompatibility study was performed for MPs, AgNPs@MPs (T), and AgNPs@MPs (UV) at three different concentrations and the XH_1, XH_1-Ag (T), and XH_1-Ag (UV) hydrogels. Human dermal fibroblasts (HDF), and mouse monocyte cells (RAW 264.7) were used. As shown in **Figure 101A-B**, all microparticles showed good biocompatibility towards RAW 264.7 and HDF cells even at high concentration of 500 µg/ml, the results are still optimal since even at the concentration corresponding to the MIC for *S. aureus* (500 µg/mL) MPs and both AgNPs@MPs (T and UV) were not cytotoxic for the tested cells (>80% viability for both RAW and for HDF in all cases at this concentration). The same tests were performed with 100 µl hydrogels and the results (**Figure 101C-D**) show that both hydrogels loaded with the AgNPs@MPs showed cell viability above 75% after 24

hours of incubation with cells. Maximum cell viability of 112% was achieved with XH_1 against HDF. Interestingly, the hydrogels loaded with the AgNPs@MPs (both T and UV) were cytocompatible, although the percentage of incorporated nano/micro-structures dosed double (1000 µg) the MIC and the previously tested maximum amount (500 µg/mL) (**Figure 101A-B**). These results showed that composite hydrogels can be considered potential biomaterials for wound healing.

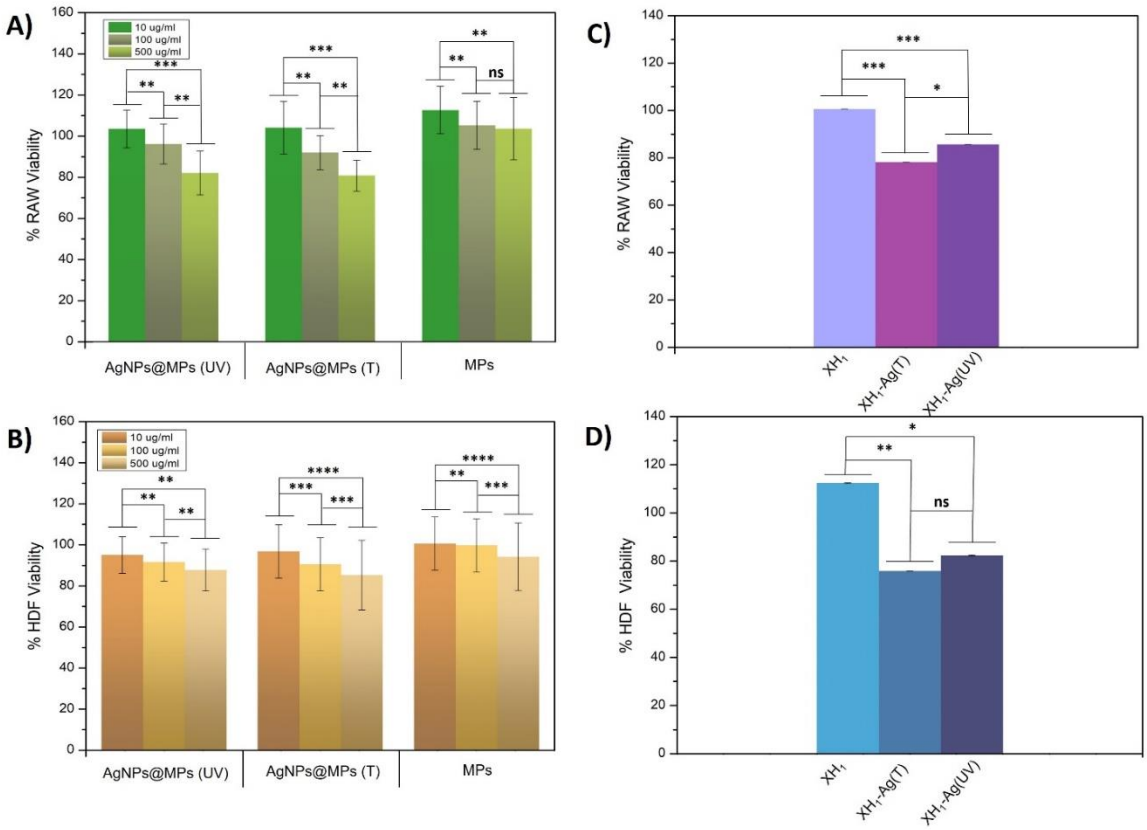

Figure 101. Cytocompatibility evaluation of the AgNPs@MPs (UV), AgNPs@MPs (T), and MPs toward RAW 264.7 (**A**) and HDF (**B**) cells. Cytocompatibility evaluation of the XH_1, XH_1-Ag (UV), and XH_1-Ag (T) toward RAW 264.7 (**C**) and HDF (**D**) cells. All data are shown as a mean value ± SD (n = 3).

3.5.7 Antibacterial activity of the microparticles and hydrogels

Extensive use of antibiotics has led to the spread of resistant organisms [389]. Nanomaterials can serve as efficient vectors to supplement and support antibiotics and generate highly performing-antimicrobial agents that can prevent antimicrobial resistance [390,391]. The antibacterial properties of MPs, AgNPs@MPs (T), and AgNPs@MPs (UV) were studied using the minimum inhibitory concentration (MIC), the lowest concentration of an agent that inhibits the visible growth of a microorganism, and the minimum bactericidal concentration (MBC), the lowest concentration of a substance necessary to kill a microorganism. MPs did not show any obvious antibacterial activity at concentrations lower than 4 mg/ml while AgNPs@MPs (T) and AgNPs@MPs (UV) showed good antibacterial properties against both gram-positive bacteria *Staphylococcus aureus* (*S. aureus*) and gram-negative strain *Escherichia coli* (*E. coli*) (**Table 8**). MIC values of AgNP@MPs (T) and AgNP@MPs (UV) were recorded at 31.2 – 15.6, and 15.6 µg/mL for *E. coli*, respectively; while at 500 and 250 µg/mL *S. aureus*. The MBC values were found to be 62.5 and 31.2 µg/mL for *E. coli*, respectively, while for *S. aureus* it was 500 µg/mL for both microparticles. Results have shown that *E. coli* was more susceptible to the microparticles with respect to *S. aureus.* Gram-positive bacteria are less susceptible to AgNPs than gram-negative bacteria because the antimicrobial activity of AgNPs is influenced by the composition and thickness of the bacterial cell wall; this is due to the difference in the ratio of peptidoglycan in the cell membrane. Thickened gram-positive cell walls and also like negatively charged peptidoglycan, can cause the trapping of silver ions in the cell wall. While gram-negative bacteria contain lipopolysaccharides (LPS) in their cell membrane and the negative charge of LPS enhances the adhesion of AgNPs and makes the bacteria more susceptible [392].

This confirms the remarkable anti-bactericidal effects of the AgNPs produced by the two methods previously described.

Table 8. Minimal inhibitory concentration (MIC) and minimal bactericidal concentration (MBC) (µg/ml) of MPs**,** AgNPs@MPs (T) and AgNPs@MPs (UV) against *E. coli 178, and S. aureus 2569.*

		E. coli 178	***S. aureus 2569***
	Sample	**µg/mL**	**µg/mL**
MIC	**AgNPs@MPs (T)**	31.2 - 15.6	500
	AgNPs@MPs (UV)	15.6	250
	MPs	> 4000	> 4000
MBC	**AgNPs@MPs (T)**	62.5	500
	AgNPs@MPs (UV)	31.2	500

The antibacterial activity of the AgNPs@MPs-charged hydrogels, XH_1-Ag (UV) and XH_1-Ag (T), was evaluated using the disk diffusion test and was compared with the XH_1 hydrogels in which no microparticles were incorporated. All hydrogels were 50 µL and were evaluated using a bacterial concentration of 10^7 CFU mL^{-1} of the two bacterial strains *E. coli* 178 and *S. aureus* 2569. All hydrogels in which the AgNPs@MPs were present showed clear zones of inhibition against both *E. coli* (**Figure 102A**) and *S. aureus* (**Figure 102B**). The XH_1 hydrogel, as expected, did not show any obvious zone of inhibition against both *E. coli* and *S. aureus*. **Figure 102C** shows the diameters of the inhibition zones, which are comparable for both *E. coli* and *S. aureus* in all hydrogels.

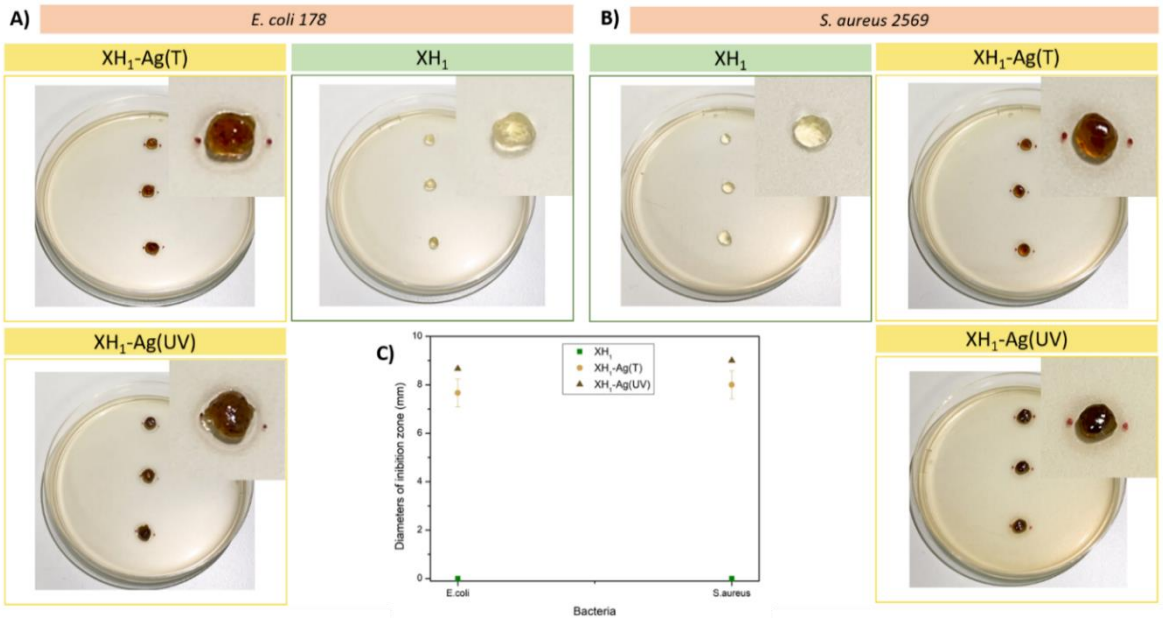

Figure 102. The disk diffusion test of XH_1, XH_1-Ag (T), and XH_1-Ag (UV) against *E. coli* 178 (**A**) and *S. aureus* 2569 (**B**). The diameters of the inhibition zone (mm) against both strains tested (**C**).

The antibacterial property of the hydrogels was also tested in a 100 µL culture medium containing bacterial concentrations of 10^5 CFU/ml. After incubation with the XH_1-Ag (T) and XH_1-Ag (UV) hydrogels at 37 °C at set times (4, 6, 8, and 24 hours), the bacterial solution was diluted and the plate count method was used to calculate the bacterial concentrations. As the results shown in **Figure 103**, all hydrogels loaded with AgNPs@MPs (XH_1-Ag (T) and XH_1-Ag (UV)) showed 100% killing capacity against both *E. coli* and *S. aureus*. This was consistent with the inhibition zone test where all hydrogels showed comparable zones of inhibition for both bacterial strains. These results are evidence that these nano/micro-structured hydrogels represented promising antibacterial systems for the treatment of both gram-positive and gram-negative bacterial infections.

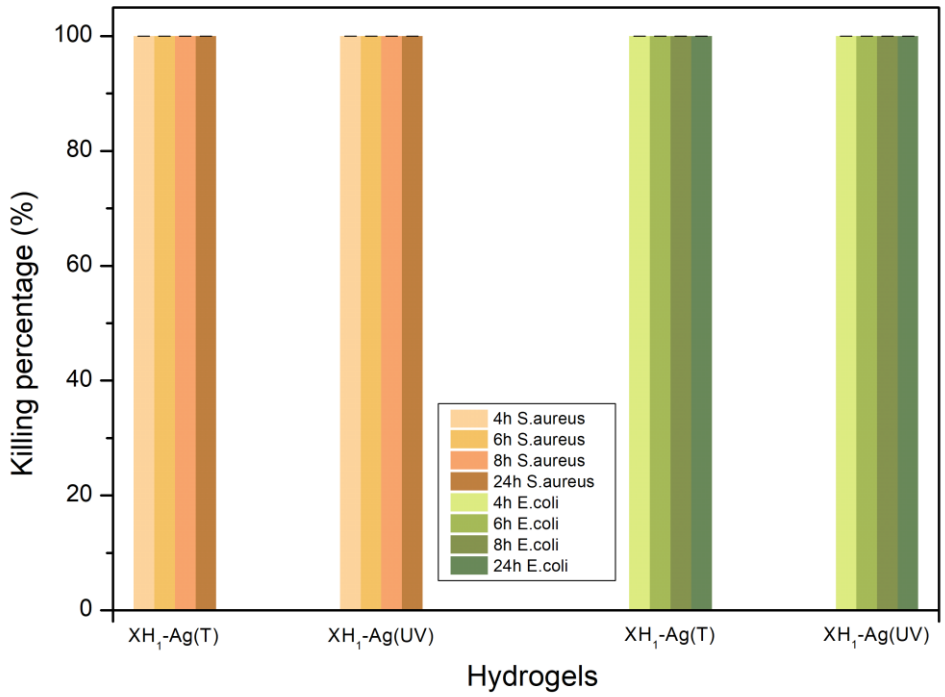

Figure 103. Killing efficiency of XH_1-Ag(T) and XH_1-Ag(UV) hydrogels against *S. aureus* (**left**), and *E. coli* (**right**) at different incubation times (from 4 hours to 24 hours, from lighter to more intense color). All data are shown as a mean value ± SD (*n* =3).

4. Conclusions

In this Ph.D. thesis work, the focus was on the development of multifunctional antibacterial injectable hydrogels for potential application in the treatment of infected skin wounds. To make the most of the potential physicochemical properties of Gellan Gum (GG) and make it easily processable through all the main biofabrication techniques, various strategies have been used so far, such as its chemical functionalization or mixing with other biomaterials. To overcome some of the inadequate properties of the high molecular weight polysaccharide, in this work, we focused on the production of different low molecular weight GG derivatives, which can be more manageable and versatile from a technological point of view. As stated above, the reduction of GG molecular weight is advantageous to obtain products that are more easily processable since they can be dispersed in water at relatively high concentrations without too stressed heating conditions and avoid the formation of too viscous solutions. Therefore, in a first work, alkaline hydrolysis of GG was conducted at 50°C in NaOH 0.1N. By varying the degradation time, four different GG with molecular weights ranging from 149 to 36 kDa were obtained. By means of thermo-rheological analysis, conducted on 5% w/v aqueous dispersions, it was demonstrated that all the obtained low molecular weight products maintain the typical temperature responsiveness of high molecular weight GG since they underwent a cooling-induced gelation mediated by the coil-to-helix transition of the polysaccharide chains. Obtained products result in being easily dispersible in DMSO facilitating those synthetic routes that make it possible to functionalize GG hydroxyl groups in spite of the carboxylic ones. Considering that the carboxylate groups play a crucial role in the gelation mechanism, this aspect could be extremely interesting. Ionotropic gelation of the aqueous dispersions, conducted by treatment with $CaCl_2$ with two different procedures, demonstrates that low molecular weight products retain the ability to crosslink as a function

of the medium ionic strength. Crosslinked procedure leads to the formation of mechanically stable hydrogels characterized by a highly porous structure on the micrometric scale as demonstrated by SEM images of the freeze-dried samples. These low molecular weight GG hydrogels can uptake high amounts of aqueous medium after 24 hours of incubation. Except for the sample named GG_{24} which has a molecular weight of 39 kDa, all the investigated samples retain their viscoelastic properties in a physiological environment at 37°C at least until 14 days. All the hydrolysis-derived GG samples resulted to be cytocompatible. The reduction in molecular weight allows to obtain fluid dispersion that can be exploited to encapsulate viable cells and eventually release them in vivo. On the whole, these studies demonstrated that despite the drastic reduction of the molar mass, the hydrolyzed GG maintains the peculiar rheological and physicochemical features of high molecular GG and can be an interesting and intelligent alternative to it in the development of biomedical devices alone or in combination with other biopolymers.

In a second work, GG (following alkaline hydrolysis followed for 24 hours, therefore the one with the lowest molecular weight), was functionalized with pendant groups of ethyldiamine (EDA), obtaining a semi-synthetic polymer called GG-EDA, which was crosslinked with vynilsulfone functionalized 4-arm PEG. Hydrogels were thus obtained which were then doped with pDA nanoparticles, obtained by exploiting auto-oxidative polymerization of dopamine in a basic environment. The presence of pDA contributes to compacting the structure of the hydrogels by creating covalent bonds with the polysaccharide as suggested by the swelling studies and rheological characterization. pDA-containing hydrogels show marked photothermal performance and produce localized hyperthermia when irradiated with NIR laser at 810nm. Photothermal stability studies reveal that pDA containing samples can be irradiated several times without losing their

photothermal properties. Medicated hydrogels, produced by dissolving ciprofloxacin hemisuccinate in the gelling solution, can control the release of the drug over a period of 72 h even if the irradiation with NIR causes a boosted release of the antibiotic. In vitro cytotoxicity studies showed that both pDA conating and pDA free hydrogels did not influences neither the viability of HDF nor their proliferative behaviour. The antimicrobial effect has been proven using *P. aeruginosa* and *S. aureus* as bacterial strains. In both cases the hyperthermic effect has an inhibitory effect in the pathogens growth in the absence of ciprofloxacin while, for the medicated samples, it enhances the hydrogel antibacterial activity both by increasing the amount of released drug, as in the case of *P.aeuriginosa*, and by potentiating its effect after 4 cycles of irradiation as occurred for *S. aureus* . These results encourage us to propose this hydrogel as an effective candidate for application as wound dressing for skin wounds, as it would be able to cover the wound bed, reduce exudate, be degraded over time without the need for painful removal or being continuously changed, as it happens for traditional wound dressings, and finally it can be activate from the external to eradicate bacterial infections both by releasing antibiotics and by exerting an hyperthermic effect. This last aspect would be particularly interesting for the treatment of multidrug resistant infections.

In another work, other GG derivatives were produced starting from the two lowest molecular weight derivatives obtained in the first work, GG_8 and GG_{24}. In both cases the starting backbone was functionalized with dopamine and polyethylene glycol, obtaining GG_8-DA-PEG and GG_{24}-DA-PEG respectively. The higher molecular weight derivative has been exploited to develop physical hydrogels by exploiting the formation of an ionic pair between carboxylate groups of the glucuronic acid residues of the polymer and the protonated amino groups of the antibiotic colistin sulfate. The GG_{24}-DA-PEG derivative was instead used

to produce polydopamine-coated microparticles, MPs@pDA, which were incorporated into the hydrogel. We have shown that the dopamine grafted to the polymer backbone improves the tissue-adhesion capacity of hydrogels *ex vivo*. Prepared hydrogels showed good pseudoplastic, shear-thinning and recovery-time properties; excellent cytocompatibility and antioxidant activity *in vitro*. Taking advantage of the photothermal effect, the hydrogels showed a controlled release of antibiotic and allowed a synergistic antibacterial effect *in vitro* by combining the photothermal effect with the on-demand release of colistin. The results of antibacterial test against *P. aeruginosa* and *S. aureus* show that these hydrogels could be good candidates for the care of the infected wound and for this reason could improve the quality of wound repair. Moreover, *P. aeruginosa* has a great ability to become antibiotic-resistant via multiple mechanisms and novel antipseudomonal strategies are urgently needed. MPs@pDA embedded composite hydrogels are encouraging tools in the fight against *P. aeruginosa* intrinsically resistant to most antibiotics.

In another work, another derivative of GG_8 was produced, again using dopamine as a functional group, GG-DA. Two new types of biocompatible and degradable polysaccharide/dendritic hybrid hydrogels have been developed by exploiting in the first case the electrostatic interactions occurring between the two biomaterials and subsequently exploiting an ionotropic crosslinking with Ca^{2+} ions and in another case the formation of dynamic imine bonds between the dopamine on the polysaccharide backbone and the amino groups of the dendrimer. Hybrid hydrogels possess flexible and tunable viscoelastic properties with storage modulus in the range of ~21.0-3.2 kPa for solid hydrogels, and in the range of ~2.1-0.5 kPa for injectable ones. The injectable hybrid hydrogels also exhibited shear-thinning and self-healing behavior, meeting flexural and motion requirements when injected into soft tissue. Furthermore, after *in vitro* co-culture, most hydrogels showed good

biocompatibility towards HDF, HaCaT, and RAW, indicating their great potential as dressing materials. Antimicrobial testing with two common bacterial strains characteristic of $Gram^+$ and $Gram^-$, *S. aureus* and *E. coli*, demonstrated that solid hydrogels cause complete eradication of bacteria after a few hours and injectable hydrogels cause a significant bacteria decrease. The results suggest that by using these two precursor materials it is possible to obtain adjustable systems for multiple applications. The two types of biocompatible and degradable hybrid hydrogels are in fact promising antibacterial systems that could be applied as dressings to prevent or treat bacterial infections.

In another work, the same GG-DA derivative was subsequently used as a reducing and/or capping agent for the *in situ* synthesis of two types of AgNPs, and then as the main vehicle for the production of microparticles (nano-in-microparticles), AgNPs@MPs. In particular, it was demonstrated that AgNPs can be produced via classical red-ox reaction, by exploiting the temperature-time dependent catechol oxidation, or via UV photoirradiation. AgNPs doped polymeric dispersions, containing 100% reduced silver, were converted into a versatile nano-into-micro antimicrobial powder named AgNPs@MPs stable in physiological media. As a proof of concept, to highlight the possibility of using the obtained powder to confer antimicrobial properties to a system that can be easily administered onto a wound bed, obtained AgNPs@MPs were dispersed into a hybrid hydrogel composed of OXG and HB10k-G5-alanine. In this way, through a bottom-up approach, made possible by the chemical versatility of the used macromolecules, it was possible to obtain nano-micro composite antimicrobial hydrogels whose viscoelastic properties can be tuned by varying the weight ratio between the two main constituents. Obtained hydrogels showed good antibacterial activities against gram-positive and gram-negative bacteria (*S. aureus* and *E. coli*) and resulted to be no toxicity toward eukaryotic cells. Based on these results we firmly

believe that these systems could be a valid alternative to eradicate bacterial infections in the wound.

5. Experimental Part

5.1 Physicochemical and rheological characterization of different low molecular weight gellan gum products and derived ionotropic crosslinked hydrogels

5.1.1 Materials

Gellan Gum (Gelrite®), sodium hydroxide (NaOH), tetramethylammonium chloride (TMACl), Live&Dead staining kit were purchased from Sigma-Aldrich (Italy). Fluorescein labelled dextran Anionic, Lysine Fixable (Dextran-FITC) (Mw 10 kDa) was purchased by Thermo Fisher Scientific. CellTiter 96® AQueous One Solution Cell Proliferation Assay (MTS) was purchased by Promega (Italy). Hydrolysis was conducted using rotating heating plate equipped with an independent temperature control/detection system. Size exclusion chromatography was conducted with an Agilent 1260 Infinity multi-detector GPC/SEC system. SEM analysis was conducted using a Phenom XL by Alfatest microscope operating at 5 kV. The rheological tests were carried out using a DHR-2 TA Instrument oscillatory rheometer equipped with a self-heating Peltier plate. Release studies were conducted with an UV-Vis spectrophotometer Shimadzu UV-240PC. Cell cultures were performed using an Eppendorf New Brunswik S41i incubator, the viability was measured with Eppendorf AF2200 spectrophotometer. Fluorescence images were obtained with AxioVert200 (Zeiss) microscope.

5.1.2 Methods

5.1.2.1 Production of low molecular weight GG

Basic hydrolysis of GG was performed as previously reported with slight modifications.[114,317] Briefly, GG was dispersed in 0.1 N NaOH solution at a concentration

of 1% w/ and kept at 50 °C using a rotating heating plate. A blade stirrer (200 rpm for 10 min) was used to disperse coarse particles and allow the hydration of the powder. At scheduled time points (4, 6, 8 and 24h), the pH of the dispersion was kept to 7 by adding HCl 1N, the dispersion was cooled down at room temperature and dialyzed against MilliQ (spectrapore RC membrane with cut-off 50 kDa) for at least 5 days. Based on the hydrolysis time, obtained samples were named GG_4, GG_6, GG_8, and GG_{24}.

5.1.2.2 Size exclusion chromatography analysis (SEC)

The absolute weight average molecular weight (Mw) and polydispersity index (PDI) of hydrolyzed GG products were measured by SEC using 0.025 M TMACl aqueous solution as a mobile phase and a Polysep P-4000 (Phenomenex) column as a stationary phase. The elution was conducted at 50 °C and with flow rate of 0.8 mL/min using 20 kDa PEG as internal standard. Before the elution, all the investigated samples were dissolved at 50 °C in the mobile phase.

5.1.2.3 Thermo-rheological and strain sweep experiments on low molecular weight GG aqueous dispersions

To conduct thermo-rheological analysis samples were dispersed in MilliQ water at a concentration of 5% w/v. Clear homogeneous dispersions were obtained placing the samples at 90 °C for 15 minutes. A parallel-plate geometry of 20 mm diameter was used for the experiments. Temperature dependence of storage modulus (G′) and loss modulus (G^2) values was analyzed by cooling the samples from 50 °C to 5 °C at a rate of 2 °C/min by applying a constant strain of 1% and a frequency of 0.5 Hz (3.14 rad/sec).

Samples were previously equilibrated at a temperature of 50 °C for 60 s and a pre-shear of 0.01 Hz for 10 s was performed. The linear viscoelastic region was preliminarily assessed at both at 50 °C and 5 °C by strain sweep experiments applying a constant frequency of 0.5 Hz in the range between 0.5–40% of deformation.

To the already described aqueous dispersions, strain sweep experiments were conducted at a constant frequency of 0.1 Hz (0.68 rad/sec) in the range from 0.01 to 100 of strain %.

5.1.2.4 GG hydrogels production, morphological study and evaluation of viscoelastic properties

Ionotropic crosslinking was carried by dispersing GG samples in MilliQ water at 80°C at a concentration of 2.5% w/v. To the hot dispersion $CaCl_2$ solution was added to get a final salt concentration of 10 or 20 mM. The final concentration of samples was set to 2% w/v. Gelation was carried out by letting the samples reach the room temperature. Obtained hydrogels were analyzed by frequency sweep test carried out at 25°C at a constant strain of 1% and frequencies ranging from 0.01 Hz to 10 Hz (0.0628 rad/sec to 62.8 rad/sec). A parallel plate geometry with radial groove and with an 8mm diameter upper plate was used for the experiments to avoid sample slippage. Each experiment was performed in triplicate. For stability tests GG hydrogels were produced as follows: 300 µL of hot aqueous dispersions (80 °C) at 5% w/v were poured into 48 well plate and cooled down to room temperature to induce the sample gelation. To the obtained hydrogels were incubated in orbital shaker incubator at 37°C with 1 mL of $CaCl_2$ 0.1 M for 1h. After this time, the medium was changed with DPBS pH 7.4 and the samples were further incubated at 37 °C refreshing the external medium every 72 hours.

At scheduled time intervals, hydrogels viscoelastic properties were investigated through rheological tests performed in frequency sweep regimes at 25 °C. Strain sweep experiments were preliminarily conducted with an oscillation frequency of 0.1 Hz (0.628 rad/sec) and variable strain percentages from 0.1% to 5% to investigate the linear viscoelastic region. Frequency sweep experiments were conducted at a constant strain of 1% and frequencies ranging from 0.01 Hz to 10 Hz (0.0628 rad/sec to 62.8 rad/sec). A parallel plate geometry with radial groove and with an 8mm diameter upper plate was used for the experiments to avoid sample slippage. Each experiment was performed in triplicate. Morphological analysis was conducted through SEM on freshly prepared samples. For this analysis hydrogels were washed with MilliQ water to eliminate the salt excess, frozen in liquid nitrogen, cut with a scalpel and freeze-dried.

5.1.2.5 Hydrogels swelling and releasing ability studies

Sample prepared as described above were washed in MilliQ water, freeze dried, accurately weighed and incubated in 1 ml of DPBS pH 7.4 at 37 °C in orbital shaker incubator. At scheduled time points, for the swelling analysis, the excess of medium was eliminated through blotting paper and swollen sample were weighed again.

Swelling percentage (Sw%) was expressed as using the following formula:

$$Sw\% = \left(\frac{W_{sw} - W_d}{W_d}\right) \times 100$$

Where W_{sw} indicates the weight of the hydrogel after swelling and W_d indicates the weight of the dry sample. Each experiment was performed in triplicate and the result was expressed as mean value ± standard deviation.

To the samples produced as already described, dextran-FITC was incorporated by mixing to the hot gelling dispersion, an aqueous solution of the fluorescent polysaccharide (1 mg/mL).

The amount of dextran-FITC into each scaffold was 0.4% w/w respect the GG weight. Release studies were conducted by submerging hydrogels (each obtained starting from 400 μL of hot gelling dispersion) in 2 mL of DPBS pH 7.4 at 37°C. After scheduled time points, the release medium was replaced with the same volume of fresh one and the amount of released dextran-FITC was calculated spectroscopically.

5.1.2.6 Cytocompatibility tests and cell encapsulation studies

Preosteoblastic cells MC3T3-E1 were cultured in DMEM medium supplemented with 10% v/v of FBS, 1% v/v of penicillin–streptomycin solution, 1% v/v of glutamine solution and 0.1% v/v amphotericin B solution. Freeze dried GG samples were sterilized by UV at 254 nm for at least 1 hour then dispersed in sterile water at a concentration of 2 mg/mL. Cells were seeded in 24 well plate ($2x10^4$ per well) and incubated for 24 h in a humidified incubator with 5% CO_2 atmosphere. A specific volume of GG dispersion was then injected in the supernatant medium to obtain 3 different concentrations. Cells viability was evaluated after 24 h by means of MTS assay following the manufacturer instructions. Each experiment was performed in triplicate. Viability was expressed as percentage compared with untreated cells. For cells encapsulation studies GG samples were sterilized as just described above and dispersed in sterile water at 2.5% w/v. MC3T3-E1 dispersion (100 μL, $1x10^6$/mL) was mixed with the polysaccharide dispersion (200 μL) into a 1 mL sterile syringe poured into a 48 well culture plate. Cells containing hydrogels were cultured for 72 h by adding 500 μL of culture medium into each culture well. The viability of cells into the constructs were evaluated with live/dead staining assay following the manufacturer instructions.

5.2 Ciprofloxacin releasing gellan gum/polydopamine based hydrogels with near-infrared activated photothermal properties

5.2.1 Materials

Gellan Gum (GelzanTM CM) of low acyl degree, 2-(3,4-Dihydroxyphenyl)ethylamine hydrochloride (Dopamine HCl), 4arm-PEG-Vinylsulfone (4-PEG-VS molecular weight 20 kDa), ciprofloxacin, succinic acid, polyvinyl alcohol (PVA molecular weight 10 kDa), Live/dead staining kit, Dulbecco's phosphate buffered saline (DPBS), TRIS buffer, were purchased from Sigma-Aldrich (Italy).

CellTiter 96® AQueous One Solution Cell Proliferation Assay (MTS) was purchased by Promega (Italy). Gellan gum-((2-aminoethyl)-carbamate) (GG-EDA) was produced as previously reported[112] the derivative used in this work had a functionalization degree in EDA moieties equal to 40±5 mol% calculated by ^{1}H-NMR analysis.

5.2.2 Methods

5.2.2.1 Synthesis of pDA

The oxidative self-polymerization reaction of dopamine hydrochloride (DA) was carried out in TRIS buffer at pH 8.5 (250 mg of DA in 100 mL) in the presence of atmospheric oxygen in a water bath at a temperature of 40 °C for 24 hours. The reaction product was purified by dialysis (membrane with 3500 Da cut-off) against a solution of 0.01M HCl and isolated by freeze drying. Average size and polydispersity index (PDI) measurements were determined by dynamic light scattering (DLS) at 25 °C using a Malvern Zetasizer NanoZS instrument fitted with a 532 nm laser at a fixed scattering angle of 173°. pDA particles used in this study showed a Z-average value of 279 nm and PDI 0,189.

5.2.2.2 Preparation of GG-EDA/PEG, GG-EDA/PEG/pDA hydrogels and morphological characterization

To prepare GG-EDA/PEG hydrogels, 4-PEG-VS MilliQ water solution was added to a GG-EDA aqueous dispersion at 80°C. The dispersion was kept at this temperature until it stops to flow upon tube inversion. The GG-EDA concentration in the obtained hydrogel was set to 5% w/v while the molar ratio between the pendant amine groups of the polysaccharide derivative and vinyl sulfone moieties of PEG was set to 5 (corresponding to a weight ratio between GG-EDA and 4-PEG-VS equal to 2). GG-EDA/PEG/pDA hydrogels were prepared dispersing pDA nanoparticles (MilliQ water solution 1 mg/ml) in the GG-EDA dispersion before the addition of synthetic crosslinker. Two different hydrogels were obtained using pDA nanoparticles at a concentration of 0.25 and 0.5% w/w respect to the GG-EDA. These samples were named GG-EDA/PEG/pDA 0.25 and GG-EDA/PEG/pDA 0.5 respectively. Round shaped samples with diameter of 11 mm and thickness of 0.5 mm were obtained by pouring of gelling solution (250 µl) into glass vials at 80°C.

Morphological analysis was conducted through scanning electron microscopy (SEM), using a Phenom XL by Alfatest operating at 5 k, on freshly prepared samples. For this analysis hydrogels were frozen in liquid nitrogen, cut with a scalpel and freeze-dried.

5.2.2.3 Rheological studies

The rheological tests were carried out using a DHR-2 TA Instrument oscillatory rheometer equipped with a flat geometry of 8 mm with radial groove and a self-heating Peltier plate. GG-EDA/PEG and GG-EDA/PEG/pDA hydrogels were analyzed at 37°C both by *amplitude sweep* experiments, performed a constant oscillation frequency of 0.1 Hz and a strain percentage ranging from 1 to 5%), and *frequency sweep* experiments, performed at a constant

strain of 1% and frequencies ranging from 0.01 to 10 Hz. Each experiment was performed in triplicate.

5.2.2.4 Studies of hydrogels swelling and hydrolytic resistance

To conduct swelling studies, as prepared GG-EDA/PEG and GG-EDA/PEG/pDA hydrogels were accurately weighed and incubated in 5 ml of DPBS pH 7.4 at 37 °C in orbital shaker incubator. At scheduled time intervals, swollen samples were weighed again after removing the excess of phosphate buffer with blotting paper. Swelling ratio (q) was expressed as the ratio between the weight of swollen sample and its starting weight. All experiments were conducted in triplicate.

Hydrolysis studies were conducted onto freeze-dried samples evaluating their weight after scheduled time intervals of incubation in DPBS pH 7.4 at 37°C.

5.2.2.5 Photothermal effect of hydrogels

Photothermal properties of GG-EDA/PEG and GG-EDA/PEG/pDA hydrogels were investigated by irradiating at 810 nm round cylindrical sample (with diameter of 11 mm and thickness of 0.5 mm) immersed in of DPBS pH 7.4 (1 mL) in a 24 well plate. Irradiation at variable power density of was conducted with a diode laser (GBox 15A/B by GIGA Laser) by positioning the irradiating source at 10 cm from the sample surface. At scheduled irradiation times the temperature was measured by immersing in the medium the fiber optical temperature probe or by means of IR thermal camera (Flir T250 Infra-Red with resolution of 240 x 180 pixels, sensitivity of 80mK NETD / 0.08 °C and measurable temperature range -20 °C/350 °C) previously calibrated.

To conduct photostability tests, five consecutive cycles of irradiation (80 sec) at different power density followed by free cooling periods were performed onto GG-EDA/PEG/pDA 0.5% samples. Temperature was registered by optical fiber probe soon after the irradiation and after each minute during the free cooling process.

5.2.2.6 Preparation of ciprofloxacin loaded GG-EDA/PEG/PDA 0.5 hydrogels and drug release experiments

Water soluble ciprofloxacin hemisuccinate microparticles were produced as reported elsewhere [393,394]. Obtained microparticles, containing 60% w/w of ciprofloxacin, resulted to be highly water soluble at room temperature. Antimicrobial loaded pDA containing hydrogles were prepared by mixing ciprofloxacin hemisuccinate (10 μL of 5mg/ml solution, corresponding to 30 μg of ciprofloxacin) with of GG-EDA/PEG/pDA 0.5% gelling solution (250 μL). Release studies were conducted by incubating hydrogels in of DPBS pH 7.4 (5 mL) at 37°C. At scheduled time intervals, medium (1 mL) was withdrawing and replaced with the same volume of fresh medium to calculate the amount of released drug by HPLC [395] using an Agilent 1260 Infinity instrument equipped with a Quaternary Pump VL G1311C and a DAD detector 1260 VL, 50 μl injector and a computer integrating apparatus (OpenLAB CDS ChemStation Workstation). A reversed phase column Luna Phenomenex C_{18} was employed as a stationary phase (25 °C), and PBS pH 2.7 /Acetonitrile (70:30) was used as a mobile phase with a flow of 0.8 ml/min. Release studies were also conducted irradiating the sample at scheduled time intervals at 810 nm (8 W cm^{-2}) for 80 sec. Unirradiated samples were used as a negative control. The amount of released ciprofloxacin was. Experiments were performed in triplicate.

5.2.2.7 In vitro cytocompatibility

In vitro cytocompatibility studies were conducted by evaluating the viability of human dermis fibroblasts (HDF) cultured in the presence of GG-EDA/PEG based hydrogels (with and without pDA). Cells were cultured in DMEM supplemented with fetal bovine serum (10% v/v), glutamine, penicillin-streptomycin solution, and amphotericin and cultured at 37° C and 5% CO_2 atmosphere. Freeze dried cylindrical hydrogels (with diameter of 11 mm and thickness of 0.5 mm) were sterilized by UV irradiation (254 nm for at least 1 hour using a 125 W UV-lamp), inserted into CellCrown insert (Sigma-Aldrich), conditioned with culture medium and placed into a 24 well plate containing $1´10^4$ cells seeded 24 hours earlier. Cell viability was measured, after 3 and 7 days of culture, by means of MTS assay following the supplier instructions and expressed as a percentage of viability compared to control cells cultured in the tissue culture plastic without hydrogels. During the experiment the culture medium was replaced every 2 days. Live/dead staining protocol was also performed following the supplier instruction. Fluorescence images were obtained with AxioVert200 (Zeiss) microscope.

5.2.2.8 In vitro antibacterial effect

According to EUCAST guidelines single colonies of *S. aureus* and *P. aeruginosa strains*, grown in Mueller-Hinton agar (Sigma-Aldrich, USA), were resuspended in sterile saline solution (0.9% NaCl) to achieve a turbidity equivalent to a 0.5 McFarland standard (1.5×10^8 CFU). Then, the bacterial suspensions were diluted 1:20 to reach an inoculum density of 7.5×10^5 CFU/mL and plated in two sterile 24 well plates where each microorganism was put into contact with GG-EDA/PEG/pDA 0.5% hydrogel. A first plate

was incubated at 37 °C overnight, while a second plate was subjected to 810 nm NIR laser exposure for 80 s before incubation. For *S. aureus* strain the experiment was repeated using four consecutive irradiation treatments (80 sec each hour). The antimicrobial effect was evaluated in each 10-fold dilution of the microbial suspensions in irradiated and non-irradiated subculture on Plate Count Agar OxoidTM and colony-forming units were counted.

5.3 Near-infrared light-responsive and antibacterial injectable hydrogels with antioxidant activity based on a Dopamine-functionalized Gellan Gum for wound healing

5.3.1 Materials

Low molecular weight gellan gum, GG_8 was produced as previously reported, starting from Gellan Gum (Gelzan™ CM), purchased from Merk (Italy).[332] Also tetrabutylammonium hydroxide (TBA-OH), bis (4-nitrophenyl) carbonate (4-NPBC), dopamine hydrochloride (DA), methoxy-polyethylene glycol amino (PEG-NH2, 2000 Da), colistin sulphate, acetone, anhydrous dimethyl sulfoxide (DMSOa), Dowex® 50WX8 resin, sodium hydroxide (NaOH), calcium chloride (CaCl2), phosphate buffer (Dulbecco's Phosphate-Buffered Saline DPBS), 1,1-diphenyl-2-picrylhydrazyl (DPPH), 2,2′-azino-bis(3-ethylbenzothiazoline-6-sulphonicacid) (ABTS) were purchased from Sigma -Aldrich (Italy). MTS reagent (CellTiter 96 AQueous One Solution Cell Proliferation Assay) was purchased from Promega. Deuterium oxide (D_2O) and sodium chloride (NaCl) were purchased from Merk (Italy).

Proton nuclear magnetic resonance (^{1}H NMR) spectra were recorded using a Bruker AC-300 instrument operating at 300.12 MHz. FT-IR analyzes were performed using Bruker Alpha equipment. UV measurements were performed using a Shimadzu UV-2401PC spectrophotometer. The rheological tests were carried out using a DHR-2 TA Instrument oscillatory rheometer equipped with a flat geometry of 20 mm in diameter and a self-heating Peltier plate (TA Instruments – Waters S.p.A.). The microparticles were produced using the BÜCHI Nano-Spray Dryer B-90. The optical microscope images were acquired through the AxioVert200 microscope (Zeiss). Scanning electron microscopy (SEM) was performed by

using a Phenom XL instrument, Alfatest. Release studies were analyzed using the Agilent 1260 Infinity HPLC instrument equipped with a G1311C VL quaternary pump, a 1260 VL DAD detector, a 50 µl injector and a computer integration apparatus (OpenLAB CDS ChemStation Workstation). A Luna Phenomenex C18 reversed phase column was used as the stationary phase (25 °C) and a mixture consisting of Na_2SO_4 (31.4mM, brought to pH = 2.5 with H_3PO_4) and Acetonitrile (70:30) with a flow of 0.6 ml / min. Hyperthermia studies were conducted through the GBox-15A / B Medical Diode Laser System and the temperature rise in the irradiated well was measured using a fiber optic temperature probe, CEM Discover SP (± 0.2 °C).

5.3.2 Methods

5.3.2.1 Synthesis and characterization of GG-DA-PEG derivatives

Both samples GG_8 and GG_{24} were produced from high molecular weight Gellan Gum (Gelzan®) as previously reported.[311] GG_8-DA-PEG and GG_{24}-DA-PEG were synthetized by dissolving 1 g of GG_8-TBA and GG_{24}-TBA in 80 ml of DMSOa each. GG_8-TBA or GG_{24}-TBA was activated in a water bath at 40 °C by adding 4-NPBC, previously dissolved in 10 ml of DMSOa, to obtain a final concentration of 1% w/v. The molar ratio set between the moles of 4-NPBC and the moles of the repetitive unit of GG_8-TBA and GG_{24}-TBA is equal to 0.5. After 4 hours of activation, the temperature was maintained at 40 °C and dopamine (DA) was added to obtain a molar ratio, Y, equal to 0.9. After 6 hours, methoxy-polyethylene glycol amino (PEG-NH_2) was added to obtain a molar ratio, Y', equal to 0.1 and the mixture was allowed to react for a further 18 hours. Then, 1 ml of NaCl saturated solution was added under stirring for 30 minutes. GG_8-DA-PEG and GG_{24}-DA-PEG were precipitated into an

excess of acetone, then washed several times with ethanol/water mixture (8: 2 v/v) and finally ethanol. After drying them to remove the washing solvent, the degree of functionalization in DA groups linked to GG_8 and GG_{24} was determined by ^1H NMR analysis (in D_2O) of both GG_8-DA-PEG and GG_{24}-DA-PEG comparing the peak at δ 6.8 attributable to the protons in the aromatic group of the dopamine (-CH_2-) with the peak at δ 1.10 attributable to the methyl group of gellan gum (-CH_3 of rhamnose portion of GG). The degree of molar derivatization in dopamine (DD_{DA}mol%) was determined by ^1H-NMR analysis. The products were also qualitatively characterized by FT-IR analysis and Uv-vis spectroscopy.

5.3.2.2 Production and characterization of MPs@pDA

GG_{24}-DA-PEG microparticles (MPs) were produced by spray-drying technique. The derivative GG_{24}-DA-PEG was dispersed in MilliQ water at a concentration equal to 0.5% (w/v). To allow the homogeneous dispersion of the polymer, the sample was placed in an oven at 90 °C for 1 hour. After cooling, the still fluid dispersion was filtered with 5 µm filters and sprayed at a temperature of 102 °C, using a spray cap with 5 µm pores. A spray rate of 78% has been set; filtered and dehumidified air was used as the drying gas at a flow rate of 117 l/min, resulting in an internal pressure of 30 mbar. The self-oxidation reaction of dopamine and the resulting polymerization was exploited produce a coating of polydopamine (pDA) on the surface of the microparticles. In particular, microparticles (100 mg) were placed in a Schlenk flask placed in an ice bath; a solution of dopamine (60 mg) in 1M $CaCl_2$ (20 ml) was added to the microparticles and slowly started to insufflate O_2. The reaction was carried out for 2 hours in a continuous flow of O_2. The dispersion was then centrifuged (8000 rpm, 4 °C, 10 min), washed three times with cold MilliQ water and finally

the MPs were freeze-dried. The morphology and size distribution of GG_{24}-DA-PEG MPs and MPs@pDA were studied through optical microscope observation and SEM analysis. 10 mg of microparticles were suspended in 1 ml of DPBS pH 7.4, the sample was sonicated for a few minutes and analyzed by optical microscope; while for SEM analysis, the sample was placed on the stub after being collected and then analyzed.

5.3.2.3 Preparation and characterization of hydrogels

It has been observed that the polymer dispersion of GG_8-DA-PEG in the presence of colistin sulfate forms a hydrogel, due to the electrostatic interactions between the polymer and the polypeptide antibiotic. Two hydrogels were prepared using two different concentrations of the polymer 2% and 3% (w/v) and a fixed concentration of colistin sulfate equal to 2.5% (w/w) Furthermore, two other hydrogels were prepared also incorporating MPs@pDA at a concentration equal to 15% (w / w) with respect to the polymer. In particular, for example, 30 mg of GG_8-DA-PEG, 0.75 mg of Colistin sulfate and 4.5 mg of MPs@pDA were used to produce 1 ml of the H3% @ MPs hydrogel. The four hydrogels thus obtained were called: H2% (GG_8-DA-PEG 2% + 2.5% Col); H3% (GG_8-DA-PEG 3% + 2.5% Col); H2%@MPs (GG_8-DA-PEG 2% + 2.5% Col + 15% MPs@pDA); H3%@MPs (GG_8-DA-PEG 3% + 2.5% Col + 15% MPs@pDA). The GG_8-DA-PEG was dispersed in an adequate volume of MilliQ water at 90 °C for 3 hours. After cooling to room temperature, the addition of colistin sulfate and MPs@pDA was carried out where necessary. Rheological analyses were carried out to study the viscoelastic behavior of the hydrogels. The region of linear viscoelasticity and the cross-point between G' and G" were determined through strain sweep analysis by applying to the sample a constant frequency equal to 0.1 Hz and an oscillation strain % between 0.01% and 1000%. The shear-thinning properties have been studied through the *flow-sweep* study

for shear rates between 1 and 1000 (1/s). The self-healing capacity was evaluated through the *recovery time* study: the samples were subjected to 7 cycles, each lasting 100 seconds, alternating a low strain% (1%) to a high strain% (500%), applying a frequency of 0.1 Hz. The analyses were performed with a plate-plate geometry with a diameter of 20 mm. For each test, 100 µl of the sample was loaded onto the bottom plate of the instrument and a gap value of 300 µm was set. All experiments were performed in triplicate at a temperature of 25 °C. The hydrogels have also been characterized by optical microscope observation and SEM analysis.

5.3.2.4 Hyperthermia studies

To study the photothermal conversion capacity, 500 µl of DPBS pH 7.4 were added to 500 µl of each of the hydrogels. Each sample was subjected to NIR light irradiating at λ=810 nm and using three different irradiation powers equal to 0.74W/cm^2, 1.48 W/cm^2 and 1.85 W/cm^2 for 10 minutes. In the same way, the photostability of the hydrogels was demonstrated through irradiation cycles (ON/OFF) lasting 5 minutes at a power of 1.48 W/cm^2.

5.3.2.5 Drug release studies

For drug release studies, 500 µl of each hydrogel were injected in 1 ml of DPBS pH 7.4 at 37 °C. The system was incubated in an orbital shaker at 37 °C and at programmed time intervals the medium was withdrawn and replaced with the same aliquot of fresh medium and stored under the same conditions. The amount of colistin released over time was determined by HPLC analysis using the equipment and method described previously in Apparatus section. In addition, 500 µl of each hydrogel were injected in 1 ml of DPBS pH 7.4 at 37 °C, then the system was incubated in an orbital shaker at 37 °C and, at programmed

time intervals, each sample was subjected to NIR irradiation at a wavelength of 810 nm, using a power of 1.48 W/cm^2 for a time of 5 minutes; subsequently the medium was withdrawn and replaced with the same aliquot of fresh medium and stored under the same conditions. The amount of colistin released over time was determined by HPLC analysis using the equipment and method described previously in the **5.3.1 paragraph**.

5.3.2.6 *In vitro* evaluation of antioxidant activity

5.3.2.6.1 DPPH free radical scavenging assay

DPPH (1,1-diphenyl-2-picrylhydrazyl) free radical scavenging assay was performed under the following protocol.[396]

A volume of 0.20 ml sample at different concentration was mixed with 0.20 ml of freshly prepared DPPH (0.1 mM) in ethanol and incubated for different times in the dark. The violet color of DPPH solution disappeared when it was reduced by test samples. The decrease in absorbance (Abs) was recorded by a spectrophotometer Shimadzu UV-2401PC at 520 nm. Results were shown in terms of SC_{50} values i.e. the minimum concentration of compounds required to scavenge 50% of DPPH radicals. All experiments were done in triplicate and compared with of starting GG. A blank (solution without samples and with a percentage of water equal to the percentage of sample used) and starting GG_8, as a control, were also used. The percentage of free radical scavenging was calculated by following equation:

$$Percentage\ of\ radical\ scavenging = \left\{\frac{[(Abs\ of\ Blank - Abs\ of\ Control) - Abs\ of\ Sample]}{(Abs\ of\ Blank - Abs\ of\ Control)}\right\} \times 100$$

5.3.2.6.2 $ABTS^{\bullet+}$ radical scavenging assay

The ($ABTS^{\bullet+}$) 2,2′-azino-bis(3-ethylbenzothiazoline-6-sulphonicacid) free radical cation scavenging ability protocol of the compounds was performed by the standard method [397]. ABTS solution and potassium persulfate solution were mixed in equal quantities and allowing to the oxidation reaction of ABTS by $K_2S_2O_8$ at room temperature in the dark to form the $ABTS^{\bullet+}$ radical. This solution was then diluted with ultrapure water to obtain an $ABTS^{\bullet+}$ radical solution which has an optical density of 0.700 ± 0.01 at 734 nm using a spectrophotometer Shimadzu UV-2401PC. 200 µl of sample were reacted with 600 µl of the $ABTS^{\bullet+}$ radical solution and the absorbance was measured at 734 nm after each set time using a spectrophotometer. The $ABTS^{\bullet+}$ scavenging capacity of the samples was compared with that of starting GG and reported with SC_{50} values (µg sample/ml). The free radical scavenging rate was calculated as reported for the previous assay.

5.3.2.7 Adhesion test

The adhesive capacity of H2%, H3%, H2%@MPs and H3%@MPs hydrogels was investigated by evaluating the ability of these hydrogels to adhere to two samples of previously cut porcine skin tissue in rectangular portions of 6 cm × 3 cm. For each hydrogel, a sample 300 µl was placed between the two swine skin samples; the contact area of the junction was equal to 9 cm^2. The overlap was pressed with a load of 200 g and left at 37 °C overnight to bond both surfaces. Therefore, the adhesion force was observed simply by placing different weights (20, 50, 100 and 200 g) at the end of one of the two substrates. As a comparison, a dispersion of GG_8-DA-PEG and a dispersion of the GG_8 at 3% (w/v) were also used, since one of the main objectives of the study is to demonstrate the improvement

of the bioadhesion properties of the gellan gum hydrogels following functionalization with dopamine.

5.3.2.8 *In vitro* cytocompatibility

HDF were cultured in DMEM supplemented with fetal bovine serum (10% v/v), glutamine, penicillin-streptomycin solution and amphotericin and cultured at 37 °C and 5% CO_2 atmosphere. *In vitro* cytocompatibility studies were conducted by evaluating the viability of HDF cultured in the presence of H2%@MPs and H3%@MPs hydrogels. To prepare the hydrogels, the starting powders were first sterilized by UV irradiation (254 nm for 30 minutes using a 125 W UV-lamp). The hydrogels were then produced as described above and 100 µl of each sample was injected into the CellCrown insert (Sigma-Aldrich), conditioned with culture medium and placed in a 24-well plate containing 2×10^4 cells seeded 24 hours earlier. Cell viability was measured, after 24 and 48 hours of culture, by means of MTS assay following the supplier's instructions and expressed as a percentage of viability compared to control cells cultured in the tissue culture plastic without hydrogels. The live/dead staining protocol was also performed following the supplier's instructions. In this experiment, fluorescence images were obtained with the AxioVert200 microscope (Zeiss).

5.3.2.9 *In vitro* evaluation of antibacterial activity

The antimicrobial activity of H2%, H3%, H2%@MPs and H3%@MPs hydrogels was investigated by modified Kirby–Bauer test. In the modified Kirby–Bauer test.[398]

P. aeruginosa ATTC 15442 reference strain was cultured in Tryptic Soy Agar (TSA) (Sigma Aldrich, USA), overnight at 37 °C. A bacterial suspension from overnight culture was prepared in NaCl 0.9 % (v/v), to a cell density of approximately 10^6 CFU/mL; then the bacterial suspension was dispensed onto TSA plates. Round-shaped H2%, H3%, H2%@MPs and H3%@MPs hydrogel samples were placed on the bacterial lawn seeded on TSA agar plates and incubated at 37 °C overnight. Other plates were prepared as described above and hydrogels were exposed to 1 NIR irradiation laser light (810 nm) for 5 minutes at 1.48 W/cm^2. After treatments, plates were incubated as above. After incubation time the plate were photographed and the average inhibition zone diameter around the dressings was measured and expressed in mm. Inhibition of planktonic growth was evaluated by the viable plate count of *P. aeruginosa* ATTC 15442 and *S. aureus* ATTC 25923. Bacterial cultures grown overnight, corresponding to 5×10^6 colony-forming unit (CFU)/ml, were prepared.[394] Then 25µl of each bacterial cultures were added to 24-well plates containing 2 mL of medium Tryptic Soy broth (TSB) (Sigma Aldrich, USA) and unique hydrogel samples without microparticles (H2%, H3%) or with microparticles (H2%@MPs and H3%@MPs). Tested samples were exposed to NIR light for 1 cycles 5 minutes at 1.48 W/cm^2. After laser treatment, plates were incubated at 37°C under stationary conditions at different times (2, 4, 6 and 24 h). Samples with hydrogels not irradiated were prepared and incubated as described. Three replicates were done for each system at different incubation times. Growth control wells containing microorganisms without hydrogels were performed for comparison under the same experimental conditions. After 24 hours of incubation, 100 µl of bacterial suspension was removed from each well and utilized for the bacterial count. Briefly, the inocula were added in test tubes with 10 ml of NaCl (0.9% w/v solution), 10-fold dilutions were prepared, and 100 µl aliquots of each dilution were plated onto Tryptic Soy Agar (TSA) (Sigma Aldrich, USA) plates. The plates were incubated at 37°C overnight. Each assay was

performed in triplicate and repeated at least twice. To quantify the number of viable bacteria in each system, the value of CFU/ml was determined.

5.4 Antibacterial broad-spectrum dendritic/gellan gum hybrid hydrogels with rapid shape-forming and self-healing for wound healing application

5.4.1 Materials

Low molecular weight gellan gum, GG was produced as previously reported.[332] Starting Gellan Gum (Gelzan™ CM), tetrabutylammonium hydroxide (TBA-OH), bis (4-nitrophenyl) carbonate (4-NPBC), dopamine hydrochloride (DA), sodium chloride (NaCl), acetone, anhydrous dimethyl sulfoxide (DMSOa), Dowex® 50WX8 resin, sodium hydroxide (NaOH), calcium chloride ($CaCl_2$), phosphate buffer (Dulbecco's Phosphate-Buffered Saline DPBS), and deuterium oxide (D_2O) were purchased from Merk (Italy). TMP-G2-alanine synthesized as previously reported.[298] Dulbecco's modified Eagle medium (DMEM) fetal bovine serum (FBS), penicillin-streptomycin, glutamine, and amphotericin B, Calcein AM and Alamar Blu reagent were purchased from Thermo Fisher Scientific. Mueller–Hinton broth (MHB II) was purchased from Fluka. MHB II agar was from Sigma-Aldrich.

Escherichia coli 178 (*E. coli* 178) was kindly provided by Prof. Paul Orndorff from North Carolina State University. *Staphylococcus aureus* 2569 (*S. aureus* 2569) was obtained from the company DSMZ. Human dermal fibroblast (HDF) and mouse monocyte (RAW 264.7) cells were purchased from the American Tissue Culture Collection (ATCC). Human epidermal keratinocyte (HaCaT) cells were obtained from kindly provided by Prof. Annelie Brauner from Karolinska Institutet (Sweden).

Fourier-transform infrared spectroscopy (FT-IR) was performed with a Perkin-Elmer spotlight 400 FTIR system (Waltham, MA, USA) equipped with a single reflection attenuated total reflectance (ATR) in the region of 600–4000 cm^{-1}. The rheological tests

were carried out using a DHR-2 TA Instrument oscillatory rheometer equipped with a flat geometry of 8 mm in diameter (TA Instruments – Waters S.p.A.). The optical microscope images were acquired through the Eclipse Ti microscope (Nikon). Scanning electron microscopy (SEM) analyses were conducted using S-4800 field emission scanning electron microscope (Hitachi, Tokyo, Japan).

5.4.2 Synthesis of GG-DA

GG was produced from high molecular weight Gellan Gum (Gelzan®) under alkaline conditions as previously reported.[332] The ammonium-tetrabutyl salt (TBA) was prepared elsewhere and reported to allow its dispersion in organic solvents.[317] GG-DA was synthesized by dissolving GG-TBA (1 g) in DMSOa (80 ml). GG-TBA was activated in a water bath at 40 °C by adding 4-NPBC, previously dissolved in DMSOa (10 ml), to obtain a final concentration of 1% w/v. The molar ratio set between the moles of 4-NPBC and the moles of the repetitive unit of GG-TBA is equal to 0.5. After 4 hours of activation, the temperature was maintained at 40 °C, and dopamine (DA) was added to obtain a molar ratio, Y, equal to 5. The mixture was allowed to react for a further 24 hours. Then, NaCl (1 ml) saturated solution was added under stirring for 30 minutes. GG-DA was precipitated into an excess of acetone, then washed several times with ethanol/water mixture (8: 2 v/v), and finally pure acetone twice. After drying them to remove the washing solvent, the derivative, previously dispersed in the minimum possible quantity of MilliQ water, is dialyzed (cut off 12-14 kDa) for 5 days in order to purify it from any remaining NaCl residues, and after this time, it is recovered by freeze-dried. The weight yield was 83% expressed with respect to the initial weight value of GG-TBA. Both the hybrid solid and injectable hydrogels have

also been characterized by Fourier Transform Infrared Spectrometry (FTIR) and Scanning Electron Microscopy (SEM) analyses, after freeze-drying.

5.4.3 Hydrogel production

The hydrogels were produced by dispersing GG-DA in DI water (80 °C 10 min). The TMP-G2-alanine, synthesized as previously reported,[298] was dispersed in DI water at the w/w concentration with respect to the GG-DA shown in **Table 9.** For the formation of hydrogels, two different approaches were used. 4 solid and 4 injectable hydrogels were produced. The pH was adjusted to 6.5 before mixing the two solutions to produce the hybrid solid hydrogels. Briefly, these solids hydrogels were produced by dispersing dendrimer and polymer at the concentrations shown in **Table 9**. The two solutions were injected and vortexed for 1 minute, then these hydrogels were placed in 0.1M $CaCl_2$ (1 ml) for 1 h to 4 °C and then washed twice with DI water. As controls, two hydrogels were produced using only the solution of GG-DA at 3% and 4% w/v and placing them in 0.1M $CaCl_2$ for 1h at 4 °C and then washed twice with DI water. The pH of GG-DA was also adjusted to 8.5 with 0.1 M NaOH, until the solution became brown, to produce the hybrid injectable hydrogels. In particular, the injectable hydrogels were prepared gently mixing directly both the solutions of GG-DA and TMP-G2-alanine into the vial, until the solution became homogeneous. Then the hydrogel was placed in a syringe using the pipette for viscous solutions HandyStep®.

Table 9. Composition of hybrid hydrogels.

Hydrogels (total volume: 1 ml)	Amount GG-DA	Amount TMP-G2-alanine
	mg	mg
$H1_{sol\ or\ inj}$	30	30
$H2_{sol\ or\ inj}$	30	15
$H3_{sol\ or\ inj}$	40	40
$H4_{sol\ or\ inj}$	40	20
H1k	30	-
H3k	40	-

5.4.4 Swelling of hybrid hydrogels

For the studies of swelling, the solid and the injectable hydrogels were prepared following the procedures described in the previous paragraphs. 50 µl of each hydrogel was then frozen, freeze-dried, and weighed carefully. The swelling studies were conducted by incubating the samples at 37 °C in DPBS (2 ml) pH 7.4 until 48 h. At the time of analysis, the swollen samples were weighed after removing the excess of buffer with blotting paper.

The swelling percentage (Sw%) was calculated as:

$$Sw\% = \left(\frac{W_{sw} - W_d}{W_d}\right) \times 100$$

Where W_{sw} is the weight of the hydrogel after swelling and W_d is the weight of the dry sample.

Each experiment was performed in triplicate and the results were expressed as mean value ± standard deviation.

5.4.5 Degradation of hybrid hydrogels

The hydrolytic degradation study was performed by incubating freeze-dried samples in DPBS pH 7.4 at 37 °C. The samples were washed with Milli-Q water twice, at scheduled time intervals, then freeze-dried, and weighed carefully. The degradation of the samples was expressed as weight recovered percentage (W_r%), calculated as:

$$Wr\% = \left(\frac{W_f}{W_i}\right) \times 100$$

Where W_f is the weight of the degraded sample at each time point and W_i is its starting weight.

Each experiment was performed in triplicate and results were expressed as mean value ± standard deviation. The degradation studies were also performed by studying the change in the viscoelastic profile of hydrogels over time. Rheological analyses were performed both amplitude sweep and frequency sweep, using the same specifications as shown in the **5.4.7 paragraph**, but at a temperature of 37 ° C. In particular, the samples were washed with Milli-Q water twice, after each time of incubation at 37 °C in DPBS pH 7.4, and then they have been analyzed.

5.4.6 Leaching analysis of the hybrid hydrogels

A leaching study of both hybrid solid and injectable hydrogels was conducted in DPBS solution (pH 7.4) at 37 °C. The hybrid hydrogels (formed with a total volume of 50 µL) were prepared and immersed in DPBS (1 ml), 5 µL aliquots were collected at different time intervals of 1, 2, 4, and 8 h, and the components of the samples were further analyzed by MALDI-TOF-MS.

5.4.7 Rheological characterization

For rheological experiments, all of the hydrogels (50 µl) were placed on a parallel plate geometry with an 8 mm diameter upper plate. The LVE (Linear Viscoelastic region) was preliminarily assessed by *strain sweep* experiments applying a constant frequency of 1 Hz and an oscillation strain % between 0.01% and 1000% at 25 °C. The measurement gap was set at 500 µm for all analyses. Viscoelastic properties were evaluated also at 25 °C by performing *frequency sweep* measurements in the range 0.01–100 Hz by applying a constant strain% of 0.1%. For the injectable hydrogels were also studied the shear-thinning and the self-healing behaviors. The shear-thinning properties have been studied through the *flow-sweep* study for shear rates between 0.1 and 1000 (1/s). The self-healing capacity was evaluated through the *recovery time* study. The samples were subjected to 7 cycles, each lasting 100 s, alternating a low strain% (1%) to a high strain% (500%), applying a frequency of 0.1 Hz. All experiments were performed in triplicate at a temperature of 25 °C.

The self-healing of the samples was calculated as:

$$Self - healing\ efficiency\ \% = \frac{G_2'}{G_1'} \times 100$$

Where G'_1 is the original storage modulus of the sample and G'_2 is its storage modulus after large strain failure, according to the rheological data.

Each experiment was performed in triplicate and results were expressed as mean value ± standard deviation.

5.4.8 Macroscopic adhesiveness tests

The adhesive ability of both solid and injectable hybrid hydrogels was investigated by evaluating the macroscopic ability of these hydrogels to adhere to different substrates, such as glass, plastic, metal, aluminum foil, wood, and pig skin. The hydrogels were simply placed on the substrates and after a few seconds, they tried to flip the substrates or move them quickly as shown in the video. In particular, for the test with porcine skin some precautions were followed, fresh porcine skin pieces (2 cm width), in which their fat layer has been removed as much as possible by a scalpel, were rinsed in PBS (pH 7.4) for 30 min before the test. Then 50 μl of each hydrogel was applied onto the surface of a wet porcine skin piece as for all other substrates.

5.4.9 Cytotoxicity tests

50 μl of each of the cylinder-shaped hydrogels were previously sterilized by UV lamp and they were placed directly into a 48-well plate containing 1×10^4 cells (HDF, HaCaT, and RAW) seeded 24 h earlier with another fresh medium (total amount 1 ml). After 24 h, Alamar Blue was added and the incubation was continued for 4 h (37 °C, 5% CO_2). The fluorescence intensity was measured at ex/em 560/590 nm for the Alamar Blue assay. The images were acquired with the Eclipse Ti microscope (Nikon). All experiments were conducted in triplicate.

5.4.10 Antibacterial assays of the hybrid hydrogels

The minimum inhibitory concentration (MIC) and minimum microbicidal concentration (MBC) of the TMP-G2-alanine were tested using the broth dilution method.[399] Briefly, a single colony of both of the bacteria (*S.aureus* 2569 and *E.coli* 178) from the agar plate was suspended in MHB II broth and incubated with shaking at 37 °C to log phase. The suspended bacteria were then diluted with broth to reach a concentration of 10^6 CFU mL^{-1}. The sample was diluted in 96-well plates using the double dilution method, and then the bacteria solutions were added to the wells to yield a final concentration of 5×10^6 CFU mL^{-1}. Wells containing bacterial cells only and containing broth only were used as controls. The optical density (OD = 620 nm) was used to determine MIC values after incubation at 37 °C with shaking for 18 h. The plate counting method was used at the end to determine microbicidal concentrations. Both MIC and MBC tests were done in triplicate. The antibacterial property of the hybrid hydrogels was tested using the disk diffusion test. *E. coli* 178 and *S. aureus* 2569, as typical gram-negative and gram-positive strains, were used in the test. The 50 µl cylinder-shaped hydrogels were put on MHB II agar containing bacteria (concentration roughly 10^7 CFU/mL). The plates were cultured at 37 °C overnight and the diameters of the inhibition zones were measured. All measurements were performed in triplicates. The antibacterial property of the 50µl cylindrical hybrid hydrogels was also tested in bacterial solution. *E. coli* 178 and *S. aureus* 2569 were cultured in MHB II broth at 37 °C with shaking of 250 rpm overnight. Each bacterial solution at the log phase was diluted to a concentration of 10^5 CFU/mL. Then the cylindrical hybrid hydrogels were added into a 48-well plate, where each well contained 1 ml of bacterial solution, and the plate was transferred into the incubator and incubated at 37 °C for 4, 6, and 8 h. After the incubation, the plate counting method was used to calculate the bacterial concentrations in the wells. Wells without the

treatment of hydrogels were used as a positive control. All measurements were performed in triplicate.

5.5 In situ synthesis of silver nanoparticles and development of nano/micro-composite injectable hydrogel with antimicrobial activity

5.5.1 Materials

Gellan Gum (Gelzan™ CM), tetrabutylammonium hydroxide (TBA-OH), bis (4-nitrophenyl) carbonate (4-NPBC), dopamine hydrochloride (DA), sodium chloride (NaCl), acetone, anhydrous dimethyl sulfoxide (DMSOa), Dowex® 50WX8 resin, sodium hydroxide (NaOH), silver nitrate ($AgNO_3$), 2,2′-azino-bis(3-ethylbenzothiazoline-6-sulphonicacid) (ABTS), calcium chloride ($CaCl_2$), phosphate buffer (Dulbecco's Phosphate-Buffered Saline - DPBS), and deuterium oxide (D_2O) were purchased from Merk (Italy). HB10K-G5-alanine synthesized as previously reported [380]. Xanthan Gum (XG) (VANZAN® NF-C) was purchased from Vanderbilt Minerals, LLC. Sodium periodate, Dulbecco's modified Eagle medium (DMEM) fetal bovine serum (FBS), penicillin-streptomycin, glutamine, and amphotericin B, Alamar Blu reagent were purchased from Thermo Fisher Scientific. Mueller–Hinton broth (MHB II) was purchased from Fluka. MHB II agar was from Sigma-Aldrich.

Escherichia coli 178 (*E. coli* 178) was kindly provided by Prof. Paul Orndorff from North Carolina State University. *Staphylococcus aureus* 2569 (*S. aureus* 2569) was obtained from the company DSMZ. Human dermal fibroblast (HDF) and mouse monocyte (RAW 264.7) cells were purchased from the American Tissue Culture Collection (ATCC).

Proton nuclear magnetic resonance (^{1}H NMR) spectra were recorded using a Bruker AC-300 instrument operating at 300.12 MHz. FT-IR analyses were performed using Bruker Alpha equipment. UV measurements were performed using a Shimadzu UV-2401PC spectrophotometer. The rheological tests were carried out using a DHR-2 TA Instrument

oscillatory rheometer equipped with a flat geometry of 20 mm in diameter and a self-heating Peltier plate (TA Instruments – Waters S.p.A.). The microparticles were produced using the BÜCHI Nano-Spray Dryer B-90. The optical microscope images were acquired through the AxioVert200 microscope (Zeiss). The samples for the scanning electron microscopy (SEM) analyses were coated with 10 nm of Pt in a 208HR high-resolution sputter coater (Cressington, Watford, UK). SEM analyses were conducted using S-4800 field emission scanning electron microscope (Hitachi, Tokyo, Japan). Transmission electron microscopy (TEM) was performed by using a transmission electron microscope HT7700 (Hitachi, Tokyo, Japan), operated at 100 kV and equipped with the 2k × 2k CCD camera (AMT XR41, USA) and a W filament.

5.5.2 Production and characterization of AgNPs in the presence of GG or GG -DA

Silver nanoparticles (AgNPs) were produced by *in situ* chemical reduction, using GG or GG-DA as a reducing and capping agent. An aqueous solution of 20 mM silver nitrate ($AgNO_3$) was prepared and mixed with a dispersion of GG or GG-DA in MilliQ water to obtain a final concentration of 0.5% (w/v) of the polymer and 5 mM in $AgNO_3$. The reduction of silver to obtain AgNPs was carried out at pH 6 at different temperatures and reaction time intervals. These nanoparticles were called AgNPs (T). Another reduction method of AgNPs was carried out by UV-irradiation (265nm 100V) for 30 minutes of the just described silver salt containing polymeric dispersion (only GG-DA was used in this case). These nanoparticles were called AgNPs (UV). The UV-Vis spectrum of the dispersions was recorded (Shimadzu UV-2401PC spectrophotometer). All the samples obtained, at the end of the analysis, were frozen and dried by freeze drying to be observed under the scanning electron microscope (SEM) (Phenom XL instrument, Alfatest).

5.5.3 Nano-into-micro AgNPs@MPs production

The microparticles were produced by a spray-drying technique using the BÜCHI Mini Spray Dryer B290. The dispersions of GG-DA with both AgNPs (T) and AgNPs (UV) produced in situ were nebulized according to the following parameters: inlet T: 130 °C; outlet T: 70–73 °C; aspiration: 100%; feed pump: 15% (4.5 mL/min); atomizer nozzle: 0.7 mm; used gas: compressed air. The particles obtained in this way were named AgNPs@MPs (T) and AgNPs@MPs (UV). Similarly, control microparticles were produced only using the 0.5% (w/v) GG-DA dispersion called MPs.

5.5.4 AgNPs@MPs characterization

5.5.4.1 Microscopy: SEM and TEM

The morphology and size distribution of MPs and both the AgNPs@MPs (T) and AgNPs@MPs (UV) were studied by SEM observation. They were coated with 10 nm of Pt in a 208HR high-resolution sputter coater (Cressington, Watford, UK) and then SEM analysis was conducted using an S-4800 field emission scanning electron microscope (Hitachi, Tokyo, Japan). The size distribution of the microparticles was done using ImageJ based on multiple registered SEM images. To perform the TEM analyses, the samples were prepared by dispersing both the AgNPs@MPs (T) and AgNPs@MPs (UV) at a concentration of 1mg/ml in ethanol absolute and placing a drop of the dispersion on a carbon-coated copper TEM grid (EM-Tec Formvar Carbon support film copper 200 square mesh) and dried at room temperature in a clean environment. Images were taken in a vacuum in high contrast mode. The size distribution of the silver nanoparticles was done using ImageJ based on multiple registered TEM images.

5.5.4.2 Spectroscopy: FTIR and XPS analyses

Fourier transform infrared (FT-IR) spectroscopy (Vertex 80 V, Bruker, USA) was carried out to examine the functional groups and purity of dry AgNPs@MPs (T and UV) and MPs samples over the infrared spectrum range from 600 cm^{-1} to 4000 cm^{-1}. The stability of the microparticles was instead studied by observation under an optical microscope.

X-ray photoelectron spectrophotometer (XPS) analyses were conducted with the PHI 5000 VersaProbe II instrument (ULVAC-PHI, Inc., Kanagawa, Japan) with a source: Al Kα (1486.6 eV) and a 128-channel hemispherical analyzer, FAT mode.

5.5.4.3 Stability of AgNPs@MPs

For the stability studies, 2 mg of microparticles for each batch produced were suspended in 1 ml of 0.1 M $CaCl_2$ and DPBS (pH = 7.4) respectively in 2 ml Eppendorf microtubes, to carry out a treatment at 4 ° C for 24 hours. After this time, all the samples were centrifuged, washed in DPBS, and carried out a sonication of 15 minutes; then they were observed under an optical microscope. Subsequently, the samples were kept in the dark and incubated at 37 °C and were observed after 1 hour, 3 hours, 24 hours, and 7 days.

5.5.4.4 Inductively Coupled Plasma Mass Spectrometry analyses

To determine the quantity of Ag present in both the AgNPs@MPs (T) and AgNPs@MPs (U) by ICP/MS experiments, the sample was previously digested and mineralized using a microwave oven MARS-5 Xpress (CEM, World Headquarters, Matthews, NC, USA) with a high-pressure rotor. [400] In particular, the carefully weighed sample was treated with 1 ml of HNO_3 (65%) and 1 ml of H_2O_2 (30%) and then mineralized at a temperature of 200 °C. The samples of AgNPs@MPs (T) and AgNPs@MPs (U) were diluted 1100 folds using 1% nitric

acid solution, and a volume of 10 ml of diluted solutions were analyzed by Inductively Coupled Plasma Mass Spectrometry (ICP-MS) (X Series II, Thermo Fisher Scientific, Rodano, Italy). Calibration standards for silver were arranged on a daily basis by stepwise dilution of the silver standard 1000 mg L^{-1}in a 1% HNO_3 medium to yield final concentrations of 0, 0.5, 0.75, 1.0, 5.0, 10.0, 25.0, 50.0, 100.0, 250.0, 500 µg L^{-1}. The silver ion was determined at m/z 107. The detection limit was assessed as 3 standard deviations (SD) of the concentration in blank sample. Solution containing, Y (50 µg L^{-1}) was used as internal standards to compensate for any signal instability or sensitivity changes during the analysis. A solution of HNO_3 2% as blank was used.

5.5.5 Preparation of oxidized Xanthan Gum (OXG)

Oxidized xanthan gum was prepared based on previous work [401]. Approximately 1.0 g of xanthan gum was dissolved in 160 mL of MilliQ water. Then, sodium periodate solution was added to the xanthan gum solution. The molar ratio between the moles of repetitive units of XG and the moles of $NaIO_4$ was set at 1:1.5. After the mixture was stirred in the dark at 40°C for 3 h, the reaction was quenched by adding 2.0 ml of ethylene glycol, which reacted with excess $NaIO_4$. The oxidized product, referring to oxidized xanthan gum (OXG), was placed under dialysis (cut-off 12-14 kDa) against MilliQ water for 4 days (the water was renewed at least 5 times per day). It was then recovered and subjected to freeze-drying (**Figure 63**). The oxidation degree (OD) of OXG was calculated as follows by potentiometric titration of the NaOH/hydroxylamine hydrochloride solution:

$$OD = \frac{n\,(NaOH)\ \times\ \Delta V}{\frac{m\,(OXG)}{M\,(OXG)}} \times \frac{1}{8} \times 100$$

Where: n(NaOH) is 0.1 M, ΔV is the recorded NaOH consumed (L), m is the mass of OXG (g), and M is the molecular weight of the repeating unit OXG (993 g/mol).[402]

5.5.6 Production of hydrogels loaded with AgNPs@MPs

First, a hydrogel was prepared using 10 mg of OXG dissolved in 400 µL of MQ water and 10 mg of HB10k-G5-ala in 100 µL of MQ water. This was called XH_1. A second hydrogel using a 2:1 ratio of the oxidized polysaccharide and the hyperbranched polymer was then prepared by mixing 10 mg of OXG and 5 mg of HB10k-G5-ala using the same volume used previously. This was called $XH_{0.5}$. Both hydrogels were loaded with 5 mg of AgNPs@MPs (pH) and AgNPs@MPs (UV). Four types of hydrogels were thus obtained. The names and concentrations are shown in **Table 10.**

Table 10. Hydrogels prepared using different amounts of OXG, HB10k-G5-alanine, and AgNPs@MPs (T or UV).

Sample	OXG (final concentration w/v)	HB10k-G5-alanine (final concentration w/v)	AgNPs@MPs (final concentration w/v)
XH_1	2%	2%	-
XH_1-Ag(T)	2%	2%	1%
XH_1-Ag(UV)	2%	2%	1%
$XH_{0.5}$	2%	1%	-
$XH_{0.5}$-Ag(T)	2%	1%	1%
$XH_{0.5}$-Ag(UV)	2%	1%	1%

5.5.7 Characterization of hydrogels loaded with AgNPs@MPs

5.5.7.1 SEM analyses

The hydrogels were frozen, fractured with a sharp razor and freeze-dried, then coated with 10 nm Pt in a 208HR high-resolution sputter coater (Cressington, Watford, UK). All

hydrogels were characterized by SEM analysis, performed with an S-4800 field emission scanning electron microscope (Hitachi, Tokyo, Japan).

5.5.7.2 Rheological characterization of the hydrogels

The rheological analyses were carried out to study the viscoelastic behavior of the hydrogels. In particular, the analyses were performed using a DHR-2 TA Instrument oscillatory rheometer equipped with a plate-plate geometry with a diameter of 20 mm (TA Instruments – Waters S.p.A.). For each test, 100 µl of the sample was loaded on the bottom plate and a gap value of 300 µm was set . All experiments were performed in triple at a temperature of 25 °C. The analysis of oscillation amplitude sweep was carried out to determine the linear viscoelasticity region (LVR), applying the sample a constant frequency of 0.1 Hz and a percentage of oscillatory strain between 0.1% and 1000%. Frequency sweep experiments have been performed to a constant strain of 1% and frequencies racing from 0.06 to 100 rad/sec. The shear thinning properties have been studied through flow-sweep analyses for shear rates between 0.1 and 1000 (1/s). In addition, the samples were subjected to 7 cycles, each lasting 100 s, alternating a low strain (1%) with a high strain (500%), applying a frequency of 0.1 Hz in order to evaluate its self-healing capacity through the analysis of recovery time. The self-healing efficiency of the samples was calculated as:

$$Self-healing\ efficiency\ \% = \frac{G_2'}{G_1'} \times 100$$

Where G'_1 is the mean of original storage modulus (strain% = 1% first cycle) of the sample and G'_2 is the mean of its storage modulus after the healing occurring following the large strain failure (strain% = 500%)[403]. Each experiment was performed in triplicate and results were expressed as mean value ± standard deviation.

5.5.8 $ABTS^{\bullet+}$ radical scavenging assay

The ($ABTS^{\bullet+}$) 2,2′-azino-bis (3-ethylbenzothiazoline-6-sulphonicacid) assay was used to evaluate the antioxidant and free radical scavenging capacity of microparticles. The radical $ABTS^{\bullet+}$ was formed following the oxidation reaction, carried out at room temperature in the dark for 16 hours, between a solution of ABTS (7 mM) and a solution of potassium persulfate (2.45 mM) mixed in the same quantity. This solution was then diluted with MilliQ water. UV spectroscopy is used to measure the resulting absorbance, to obtain an $ABTS^{\bullet+}$ radical solution with an optical density of 0.700 ± 0.01 at 734 nm. The MPs and both AgNPs@MPs(T) and AgNPs@MPs(UV) were placed in contact with the radical solution at increasing concentrations (0.03125 - 1 mg/ml) and the absorbance was measured at 734 nm within 15 minutes. The $ABTS^{\bullet+}$ scavenging ability of samples was reported with SC50 values (mg sample/mL). The free radical scavenging percentage was calculated using the following equation:

$$Radical\ scavenging\ (\%) = \left(\frac{Abs\ Control - Abs\ Sample}{Abs\ Control}\right) \times 100$$

Where *Abs Control* is the absorbance corresponding to the $ABTS^{\bullet+}$ solution and *Abs Sample* is the one corresponding to the $ABTS^{\bullet+}$ solution after reacting with the microparticles.

For the radical scavenging assay of the hydrogels, the same procedure was carried out. In particular, 50 µL of each hydrogel, $XH_{0.5}$, $XH_{0.5}$-Ag (T), and $XH_{0.5}$-Ag (UV), was placed in contact with 600 µL of $ABTS^{\bullet+}$ radical solution. The absorbance was measured at 734 nm within 15 minutes. The free radical scavenging percentage was calculated using the above equation. Each experiment was performed in triplicate and results were expressed as mean value ± standard deviation.

5.5.9 *In vitro* cytotoxicity tests

Weighed quantities of MPs and both AgNPs@MPs(T) and AgNPs@MPs(UV) were previously sterilized by a UV lamp. Then the samples were dispersed in MilliQ water at a known concentration. Then the dispersions were inserted into ThinCert™ insert (Greiner bio-one) and conditioned with DMEM cells-medium for 10 min. Subsequently, the samples were placed into a 24-wells plate containing 2×10^4 cells (RAW and HDF) seeded 24h earlier with fresh medium (total amount 1ml). The final concentrations of all samples were: 500 µg/ml; 100 µg/ml and 10 µg/ml. After 24h, Alamar Blue was added and the incubation was continued for 4 h (37 °C, 5% CO_2). The fluorescence intensity was measured at ex/em 560/590 nm for the Alamar Blue assay. To prepare the composite hydrogels, XH_1, XH_1-Ag (T), and XH_1-Ag (UV), the starting powders were first sterilized by UV irradiation (254 nm for 30 min using a 125 W UV lamp). The hydrogels were then produced as described above and 100 µl of each sample was injected directly into the 24-well plate containing 2×10^4 cells seeded 24 h earlier (RAW and HDF cells). After 24 h of incubation, cell viability was measured by means of the MTS assay following the supplier's instructions and expressed as a percentage of viability compared to control cells cultured in the tissue culture plastic without hydrogels. All experiments were conducted in triplicate.

5.5.10 Antimicrobial assays

5.5.10.1 MIC and MBC of microparticles

MIC was conducted using the broth dilution method [399]. A single colony of the bacteria from the agar plate was suspended in MHB II broth and incubated with shaking at 37 °C until log phase concentration. The bacteria solution was then diluted with fresh broth to reach a

concentration of 10^6 CFU mL^{-1}. MPs, AgNPs@MPs(T), and AgNPs@MPs(UV) were dissolved totally in MilliQ water, and then the compounds were diluted using the double dilution method. The bacteria solution was added to the wells with equal compound solutions, yielding a final concentration of 5×10^5 CFU mL^{-1}. Wells containing bacterial cells only and those containing MHB only were used as controls. The plates were incubated at 37 °C with shaking for 18 h and then the optical density (OD = 620 nm) was used to determine the MIC values. For the MBC the same procedure was conducted, except that the plate counting method was used at the end to determine the microbicidal concentrations.

5.5.10.2 In vitro evaluation of the antibacterial activity of the nano/micro-composite hydrogels

As a preliminary antibacterial study, the disk diffusion test was performed using two different bacterial strains, *S. aureus*, and *E. coli*. Composite hydrogels loaded with AgNPs@MPs(T or UV), XH_1-Ag(T), and XH_1-Ag(UV), and free of microparticles, XH_1 (negative control), were prepared for testing. Cylinder-shaped composite hydrogels were formed from 50 µL. The final amounts of AgNPs@MPs(T or UV) in each hydrogel corresponded to 500 µg. The composite and no-composite hydrogels were then placed on MHB II agar plates containing bacteria in a concentration of $\approx 1 \times 10^7$ CFU mL^{-1}. Then the plates were incubated at 37°C for 24 hours. The diameters of the inhibition zones were measured after this time. The test was performed in triplicate for each sample. The antibacterial activity of the hydrogels was tested following an established protocol with changes [404]. Briefly, the composite hydrogels XH_1-Ag(T), XH_1-Ag(UV), and XH_1 were prepared in the 96 well plates with a final volume of 50 µL.

Bacterial solutions in the log phase were diluted with MHB II broth to the concentration of 10^5 CFU mL^{-1}, and 25 µL of the bacterial solution was added above the hydrogels. Untreated 96-well plates were used as control. The 96-well plates were incubated at 37 °C for different times, from 4 to 24 hours. After each time of incubation, the plate counting method was used to calculate the killing percentages of the hydrogels toward different bacterial strains. Each sample was tested in triplicate.

6. Bibliography

1. Mofazzal Jahromi, M. A. *et al.* Nanomedicine and advanced technologies for burns: Preventing infection and facilitating wound healing. *Adv Drug Deliv Rev* **123**, 33–64 (2018).
2. Fuchs, E. Skin stem cells: rising to the surface. *J Cell Biol* **180**, 273 (2008).
3. E, F. Skin stem cells: rising to the surface. *J Cell Biol* **180**, 273–284 (2008).
4. M, M., F, G. & M, C. Origin, homeostasis and function of Langerhans cells and other langerin-expressing dendritic cells. *Nat Rev Immunol* **8**, 935–947 (2008).
5. FO, N., P, D. M., JZ, Q. & BJ, N. Skin immune sentinels in health and disease. *Nat Rev Immunol* **9**, 679–691 (2009).
6. C, B. & E, F. Epidermal stem cells of the skin. *Annu Rev Cell Dev Biol* **22**, 339–373 (2006).
7. Gurtner, G. C., Werner, S., Barrandon, Y. & Longaker, M. T. Wound repair and regeneration. *Nature 2008 453:7193* **453**, 314–321 (2008).
8. K, S. & D, K. Skin mesenchymal stem cells: prospects for clinical dermatology. *J Am Acad Dermatol* **63**, 859–865 (2010).
9. Martin, P. & Nunan, R. Cellular and molecular mechanisms of repair in acute and chronic wound healing. *British Journal of Dermatology* **173**, 370–378 (2015).
10. Price, A., Naik, G. & Harding, K. Skin repair technology. in *Biomaterials for Skin Repair and Regeneration* 27–57 (Elsevier, 2019). doi:10.1016/B978-0-08-102546-8.00002-9.
11. E, B., M, S., J, G. & DL, K. In vitro 3D full-thickness skin-equivalent tissue model using silk and collagen biomaterials. *Macromol Biosci* **12**, 1627–1636 (2012).
12. Zhao, X. *et al.* Antibacterial anti-oxidant electroactive injectable hydrogel as self-healing wound dressing with hemostasis and adhesiveness for cutaneous wound healing. *Biomaterials* **122**, 34–47 (2017).
13. Las Heras, K., Igartua, M., Santos-Vizcaino, E. & Hernandez, R. M. Chronic wounds: Current status, available strategies and emerging therapeutic solutions. *Journal of Controlled Release* **328**, 532–550 (2020).
14. Sun, B. K., Siprashvili, Z. & Khavari, P. A. Advances in skin grafting and treatment of cutaneous wounds. *Science (1979)* **346**, 941–945 (2014).
15. Reish, R. G. & Eriksson, E. Scars: A review of emerging and currently available therapies. *Plastic and Reconstructive Surgery* vol. 122 1068–1078 Preprint at https://doi.org/10.1097/PRS.0b013e318185d38f (2008).
16. Rodrigues, M., Kosaric, N., Bonham, C. A. & Gurtner, G. C. Wound healing: A cellular perspective. *Physiol Rev* **99**, 665–706 (2019).
17. Golebiewska, E. M. & Poole, A. W. Platelet secretion: From haemostasis to wound healing and beyond. *Blood Rev* **29**, 153–162 (2015).

18. Hardwicke, J., Schmaljohann, D., Boyce, D. & Thomas, D. Epidermal growth factor therapy and wound healing - Past, present and future perspectives. *Surgeon* vol. 6 172–177 Preprint at https://doi.org/10.1016/S1479-666X(08)80114-X (2008).

19. Thushara, R. M. *et al.* Biologicals, platelet apoptosis and human diseases: An outlook. *Critical Reviews in Oncology/Hematology* vol. 93 149–158 Preprint at https://doi.org/10.1016/j.critrevonc.2014.11.002 (2015).

20. Wilgus, T. A., Roy, S. & McDaniel, J. C. Neutrophils and Wound Repair: Positive Actions and Negative Reactions. *Adv Wound Care (New Rochelle)* **2**, 379–388 (2013).

21. Cohen, I. K. Lessons from the history of wound healing. *Clin Dermatol* **25**, 3–8 (2007).

22. Eming, S. A., Martin, P. & Tomic-Canic, M. Wound repair and regeneration: Mechanisms, signaling, and translation. *Science Translational Medicine* vol. 6 265sr6-265sr6 Preprint at https://doi.org/10.1126/scitranslmed.3009337 (2014).

23. Havran, W. L. & Jameson, J. M. Epidermal T Cells and Wound Healing. *The Journal of Immunology* **184**, 5423–5428 (2010).

24. Krzyszczyk, P., Schloss, R., Palmer, A. & Berthiaume, F. The role of macrophages in acute and chronic wound healing and interventions to promote pro-wound healing phenotypes. *Frontiers in Physiology* vol. 9 419 Preprint at https://doi.org/10.3389/fphys.2018.00419 (2018).

25. Liu, L. *et al.* Human umbilical cord mesenchymal stem cells transplantation promotes cutaneous wound healing of severe burned rats. *PLoS One* **9**, e88348 (2014).

26. Yeung, A. W. S., Terentis, A. C., King, N. J. C. & Thomas, S. R. Role of indoleamine 2,3-dioxygenase in health and disease. *Clinical Science* vol. 129 601–672 Preprint at https://doi.org/10.1042/CS20140392 (2015).

27. AUKHIL, I. Biology of wound healing. *Periodontol 2000* **22**, 44–50 (2000).

28. I, P. *et al.* Epithelialization in Wound Healing: A Comprehensive Review. *Adv Wound Care (New Rochelle)* **3**, 445–464 (2014).

29. A, R., JTM, T. & CA, B. The Role of Chemokines in Wound Healing. *Int J Mol Sci* **19**, (2018).

30. Reinke, J. M. & Sorg, H. Wound repair and regeneration. *European Surgical Research* vol. 49 35–43 Preprint at https://doi.org/10.1159/000339613 (2012).

31. Xue, M. & Jackson, C. J. Extracellular Matrix Reorganization During Wound Healing and Its Impact on Abnormal Scarring. *Adv Wound Care (New Rochelle)* **4**, 119–136 (2015).

32. Werdin, F., Tenenhaus, M. & Rennekampff, H. O. Chronic wound care. *The Lancet* vol. 372 1860–1862 Preprint at https://doi.org/10.1016/S0140-6736(08)61793-6 (2008).

33. Stojadinovic, A., Carlson, J. W., Schultz, G. S., Davis, T. A. & Elster, E. A. Topical advances in wound care. *Gynecol Oncol* **111**, (2008).

34. Barrientos, S., Stojadinovic, O., Golinko, M. S., Brem, H. & Tomic-Canic, M. Growth factors and cytokines in wound healing. *Wound Repair and Regeneration* vol. 16 585–601 Preprint at https://doi.org/10.1111/j.1524-475X.2008.00410.x (2008).

35. Soehnlein, O., Steffens, S., Hidalgo, A. & Weber, C. Neutrophils as protagonists and targets in chronic inflammation. *Nature Reviews Immunology* vol. 17 248–261 Preprint at https://doi.org/10.1038/nri.2017.10 (2017).

36. Kolaczkowska, E. & Kubes, P. Neutrophil recruitment and function in health and inflammation. *Nature Reviews Immunology* vol. 13 159–175 Preprint at https://doi.org/10.1038/nri3399 (2013).

37. Wynn, T. A. & Vannella, K. M. Macrophages in Tissue Repair, Regeneration, and Fibrosis. *Immunity* vol. 44 450–462 Preprint at https://doi.org/10.1016/j.immuni.2016.02.015 (2016).

38. Xue, M., Zhao, R., Lin, H. & Jackson, C. Delivery systems of current biologicals for the treatment of chronic cutaneous wounds and severe burns. *Advanced Drug Delivery Reviews* vol. 129 219–241 Preprint at https://doi.org/10.1016/j.addr.2018.03.002 (2018).

39. De Oliveira, S., Rosowski, E. E. & Huttenlocher, A. Neutrophil migration in infection and wound repair: Going forward in reverse. *Nat Rev Immunol* **16**, 378–391 (2016).

40. Wang, S. *et al.* Injectable redox and light responsive MnO2 hybrid hydrogel for simultaneous melanoma therapy and multidrug-resistant bacteria-infected wound healing. *Biomaterials* **260**, 120314 (2020).

41. Y, L., X, Z., T, H., Y, H. & B, G. Mussel-inspired, antibacterial, conductive, antioxidant, injectable composite hydrogel wound dressing to promote the regeneration of infected skin. *J Colloid Interface Sci* **556**, 514–528 (2019).

42. Zhang, X. *et al.* The fabrication of antibacterial hydrogels for wound healing. *Eur Polym J* **146**, 110268 (2021).

43. Rahim, K. *et al.* Bacterial Contribution in Chronicity of Wounds. *Microb Ecol* **73**, 710–721 (2017).

44. Leaper, D. J. Silver dressings: their role in wound management. *Int Wound J* **3**, 282–294 (2006).

45. Han, G. & Ceilley, R. Chronic Wound Healing: A Review of Current Management and Treatments. *Adv Ther* **34**, 599–610 (2017).

46. M, M. J., A, A. C., T, K. I. & Qijing, Z. Mechanisms of Antibiotic Resistance. *Microbiol Spectr* **4**, 4.2.15 (2016).

47. Wang, Y., Yang, Y., Shi, Y., Song, H. & Yu, C. Antibiotic-Free Antibacterial Strategies Enabled by Nanomaterials: Progress and Perspectives. *Advanced Materials* **32**, 1904106 (2020).

48. Bergeron, M. G. & Ouellette, M. Preventing Antibiotic Resistance Using Rapid DNA-Based Diagnostic Tests. *Infect Control Hosp Epidemiol* **19**, 560–564 (1998).

49. Powers, J. G., Higham, C., Broussard, K. & Phillips, T. J. Wound healing and treating wounds Chronic wound care and management. *Journal of the American Academy of Dermatology* vol. 74 607–625 Preprint at https://doi.org/10.1016/j.jaad.2015.08.070 (2016).

50. Cheng, Q., Gibb, M., Graves, N., Finlayson, K. & Pacella, R. E. Cost-effectiveness analysis of guideline-based optimal care for venous leg ulcers in Australia. *BMC Health Serv Res* **18**, (2018).

51. Forrest, R. D. Early history of wound treatment. *J R Soc Med* **75**, 198–205 (1982).

52. Qu, J. *et al.* Antibacterial adhesive injectable hydrogels with rapid self-healing, extensibility and compressibility as wound dressing for joints skin wound healing. *Biomaterials* **183**, 185–199 (2018).

53. Shah, J. B. The history of wound care. *Journal of the American College of Certified Wound Specialists* **3**, 65–66 (2011).

54. Koehler, J., Brandl, F. P. & Goepferich, A. M. Hydrogel wound dressings for bioactive treatment of acute and chronic wounds. *Eur Polym J* **100**, 1–11 (2018).

55. Sun, X. *et al.* Biological properties of sulfanilamide-loaded alginate hydrogel fibers based on ionic and chemical crosslinking for wound dressings. *Int J Biol Macromol* **157**, 522–529 (2020).

56. Laftah, W. A., Hashim, S. & Ibrahim, A. N. Polymer hydrogels: A review. *Polymer - Plastics Technology and Engineering* **50**, 1475–1486 (2011).

57. B, S. & A, K. Graft and crosslinked polymerization of polysaccharide gum to form hydrogel wound dressings for drug delivery applications. *Carbohydr Res* **489**, (2020).

58. Ma, S. *et al.* A Novel Method for Preparing Poly(vinyl alcohol) Hydrogels: Preparation, Characterization, and Application. *Ind Eng Chem Res* **56**, 7971–7976 (2017).

59. Kalantari, K., Mostafavi, E., Saleh, B., Soltantabar, P. & Webster, T. J. Chitosan/PVA hydrogels incorporated with green synthesized cerium oxide nanoparticles for wound healing applications. *Eur Polym J* **134**, (2020).

60. Y, C. *et al.* A Biocompatible, Stimuli-Responsive, and Injectable Hydrogel with Triple Dynamic Bonds. *Molecules* **25**, (2020).

61. Jalalvandi, E. & Shavandi, A. Shear thinning/self-healing hydrogel based on natural polymers with secondary photocrosslinking for biomedical applications. *J Mech Behav Biomed Mater* **90**, 191–201 (2019).

62. E, J., J, C., LR, H. & SC, M. Cyclodextrin-polyhydrazine degradable gels for hydrophobic drug delivery. *Mater Sci Eng C Mater Biol Appl* **69**, 144–153 (2016).

63. Y, M. *et al.* Bioprinting-Based PDLSC-ECM Screening for in Vivo Repair of Alveolar Bone Defect Using Cell-Laden, Injectable and Photocrosslinkable Hydrogels. *ACS Biomater Sci Eng* **3**, 3534–3545 (2017).

64. Teodorescu, M. *et al.* Novel Thermoreversible Injectable Hydrogel Formulations Based on Sodium Alginate and Poly(N-Isopropylacrylamide). *http://dx.doi.org/10.1080/00914037.2015.1030646* **64**, 763–771 (2015).

65. Yesilyurt, V. *et al.* Injectable Self-Healing Glucose-Responsive Hydrogels with pH-Regulated Mechanical Properties. *Advanced Materials* **28**, 86–91 (2016).

66. Brooks, W. L. A. & Sumerlin, B. S. Synthesis and Applications of Boronic Acid-Containing Polymers: From Materials to Medicine. *Chem Rev* **116**, 1375–1397 (2016).

67. Meredith Roberts, B. C. *et al.* Dynamically Restructuring Hydrogel Networks Formed with Reversible Covalent Crosslinks. *Advanced Materials* **19**, 2503–2507 (2007).

68. Zheng, N., Xu, Y., Zhao, Q. & Xie, T. Dynamic Covalent Polymer Networks: A Molecular Platform for Designing Functions beyond Chemical Recycling and Self-Healing. *Chem Rev* **121**, 1716–1745 (2021).

69. Taylor, D. L. & in het Panhuis, M. Self-Healing Hydrogels. *Advanced Materials* **28**, 9060–9093 (2016).

70. Zhang, Z., He, C. & Chen, X. Hydrogels based on pH-responsive reversible carbon–nitrogen double-bond linkages for biomedical applications. *Mater Chem Front* **2**, 1765–1778 (2018).

71. Kölmel, D. K. & Kool, E. T. Oximes and Hydrazones in Bioconjugation: Mechanism and Catalysis. *Chem Rev* **117**, 10358–10376 (2017).

72. McBride, M. K. *et al.* Enabling Applications of Covalent Adaptable Networks. *https://doi.org/10.1146/annurev-chembioeng-060718-030217* **10**, 175–198 (2019).

73. Li, J., Nowak, P. & Otto, S. Dynamic combinatorial libraries: From exploring molecular recognition to systems chemistry. *J Am Chem Soc* **135**, 9222–9239 (2013).

74. Wang, H. & Heilshorn, S. C. Adaptable Hydrogel Networks with Reversible Linkages for Tissue Engineering. *Advanced Materials* **27**, 3717–3736 (2015).

75. Mukherjee, S., Cash, J. J. & Sumerlin, B. S. Responsive Dynamic Covalent Polymers. *Dynamic Covalent Chemistry* 321–358 (2017) doi:10.1002/9781119075738.CH8.

76. Rizwan, M., Baker, A. E. G. & Shoichet, M. S. Designing Hydrogels for 3D Cell Culture Using Dynamic Covalent Crosslinking. *Adv Healthc Mater* **10**, 2100234 (2021).

77. Azagarsamy, M. A., Marozas, I. A., Spaans, S. & Anseth, K. S. Photoregulated Hydrazone-Based Hydrogel Formation for Biochemically Patterning 3D Cellular Microenvironments. *ACS Macro Lett* **5**, 19–23 (2016).

78. Dupont, S. *et al.* Role of YAP/TAZ in mechanotransduction. *Nature 2011 474:7350* **474**, 179–183 (2011).

79. Perera, M. M. & Ayres, N. Dynamic covalent bonds in self-healing, shape memory, and controllable stiffness hydrogels. *Polym Chem* **11**, 1410–1423 (2020).

80. Chester, D., Kathard, R., Nortey, J., Nellenbach, K. & Brown, A. C. Viscoelastic properties of microgel thin films control fibroblast modes of migration and pro-fibrotic responses. *Biomaterials* **185**, 371–382 (2018).

81. Kloxin, C. J. & Bowman, C. N. Covalent adaptable networks: smart, reconfigurable and responsive network systems. *Chem Soc Rev* **42**, 7161–7173 (2013).

82. Nam, S., Hu, K. H., Butte, M. J. & Chaudhuri, O. Strain-enhanced stress relaxation impacts nonlinear elasticity in collagen gels. *Proc Natl Acad Sci U S A* **113**, 5492–5497 (2016).

83. J, B. & O, C. Advanced Therapeutic Dressings for Effective Wound Healing--A Review. *J Pharm Sci* **104**, 3653–3680 (2015).

84. DR, G., WM, W., PO, S., D, D. C. & T, S. Accelerated wound healing by injectable microporous gel scaffolds assembled from annealed building blocks. *Nat Mater* **14**, 737–744 (2015).

85. J, H., B, B., RG, P., K, P. & J, H. Dual Function Injectable Hydrogel for Controlled Release of Antibiotic and Local Antibacterial Therapy. *Biomacromolecules* **19**, 267–278 (2018).

86. M, Y., H, N. & M, A. Antibacterial carboxymethyl cellulose/Ag nanocomposite hydrogels cross-linked with layered double hydroxides. *Int J Biol Macromol* **79**, 269–277 (2015).

87. Yu, M. & Deming, T. J. Synthetic polypeptide mimics of marine adhesives. *Macromolecules* **31**, 4739–4745 (1998).

88. Krogsgaard, M., Behrens, M. A., Pedersen, J. S. & Birkedal, H. Self-healing mussel-inspired multi-pH-responsive hydrogels. *Biomacromolecules* **14**, 297–301 (2013).

89. Yu, M., Hwang, J. & Deming, T. J. Role of 1-3,4-dihydroxyphenylalanine in mussel adhesive proteins. *J Am Chem Soc* **121**, 5825–5826 (1999).

90. Deming, T. J. Mussel byssus and biomolecular materials. *Curr Opin Chem Biol* **3**, 100–105 (1999).

91. Li, L., Smitthipong, W. & Zeng, H. Mussel-inspired hydrogels for biomedical and environmental applications. *Polym Chem* **6**, 353–358 (2014).

92. Vale, A. C., Pereira, P. R. & Alves, N. M. Polymeric biomaterials inspired by marine mussel adhesive proteins. *React Funct Polym* **159**, 104802 (2021).

93. Madhurakkat Perikamana, S. K. *et al.* Materials from Mussel-Inspired Chemistry for Cell and Tissue Engineering Applications. *Biomacromolecules* **16**, 2541–2555 (2015).

94. Liu, Y., Ai, K. & Lu, L. Polydopamine and its derivative materials: Synthesis and promising applications in energy, environmental, and biomedical fields. *Chem Rev* **114**, 5057–5115 (2014).

95. Fullenkamp, D. E. *et al.* Mussel-inspired silver-releasing antibacterial hydrogels. *Biomaterials* **33**, 3783–3791 (2012).

96. Callow, J. A. & Callow, M. E. Trends in the development of environmentally friendly fouling-resistant marine coatings. *Nature Communications 2011 2:1* **2**, 1–10 (2011).

97. Lee, H., Scherer, N. F. & Messersmith, P. B. Single-molecule mechanics of mussel adhesion. *Proc Natl Acad Sci U S A* **103**, 12999–13003 (2006).

98. Silverman, H. G. & Roberto, F. F. Understanding marine mussel adhesion. *Marine Biotechnology* **9**, 661–681 (2007).

99. Sever, M. J., Weisser, J. T., Monahan, J., Srinivasan, S. & Wilker, J. J. Metal-Mediated Cross-Linking in the Generation of a Marine-Mussel Adhesive. *Angewandte Chemie International Edition* **43**, 448–450 (2004).

100. Shafiq, Z. *et al.* Bioinspired Underwater Bonding and Debonding on Demand. *Angewandte Chemie* **124**, 4408–4411 (2012).

101. Xu, J., Soliman, G. M., Barralet, J. & Cerruti, M. Mollusk glue inspired mucoadhesives for biomedical applications. *Langmuir* **28**, 14010–14017 (2012).

102. Krogsgaard, M., Nue, V. & Birkedal, H. Mussel-Inspired Materials: Self-Healing through Coordination Chemistry. *Chemistry – A European Journal* **22**, 844–857 (2016).

103. Sun, J. *et al.* Reversible swelling-shrinking behavior of hydrogen-bonded free-standing thin film stabilized by catechol reaction. *Langmuir* **31**, 5147–5154 (2015).

104. Neto, A. I., Meredith, H. J., Jenkins, C. L., Wilker, J. J. & Mano, J. F. Combining biomimetic principles from the lotus leaf and mussel adhesive: polystyrene films with superhydrophobic and adhesive layers. *RSC Adv* **3**, 9352–9356 (2013).

105. Hong, S. *et al.* Hyaluronic Acid Catechol: A Biopolymer Exhibiting a pH-Dependent Adhesive or Cohesive Property for Human Neural Stem Cell Engineering. *Adv Funct Mater* **23**, 1774–1780 (2013).

106. Kim, B. J. *et al.* Mussel-mimetic protein-based adhesive hydrogel. *Biomacromolecules* **15**, 1579–1585 (2014).

107. Feng, J., Ton, X. A., Zhao, S., Paez, J. I. & del Campo, A. Mechanically reinforced catechol-containing hydrogels with improved tissue gluing performance. *Biomimetics* **2**, 1–15 (2017).

108. Khurana, B., Gierlich, P., Meindl, A., Gomes-Da-Silva, L. C. & Senge, M. O. Hydrogels: Soft matters in photomedicine. *Photochemical and Photobiological Sciences* **18**, 2613–2656 (2019).

109. Salachna, P., Mizielińska, M. & Soból, M. Exopolysaccharide gellan gum and derived oligo-gellan enhance growth and antimicrobial activity in eucomis plants. *Polymers (Basel)* **10**, (2018).

110. Leone, G. *et al.* Enriched Gellan Gum hydrogel as visco-supplement. *Carbohydr Polym* **227**, 115347 (2020).

111. Coviello, T., Matricardi, P., Marianecci, C. & Alhaique, F. Polysaccharide hydrogels for modified release formulations. *Journal of Controlled Release* **119**, 5–24 (2007).

112. Fiorica, C. *et al.* Production and physicochemical characterization of a new amine derivative of gellan gum and rheological study of derived hydrogels. *Carbohydr Polym* **236**, 116033 (2020).

113. Kuo, M. S., Mort, A. J. & Dell, A. Identification and location of l-glycerate, an unusual acyl substituent in gellan gum. *Carbohydr Res* **156**, 173–187 (1986).

114. Nitta, Y., Takahashi, R. & Nishinari, K. Viscoelasticity and phase separation of aqueous Na-type gellan solution. *Biomacromolecules* **11**, 187–191 (2010).

115. Osmałek, T., Froelich, A. & Tasarek, S. Application of gellan gum in pharmacy and medicine. *Int J Pharm* **466**, 328–340 (2014).

116. Morris, E. R., Nishinari, K. & Rinaudo, M. Gelation of gellan – A review. *Food Hydrocoll* **28**, 373–411 (2012).

117. Zheng, Y. *et al.* Gelatin-Based Hydrogels Blended with Gellan as an Injectable Wound Dressing. *ACS Omega* **3**, 4766–4775 (2018).

118. Palumbo, F. S., Federico, S., Pitarresi, G., Fiorica, C. & Giammona, G. Gellan gum-based delivery systems of therapeutic agents and cells. *Carbohydr Polym* **229**, 115430 (2020).

119. Prajapati, V. D., Jani, G. K., Zala, B. S. & Khutliwala, T. A. An insight into the emerging exopolysaccharide gellan gum as a novel polymer. *Carbohydr Polym* **93**, 670–678 (2013).

120. Aadil, K. R., Nathani, A., Sharma, C. S., Lenka, N. & Gupta, P. Investigation of poly(vinyl) alcohol-gellan gum based nanofiber as scaffolds for tissue engineering applications. *J Drug Deliv Sci Technol* **54**, 101276 (2019).

121. Coutinho, D. F. *et al.* Modified Gellan Gum hydrogels with tunable physical and mechanical properties. *Biomaterials* **31**, 7494–7502 (2010).

122. Bacelar, A. H., Silva-Correia, J., Oliveira, J. M. & Reis, R. L. Recent progress in gellan gum hydrogels provided by functionalization strategies. *J Mater Chem B* **4**, 6164–6174 (2016).

123. Xu, Z., Li, Z., Jiang, S. & Bratlie, K. M. Chemically Modified Gellan Gum Hydrogels with Tunable Properties for Use as Tissue Engineering Scaffolds. *ACS Omega* **3**, 6998–7007 (2018).

124. Ferris, C. J., Gilmore, K. J., Wallace, G. G. & Panhuis, M. in het. Modified gellan gum hydrogels for tissue engineering applications. *Soft Matter* **9**, 3705 (2013).

125. Abu Elella, M. H. *et al.* Xanthan gum-derived materials for applications in environment and eco-friendly materials: A review. *J Environ Chem Eng* **9**, 104702 (2021).

126. Tao, F. *et al.* Genome sequence of Xanthomonas campestris JX, an industrially productive strain for xanthan gum. *J Bacteriol* **194**, 4755–4756 (2012).

127. Le, X. T. & Turgeon, S. L. Rheological and structural study of electrostatic cross-linked xanthan gum hydrogels induced by β-lactoglobulin. *Soft Matter* **9**, 3063–3073 (2013).

128. Rao, K. M., Kumar, A., Haider, A. & Han, S. S. Polysaccharides based antibacterial polyelectrolyte hydrogels with silver nanoparticles. *Mater Lett* **184**, 189–192 (2016).

129. Kumar, A., Rao, K. M. & Han, S. S. Application of xanthan gum as polysaccharide in tissue engineering: A review. *Carbohydr Polym* **180**, 128–144 (2018).

130. Faria, S. *et al.* Characterization of xanthan gum produced from sugar cane broth. *Carbohydr Polym* **86**, 469–476 (2011).

131. Jansson, P. erik, Kenne, L. & Lindberg, B. Structure of the extracellular polysaccharide from xanthomonas campestris. *Carbohydr Res* **45**, 275–282 (1975).

132. Abbaszadeh, A. *et al.* A novel approach to the determination of the pyruvate and acetate distribution in xanthan. *Food Hydrocoll* **44**, 162–171 (2015).

133. Wang, Z., Wu, J., Zhu, L. & Zhan, X. Characterization of xanthan gum produced from glycerol by a mutant strain Xanthomonas campestris CCTCC M2015714. *Carbohydr Polym* **157**, 521–526 (2017).

134. Tait, M. I., Sutherland, I. W. & Clarke-Sturman, A. J. Effect of growth conditions on the production, composition and viscosity of Xanthomonas campestris exopolysaccharide. *J Gen Microbiol* **132**, 1483–1492 (1986).

135. Sutherland, I. W. Xanthomonas polysaccharides — Improved methods for their comparison. *Carbohydr Polym* **1**, 107–115 (1981).

136. Cadmus, M. C. *et al.* Colonial variation in Xanthomonas campestris NRRL B-1459 and characterization of the polysaccharide from a variant strain. *https://doi.org/10.1139/m76-136* **22**, 942–948 (2011).

137. MOORHOUSE, R., WALKINSHAW, M. D. & ARNOTT, S. Xanthan Gum—Molecular Conformation and Interactions. 90–102 (1977) doi:10.1021/BK-1977-0045.CH007.

138. Katzbauer, B. Properties and applications of xanthan gum. *Polym Degrad Stab* **59**, 81–84 (1998).

139. Cheetham, N. W. H. & Mashimba, E. N. M. Proton and carbon-13 NMR studies on xanthan derivatives. *Carbohydr Polym* **17**, 127–136 (1992).

140. Rinaudo, M. & Milas, M. Enzymic hydrolysis of the bacterial polysaccharide xanthan by cellulase. *Int J Biol Macromol* **2**, 45–48 (1980).

141. Palaniraj, A. & Jayaraman, V. Production, recovery and applications of xanthan gum by Xanthomonas campestris. *J Food Eng* **106**, 1–12 (2011).

142. Petri, D. F. S. Xanthan gum: A versatile biopolymer for biomedical and technological applications. *J Appl Polym Sci* **132**, (2015).

143. García-Ochoa, F., Santos, V. E., Casas, J. A. & Gómez, E. Xanthan gum: production, recovery, and properties. *Biotechnol Adv* **18**, 549–579 (2000).

144. Milas, M., Rinaudo, M., Knipper, M. & Schuppiser, J. L. Flow and Viscoelastic Properties of Xanthan Gum Solutions. *Macromolecules* **23**, 2506–2511 (1990).

145. Rosalam, S. & England, R. Review of xanthan gum production from unmodified starches by Xanthomonas comprestris sp. *Enzyme Microb Technol* **39**, 197–207 (2006).

146. Murphy, W. L., McDevitt, T. C. & Engler, A. J. Materials as stem cell regulators. *Nature Materials 2014 13:6* **13**, 547–557 (2014).

147. Qiu, Y. & Park, K. Environment-sensitive hydrogels for drug delivery. *Adv Drug Deliv Rev* **53**, 321–339 (2001).

148. Qu, J. *et al.* Degradable conductive injectable hydrogels as novel antibacterial, anti-oxidant wound dressings for wound healing. *Chemical Engineering Journal* **362**, 548–560 (2019).

149. S, I. E., F, A. N. & U, Y. Genipin crosslinked gelatin-diosgenin-nanocellulose hydrogels for potential wound dressing and healing applications. *Int J Biol Macromol* **149**, 651–663 (2020).

150. Abbasi, A. R. *et al.* Bioinspired sodium alginate based thermosensitive hydrogel membranes for accelerated wound healing. *Int J Biol Macromol* **155**, 751–765 (2020).

151. Ahmed, A. *et al.* In-vitro and in-vivo study of superabsorbent PVA/Starch/g-C3N4/Ag@TiO2 NPs hydrogel membranes for wound dressing. *Eur Polym J* **130**, 109650 (2020).

152. Zhu, J., Li, F., Wang, X., Yu, J. & Wu, D. Hyaluronic Acid and Polyethylene Glycol Hybrid Hydrogel Encapsulating Nanogel with Hemostasis and Sustainable Antibacterial Property for Wound Healing. *ACS Appl Mater Interfaces* **10**, 13304–13316 (2018).

153. Pawar, V., Dhanka, M. & Srivastava, R. Cefuroxime conjugated chitosan hydrogel for treatment of wound infections. *Colloids Surf B Biointerfaces* **173**, 776–787 (2019).

154. Wei, G. *et al.* Phototherapy-based combination strategies for bacterial infection treatment. *Theranostics* **10**, 12241 (2020).

155. AP, C., TN, D. & MR, H. Mechanisms in photodynamic therapy: part one-photosensitizers, photochemistry and cellular localization. *Photodiagnosis Photodyn Ther* **1**, 279–293 (2004).

156. Wentao, W. *et al.* Functionalization of polyvinyl alcohol composite film wrapped in am-ZnO@CuO@Au nanoparticles for antibacterial application and wound healing. *Appl Mater Today* **17**, 36–44 (2019).

157. Mai, B. *et al.* Smart Hydrogel-Based DVDMS/bFGF Nanohybrids for Antibacterial Phototherapy with Multiple Damaging Sites and Accelerated Wound Healing. *ACS Appl Mater Interfaces* **12**, 10156–10169 (2020).

158. Jaque, D. *et al.* Nanoparticles for photothermal therapies. *Nanoscale* **6**, 9494–9530 (2014).

159. S, H. *et al.* Functionalized GO Nanovehicles with Nitric Oxide Release and Photothermal Activity-Based Hydrogels for Bacteria-Infected Wound Healing. *ACS Appl Mater Interfaces* **12**, 28952–28964 (2020).

160. Zhi, D., Yang, T., O'Hagan, J., Zhang, S. & Donnelly, R. F. Photothermal therapy. *Journal of Controlled Release* **325**, 52–71 (2020).

161. Hussein, E. A., Zagho, M. M., Nasrallah, G. K. & Elzatahry, A. A. Recent advances in functional nanostructures as cancer photothermal therapy. *Int J Nanomedicine* **13**, 2897–2906 (2018).

162. Wang, H., Zhou, S., Guo, L., Wang, Y. & Feng, L. Intelligent Hybrid Hydrogels for Rapid in Situ Detection and Photothermal Therapy of Bacterial Infection. *ACS Appl Mater Interfaces* **12**, 39685–39694 (2020).

163. Yu, Y. *et al.* Multifunctional and Recyclable Photothermally Responsive Cryogels as Efficient Platforms for Wound Healing. *Adv Funct Mater* **29**, 1904402 (2019).

164. Yan, S. *et al.* Biodegradable Supramolecular Materials Based on Cationic Polyaspartamides and Pillar[5]arene for Targeting Gram-Positive Bacteria and Mitigating Antimicrobial Resistance. *Adv Funct Mater* **29**, 1904683 (2019).

165. Thoenen, H., Angeletti, P. U., Levi-Montalcini, R. & Kettler, R. Selective Induction by Nerve Growth Factor of Tyrosine Hydroxylase and Dopamine-β-Hydroxylase in the Rat Superior Cervical Ganglia. *Proc Natl Acad Sci U S A* **68**, 1598 (1971).

166. A, Z., JL, N. & RJ, B. Recent progress in development of dopamine receptor subtype-selective agents: potential therapeutics for neurological and psychiatric disorders. *Chem Rev* **107**, 274–302 (2007).

167. Cheng, W. *et al.* Versatile Polydopamine Platforms: Synthesis and Promising Applications for Surface Modification and Advanced Nanomedicine. *ACS Nano* **13**, 8537–8565 (2019).

168. Łuczak, T. Preparation and characterization of the dopamine film electrochemically deposited on a gold template and its applications for dopamine sensing in aqueous solution. *Electrochim Acta* **53**, 5725–5731 (2008).

169. S, G. & PJ, F. Redox behavior of melanins: direct electrochemistry of dihydroxyindole-melanin and its Cu and Zn adducts. *J Inorg Biochem* **89**, 54–60 (2002).

170. Hong, S. *et al.* Non-Covalent Self-Assembly and Covalent Polymerization Co-Contribute to Polydopamine Formation. *Adv Funct Mater* **22**, 4711–4717 (2012).

171. Wang, C., Bai, J., Liu, Y., Jia, X. & Jiang, X. Polydopamine Coated Selenide Molybdenum: A New Photothermal Nanocarrier for Highly Effective Chemo-Photothermal Synergistic Therapy. *ACS Biomater Sci Eng* **2**, 2011–2017 (2016).

172. Shanmugam, V., Selvakumar, S. & Yeh, C.-S. Near-infrared light-responsive nanomaterials in cancer therapeutics. *Chem Soc Rev* **43**, 6254–6287 (2014).

173. Hu, D. *et al.* Photothermal Killing of Methicillin-Resistant Staphylococcus aureus by Bacteria-Targeted Polydopamine Nanoparticles with Nano-Localized Hyperpyrexia. *ACS Biomater Sci Eng* 5169–5179 (2019) doi:10.1021/acsbiomaterials.9b01173.

174. XL, F. *et al.* Magainin-modified polydopamine nanoparticles for photothermal killing of bacteria at low temperature. *Colloids Surf B Biointerfaces* **183**, (2019).

175. Zhu, D. *et al.* Docetaxel (DTX)-loaded polydopamine-modified TPGS-PLA nanoparticles as a targeted drug delivery system for the treatment of liver cancer. *Acta Biomater* **30**, 144–154 (2016).

176. Li, H. *et al.* Polydopamine-based nanomaterials and their potentials in advanced drug delivery and therapy. *Colloids Surf B Biointerfaces* **199**, 111502 (2021).

177. Black, K. C. L., Yi, J., Rivera, J. G., Zelasko-Leon, D. C. & Messersmith, P. B. Polydopamine-enabled surface functionalization of gold nanorods for cancer cell-targeted imaging and photothermal therapy. *Nanomedicine* **8**, 17–28 (2013).

178. Liu, H. *et al.* Role of polydopamine's redox-activity on its pro-oxidant, radical-scavenging, and antimicrobial activities. *Acta Biomater* **88**, 181–196 (2019).

179. Xu, Q. *et al. PDA/Cu Bioactive Hydrogel with 'hot Ions Effect' for Inhibition of Drug-Resistant Bacteria and Enhancement of Infectious Skin Wound Healing*. *ACS Applied Materials and Interfaces* vol. 12 (2020).

180. Z, P., R, R., BR, G., TJ, L. & Z, C. Antibiotic resistance in Pseudomonas aeruginosa: mechanisms and alternative therapeutic strategies. *Biotechnol Adv* **37**, 177–192 (2019).

181. Avedissian, S. N. *et al.* A review of the clinical pharmacokinetics of polymyxin b. *Antibiotics* **8**, 1–11 (2019).

182. ME, F. & SK, K. Colistin: the revival of polymyxins for the management of multidrug-resistant gram-negative bacterial infections. *Clin Infect Dis* **40**, 1333–1341 (2005).

183. Orwa, J. A., Gerven, A. Van, Roets, E. & Hoogmartens, J. Development and validation of a liquid chromatography method for analysis of colistin sulphate. *Chromatographia 2000 51:7* **51**, 433–436 (2000).

184. Cao, G. *et al.* Development and validation of a reversed-phase high-performance liquid chromatography assay for polymyxin B in human plasma. *Journal of Antimicrobial Chemotherapy* **62**, 1009–1014 (2008).

185. C, P. *et al.* Purity determination of amphotericin B, colistin sulfate and tobramycin sulfate in a hydrophilic suspension by HPLC. *J Chromatogr B Analyt Technol Biomed Life Sci* **990**, 7–14 (2015).

186. Xu, L., Burkin, M., Eremin, S., Dias, A. C. P. & Zhang, X. Development of Competitive ELISA and CLEIA for Quantitative Analysis of Polymyxin B. *Food Analytical Methods 2019 12:6* **12**, 1412–1419 (2019).

187. D, D., P, L., A, N. & P, A. Hyphenated liquid chromatographic method for the determination of colistin residues in bovine tissues. *J Chromatogr Sci* **35**, 557–564 (1997).

188. JA, O. *et al.* Isolation and structural characterization of colistin components. *J Antibiot (Tokyo)* **54**, 595–599 (2001).

189. SJ, W. *et al.* Self-assembly behavior of colistin and its prodrug colistin methanesulfonate: implications for solution stability and solubilization. *J Phys Chem B* **114**, 4836–4840 (2010).

190. MD, R., RC, S., MA, O. & JL, B. The pharmacokinetics of colistin in patients with cystic fibrosis. *J Clin Pharmacol* **41**, 645–654 (2001).

191. Zgurskaya, H. I., López, C. A. & Gnanakaran, S. Permeability Barrier of Gram-Negative Cell Envelopes and Approaches To Bypass It. *ACS Infect Dis* **1**, 512–522 (2015).

192. Nishino, K. *et al.* Identification of the lipopolysaccharide modifications controlled by the Salmonella PmrA/PmrB system mediating resistance to Fe(III) and Al(III). *Mol Microbiol* **61**, 645–654 (2006).

193. RE, H. Antibacterial peptides and the outer membranes of gram-negative bacilli. *J Med Microbiol* **46**, 1–3 (1997).

194. Hancock, R. E. W. & Lehrer, R. Cationic peptides: a new source of antibiotics. *Trends Biotechnol* **16**, 82–88 (1998).

195. Dubashynskaya, N. V. & Skorik, Y. A. Polymyxin delivery systems: Recent advances and challenges. *Pharmaceuticals* **13**, (2020).

196. RK, T., DB, D. & HH, T. Topical antimicrobial peptide formulations for wound healing: Current developments and future prospects. *Acta Biomater* **103**, 52–67 (2020).

197. Öhnstedt, E., Tomenius, H. L., Vågesjö, E. & Phillipson, M. The discovery and development of topical medicines for wound healing. *https://doi.org/10.1080/17460441.2019.1588879* **14**, 485–497 (2019).

198. Ambekar, R. S. & Kandasubramanian, B. Advancements in nanofibers for wound dressing: A review. *Eur Polym J* **117**, 304–336 (2019).

199. Song, D. W. *et al.* Multi-biofunction of antimicrobial peptide-immobilized silk fibroin nanofiber membrane: Implications for wound healing. *Acta Biomater* **39**, 146–155 (2016).

200. Brogden, K. A. Antimicrobial peptides: pore formers or metabolic inhibitors in bacteria? *Nat Rev Microbiol* **3**, 238–250 (2005).

201. Slavin, Y. N., Asnis, J., Häfeli, U. O. & Bach, H. Metal nanoparticles: understanding the mechanisms behind antibacterial activity. *J Nanobiotechnology* **15**, 65 (2017).

202. Maas, M. Carbon Nanomaterials as Antibacterial Colloids. *Materials* **9**, 617 (2016).

203. Zubris, D. L., Minbiole, K. P. C. & Wuest, W. M. The international journal for in-depth reviews on Current Topics in Medicinal Chemistry Impact Factor: 2.9. *Curr Top Med Chem* **17**, (2017).

204. Rahimi, M. *et al.* Carbohydrate polymer-based silver nanocomposites: Recent progress in the antimicrobial wound dressings. *Carbohydr Polym* **231**, 115696 (2020).

205. Möhler, J. S., Sim, W., Blaskovich, M. A. T., Cooper, M. A. & Ziora, Z. M. Silver bullets: A new lustre on an old antimicrobial agent. *Biotechnol Adv* **36**, 1391–1411 (2018).

206. Rizzello, L. & Pompa, P. P. Nanosilver-based antibacterial drugs and devices: Mechanisms, methodological drawbacks, and guidelines. *Chem Soc Rev* **43**, 1501–1518 (2014).

207. Chernousova, S. & Epple, M. Silver as Antibacterial Agent: Ion, Nanoparticle, and Metal. *Angewandte Chemie International Edition* **52**, 1636–1653 (2013).

208. Zahran, M. & Marei, A. H. Innovative natural polymer metal nanocomposites and their antimicrobial activity. *Int J Biol Macromol* **136**, 586–596 (2019).

209. Liu, J., Sonshine, D. A., Shervani, S. & Hurt, R. H. Controlled Release of Biologically Active Silver from Nanosilver Surfaces. *ACS Nano* **4**, 6903–6913 (2010).

210. le Ouay, B. & Stellacci, F. Antibacterial activity of silver nanoparticles: A surface science insight. *Nano Today* **10**, 339–354 (2015).

211. Zahran, M., El-Kemary, M., Khalifa, S. & El-Seedi, H. Spectral studies of silver nanoparticles biosynthesized by Origanum majorana. *Green Processing and Synthesis* **7**, 100–105 (2018).

212. Chen, X. *et al.* Agarose oligosaccharide- silver nanoparticle- antimicrobial peptide-composite for wound dressing. *Carbohydr Polym* **269**, 118258 (2021).

213. Brahmkhatri, V. P., Chandra, K., Dubey, A. & Atreya, H. S. An ultrastable conjugate of silver nanoparticles and protein formed through weak interactions. *Nanoscale* **7**, 12921–12931 (2015).

214. Dai, X. *et al.* Functional Silver Nanoparticle as a Benign Antimicrobial Agent That Eradicates Antibiotic-Resistant Bacteria and Promotes Wound Healing. *ACS Applied Materials & Interfaces* **8**, 25798–25807 (2016).

215. Sánchez-López, E. *et al.* Metal-Based Nanoparticles as Antimicrobial Agents: An Overview. *Nanomaterials (Basel)* **10**, 292 (2020).

216. Ider, M., Abderrafi, K., Eddahbi, A., Ouaskit, S. & Kassiba, A. Silver Metallic Nanoparticles with Surface Plasmon Resonance: Synthesis and Characterizations. *J Clust Sci* **28**, 1051–1069 (2017).

217. Kim, J. S. *et al.* Antimicrobial effects of silver nanoparticles. *Nanomedicine* **3**, 95–101 (2007).

218. Mogensen, K. B. & Kneipp, K. Size-Dependent Shifts of Plasmon Resonance in Silver Nanoparticle Films Using Controlled Dissolution: Monitoring the Onset of Surface Screening Effect. *J. Phys. Chem. C* **118**, 25 (2014).

219. Shervani, Z. *et al.* Morphology and size-controlled synthesis of silver nanoparticles in aqueous surfactant polymer solutions. *Colloid Polym Sci* **286**, 403–410 (2008).

220. Wang, W. *et al.* Amperometric hydrogen peroxide biosensor based on the immobilization of heme proteins on gold nanoparticles–bacteria cellulose nanofibers nanocomposite. *Talanta* **84**, 71–77 (2011).

221. Seo, S. Y. *et al.* Alginate-based composite sponge containing silver nanoparticles synthesized in situ. *Carbohydr Polym* **90**, 109–115 (2012).

222. Wang, W. *et al.* Microencapsulation using natural polysaccharides for drug delivery and cell implantation. *J Mater Chem* **16**, 3252–3267 (2006).

223. Rahimi, M., Safa, K. D., Alizadeh, E. & Salehi, R. Dendritic chitosan as a magnetic and biocompatible nanocarrier for the simultaneous delivery of doxorubicin and methotrexate to MCF-7 cell line. *New Journal of Chemistry* **41**, 3177–3189 (2017).

224. Swierczewska, M., Han, H. S., Kim, K., Park, J. H. & Lee, S. Polysaccharide-based nanoparticles for theranostic nanomedicine. *Adv Drug Deliv Rev* **99**, 70–84 (2016).

225. Pooja, D. *et al.* Natural polysaccharide functionalized gold nanoparticles as biocompatible drug delivery carrier. *Int J Biol Macromol* **80**, 48–56 (2015).

226. Li, W. *et al.* Preparation of sodium hyaluronate/dopamine/AgNPs hydrogel based on the natural eutetic solvent as an antibaterial wound dressing. *Int J Biol Macromol* **191**, 60–70 (2021).

227. Masood, N. *et al.* Silver nanoparticle impregnated chitosan-PEG hydrogel enhances wound healing in diabetes induced rabbits. *Int J Pharm* **559**, 23–36 (2019).

228. Diniz, F. R. *et al.* Silver Nanoparticles-Composing Alginate/Gelatine Hydrogel Improves Wound Healing In Vivo. *Nanomaterials* **10**, 390 (2020).

229. Dhar, S., Murawala, P., Shiras, A., Pokharkar, V. & Prasad, B. L. V. Gellan gum capped silver nanoparticle dispersions and hydrogels: cytotoxicity and in vitro diffusion studies. *Nanoscale* **4**, 563–567 (2012).

230. Yoosaf, K., Itty Ipe, B., H. Suresh, C. & George Thomas, K. In Situ Synthesis of Metal Nanoparticles and Selective Naked-Eye Detection of Lead Ions from Aqueous Media. *The Journal of Physical Chemistry C* **111**, 12839–12847 (2007).

231. Ma, Y., Niu, H., Zhang, X. & Cai, Y. One-step synthesis of silver/dopamine nanoparticles and visual detection of melamine in raw milk. *Analyst* **136**, 4192–4196 (2011).

232. Xiang, J. *et al.* Mussel-inspired immobilization of zwitterionic silver nanoparticles toward antibacterial cotton gauze for promoting wound healing. *Chemical Engineering Journal* **409**, 128291 (2021).

233. Cao, C. *et al.* Radical Scavenging Activities of Biomimetic Catechol-Chitosan Films. *Biomacromolecules* **19**, 3502–3514 (2018).

234. Lee, K. Y. & Mooney, D. J. Hydrogels for Tissue Engineering. *Chem Rev* **101**, 1869–1880 (2001).

235. Nguyen, M. K. & Lee, D. S. Injectable Biodegradable Hydrogels. *Macromol Biosci* **10**, 563–579 (2010).

236. Martins, A. F. *et al.* Bactericidal activity of hydrogel beads based on N,N,N-trimethyl chitosan/alginate complexes loaded with silver nanoparticles. *Chinese Chemical Letters* **26**, 1129–1132 (2015).

237. Azizi, S., Mohamad, R., Abdul Rahim, R., Mohammadinejad, R. & bin Ariff, A. Hydrogel beads bio-nanocomposite based on Kappa-Carrageenan and green synthesized silver nanoparticles for biomedical applications. *Int J Biol Macromol* **104**, 423–431 (2017).

238. Yadollahi, M., Farhoudian, S. & Namazi, H. One-pot synthesis of antibacterial chitosan/silver bio-nanocomposite hydrogel beads as drug delivery systems. *Int J Biol Macromol* **79**, 37–43 (2015).

239. Zhou, Q. *et al.* Synthesis and characterization of silver nanoparticles-doped hydroxyapatite/alginate microparticles with promising cytocompatibility and antibacterial properties. *Colloids Surf A Physicochem Eng Asp* **585**, 124081 (2020).

240. Yang, C.-H. *et al.* Microfluidic assisted synthesis of silver nanoparticle–chitosan composite microparticles for antibacterial applications. *Int J Pharm* **510**, 493–500 (2016).

241. Dilshad, E. *et al.* Synthesis of Functional Silver Nanoparticles and Microparticles with Modifiers and Evaluation of Their Antimicrobial, Anticancer, and Antioxidant Activity. *J Funct Biomater* **11**, 76 (2020).

242. Nagaich, U., Gulati, N. & Chauhan, S. Antioxidant and Antibacterial Potential of Silver Nanoparticles: Biogenic Synthesis Utilizing Apple Extract. *J Pharm (Cairo)* **2016**, 1–8 (2016).

243. Kazemi, M., Hadavi, E. & Hekmati, J. Effect of Salicylic Acid, Malic Acid, Citric Acid and Sucrose on Antioxidant Activity, Membrane Stability and ACC-oxidase Activity in Relation to Vase Life of Carnation Cut Flowers. *Journal of Plant Sciences* **7**, 78–84 (2012).

244. Eroğlu, I. *et al.* Evaluation of characteristics and in vitro antioxidant properties of RSV loaded hyaluronic acid–DPPC microparticles as a wound healing system. *Colloids Surf B Biointerfaces* **126**, 50–57 (2015).

245. Pereira, G. G. *et al.* Microparticles of Aloe vera/vitamin E/chitosan: Microscopic, a nuclear imaging and an in vivo test analysis for burn treatment. *European Journal of Pharmaceutics and Biopharmaceutics* **86**, 292–300 (2014).

246. Kamaruzzaman, N. F. *et al.* Antimicrobial Polymers: The Potential Replacement of Existing Antibiotics? *Int J Mol Sci* **20**, (2019).

247. Manzo, G., Carboni, M., Rinaldi, A. C., Casu, M. & Scorciapino, M. A. Characterization of sodium dodecylsulphate and dodecylphosphocholine mixed micelles through NMR and dynamic light scattering. *Magnetic Resonance in Chemistry* **51**, 176–183 (2013).

248. Ahmad, A. *et al.* Identification and Design of Antimicrobial Peptides for Therapeutic Applications. *Curr Protein Pept Sci* **13**, 211–223 (2012).

249. Giuliani, A., Pirri, G. & Rinaldi, A. C. Antimicrobial peptides: the LPS connection. *Methods Mol Biol* **618**, 137–154 (2010).

250. Giuliani, A. *et al.* Antimicrobial peptides: Natural templates for synthetic membrane-active compounds. *Cellular and Molecular Life Sciences* **65**, 2450–2460 (2008).

251. Zasloff, M. Antimicrobial peptides of multicellular organisms. *Nature 2002 415:6870* **415**, 389–395 (2002).

252. Bechinger, B. & Gorr, S. U. Antimicrobial Peptides: Mechanisms of Action and Resistance. *http://dx.doi.org/10.1177/0022034516679973* **96**, 254–260 (2016).

253. Giuliani, A. & Rinaldi, A. C. Beyond natural antimicrobial peptides: Multimeric peptides and other peptidomimetic approaches. *Cellular and Molecular Life Sciences* **68**, 2255–2266 (2011).

254. Scorciapino, M. A. & Rinaldi, A. C. Antimicrobial peptidomimetics: Reinterpreting nature to deliver innovative therapeutics. *Front Immunol* **3**, 31043 (2012).

255. Mowery, B. P. *et al.* Mimicry of antimicrobial host-defense peptides by random copolymers. *J Am Chem Soc* **129**, 15474–15476 (2007).

256. Takahashi, H., Palermo, E. F., Yasuhara, K., Caputo, G. A. & Kuroda, K. Molecular Design, Structures, and Activity of Antimicrobial Peptide-Mimetic Polymers. *Macromol Biosci* **13**, 1285–1299 (2013).

257. Foster, L. L., Mizutani, M., Oda, Y., Palermo, E. F. & Kuroda, K. Design and Synthesis of Amphiphilic Vinyl Copolymers with Antimicrobial Activity. *Polymers for Biomedicine* 243–272 (2017) doi:10.1002/9781118967904.CH8.

258. Locock, K. E. S., Michl, T. D., Griesser, H. J., Haeussler, M. & Meagher, L. Structure–activity relationships of guanylated antimicrobial polymethacrylates. *Pure and Applied Chemistry* **86**, 1281–1291 (2014).

259. Palermo, E. F., Lienkamp, K., Gillies, E. R. & Ragogna, P. J. Antibacterial Activity of Polymers: Discussions on the Nature of Amphiphilic Balance. *Angewandte Chemie International Edition* **58**, 3690–3693 (2019).

260. Mankoci, S., Kaiser, R. L., Sahai, N., Barton, H. A. & Joy, A. Bactericidal Peptidomimetic Polyurethanes with Remarkable Selectivity against Escherichia coli. *ACS Biomater Sci Eng* **3**, 2588–2597 (2017).

261. Mizutani, M. *et al.* Design and synthesis of self-degradable antibacterial polymers by simultaneous chain- and step-growth radical copolymerization. *Biomacromolecules* **13**, 1554–1563 (2012).

262. Delplace, V. & Nicolas, J. Degradable vinyl polymers for biomedical applications. *Nature Chemistry 2015 7:10* **7**, 771–784 (2015).

263. Holden, M. T. G. *et al.* Rapid Evolution of Virulence and Drug Resistance in the Emerging Zoonotic Pathogen Streptococcus suis. *PLoS One* **4**, e6072 (2009).

264. García-Gallego, S. *et al.* Function Oriented Molecular Design: Dendrimers as Novel Antimicrobials. *Molecules 2017, Vol. 22, Page 1581* **22**, 1581 (2017).

265. Van Dongen, M. A. *et al.* Avidity mechanism of dendrimer-folic acid conjugates. *Mol Pharm* **11**, 1696–1706 (2014).

266. Gupta, U. & Perumal, O. Dendrimers and Its Biomedical Applications. *Natural and Synthetic Biomedical Polymers* 243–257 (2014) doi:10.1016/B978-0-12-396983-5.00016-8.

267. Freeman, E. C., Weiland, L. M. & Meng, W. S. Modeling the proton sponge hypothesis: examining proton sponge effectiveness for enhancing intracellular gene delivery through multiscale modeling. *http://dx.doi.org/10.1080/09205063.2012.690282* **24**, 398–416 (2013).

268. Tomalia, D. A. *et al.* A New Class of Polymers: Starburst-Dendritic Macromolecules. *Polymer Journal 1985 17:1* **17**, 117–132 (1985).

269. Newkome, G. R., Yao, Z. Q., Baker, G. R. & Gupta, V. K. Cascade Molecules: A New Approach to Micelles.1aA [27]-Arborol. *Journal of Organic Chemistry* **50**, 2003–2004 (1985).

270. Falanga, A., Del Genio, V. & Galdiero, S. Peptides and Dendrimers: How to Combat Viral and Bacterial Infections. *Pharmaceutics 2021, Vol. 13, Page 101* **13**, 101 (2021).

271. Wrońska, N., Majoral, J. P., Appelhans, D., Bryszewska, M. & Lisowska, K. Synergistic Effects of Anionic/Cationic Dendrimers and Levofloxacin on Antibacterial Activities. *Molecules 2019, Vol. 24, Page 2894* **24**, 2894 (2019).

272. Cheng, Y. *et al.* Polyamidoamine (PAMAM) dendrimers as biocompatible carriers of quinolone antimicrobials: An in vitro study. *Eur J Med Chem* **42**, 1032–1038 (2007).

273. Mosca, S. *et al.* Amphiphilic cationic β3R3-peptides: Membrane active peptidomimetics and their potential as antimicrobial agents. *Biomacromolecules* **15**, 1687–1695 (2014).

274. Lee, J. *et al.* Effect of side chain hydrophobicity and cationic charge on antimicrobial activity and cytotoxicity of helical peptoids. *Bioorg Med Chem Lett* **28**, 170–173 (2018).

275. Winnicka, K., Wroblewska, M., Wieczorek, P., Sacha, P. T. & Tryniszewska, E. A. The Effect of PAMAM Dendrimers on the Antibacterial Activity of Antibiotics with Different Water Solubility. *Molecules 2013, Vol. 18, Pages 8607-8617* **18**, 8607–8617 (2013).

276. Gholami, M. *et al.* In vitro antibacterial activity of poly (amidoamine)-G7 dendrimer. *BMC Infect Dis* **17**, 1–11 (2017).

277. McNerny, D. Q., Leroueil, P. R. & Baker, J. R. Understanding specific and nonspecific toxicities: a requirement for the development of dendrimer-based pharmaceuticals. *Wiley Interdiscip Rev Nanomed Nanobiotechnol* **2**, 249–259 (2010).

278. Ortega, P. *et al.* Amine and ammonium functionalization of chloromethylsilane-ended dendrimers. Antimicrobial activity studies. *Org Biomol Chem* **6**, 3264–3269 (2008).

279. Xue, X. *et al.* Amino-terminated generation 2 poly(amidoamine) dendrimer as a potential broad-spectrum, nonresistance-inducing antibacterial agent. *AAPS Journal* **15**, 132–142 (2013).

280. Worley, B. V., Slomberg, D. L. & Schoenfisch, M. H. Nitric oxide-releasing quaternary ammonium-modified poly(amidoamine) dendrimers as dual action antibacterial agents. *Bioconjug Chem* **25**, 918–927 (2014).

281. Sun, B., Slomberg, D. L., Chudasama, S. L., Lu, Y. & Schoenfisch, M. H. Nitric oxide-releasing dendrimers as antibacterial agents. *Biomacromolecules* **13**, 3343–3354 (2012).

282. Jevprasesphant, R. *et al.* The influence of surface modification on the cytotoxicity of PAMAM dendrimers. *Int J Pharm* **252**, 263–266 (2003).

283. De Queiroz, A. A. A. *et al.* Physicochemical and antimicrobial properties of boron-complexed polyglycerol–chitosan dendrimers. *http://dx.doi.org/10.1163/156856206777346313* **17**, 689–707 (2012).

284. Felczak, A. *et al.* Antimicrobial activity of poly(propylene imine) dendrimers. *New Journal of Chemistry* **36**, 2215–2222 (2012).

285. Mohammadi, M. J. *et al.* The antibacterial effect of G3-poly-amidoamine dendrimer on gram negative and gram positive bacteria in aqueous solutions. *Desalination Water Treat* **124**, 223–231 (2018).

286. Pires, J. *et al.* In Vitro activity of the novel antimicrobial peptide dendrimer G3KL against multidrug-resistant Acinetobacter baumannii and Pseudomonas aeruginosa. *Antimicrob Agents Chemother* **59**, 7915–7918 (2015).

287. Jain, K., Kesharwani, P., Gupta, U. & Jain, N. K. Dendrimer toxicity: Let's meet the challenge. *Int J Pharm* **394**, 122–142 (2010).

288. Malik, N. *et al.* Dendrimers:: Relationship between structure and biocompatibility in vitro, and preliminary studies on the biodistribution of 125I-labelled polyamidoamine dendrimers in vivo. *Journal of Controlled Release* **65**, 133–148 (2000).

289. Mukherjee, S. P., Davoren, M. & Byrne, H. J. In vitro mammalian cytotoxicological study of PAMAM dendrimers – Towards quantitative structure activity relationships. *Toxicology in Vitro* **24**, 169–177 (2010).

290. Mukherjee, S. P., Lyng, F. M., Garcia, A., Davoren, M. & Byrne, H. J. Mechanistic studies of in vitro cytotoxicity of poly(amidoamine) dendrimers in mammalian cells. *Toxicol Appl Pharmacol* **248**, 259–268 (2010).

291. Hong, S. *et al.* Interaction of Polycationic Polymers with Supported Lipid Bilayers and Cells: Nanoscale Hole Formation and Enhanced Membrane Permeability. *Bioconjug Chem* **17**, 728–734 (2006).

292. Wang, R. E. *et al.* Development of self-immolative dendrimers for drug delivery and sensing. *Journal of Controlled Release* **159**, 154–163 (2012).

293. García-Gallego, S., Hult, D., Olsson, J. V. & Malkoch, M. Fluoride-Promoted Esterification with Imidazolide-Activated Compounds: A Modular and Sustainable Approach to Dendrimers. *Angewandte Chemie International Edition* **54**, 2416–2419 (2015).

294. Carlmark, A., Hawker, C., Hult, A. & Malkoch, M. New methodologies in the construction of dendritic materials. *Chem Soc Rev* **38**, 352–362 (2009).

295. Carlmark, A., Malmström, E. & Malkoch, M. Dendritic architectures based on bis-MPA: functional polymeric scaffolds for application-driven research. *Chem Soc Rev* **42**, 5858–5879 (2013).

296. Feliu, N. *et al.* Stability and biocompatibility of a library of polyester dendrimers in comparison to polyamidoamine dendrimers. *Biomaterials* **33**, 1970–1981 (2012).

297. Fan, Y. *et al.* Self-Assembled Polyester Dendrimer/Cellulose Nanofibril Hydrogels with Extraordinary Antibacterial Activity. *Pharmaceutics 2020, Vol. 12, Page 1139* **12**, 1139 (2020).

298. Stenström, P. *et al.* Synthesis and in Vitro Evaluation of Monodisperse Amino-Functional Polyester Dendrimers with Rapid Degradability and Antibacterial Properties. *Biomacromolecules* **18**, 4323–4330 (2017).

299. Stenström, P. *et al.* UV-Cured Antibacterial Hydrogels Based on PEG and Monodisperse Heterofunctional Bis-MPA Dendrimers. *Molecules 2021, Vol. 26, Page 2364* **26**, 2364 (2021).

300. Namata, F., Sanz del Olmo, N., Molina, N. & Malkoch, M. Synthesis and Characterization of Amino-Functional Polyester Dendrimers Based On Bis-MPA with Enhanced Hydrolytic Stability and Inherent Antibacterial Properties. *Biomacromolecules* **24**, 858–867 (2023).

301. Del Olmo, N. S. *et al.* Antioxidant and Antibacterial Properties of Carbosilane Dendrimers Functionalized with Polyphenolic Moieties. *Pharmaceutics 2020, Vol. 12, Page 698* **12**, 698 (2020).

302. Rodríguez-Prieto, T. *et al.* Silver (I) N-Heterocyclic Carbenes Carbosilane Dendritic Systems and Their Imidazolium-Terminated Analogues as Antibacterial Agents: Study of Their Mode of Action. *Pharmaceutics 2020, Vol. 12, Page 968* **12**, 968 (2020).

303. Kumar, B., Smita, K., Cumbal, L. & Debut, A. Green synthesis of silver nanoparticles using Andean blackberry fruit extract. *Saudi J Biol Sci* **24**, 45–50 (2017).

304. Moritaka, H., Nishinari, K., Nakahama, N. & Fukuba, H. Effects of Potassium Chloride and Sodium Chloride on the Thermal Properties of Gellan Gum Gels. *Biosci Biotechnol Biochem* **56**, 595–599 (1992).

305. Nishinari, K. Rheological and DSC study of sol-gel transition in aqueous dispersions of industrially important polymers and colloids. *Colloid Polym Sci* **275**, 1093–1107 (1997).

306. Ogawa, E., Matsuzawa, H. & Iwahashi, M. Conformational transition of gellan gum of sodium, lithium, and potassium types in aqueous solutions. *Food Hydrocoll* **16**, 1–9 (2002).

307. Buck, E., Maisuria, V., Tufenkji, N. & Cerruti, M. Antibacterial Properties of PLGA Electrospun Scaffolds Containing Ciprofloxacin Incorporated by Blending or Physisorption. *ACS Appl Bio Mater* **1**, 627–635 (2018).

308. Bayat, F. & Karimi, A. R. Design of photodynamic chitosan hydrogels bearing phthalocyanine-colistin conjugate as an antibacterial agent. *Int J Biol Macromol* **129**, 927–935 (2019).

309. Panáček, A. *et al.* Bacterial resistance to silver nanoparticles and how to overcome it. *Nature Nanotechnology 2017 13:1* **13**, 65–71 (2017).

310. Pitarresi, G., Martorana, A., Palumbo, F. S., Fiorica, C. & Giammona, G. New gellan gum-graft-poly(d,l-lactide-co-glycolide) copolymers as promising bioinks: Synthesis and characterization. *Int J Biol Macromol* **162**, 1653–1667 (2020).

311. Agnello, S. *et al.* Synthesis, mechanical and thermal rheological properties of new gellan gum derivatives. *Int J Biol Macromol* **98**, 646–653 (2017).

312. Ravindranath, S. & Wang, S.-Q. Large amplitude oscillatory shear behavior of entangled polymer solutions: Particle tracking velocimetric investigation. *J Rheol (N Y N Y)* **52**, 341–358 (2008).

313. Hyun, C. *et al.* Review of Nonlinear Oscillatory Shear Tests: Analysis and Application of Large Amplitude Oscillatory Shear (LAOS). *Prog Polym Sci* **36**, 1697–1753 (2011).

314. Tong, K., Xiao, G., Cheng, W., Chen, J. & Sun, P. Large amplitude oscillatory shear behavior and gelation procedure of high and low acyl gellan gum in aqueous solution. *Carbohydr Polym* **199**, 397–405 (2018).

315. Ogawa, E., Takahashi, R., Yajima, H. & Nishinari, K. Effects of molar mass on the coil to helix transition of sodium-type gellan gums in aqueous solutions. *Food Hydrocoll* **20**, 378–385 (2006).

316. Pitarresi, G., Fiorica, C., Licciardi, M., Palumbo, F. S. & Giammona, G. New hyaluronic acid based brush copolymers synthesized by atom transfer radical polymerization. *Carbohydr Polym* **92**, 1054–1063 (2013).

317. Agnello, S., Palumbo, F. S., Pitarresi, G., Fiorica, C. & Giammona, G. Synthesis and evaluation of thermo-rheological behaviour and ionotropic crosslinking of new gellan gum-alkyl derivatives. *Carbohydr Polym* **185**, 73–84 (2018).

318. Palumbo, F. S. *et al.* In situ forming hydrogels of hyaluronic acid and inulin derivatives for cartilage regeneration. *Carbohydr Polym* **122**, 408–16 (2014).

319. Fiorica, C., Palumbo, F. S., Pitarresi, G., Bongiovì, F. & Giammona, G. Hyaluronic acid and beta cyclodextrins films for the release of corneal epithelial cells and dexamethasone. *Carbohydr Polym* **166**, 281–290 (2017).

320. Fiorica, C. *et al.* Double-Network-Structured Graphene Oxide-Containing Nanogels as Photothermal Agents for the Treatment of Colorectal Cancer. *Biomacromolecules* **18**, 1010–1018 (2017).

321. Shojaee Kang Sofla, M., Mortazavi, S. & Seyfi, J. Preparation and characterization of polyvinyl alcohol/chitosan blends plasticized and compatibilized by glycerol/polyethylene glycol. *Carbohydr Polym* **232**, 115784 (2020).

322. Li, D. *et al.* Preparation of plasticized poly (lactic acid) and its influence on the properties of composite materials. *PLoS One* **13**, e0193520 (2018).

323. Wang, X. *et al.* A Polydopamine Nanoparticle-Knotted Poly(ethylene glycol) Hydrogel for On-Demand Drug Delivery and Chemo-photothermal Therapy. *Chemistry of Materials* **29**, 1370–1376 (2017).

324. Naseri-Nosar, M. & Ziora, Z. M. Wound dressings from naturally-occurring polymers: A review on homopolysaccharide-based composites. *Carbohydr Polym* **189**, 379–398 (2018).

325. Vieira, S. *et al.* Self-mineralizing Ca-enriched methacrylated gellan gum beads for bone tissue engineering. *Acta Biomater* **93**, 74–85 (2019).

326. Chen, H. *et al.* Bone Marrow-Derived Mesenchymal Stem Cells Encapsulated in Functionalized Gellan Gum/Collagen Hydrogel for Effective Vascularization. *ACS Appl Bio Mater* **1**, 1408–1415 (2018).

327. Wiegand, C., Abel, M., Hipler, U.-C. & Elsner, P. Effect of non-adhering dressings on promotion of fibroblast proliferation and wound healing in vitro. *Sci Rep* **9**, 4320 (2019).

328. Chang, P.-H. *et al.* Interaction of ciprofloxacin and probe compounds with palygorskite PFl-1. *J Hazard Mater* **303**, 55–63 (2016).

329. Tao, B. *et al.* Near infrared light-triggered on-demand Cur release from Gel-PDA@Cur composite hydrogel for antibacterial wound healing. *Chemical Engineering Journal* **403**, 126182 (2021).

330. Sahu, A. *et al.* Nanographene oxide as a switch for CW/pulsed NIR laser triggered drug release from liposomes. *Materials Science and Engineering: C* **82**, 19–24 (2018).

331. Mauro, N. *et al.* A self-sterilizing fluorescent nanocomposite as versatile material with broad-spectrum antibiofilm features. *Materials Science and Engineering: C* **117**, 111308 (2020).

332. Fiorica, C. *et al.* Physicochemical and rheological characterization of different low molecular weight gellan gum products and derived ionotropic crosslinked hydrogels. *Gels* **7**, (2021).

333. Kim, H. S. *et al.* Engineering retinal pigment epithelial cells regeneration for transplantation in regenerative medicine using PEG/Gellan gum hydrogels. *Int J Biol Macromol* **130**, 220–228 (2019).

334. Learmonth, D. A. *et al.* Synthesis and biological evaluation of a bioinspired, tissue-adhesive gellan gum-based hydrogel designed for minimally invasive delivery and retention of chondrogenic cells †. *Cite this: Biomater. Sci* **8**, 3697 (2020).

335. Iudin, D. *et al.* Hybrid Nanoparticles and Composite Hydrogel Systems for Delivery of Peptide Antibiotics. *Int J Mol Sci* **23**, (2022).

336. Phogat, K. & Bandyopadhyay-Ghosh, S. Nanocellulose mediated injectable bio-nanocomposite hydrogel scaffold-microstructure and rheological properties. *Cellulose* **25**, 5821–5830 (2018).

337. Gong, C., Lu, C., Li, B., Meng, S. & Wu, G. Dopamine-modified poly(amino acid): an efficient near-infrared photothermal therapeutic agent for cancer therapy. doi:10.1007/s10853-016-0391-9.

338. Chiron, E. *et al.* A physicochemical assessment of the thermal stability of dextrin-colistin conjugates. *Scientific Reports* | **11**, 10600 (123AD).

339. Li, J., Milne, R. W., Nation, R. L., Turnidge, J. D. & Coulthard, K. Stability of colistin and colistin methanesulfonate in aqueous media and plasma as determined by high-performance liquid chromatography. *Antimicrob Agents Chemother* **47**, 1364–1370 (2003).

340. Zhao, C. *et al.* 2102391 (1 of 14) Site-Specific Biomimicry of Antioxidative Melanin Formation and Its Application for Acute Liver Injury Therapy and Imaging. (2021) doi:10.1002/adma.202102391.

341. Hu, J. *et al.* Biomaterials Science REVIEW Polydopamine free radical scavengers. *Cite this: Biomater. Sci* **8**, 4940 (2020).

342. Hou, J., Li, C., Guan, Y., Zhang, Y. & Zhu, X. X. Enzymatically crosslinked alginate hydrogels with improved adhesion properties. *Polym Chem* **6**, 2204–2213 (2015).

343. Biscari, G. *et al.* Near-infrared light-responsive and antibacterial injectable hydrogels with antioxidant activity based on a Dopamine-functionalized Gellan Gum for wound healing. *Int J Pharm* **627**, 122257 (2022).

344. Liang, Y., He, J. & Guo, B. Functional Hydrogels as Wound Dressing to Enhance Wound Healing. *ACS Nano* **15**, 12687–12722 (2021).

345. Zhang, A. *et al.* Research status of self-healing hydrogel for wound management: A review. *Int J Biol Macromol* **164**, 2108–2123 (2020).

346. Watters, C., Yuan, T. T. & Rumbaugh, K. P. Beneficial and deleterious bacterial–host interactions in chronic wound pathophysiology. *Chronic Wound Care Management and Research* **2**, 53–62 (2015).

347. Yang, J., Cohen Stuart, M. A. & Kamperman, M. Jack of all trades: versatile catechol crosslinking mechanisms. *Chem Soc Rev* **43**, 8271–8298 (2014).

348. Ma, Y. *et al.* Chitosan membrane dressings toughened by glycerol to load antibacterial drugs for wound healing. *Materials Science and Engineering: C* **81**, 522–531 (2017).

349. Chen, X. Making Electrodes Stretchable. *Small Methods* **1**, 1600029 (2017).

350. Zhao, X. *et al.* Physical Double-Network Hydrogel Adhesives with Rapid Shape Adaptability, Fast Self-Healing, Antioxidant and NIR/pH Stimulus-Responsiveness for Multidrug-Resistant Bacterial Infection and Removable Wound Dressing. *Adv Funct Mater* **30**, 1910748 (2020).

351. Wei, Z. *et al.* Novel Biocompatible Polysaccharide-Based Self-Healing Hydrogel. *Adv Funct Mater* **25**, 1352–1359 (2015).

352. Bielfeldt, S., Brandt, M. & Waring, M. Skin adhesion properties of three dressings used for acute wounds. (2009).

353. Fischer, L. *et al.* Sequence-defined positioning of amine and amide residues to control catechol driven wet adhesion. *Chem Sci* **11**, 9919–9924 (2020).

354. You, H. J. & Han, S. K. Cell Therapy for Wound Healing. *J Korean Med Sci* **29**, 311–319 (2014).

355. Edmonds, M. & Group, E. and A. A. D. F. U. S. Apligraf in the Treatment of Neuropathic Diabetic Foot Ulcers. *http://dx.doi.org/10.1177/1534734609331597* **8**, 11–18 (2009).

356. Da Silva, L. P., Reis, R. L., Correlo, V. M. & Marques, A. P. Hydrogel-Based Strategies to Advance Therapies for Chronic Skin Wounds. *https://doi.org/10.1146/annurev-bioeng-060418-052422* **21**, 145–169 (2019).

357. Wojtowicz, A. M. *et al.* The importance of both fibroblasts and keratinocytes in a bilayered living cellular construct used in wound healing. *Wound Repair and Regeneration* **22**, 246–255 (2014).

358. Hu, M. S. *et al.* Delivery of monocyte lineage cells in a biomimetic scaffold enhances tissue repair. *JCI Insight* **2**, (2017).

359. Pitarresi, G. *et al.* Developing Antibiofilm Fibrillar Scaffold with Intrinsic Capacity to Produce Silver Nanoparticles. *Int J Mol Sci* **23**, 15378 (2022).

360. Biscari, G. *et al.* Antibacterial Broad-Spectrum Dendritic/Gellan Gum Hybrid Hydrogels with Rapid Shape-Forming and Self-Healing for Wound Healing Application. *Macromol Biosci* 2300224 (2023) doi:10.1002/MABI.202300224.

361. Kajani, A. A., Bordbar, A. K., Zarkesh Esfahani, S. H., Khosropour, A. R. & Razmjou, A. Green synthesis of anisotropic silver nanoparticles with potent anticancer activity using Taxus baccata extract. *RSC Adv* **4**, 61394–61403 (2014).

362. Radoń, A. & Łukowiec, D. Silver nanoparticles synthesized by UV-irradiation method using chloramine T as modifier: structure, formation mechanism and catalytic activity. *CrystEngComm* **20**, 7130–7136 (2018).

363. Shrestha, S., Wang, B. & Dutta, P. Nanoparticle processing: Understanding and controlling aggregation. *Adv Colloid Interface Sci* **279**, 102162 (2020).

364. Bekhit, M., Abu el-naga, M. N., Sokary, R., Fahim, R. A. & El-Sawy, N. M. Radiation-induced synthesis of tween 80 stabilized silver nanoparticles for antibacterial applications. *https://doi.org/10.1080/10934529.2020.1784656* **55**, 1210–1217 (2020).

365. Craparo, E. F., Drago, S. E., Quaglia, F., Ungaro, F. & Cavallaro, G. Development of a novel rapamycin loaded nano- into micro-formulation for treatment of lung inflammation. *Drug Deliv Transl Res* **12**, 1859–1872 (2022).

366. Devi, B. L., Rao, K. M. & Ramananda, D. Spectroscopic investigation of green synthesized ZnS nanoparticles encapsulated by sodium carboxy methyl cellulose. *Appl Phys A Mater Sci Process* **126**, 1–11 (2020).

367. Alshehri, A. A. & Malik, M. A. Phytomediated Photo-Induced Green Synthesis of Silver Nanoparticles Using Matricaria chamomilla L. and Its Catalytic Activity against Rhodamine B. *Biomolecules 2020, Vol. 10, Page 1604* **10**, 1604 (2020).

368. Monisha, S. *et al.* Investigation of bio polymer electrolyte based on cellulose acetate-ammonium nitrate for potential use in electrochemical devices. *Carbohydr Polym* **157**, 38–47 (2017).

369. Ghavaminejad, A., Park, C. H. & Kim, C. S. In Situ Synthesis of Antimicrobial Silver Nanoparticles within Antifouling Zwitterionic Hydrogels by Catecholic Redox Chemistry for Wound Healing Application. *Biomacromolecules* **17**, 1213–1223 (2016).

370. Pirtarighat, S., Ghannadnia, M. & Baghshahi, S. Green synthesis of silver nanoparticles using the plant extract of Salvia spinosa grown in vitro and their antibacterial activity assessment. *J Nanostructure Chem* **9**, 1–9 (2019).

371. Ssekatawa, K. *et al.* Green Strategy–Based Synthesis of Silver Nanoparticles for Antibacterial Applications. *Frontiers in Nanotechnology* **3**, 59 (2021).

372. Bootharaju, M. S. & Pradeep, T. Uptake of toxic metal ions from water by naked and monolayer protected silver nanoparticles: An x-ray photoelectron spectroscopic investigation. *Journal of Physical Chemistry C* **114**, 8328–8336 (2010).

373. Macková, A. *et al.* RBS, XPS, and TEM study of metal and polymer interface modified by plasma treatment. *Vacuum* **82**, 307–310 (2007).

374. Abazari, M. *et al.* Polysaccharide-based hydrogels containing herbal extracts for wound healing applications. *Carbohydr Polym* **294**, 119808 (2022).

375. Hu, H. & Xu, F. J. Rational design and latest advances of polysaccharide-based hydrogels for wound healing. *Biomater Sci* **8**, 2084–2101 (2020).

376. Raina, N., Pahwa, R., Thakur, V. K. & Gupta, M. Polysaccharide-based hydrogels: New insights and futuristic prospects in wound healing. *Int J Biol Macromol* **223**, 1586–1603 (2022).

377. Yang, Y. *et al.* Recent advances in polysaccharide-based self-healing hydrogels for biomedical applications. *Carbohydr Polym* **283**, 119161 (2022).

378. Tang, X. *et al.* Stable antibacterial polysaccharide-based hydrogels as tissue adhesives for wound healing. *RSC Adv* **10**, 17280–17287 (2020).

379. Paiva, D., Gonçalves, C., Vale, I., Bastos, M. M. S. M. & Magalhães, F. D. Oxidized Xanthan Gum and Chitosan as Natural Adhesives for Cork. *Polymers 2016, Vol. 8, Page 259* **8**, 259 (2016).

380. Fan, Y. *et al.* Dendritic Hydrogels Induce Immune Modulation in Human Keratinocytes and Effectively Eradicate Bacterial Pathogens. *J Am Chem Soc* **143**, 17180–17190 (2021).

381. Lv, Y. *et al.* Multi-crosslinked hydrogels with strong wet adhesion, self-healing, antibacterial property, reactive oxygen species scavenging activity, and on-demand removability for seawater-immersed wound healing. *Acta Biomater* **159**, 95–110 (2023).

382. Zhang, Q. *et al.* Nucleotide-Regulated Tough and Rapidly Self-Recoverable Hydrogels for Highly Sensitive and Durable Pressure and Strain Sensors. *Chemistry of Materials* **31**, 5881–5889 (2019).

383. Yan, L. *et al.* Conductive Cellulose Bio-Nanosheets Assembled Biostable Hydrogel for Reliable Bioelectronics. *Adv Funct Mater* **31**, 2010465 (2021).

384. Li, S. *et al.* Rapid Fabrication of Self-Healing, Conductive, and Injectable Gel as Dressings for Healing Wounds in Stretchable Parts of the Body. *Adv Funct Mater* **30**, 2002370 (2020).

385. Hirose, R. *et al.* Differences between two sodium hyaluronate-based submucosal injection materials currently used in Japan based on viscosity analysis. *Scientific Reports 2021 11:1* **11**, 1–10 (2021).

386. Chen, M. *et al.* A self-healing, magnetic and injectable biopolymer hydrogel generated by dual cross-linking for drug delivery and bone repair. *Acta Biomater* **153**, 159–177 (2022).

387. Shiekh, P. A., Singh, A. & Kumar, A. Exosome laden oxygen releasing antioxidant and antibacterial cryogel wound dressing OxOBand alleviate diabetic and infectious wound healing. *Biomaterials* **249**, 120020 (2020).

388. Zhang, H. *et al.* Multifunctional Injectable Hydrogel Dressings for Effectively Accelerating Wound Healing: Enhancing Biomineralization Strategy. *Adv Funct Mater* **31**, 2100093 (2021).

389. Wang, L., Hu, C. & Shao, L. The antimicrobial activity of nanoparticles: present situation and prospects for the future. *Int J Nanomedicine* **12**, 1227 (2017).

390. Zhang, L., Pornpattananangkul, D., Hu, C.-M. J. & Huang, C.-M. Development of Nanoparticles for Antimicrobial Drug Delivery. *Curr Med Chem* **17**, 585–594 (2010).

391. Beyth, N., Houri-Haddad, Y., Domb, A., Khan, W. & Hazan, R. Alternative antimicrobial approach: Nano-antimicrobial materials. *Evidence-based Complementary and Alternative Medicine* **2015**, (2015).

392. Dakal, T. C., Kumar, A., Majumdar, R. S. & Yadav, V. Mechanistic basis of antimicrobial actions of silver nanoparticles. *Front Microbiol* **7**, 1831 (2016).

393. Mesallati, H. & Tajber, L. Polymer/Amorphous Salt Solid Dispersions of Ciprofloxacin. doi:10.1007/s11095-017-2250-z.

394. Federico, S. *et al.* An asymmetric electrospun membrane for the controlled release of ciprofloxacin and FGF-2: Evaluation of antimicrobial and chemoattractant properties. *Materials Science and Engineering: C* **123**, 112001 (2021).

395. Vella, J. *et al.* A simple HPLC–UV method for the determination of ciprofloxacin in human plasma. *Journal of Chromatography B* **989**, 80–85 (2015).

396. Wang, Q. *et al.* Bioinspired Polydopamine-Coated Hemoglobin as Potential Oxygen Carrier with Antioxidant Properties. (2017) doi:10.1021/acs.biomac.7b00077.

397. Re, R. *et al. Original Contribution ANTIOXIDANT ACTIVITY APPLYING AN IMPROVED ABTS RADICAL CATION DECOLORIZATION ASSAY*. (1999).

398. Federico, S. *et al.* Photothermal nanofibrillar membrane based on hyaluronic acid and graphene oxide to treat Staphylococcus aureus and Pseudomonas aeruginosa infected wounds. *Int J Biol Macromol* **214**, 470–479 (2022).

399. Wiegand, I., Hilpert, K. & Hancock, R. E. W. Agar and broth dilution methods to determine the minimal inhibitory concentration (MIC) of antimicrobial substances. *Nature Protocols 2008 3:2* **3**, 163–175 (2008).

400. Jiang, Y. *et al.* Controlled release of silver ions from AgNPs using a hydrogel based on konjac glucomannan and chitosan for infected wounds. *Int J Biol Macromol* **149**, 148–157 (2020).

401. Huang, J. *et al.* Novel in situ forming hydrogel based on xanthan and chitosan re-gelifying in liquids for local drug delivery. *Carbohydr Polym* **186**, 54–63 (2018).

402. Guo, J., Ge, L., Li, X., Mu, C. & Li, D. Periodate oxidation of xanthan gum and its crosslinking effects on gelatin-based edible films. *Food Hydrocoll* **39**, 243–250 (2014).

403. Li, P. *et al.* Building a Poly(amino acid)/Chitosan-Based Self-Healing Hydrogel via Host–Guest Interaction for Cartilage Regeneration. *ACS Biomater Sci Eng* (2023) doi:10.1021/ACSBIOMATERIALS.2C01547/ASSET/IMAGES/LARGE/AB2C01547_0008.JPEG.

404. Salick, D. A., Kretsinger, J. K., Pochan, D. J. & Schneider, J. P. Inherent antibacterial activity of a peptide-based β-hairpin hydrogel. *J Am Chem Soc* **129**, 14793–14799 (2007).

Publications:

- PHYSICOCHEMICAL AND RHEOLOGICAL CHARACTERIZATION OF DIFFERENT LOW MOLECULAR WEIGHT GELLAN GUM PRODUCTS AND DERIVED IONOTROPIC CROSSLINKED HYDROGELS
  Calogero Fiorica, Giuseppina Biscari, Fabio Salvatore Palumbo, Giovanna Pitarresi, Annalisa Martorana, Gaetano Giammona
  Gels, 2021, 7, 62 (pp14).

- CIPROFLOXACIN RELEASING GELLAN GUM/POLYDOPAMINE BASED HYDROGELS WITH NEAR INFRARED ACTIVATED PHOTOTHERMAL PROPERTIES
  Calogero Fiorica, Fabio S. Palumbo, Giovanna Pitarresi, Giuseppina Biscari, Annalisa Martorana, Cinzia Calà, Carmelo M. Maida, Gaetano Giammona
  International Journal of Pharmaceutics, 610 (2021) 121231.

- NEAR-INFRARED LIGHT-RESPONSIVE AND ANTIBACTERIAL INJECTABLE HYDROGELS WITH ANTIOXIDANT ACTIVITY BASED ON A DOPAMINE-FUNCTIONALIZED GELLAN GUM FOR WOUND HEALING
  Giuseppina Biscari, Giovanna Pitarresi, Calogero Fiorica, Domenico Schillaci, Valentina Catania, Fabio Salvatore Palumbo, Gaetano Giammona
  International Journal of Pharmaceutics, 627 (2022) 122257.

- DEVELOPING ANTIBIOFILM FIBRILLAR SCAFFOLD WITH INTRINSIC CAPACITY TO PRODUCE SILVER NANOPARTICLES
  Giovanna Pitarresi, Giuseppe Barberi, Fabio Salvatore Palumbo, Domenico Schillaci, Calogero Fiorica, Valentina Catania, Serena indelicato, David Bongiorno, Giuseppina Biscari, Gaetano Giammona
  International Journal of Molecular Sciences, 23 (2022) 15378.

- ANTIBACTERIAL BROAD-SPECTRUM DENDRITIC/GELLAN GUM HYBRID HYDROGELS WITH RAPID SHAPE-FORMING AND SELF-HEALING FOR WOUND HEALING APPLICATION
  Giuseppina Biscari, Yanmiao Fan, Faridah Namata, Calogero Fiorica, Michael Malkoch, Fabio Salvatore Palumbo, Giovanna Pitarresi
  Macromolecular Bioscience (2023) 2300224.

Publications under review:

- IN SITU SYNTHESIS OF SILVER NANOPARTICLES AND DEVELOPMENT OF NANO/MICRO-COMPOSITE INJECTABLE HYDROGEL WITH ANTIMICROBIAL ACTIVITY
  Giuseppina Biscari, Michael Malkoch, Calogero Fiorica, Yanmiao Fan, Fabio Salvatore Palumbo, Serena Indelicato, David Bongiorno, Giovanna Pitarresi